Synthesis and transfer of nanosheets seed layers on various substrates for the preferentially oriented growth of complex oxides thin films

Florent Baudouin

UNIVERSITÉ DE RENNES 1

THESE DE DOCTORAT DE

L'UNIVERSITE DE RENNES 1

ECOLE DOCTORALE N° 596
Matière, Molécules, Matériaux
Spécialité : *Sciences des matériaux*

Par
Florent BAUDOUIN

Synthesis and transfer of nanosheets seed layers on various substrates for the preferentially oriented growth of complex oxides thin films

Soutenance prévue à Rennes, le 7 décembre 2021
Unité de recherche : Institut des Sciences Chimiques de Rennes – UMR CNRS 6226

Composition du Jury :

Président :	**Andre TEN ELSHOF**	Professeur – MESA+ Institute, Twente, Pays Bas
Rapporteurs :	**Nathalie LEMÉE**	Maître de conférences – LPMC, Amiens, France
	Guillaume ROGEZ	Directeur de recherche CNRS – IPCMS, Strasbourg, France
Examinateurs :	**Aline ROUGIER**	Directrice de recherche CNRS – ICMCB, Bordeaux, France
	Christophe CIBERT	Maître de conférences – CRISMAT, Caen, France
	Arnaud FOUCHET	Chargé de recherche CNRS – CRISMAT, Caen, France
Dir. de thèse :	**Maryline GUILLOUX-VIRY**	Professeure – ISCR Rennes, France
Co-dir. de thèse :	**Valérie DEMANGE**	Chargée de recherche CNRS – ISCR Rennes, France

Remerciements

Ces travaux de thèse ont été réalisés à l'Institut des Sciences Chimiques de Rennes (ISCR – UMR CNRS 6226) dirigé par Monsieur Marc Fourmigué, au sein de l'équipe Chimie du Solide et Matériaux dirigée par Monsieur Stéphane Cordier.

Je remercie vivement Monsieur André Ten Elshof, professeur à l'Institut MESA+ (Twente, Pays-Bas) d'avoir présidé le jury de thèse, Madame Nathalie Lemée, maître de conférences au LPMC (Amiens) et Monsieur Guillaume Rogez, directeur de recherche CNRS à l'IPCMS (Strasbourg), d'avoir accepté d'être rapporteurs de cette thèse. Je remercie également Madame Aline Rougier, directrice de recherche CNRS à l'ICMCB (Bordeaux), Monsieur Arnaud Fouchet, chargé de recherche CNRS au laboratoire CRISMAT (Caen), et Monsieur Christophe Cibert, maître de conférences au laboratoire CRISMAT (Caen), pour m'avoir fait l'honneur d'examiner ce travail.

J'adresse un immense merci à Madame Valérie Demange, co-directrice de thèse, qui a majoritairement supervisé ce travail. Merci de m'avoir fait confiance depuis le master sur ce sujet de recherche. Merci de ta disponibilité et de ton soutien sans faille. Ce fût un plaisir de travailler avec toi pendant plus de 3 ans ! Je remercie sincèrement Madame Maryline Guilloux-Viry, directrice de thèse, pour ses précieux conseils et d'avoir toujours eu les mots pour me rassurer et m'encourager tout au long de cette thèse. Je suis très reconnaissant d'avoir eu l'opportunité de travailler sous la direction de ces deux encadrantes qui, par leur gentillesse et leurs compétences scientifiques, m'ont permis de pleinement m'épanouir lors de cette thèse.

J'adresse un grand merci à tous les membres du groupe « couches minces ». Je remercie particulièrement Sophie Ollivier pour toute l'aide expérimentale qu'elle a pu m'apporter, que ce soit pour l'AFM ou pour les dépôts laser. J'adresse également mes remerciements à Stéphanie Députier et Valérie Bouquet pour toutes nos discussions et leurs nombreux conseils. Je remercie les stagiaires Amélia, Elias (master 2) et Ryan (L3) avec qui j'ai eu le plaisir de travailler et de partager mon expérience.

Je tiens à vivement remercier tous les collaborateurs de l'ANR PolyNASH du laboratoire CRISMAT de Caen et GEMaC de Versailles : Arnaud Fouchet (coordinateur du projet), Alexis Boileau, Marie Dallocchio, Jacques Junior Manguele et Yoann Bourlier (doctorants et post-doctorants) mais aussi Christophe Cibert, Gilles Poullain, Bruno Bérini, Ulrike Lüders, Adrian David, Elena Popova et Yves Dumont. Ce fût un plaisir de travailler avec vous ! Mon seul regret est que la période de coronavirus ne nous a pas permis de nous réunir plus souvent …

J'exprime ma reconnaissance à tous les membres de l'équipe Chimie du Solide et Matériaux et personnels PRTS. Merci à Pierric Lemoine, Mathieu Pasturel, Fabien Grasset, Guillaume Gouget et Adèle Renaud pour les nombreuses discussions, leurs précieux conseils, et toute l'aide qu'ils ont pu m'apporter durant cette thèse. Je remercie Nathalie Troalic, gestionnaire de l'équipe CSM, pour tout son travail et sa gentillesse. Je remercie également Valérie Le Cam et Christophe Derouet pour leur soutien technique, Thierry Guizouarn pour les mesures de magnétisme, Noée Dumait et Stéphanie Fryars pour leur aide expérimentale et Thibault Reynaldo pour la résolution de mes (nombreux) problèmes informatiques et pour nos discussions divagantes. Je remercie Francis Gouttefangeas et Loïc Joanny du CMEBA pour les analyses de microscopie électronique à balayage ainsi que Ludivine Rault et Vincent Dorcet de la plateforme THEMIS de m'avoir formé à la microscopie électronique en transmission. Merci également aux physiciens de l'Institut de Physique de Rennes (IPR) : Pascal Turban pour les manips de microscopie à effet tunnel, Bruno Lépine pour les manips XPS et Jean Christophe Le Breton pour nos nombreuses discussions, notamment sur l'exfoliation des oxydes. Je remercie également Aude et Hayley, stagiaires à l'IPR, qui ont participé aux observations et mesures réalisées à l'IPR.

Je remercie tous les doctorants que j'ai pu côtoyer lors de ma thèse. Merci à Clément, avec qui j'ai commencé et fini ma thèse, pour sa bonne humeur et tous les bons moments passés au bureau. Merci à Barthélemy, avec qui j'ai passé presque deux ans dans le « bureau 058 », pour ses conseils et nos discussions de bureau. Merci également à Soumaya pour sa bonne humeur, Sylvain pour ses anecdotes alcoolisées, Praveen pour sa gentillesse, Anne-Gaëlle pour m'avoir plusieurs fois filé un coup de main, Julien avec qui c'était un plaisir de discuter quand il passait sur Rennes. Merci également à Florentine et

Coralie, doctorantes récemment arrivées au laboratoire, pour le dynamisme et la bonne humeur qu'elles ont apportés au labo. Merci à Andreas pour nos discussions (malheureusement) éphémères mais toujours sympathiques ! Je remercie également ici Morgan, stagiaire de L3, qui m'a marqué par sa gentillesse, son sérieux et sa curiosité.

Je remercie bien sûr ma famille et particulièrement mes parents pour leur soutien sans faille tout au long de mes études. Merci de m'avoir poussé depuis tout petit à donner le meilleur de moi-même, ce qui m'a permis d'en arriver jusqu'ici. Je remercie également mon frangin David pour m'avoir transmis sa passion pour la chimie. Je profite de ces remerciements pour saluer mes amis des « Mauges » ainsi que mes amis « minéralo » qui m'ont également beaucoup soutenu !

Je termine par infiniment remercier Doha, mon épouse, pour son soutien, son amour et tout le courage qu'elle a pu me donner tout au long de mon doctorat. À cause du coronavirus, nous avons été longtemps séparés, ce qui a rendu encore plus compliqué cette période. Cependant, notre patience a été récompensée et j'ai eu l'immense joie et fierté qu'elle puisse assister à la soutenance de cette thèse. Je t'aime !

Je dédie ce manuscrit à mon grand-père « Papy Jean »

Résumé en français - French summary

En microélectronique, les propriétés physiques des dispositifs dépendent de l'orientation cristalline des couches minces. Différents types de croissances sont possibles (Figure 1) :

- Aléatoire avec aucune orientation particulière dans le plan et hors du plan,
- Texturée avec une orientation hors du plan mais pas dans le plan,
- Épitaxiée avec une orientation hors du plan et dans le plan.

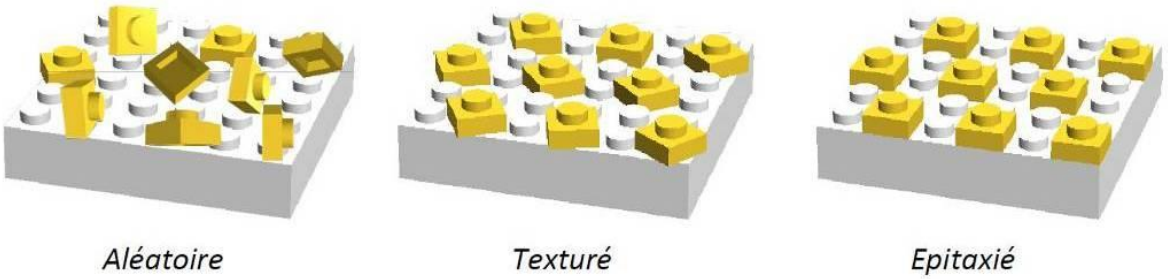

Figure 1. Représentation schématique des différents types de croissance des couches minces.

Les meilleures propriétés physiques des matériaux oxydes fonctionnels sont généralement obtenues par croissance épitaxiale sur des substrats monocristallins, souvent eux-mêmes des oxydes, ou sur silicium monocristallin après le dépôt d'une première couche tampon oxyde permettant à la fois la reprise d'épitaxie et l'absence de diffusion, fréquente aux températures de dépôt requises. Cependant, les substrats monocristallins sont coûteux et peu sont produits avec une grande surface, ce qui limite les applications des dispositifs.

Le but de cette thèse est donc de développer de nouveaux substrats à bas coût pour la croissance contrôlée et l'étude d'oxydes fonctionnels, et ainsi de pouvoir proposer une nouvelle solution pour l'intégration d'oxydes complexes à propriétés multifonctionnelles pour l'électronique sur grandes surfaces. Ce travail a été réalisé dans le cadre du projet PolyNASH, financé par l'ANR, associant l'Institut des Sciences Chimique de Rennes (ISCR), le Laboratoire de Cristallographie et Sciences des Matériaux de Caen (CRISMAT) et le Groupe d'Étude de la Matière Condensée de Versailles (GEMaC). L'objectif principal de ce travail est de remplacer ces substrats monocristallins coûteux par des substrats

polycristallins ou amorphes peu onéreux, ou encore de déposer directement sur du silicium monocristallin standard de la filière microélectronique. Dans ce but, les substrats seront recouverts d'un "template" cristallisé d'épaisseur « moléculaire », sous forme de nanofeuillets, qui servira de couche de germination pour la croissance épitaxiale ultérieure des oxydes fonctionnels (Figure 2). Ainsi, la croissance de certains matériaux, jusqu'alors difficile ou impossible sur silicium par exemple, devient envisageable en utilisant une couche de germination appropriée, c'est-à-dire présentant une composition, une symétrie et des paramètres de maille en adéquation avec le matériau à déposer.

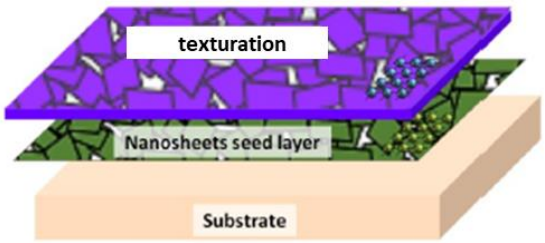

Figure 2. Figure résumée de l'objectif de la thèse : déposer une couche dense de nanofeuillets sur un substrat à bas coût. Les nanofeuillets vont induire une texturation de la couche mince d'oxyde déposé en surface.

Lors de cette thèse, différentes phases lamellaires ont été synthétisées : $KCa_2Nb_3O_{10}$, $K_4Nb_6O_{17}$, $K_{0.8}Ti_{1.73}Li_{0.27}O_4$, $Cs_6W_{11}O_{36}$ et K_xMnO_2 par réaction à l'état solide, par synthèse en milieux sels fondus ou par chimie en solution. Dans une seconde étape, une exfoliation en solution de ces matériaux a permis d'obtenir les nanofeuillets à 2 dimensions $[Ca_2Nb_3O_{10}]^-$, $[K_{4-x}Nb_6O_{17}]^{x-}$, $[Ti_{0.87}O_2]^{0.52-}$, $[Cs_4W_{11}O_{36}]^{2-}$ et $[MnO_2]^{x-}$ qui ont été ensuite transférés sur des substrats par les techniques de Langmuir-Blodgett et de drop casting. Ces nanofeuillets, qui présentent des réseaux cristallographiques 2D différents, carré pour $[Ca_2Nb_3O_{10}]^-$, rectangulaire pour $[K_{4-x}Nb_6O_{17}]^{x-}$ et $[Ti_{0.87}O_2]^{0.52-}$, et hexagonal pour $[Cs_4W_{11}O_{36}]^{2-}$ et $[MnO_2]^{x-}$, ont servi de sites de germination pour la croissance d'oxydes complexes de symétrie cubique, orthorhombique ou hexagonale (Figure 3). Des films minces d'oxydes complexes ou métalliques ont été synthétisés par ablation laser pulsée (PLD), pulvérisation cathodique et par voie chimique en solution (CSD) sur ces nanofeuillets.

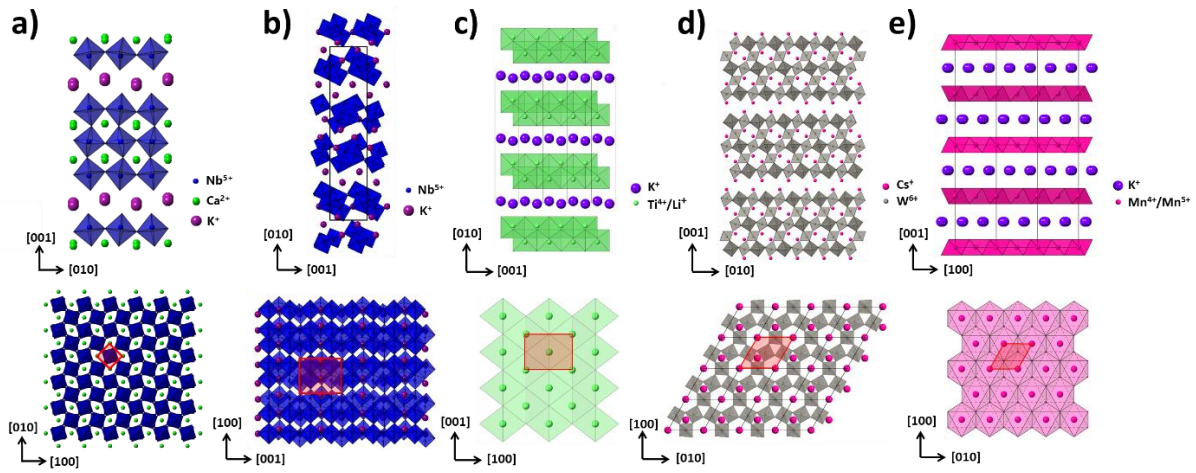

Figure 3. Structures des différentes phases lamellaires synthétisées lors de cette thèse et structures des nanofeuillets obtenus après exfoliation : a) $KCa_2Nb_3O_{10}$, b) $K_4Nb_6O_{17}$, c) $K_{0.8}Ti_{1.73}Li_{0.27}O_4$, d) $Cs_6W_{11}O_{36}$ et e) K_xMnO_2.

La phase lamellaire Dion-Jacobson $KCa_2Nb_3O_{10}$ (KCN) a été synthétisée par réaction à l'état solide (SSR) [1] et par synthèse en milieu sels fondus (MSS, sels : K_2SO_4 et K_2MoO_4) [2,3]. L'objectif des synthèses en milieu sels fondus est d'obtenir des cristaux de plus grande taille par rapport à ceux obtenus par réaction à l'état solide classique. Nous avons obtenu des cristaux de dimensions latérales 600 µm avec K_2MoO_4 et 60 µm avec K_2SO_4, ce qui est bien supérieur aux 10 µm obtenus par réaction à l'état solide. Lors des premières synthèses par sels fondus, les phases secondaires $CaNb_2O_6$ et $KNbO_3$ étaient présentes. Une étude systématique sur le taux de potassium durant la synthèse a été réalisée pour obtenir la phase pure. Nous avons également réalisé des doubles synthèses SSR/MSS K_2MoO_4 et MSS K_2SO_4/MSS K_2MoO_4 afin d'obtenir de grands cristaux homogènes en taille dans le but d'exfolier de grands nanofeuillets. Les cristaux KCN ont été caractérisés par diffraction des rayons X (DRX), microscopie électronique à balayage (MEB), microscopie électronique en transmission (MET) et par spectroscopie de dispersion en énergie des rayons X (EDXS). L'exfoliation des cristaux est obtenue en deux étapes : par protonation (échange des ions potassium par des protons) puis par exfoliation à l'aide d'hydroxyde de tétrabutylammonium (TBAOH), ce qui conduit à des nanofeuillets $[Ca_2Nb_3O_{10}]^-$ en solution colloïdale (Figure 4). Ils ont été observés par MET et la diffraction des électrons montre que les nanofeuillets sont bien cristallisés, avec le paramètre de maille attendu $a \simeq 3{,}85$ Å. Nous avons réussi à exfolier des feuillets jusqu'à 5 µm à partir de cristaux obtenus par réaction à l'état solide, et jusqu'à 20 µm à partir de cristaux issus des synthèses en sels fondus. Nous avons également confirmé que l'exfoliation des nanofeuillets $[Ca_2Nb_3O_{10}]^-$ est instantanée lorsque le TBAOH est ajouté

[4] et ne nécessite pas d'agitation longue comme décrite jusqu'à présent dans la littérature. Ce type de nanofeuillets carrés servira à la germination d'oxydes selon leur orientation (100).

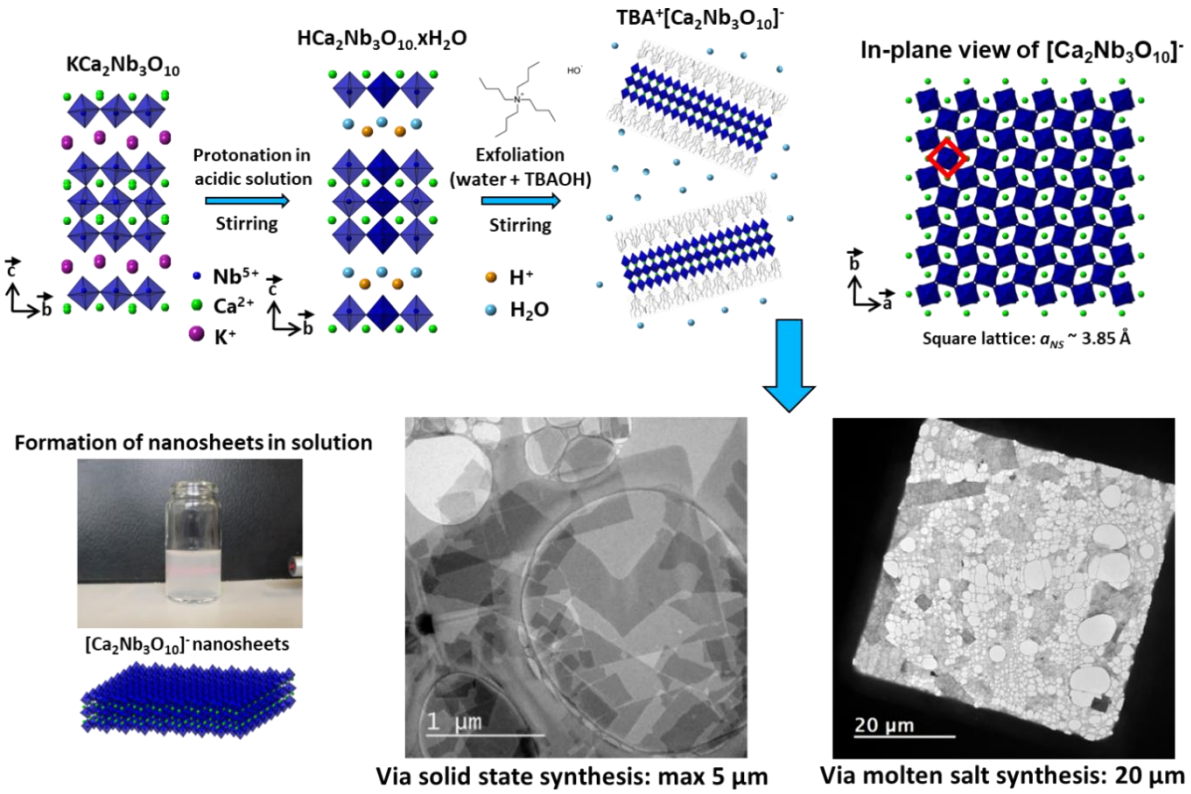

Figure 4. Résumé des différentes étapes de l'exfoliation de $KCa_2Nb_3O_{10}$: protonation de la phase de départ puis exfoliation de la phase protonée avec TBAOH. Une solution colloïdale de nanofeuillets est obtenue.

Les nanofeuillets ont ensuite été déposés par la technique de Langmuir-Blodgett mise en place au laboratoire dans le cadre de ce projet. Ainsi toutes les conditions expérimentales ont dû être déterminées. Les données disponibles dans la littérature ont été utilisées comme point de départ [5]. Cependant, une étude systématique s'est avérée indispensable, montrant la nécessité d'apporter des modifications au dispositif. Plus récemment, la technique de dépôt par drop casting a également été mise en place au laboratoire [6]. Cette technique s'est révélée donner des résultats identiques à la méthode de Langmuir-Blodgett avec un temps de dépôt considérablement réduit. De plus, elle a l'avantage d'utiliser des quantités de solution très faibles, ce qui permet une importante économie de matériaux. Les nanofeuillets ont été déposés sur différents substrats (Si, SiO_2, Pt/Si, mica, …) à l'aide de ces deux différentes techniques. Leurs épaisseurs et leurs taux de recouvrement sur le substrat ont été évalués par microscopie à force atomique (AFM) et par MEB. Des taux de recouvrement élevés ont été obtenus sur chaque substrat.

Des expériences de spectrométrie photoélectronique X (XPS) et de microscopie à effet tunnel (STM) sur $[Ca_2Nb_3O_{10}]^-$/Si ont été réalisées en collaboration avec l'Institut de Physique de Rennes afin d'étudier l'influence de la température et d'un traitement à l'acide fluorhydrique (HF), ce dernier étant communément utilisé pour retirer l'oxyde natif en surface des substrats de silicium. Il a été démontré qu'à 160°C sous ultravide (UHV), les nanofeuillets sont stables mais qu'à une température de 360°C sous UHV, des lacunes d'oxygène à la surface des nanofeuillets apparaissent. Le phénomène est réversible après chauffage à l'air. Il a également été montré que le traitement HF permettait bien le retrait de l'oxyde natif de silicium sous les nanofeuillets et que les nanofeuillets ne sont pas affectés par ce traitement.

La phase $K_4Nb_6O_{17}$ a été synthétisée par réaction à l'état solide donnant des cristaux de dimension latérale jusqu'à 5 mm. Les cristaux ainsi que leur forme protonée ont été caractérisés par DRX, MEB et EDXS. La protonation et l'exfoliation de ces cristaux avec TBAOH conduit à une solution colloïdale. Les analyses par MET montrent la présence de nanofeuillets et de nanotubes $[K_{4-x}Nb_6O_{17}]^{x-}$, les nanotubes correspondant à des nanofeuillets enroulés [7,8]. La diffraction des électrons montre que les nanofeuillets/nanotubes sont bien cristallisés, avec les paramètres de maille attendus a = 7,8 Å et c = 6,5 Å. Il n'a été possible d'obtenir les nanofeuillets non enroulés qu'en exfoliant la forme protonée $[H_xK_{4-x}Nb_6O_{17}]^{x-}$ avec de la *n*-propylamine. L'utilisation de cet exfoliant pour ce matériau a déjà été décrite dans la littérature mais avec peu d'informations sur les protocoles expérimentaux [9,10]. Il a par conséquent été nécessaire de mener une étude systématique sur le ratio TBAOH/*n*-propylamine afin d'obtenir une exfoliation optimale. Les observations par MET et la diffraction des électrons montrent des nanofeuillets de dimensions latérales comprises entre 500 nm et 25 µm. Ces nanofeuillets ont ensuite été déposés avec succès sur SiO_2 par la technique de Langmuir-Blodgett et par drop casting. Ces nanofeuillets rectangulaires seront utilisés comme couche de germination d'oxydes afin de promouvoir leur orientation (110).

La phase $K_{0.8}Ti_{1.73}Li_{0.27}O_4$ a également été synthétisée par la méthode en sels fondus et des cristaux de taille millimétrique ont été obtenus [2]. Les cristaux ont été caractérisés par DRX, MEB et EDXS. Leur exfoliation est également obtenue par protonation suivie d'une exfoliation à l'aide de TBAOH, ce qui conduit à des nanofeuillets $[Ti_{0.87}O_2]^{0.52-}$ en solution colloïdale. Les premières images obtenues par MET montrent des

nanofeuillets de taille allant de 0,5 à 2 µm. La diffraction des électrons montre que les feuillets sont bien cristallisés. Ces nanofeuillets serviront comme couche de germination d'oxydes pour obtenir leur orientation (110).

Les nanofeuillets $[Cs_4W_{11}O_{36}]^{2-}$ ont été également synthétisés lors de cette thèse par réaction à l'état solide [11,12]. Des cristaux millimétriques ont été obtenus et caractérisés par DRX, MEB et EDXS. La protonation et l'exfoliation de cette phase a également été réalisée à l'aide de TBAOH. La solution obtenue a été observée par MET. Des nanofeuillets de dimension entre 500 nm et 20 µm ont été observés. La diffraction des électrons montre des nanofeuillets bien cristallisés avec un paramètre de maille proches de celui attendu a = 7,25 Å. Ces nanofeuillets ont été déposés avec succès par la technique de Langmuir-Blodgett et de drop casting sur différents substrats. Ces nanofeuillets hexagonaux seront utilisés comme couche de germination d'oxydes afin de favoriser leur orientation (111).

Les nanofeuillets $[MnO_2]^{x-}$ ont été synthétisés par différentes voies de synthèses : par oxydation du chlorure de manganèse [13] et par réduction du permanganate de potassium par du laurylsulfate de sodium [14]. Les solutions colloïdales obtenues ont été observées par MET. L'oxydation du chlorure de manganèse, qui a l'avantage d'être une réaction d'être rapide, montrent un mélange de nanofeuillets de dimension moindre (< 150 nm) et de nanobâtonnets. La réduction du permanganate de potassium conduit à des dimensions de nanofeuillets bien plus importantes comparées à la méthode précédente (entre 500 nm et 4 µm). Cependant cette synthèse nécessite plusieurs étapes de purification et la solution obtenue n'est pas stable dans le temps. Des tests de dépôts sont en cours sur différents substrats. Ces nanofeuillets également hexagonaux serviront comme couche de germination d'oxydes pour obtenir leur orientation (111).

La suite de notre travail a donc consisté à déposer des oxydes sur ces nanofeuillets. Différents oxydes ont pu être déposés sur les nanofeuillets $[Ca_2Nb_3O_{10}]^-$ pour obtenir leur orientation (100). Des couches minces du composé ferroélectrique $KNbO_3$ ont été préparées par PLD sur les nanofeuillets déposés sur silice, et sur le substrat monocristallin $SrTiO_3$ (STO) [15]. Les résultats de DRX ont montré une orientation préférentielle (100) de $KNbO_3/[Ca_2Nb_3O_{10}]^-/SiO_2$. La mesure de la mosaïcité du film par ω-scan (« rocking curve ») montre une largeur à mi-hauteur légèrement plus importante

comparée à celle du film $KNbO_3$/STO. La microstructure du film sur nanofeuillets se révèle identique à celle du film obtenu directement sur STO.

L'oxyde multiferroïque $BiFeO_3$ a également été déposé sur des substrats sur des substrats en silicium et en silice, cette fois par CSD [16]. La diffraction des rayons X montre que $BiFeO_3$ croît avec l'orientation préférentielle (100) sur les deux substrats grâce aux nanofeuillets. Des pics de faibles intensités sont également visibles à des angles de diffraction suggérant la présence d'une autre phase. Ils pourraient correspondre à la formation d'une nouvelle phase engendrée par réaction chimique de $BiFeO_3$ avec les nanofeuillets $[Ca_2Nb_3O_{10}]^-$.

D'autres oxydes ont été déposés en collaboration avec les laboratoires CRISMAT de Caen et GEMaC de Versailles. Le matériau magnétique $La_{0.67}Sr_{0.33}MnO_3$ (LSMO) a été déposé par PLD sur $[Ca_2Nb_3O_{10}]^-$/silice. La diffraction des rayons X ainsi que la diffraction d'électrons rétrodiffusés (EBSD) montrent une orientation (100) du film sur les nanofeuillets. Une étude des propriétés magnétiques de LSMO/$[Ca_2Nb_3O_{10}]^-$/SiO_2 a été réalisée et les résultats ont été comparés aux valeurs obtenues pour des films déposés directement sur SiO_2 (film polycristallin) et sur $SrTiO_3$ (film épitaxié). Il a été montré que les propriétés magnétiques des films déposés sur nanofeuillets sur silice sont très proches de celles du composé LSMO épitaxié sur $SrTiO_3$. De plus, les mesures de transport montrent que LSMO/$[Ca_2Nb_3O_{10}]^-$ présente une magnétorésistance à champ faible et à basse température de 40% de 10 à 300K, ce qui rend le dispositif intéressant pour des applications comme capteurs.

Des films d'oxydes transparents conducteurs (TCO) $CaVO_3$ et $SrVO_3$ ont également été élaborés sur les nanofeuillets $[Ca_2Nb_3O_{10}]^-$ sur des substrats en verre par ablation laser [17]. L'oxyde d'étain et d'indium (ITO) est aujourd'hui le TCO le plus largement utilisé. Cependant le prix et la diminution des ressources en indium incitent à chercher des alternatives. $CaVO_3$ et $SrVO_3$ ont montré avoir des propriétés proches de l'ITO [18]. Cependant, ces résultats ont uniquement été obtenus pour des couches minces cristallisées, ce qui est impossible à obtenir par dépôt directement sur verre. Les nanofeuillets, de très faible épaisseur (1,5-3 nm), ont permis à la fois la cristallisation des deux vanadates sur verre et la conservation de la transparence des films, dont l'épaisseur est d'environ 40 nm. Les films déposés sur les nanofeuillets présentent une orientation préférentielle (100). Les analyses par ellipsométrie spectroscopique (collaboration

Institut Pprime, Poitiers) ainsi que les mesures optiques (collaboration CIMAP, Caen) et de transport ont montré que les propriétés des couches sur nanofeuillets sont très proches des résultats obtenus sur substrats monocristallins [17].

En complément des dépôts d'oxydes, des dépôts de platine par pulvérisation cathodique ont également été réalisés sur les nanofeuillets $[Ca_2Nb_3O_{10}]^-$ [19] par Jacques Manguele au laboratoire CRISMAT de Caen, dans le cadre de son doctorat. Le platine est largement utilisé en microélectronique, notamment en tant qu'électrode inférieure pour l'intégration d'oxydes dans les dispositifs. Il est conventionnellement déposé sur un substrat SiO_2/Si avec une couche d'adhésion de TiO_2 de quelques manomètres. Les électrodes de platine doivent être cristallisées afin de permettre la croissance d'oxydes cristallisés. Cependant, la cristallisation du platine sur ce type de substrat ne peut être obtenue qu'à partir de 600°C, ce qui limite les applications, notamment pour les circuits silicium dont les températures de dépôt ne doivent pas dépasser 500°C. L'étude dans le cadre de cette collaboration a donc consisté à comparer la croissance du platine (111) sur $TiO_2/SiO_2/Si$ et sur $[Ca_2Nb_3O_{10}]^-/SiO_2/Si$. Il a été démontré par DRX que du platine de haute qualité (largeur à mi-hauteur du pic issu du balayage en ω sur la raie 111 < 1°) a été obtenu sur nanofeuillets à une température de dépôt de 200°C comparé à celle de 600°C requise sur $TiO_2/SiO_2/Si$. Du Pt (200) a également été déposé sur nanofeuillets en changeant les conditions de dépôts (argon + oxygène). Cette orientation du platine sur silicium n'a été obtenue jusqu'à présent qu'à très hautes températures (> 650°C). Grâce aux nanofeuillets, il a été possible d'obtenir cette orientation à 550°C, alors qu'elle n'a pu être obtenue sur $TiO_2/SiO_2/Si$. Ces résultats ouvrent de nouvelles opportunités pour l'élaboration de circuits sur silicium.

En résumé, cette thèse a permis de maitriser la synthèse, l'exfoliation et le dépôt sur substrats de 5 nanofeuillets différents. Cette palette de nanofeuillets offre une large possibilité de croissance d'oxydes selon leurs orientations (100), (110) et (111). Des dépôts de différents matériaux ont été réalisés sur les nanofeuillets $[Ca_2Nb_3O_{10}]^-$ sur des substrats à bas coût (silicium, verre). Les résultats confirment une texturation (100) pour les pérovskites et (111) et (200) pour le platine. Dans le cas de $LSMO/[Ca_2Nb_3O_{10}]^-$, les propriétés magnétiques sont proches du film épitaxié et la texturation engendre une magnétorésistance à faible champ. Les nanofeuillets ont également permis l'intégration des oxydes transparents conducteurs $CaVO_3$ et $SrVO_3$ sur verre, avec des propriétés

physiques proches de celles obtenues sur substrat monocristallin. Les dépôts de platine (111) réalisés sur les nanofeuillets montrent une haute qualité cristalline à une température très inférieure à celle des dépôts sur $TiO_2/SiO_2/Si$. En changeant les conditions de dépôt, du platine (200) a également pu être obtenu sur les nanofeuillets à température modérée. Ces résultats démontrent le grand intérêt des nanofeuillets pour la croissance d'oxydes et de platine sur substrats à bas coût. Des dépôts d'oxydes sur les autres nanofeuillets synthétisés durant cette thèse sont en cours.

Références

[1] Y. Ebina, K. Akatsuka, K. Fukuda, T. Sasaki, Synthesis and In Situ X-ray Diffraction Characterization of Two-Dimensional Perovskite-Type Oxide Colloids with a Controlled Molecular Thickness, Chem. Mater. 24 (2012) 4201–4208. https://doi.org/10.1021/cm302480h.

[2] T. Tanaka, Y. Ebina, K. Takada, K. Kurashima, T. Sasaki, Oversized Titania Nanosheet Crystallites Derived from Flux-Grown Layered Titanate Single Crystals, Chem. Mater. 15 (2003) 3564–3568. https://doi.org/10.1021/cm034307j.

[3] H. Yuan, M. Nguyen, T. Hammer, G. Koster, G. Rijnders, J.E. ten Elshof, Synthesis of $KCa_2Nb_3O_{10}$ Crystals with Varying Grain Sizes and Their Nanosheet Monolayer Films As Seed Layers for PiezoMEMS Applications, ACS Appl. Mater. Interfaces. 7 (2015) 27473–27478. https://doi.org/10.1021/acsami.5b09456.

[4] H. Yuan, D. Dubbink, R. Besselink, J.E. ten Elshof, The Rapid Exfoliation and Subsequent Restacking of Layered Titanates Driven by an Acid-Base Reaction, Angew. Chem. Int. Ed. 54 (2015) 9239–9243. https://doi.org/10.1002/anie.201502539.

[5] A.P. Dral, D. Dubbink, M. Nijland, J.E. ten Elshof, G. Rijnders, G. Koster, Atomically Defined Templates for Epitaxial Growth of Complex Oxide Thin Films, J. Vis. Exp. (2014) 52209. https://doi.org/10.3791/52209.

[6] Y. Shi, M. Osada, Y. Ebina, T. Sasaki, Single Droplet Assembly for Two-Dimensional Nanosheet Tiling, ACS Nano. 14 (2020) 15216–15226. https://doi.org/10.1021/acsnano.0c05434.

[7] G.B. Saupe, C.C. Waraksa, H.-N. Kim, Y.J. Han, D.M. Kaschak, D.M. Skinner, T.E. Mallouk, Nanoscale Tubules Formed by Exfoliation of Potassium Hexaniobate, Chem. Mater. 12 (2000) 1556–1562. https://doi.org/10.1021/cm981136n.

[8] G. Du, Q. Chen, Y. Yu, S. Zhang, W. Zhou, L.-M. Peng, Synthesis, modification and characterization of $K_4Nb_6O_{17}$-type nanotubes, J. Mater. Chem. 14 (2004) 1437. https://doi.org/10.1039/b317095k.

[9] M.A. Bizeto, V.R.L. Constantino, Layered $H_2K_2Nb_6O_{17}$ exfoliation promoted by n-butylamine, Mater. Res. Bull. 39 (2004) 1811–1820. https://doi.org/10.1016/j.materresbull.2004.07.001.

[10] M.C. Sarahan, E.C. Carroll, M. Allen, D.S. Larsen, N.D. Browning, F.E. Osterloh, $K_4Nb_6O_{17}$-derived photocatalysts for hydrogen evolution from water: Nanoscrolls versus nanosheets, J. Solid State Chem. 181 (2008) 1678–1683. https://doi.org/10.1016/j.jssc.2008.06.021.

[11] K. Fukuda, K. Akatsuka, Y. Ebina, R. Ma, K. Takada, I. Nakai, T. Sasaki, Exfoliated Nanosheet Crystallite of Cesium Tungstate with 2D Pyrochlore Structure: Synthesis, Characterization, and Photochromic Properties, ACS Nano. 2 (2008) 1689–1695. https://doi.org/10.1021/nn800184w.

[12] M. Miyauchi, A. Kondo, D. Atarashi, E. Sakai, Tungstate nanosheet ink as a photonless and electroless chromic device, J Mater Chem C. 2 (2014) 3732–3737. https://doi.org/10.1039/C3TC32513J.

[13] Y. Wang, Y.-Z. Zhang, D. Dubbink, J.E. ten Elshof, Inkjet printing of δ-MnO_2 nanosheets for flexible solid-state micro-supercapacitor, Nano Energy. 49 (2018) 481–488. https://doi.org/10.1016/j.nanoen.2018.05.002.

[14] Z. Liu, K. Xu, H. Sun, S. Yin, One-Step Synthesis of Single-Layer MnO_2 Nanosheets with Multi-Role Sodium Dodecyl Sulfate for High-Performance Pseudocapacitors, Small. 11 (2015) 2182–2191. https://doi.org/10.1002/smll.201402222.

[15] F. Baudouin, V. Demange, S. Ollivier, L. Rault, A.S. Brito, A.S. Maia, F. Gouttefangeas, V. Bouquet, S. Députier, B. Bérini, A. Fouchet, M. Guilloux-Viry, Orientation control of $KNbO_3$ film grown on glass

substrates by $Ca_2Nb_3O_{10}^-$ nanosheets seed layer, Thin Solid Films. 693 (2020) 137682. https://doi.org/10.1016/j.tsf.2019.137682.
[16] V. Bouquet, F. Baudouin, V. Demange, S. Députier, S. Ollivier, L. Joanny, L. Rault, A. Fouchet, M. Guilloux-Viry, Influence of two-dimensional oxide nanosheets seed layers on the growth of (100)$BiFeO_3$ thin films synthesized by chemical solution deposition, Thin Solid Films. 693 (2020) 137687. https://doi.org/10.1016/j.tsf.2019.137687.
[17] A. Boileau, S. Hurand, F. Baudouin, U. Lüders, M. Dallocchio, B. Bérini, A. Cheikh, A. David, F. Paumier, T. Girardeau, P. Marie, C. Labbé, J. Cardin, D. Aureau, M. Frégnaux, M. Guilloux-Viry, W. Prellier, Y. Dumont, V. Demange, A. Fouchet, Highly Transparent and Conductive Indium-Free Vanadates Crystallized at Reduced Temperature on Glass Using a 2D Transparent Nanosheet Seed Layer, Adv. Funct. Mater. (2021) 2108047. https://doi.org/10.1002/adfm.202108047.
[18] L. Zhang, Y. Zhou, L. Guo, W. Zhao, A. Barnes, H.-T. Zhang, C. Eaton, Y. Zheng, M. Brahlek, H.F. Haneef, N.J. Podraza, M.H.W. Chan, V. Gopalan, K.M. Rabe, R. Engel-Herbert, Correlated metals as transparent conductors, Nat. Mater. 15 (2016) 204–210. https://doi.org/10.1038/nmat4493.
[19] J.J. Manguele, F. Baudouin, C. Cibert, B. Domengès, V. Demange, M. Guilloux-Viry, A. Fouchet, G. Poullain, Highly textured Pt thin film grown at very low temperature using $Ca_2Nb_3O_{10}$ nanosheets as seed layer, SN Appl. Sci. 2 (2020) 453. https://doi.org/10.1007/s42452-020-2271-9.

Table of contents

Résumé en français - French summary **1**

List of acronyms **20**

General introduction **25**

Chapter 1: State of art **29**

1. Nanosheets: a recent class of materials 29

2. Exfoliation of the oxide nanosheets 31

2.1. Protonation **31**

2.2. Exfoliation **32**

3. From layered oxides to oxide nanosheets 33

3.1. Layered perovskites **35**

3.1.1. Dion-Jacobson phases and their nanosheets *35*

3.1.2. Aurivillius and Ruddlesden-Popper phases *37*

3.2. Other layered oxide and nanosheets with 2D-square lattices **39**

3.3. Nanosheets with 2D-rectangle lattice **40**

3.3.1. $[K_xNb_6O_{17}]^{4-x}$ nanosheets from the $K_4Nb_6O_{17}$ phase *40*

3.3.2. $[Ti_{0.87}O_2]^{0.52-}$ nanosheets from the $K_{0.8}Ti_{1.73}Li_{0.27}O_4$ phase *42*

3.3.3. $[Ti_{0.91}O_2]^{0.36-}$ nanosheets from the $Cs_{0.7}Ti_{1.825}\square_{0.175}O_4$ phase *44*

3.3.4. Doped Co/Fe titanate nanosheets *45*

3.4. Nanosheets with 2D hexagonal lattices **46**

3.4.1. $[Cs_4W_{11}O_{36}]^{2-}$ nanosheets from the $Cs_6W_{11}O_{36}$ phase *46*

3.4.2. $[MnO_2]^{\delta-}$ nanosheets from the $(K, Na)_xMnO_2$ birnessite phase *47*

3.4.3. $[Ru_{0.95}O_2]^{0.2-}$ nanosheets from the $(K, Na)RuO_2$ phase *49*

3.4.4. $[MoO_2]^{x-}$ nanosheets from the $Na_{0.9}MoO_2$ phase *50*

3.5. Other oxide nanosheets **51**

3.5.1. $[TaO_3]^-$ nanosheets from the $RbTaO_3$ phase *51*

3.5.2. $[Nb_3O_8]^-$ nanosheets from the KNb_3O_8 phase *52*

4. Nanosheets deposition techniques 53

4.1. Langmuir-Blodgett technique **53**

4.2. Spin coating deposition **54**

4.3. Electrophoretic deposition **55**

4.4. The drop casting method **56**

Conclusions 60

References 61

Chapter 2: Syntheses, depositions, and characterization methods 72

Introduction 72

1. Powders syntheses, protonation, and exfoliation 72

1.1. The solid state reaction **72**

1.2. The molten salt synthesis **73**

1.3. Protonation of the layered phases **73**

1.4. Liquid exfoliation of the protonated powders **74**

2. Nanosheets depositions techniques 74

2.1. The Langmuir-Blodgett technique **74**

2.2. The drop casting method **76**

3. Morphological and structural characterizations 77

3.1. X-ray diffraction **77**

3.2. In-plane X-ray diffraction **78**

3.3. Scanning electron microscopy **79**

3.4. Transmission electron microscopy **80**

3.5. Atomic force microscopy **82**

3.6. Scanning tunneling microscopy **83**

3.7. X-ray photoelectron spectroscopy **84**

4. Thin films depositions 85

4.1. Pulsed laser deposition **85**

4.2. Radio frequency magnetron sputtering **86**

4.3. Chemical solution deposition **87**

References 88

Chapter 3: Syntheses, depositions, and characterization of nanosheets **95**

Introduction 95

1. Synthesis, deposition, and characterizations of $[Ca_2Nb_3O_{10}]^-$ nanosheets 96

1.1. Synthesis of $KCa_2Nb_3O_{10}$ Dion-Jacobson phase **96**

1.1.1. Synthesis of $KCa_2Nb_3O_{10}$ by solid state reaction *96*

1.1.2. Synthesis of $KCa_2Nb_3O_{10}$ by molten salt synthesis *98*

1.2. Protonation of the $KCa_2Nb_3O_{10}$ phase **103**

1.3. Exfoliation of the $HCa_2Nb_3O_{10}$ phase **106**

1.4. Deposition of the $[Ca_2Nb_3O_{10}]^-$ nanosheets on substrates **108**

1.4.1. Deposition on substrates using the Langmuir-Blodgett technique *108*

1.4.2. Deposition of the $[Ca_2Nb_3O_{10}]^-$ nanosheets on substrates using the drop casting technique *110*

1.5. In-plane diffraction of the $[Ca_2Nb_3O_{10}]^-$ nanosheets **112**

1.6. XPS experiments on $[Ca_2Nb_3O_{10}]^-$ nanosheets **113**

1.6.1. HF treatment on $[Ca_2Nb_3O_{10}]^-$/Si substrate followed by XPS *113*

1.6.2. XPS experiments on $[Ca_2Nb_3O_{10}]^-$/Si substrates at different annealing temperatures *115*

1.7. STM experiments on $[Ca_2Nb_3O_{10}]^-$ nanosheets **117**

2. Synthesis, deposition, and characterizations of $[K_{4-x}Nb_6O_{17}]^{x-}$ nanosheets 120

2.1. Synthesis of the $K_4Nb_6O_{17}$ phase **120**

2.2. Protonation of the $K_4Nb_6O_{17}$ phase **121**

2.3. Exfoliation of the $H_xK_{4-x}Nb_6O_{17}$ phase 123

2.3.1. Exfoliation with TBAOH 123

2.3.2. Exfoliation with n-alkylamine 124

2.4. Deposition on substrates using the Langmuir-Blodgett technique 125

2.5. Deposition on substrates using the drop casting technique 127

2.6. In-plane diffraction of the $[K_{4-x}Nb_6O_{17}]^{x-}$ nanosheets 128

3. Synthesis, deposition, and characterizations of titanate nanosheets 129

3.1. Synthesis of the titanate nanosheets 129

3.1.1. Synthesis of $K_{0.8}Ti_{1.73}Li_{0.27}O_4$ by molten salt synthesis 129

3.2. Protonation of the $K_{0.8}Ti_{1.73}Li_{0.27}O_4$ phase 130

3.3. Exfoliation of the $H_{1.07}Ti_{1.73}O_4$ phase 131

3.4. Deposition on substrates using the drop casting technique 132

3.4.1. Deposition of the $[Ti_{0.87}O_2]^{0.52-}$ nanosheets by drop casting 132

3.5. In-plane diffraction of the $[Ti_{0.87}O_2]^{0.52-}$ nanosheets 133

4. Synthesis, deposition, and characterizations of $[Cs_4W_{11}O_{36}]^{2-}$ nanosheets 134

4.1. Synthesis of the $Cs_6W_{11}O_{36}$ phase 134

4.2. Protonation of the $Cs_6W_{11}O_{36}$ phase 136

4.3. Exfoliation of the $H_2Cs_4W_{11}O_{36}$ phase 136

4.4. Deposition on substrates using the Langmuir-Blodgett technique 137

4.5. Deposition on substrates using the drop casting technique 138

3.6. In-plane diffraction of the $[Cs_4W_{11}O_{36}]^{2-}$ nanosheets 139

5. Synthesis and characterizations of $[MnO_2]^{\delta-}$ nanosheets 140

5.1. Synthesis of MnO_2 nanosheets by the oxidation of $MnCl_2$ 140

5.2. Synthesis of MnO_2 nanosheets by the reduction of $KMnO_4$ 141

Conclusions and perspectives 143

References 144

Chapter 4: Orientation control of oxides and metal grown on nanosheets seed layers.....149

Introduction.....149

1. Orientation control of $KNbO_3$ film grown on glass substrates by $[Ca_2Nb_3O_{10}]^-$ nanosheets seed layer.....150

1.1. Introduction.....**150**

1.2. Thin films deposition conditions.....**151**

1.3. Thin films characterizations.....**152**

1.4. Conclusion.....**153**

2. Influence of nanosheets seed layers on the growth of $BiFeO_3$ thin films synthesized by CSD.....154

2.1 Introduction.....**154**

2.2. Thin films deposition conditions.....**154**

2.3. Thin films characterizations.....**155**

2.4. Conclusion.....**156**

3. Orientation control and physical properties of $La_{0.67}Sr_{0.33}MnO_3$ films grown on glass substrates covered by $[Ca_2Nb_3O_{10}]^-$ nanosheets seed layer.....157

3.1. Introduction.....**157**

3.2. Thin films deposition conditions.....**157**

3.3. Structural analyses of the films.....**158**

3.4. Magnetism measurements.....**160**

3.5. Transport properties.....**161**

3.6. Conclusion.....**163**

4. $SrVO_3$ and $CaVO_3$ transparent conducting oxides grown on $[Ca_2Nb_3O_{10}]^-$ nanosheets.....164

4.1. Introduction.....**164**

4.2. Thin films deposition conditions.....**165**

4.3. Structural analyses of the $SrVO_3$ and $CaVO_3$ thin films on NS.....165

4.4. DC transport properties.....167

4.5. Optical properties of the vanadate films.....169

4.6. Conclusion.....169

5. Orientation control of platinum electrode grown on silicon using $[Ca_2Nb_3O_{10}]^-$ nanosheets as a seed layer.....170

5.1. Introduction.....170

5.2. Thin films deposition conditions.....171

5.3. Structural analyses of the (111)Pt thin films.....171

5.4. Structural analyses of the (200)Pt thin films.....174

5.5. Resistivity measurements of the (111) and (200)Pt thin films.....175

Conclusion.....176

Conclusion.....176

References.....178

Conclusions and perspectives.....183

Annexes.....187

Annexe A: ICDD index cards.....187

Annexe B: List of publications, posters, and oral presentations.....217

List of acronyms

2D: 2-dimensional

AA: alkylamine

AFM: Atomic force microscopy

BFO: $BiFeO_3$

CMOS: Complementary metal oxide semiconductor

CNO: $[Ca_2Nb_3O_{10}]^-$

CSD: Chemical solution deposition

CVO: $CaVO_3$

CWO: $[Cs_4W_{11}O_{36}]^{2-}$

DC: Drop casting

DJ: Dion-Jacobson

EBSD: Electron back scattered diffraction

EDXS: Energy dispersive X-ray spectroscopy

EDP: Electron diffraction pattern

ELD: Electroless deposition

EPD: Electrophoretic deposition

FFT: Fast Fourier transformation

FWHM: Full-width-at-half-maximum

GO: Graphene oxide

GS: Glass substrate

HCN: $HCa_2Nb_3O_{10}$

HCWO: $H_2Cs_4W_{11}O_{36}$

HKN: $H_xK_{4-x}Nb_6O_{17}$

HOPG: Highly oriented pyrolytic graphite

HRTEM: High resolution transmission electron microscopy

HTO: $H_{1.07}Ti_{1.73}O_4$

ITO: Indium tin oxide

JCPDS: Powder Diffraction Standards

KCN: $KCa_2Nb_3O_{10}$

KN: $K_4Nb_6O_{17}$

KNO: $KNbO_3$

KNN: $(K,Na)NbO_3$

KTLO: $K_{0.8}Ti_{1.73}Li_{0.27}O_4$

LB: Langmuir-Blodgett

LSMO: $La_{0.67}Sr_{0.33}MnO_3$

MBE: molecular beam epitaxy

MR: magnetoresistance

MSS: Molten salt synthesis

NS: Nanosheets

PA: Propylamine

PLD: Pulsed laser deposition

PZT: $PbZr_{1-x}Ti_xO_3$

RF: Radio frequency

RP: Ruddlesden-Popper

SSR: Solid state reaction

SDS: sodium dodecyl sulfate

SEM: Scanning electron microscopy

STM: Scanning tunneling microscopy

SVO: $SrVO_3$

TBAOH: Tetrabutylammonium hydroxide

TBPOH: Tetraphospylammonium hydroxide

TCO: Transparent conducting oxide

TEM: Transmission electron microscopy

UHV: Ultra high vacuum

XPS: X-ray photoelectron spectroscopy

XRD: X-ray diffraction

General introduction

The miniaturization of electronic devices since the ’70s has led to the physical limits of microelectronics. The nanometric transistors currently used can not be further downscaled due to electron leakages. G. Moore had predicted this limit (Moore’s law) by supposing that the number of transistors in an integrated circuit exponentially increases as a function of the years [1]. Therefore, the “More than Moore” concept was introduced with the objective to find new materials with multifunctional properties beyond the mainly used CMOS (Complementary Metal Oxide Semiconductor) [2]. Complex oxides are potential candidates thanks to their functional properties such as high-T_C superconductivity, ferroelectricity, or magnetic properties. Moreover, some oxides combine properties, such as magnetoresistance or multiferroics.

The optimal performances of these materials are usually obtained by epitaxial growth on single crystalline substrates with a lattice parameter and a symmetry close to the thin film material. However, these substrates are relatively expensive and difficult to process because of their high chemical stability, leading to a limited choice of materials and crystallographic orientations commercially available. Efforts have been realized for the integration of oxides on Si, especially using molecular beam epitaxy (MBE) [3]. However, MBE is a slow, complex, and onerous technique that is not adapted to large-scale production. Therefore, new approaches regarding the use of complex oxides are necessary for the introduction of complex oxides in multifunctional More-than-Moore electronics.

This work aims to propose a new solution for the growth of functional oxides on low-cost substrates and to develop the integration of high-quality complex oxides with multifunctional properties for large surface electronics. This thesis focuses on the replacement of these single crystalline substrates by low-cost (as silicon), and/or amorphous (as glass) substrates. Direct growth on these substrates leads to very poorly crystallized films with degraded properties. To overcome these difficulties, the substrates can be covered by a crystalline template of molecular thickness (oxide nanosheets) that can be used as seed layers to induce the preferentially oriented growth of complex oxides

thin films, thanks to a small lattices mismatch between nanosheets and films [4]. Different nanosheets can be synthesized in order to enable the growth of a material in different orientations depending on its lattice parameters [5,6].

This thesis is organized into four chapters. The first chapter displays a state of the art of the oxides nanosheets. The different synthesis steps to obtain oxides nanosheets will be detailed. Then, a non-exhaustive list of nanosheets for oriented growth application with a description of their structures, properties, and applications will be presented. This list has been extended to oxide nanosheets exhibiting remarkable properties. Afterward, the deposition techniques used for the deposition of the nanosheets on substrates will be developed.

The second chapter focuses on the syntheses, depositions, and characterization methods used during this work. Firstly, the solid state and molten salt reactions will be described, followed by a presentation of the protonation and exfoliation process. Then, the Langmuir-Blodgett and drop casting deposition methods used during this thesis will be described. Afterward, the methods used for the characterization of the nanosheets, and thin films will be presented. Finally, the thin films deposition methods will be described.

The third chapter gathers the experimental results on the synthesis, deposition, and characterization of five different nanosheets: $[Ca_2Nb_3O_{10}]^-$, $[K_{4-x}Nb_6O_{17}]^{x-}$, $[Ti_{0.87}O_2]^{0.52-}$, $[Cs_4W_{11}O_{36}]^{2-}$, and $[MnO_2]^{\delta-}$. The nanosheets were obtained by protonation and exfoliation of layered phases. Their transfer on different substrates was performed by the Langmuir-Blodgett process and the drop casting technique, which showed a high coverage rate on the surface.

The fourth and last chapter displays the growth of complex oxide perovskites and metallic thin films on $[Ca_2Nb_3O_{10}]^-$ nanosheets on various substrates. Different materials such as the ferroelectric $KNbO_3$ and the multiferroic $BiFeO_3$ were deposited on these nanosheets to obtain the pseudocubic [001] preferential orientation. $La_{0.67}Sr_{0.33}MnO_3$ was also deposited and the magnetic properties were compared to those measured for a film grown on a single-crystal substrate. Significant results were also obtained using these nanosheets for the integration of $SrVO_3$ and $CaVO_3$ as transparent conducting films on glass substrate. Pt thin films were grown along their [111] orientation deposited at lower temperature than usual, and along their [200] direction. The oxides and metal depositions

have been achieved using different techniques as pulsed laser deposition, chemical solution deposition, and sputtering.

This thesis is part of the PolyNASH project financed by French National Research Agency (ANR) involving three laboratories: the Rennes Institute of Chemical Sciences (ISCR), the Crystallography and Material Sciences Laboratory of Caen (CRISMAT), and the Condensed Matter Study Group of Versailles (GEMaC).

References

[1] G.E. Moore, Cramming more components onto integrated circuits, Reprinted from Electronics, volume 38, number 8, April 19, 1965, pp.114 ff., IEEE Solid-State Circuits Soc. Newsl. 11 (2006) 33–35. https://doi.org/10.1109/N-SSC.2006.4785860.

[2] G.Q. Kouchi Zhang, M. Graef, F. van Roosmalen, The Rationale and Paradigm of "More than Moore," in: 56th Electron. Compon. Technol. Conf. 2006, IEEE, San Diego, CA, 2006: pp. 151–157. https://doi.org/10.1109/ECTC.2006.1645639.

[3] R.A. McKee, F.J. Walker, M.F. Chisholm, Crystalline Oxides on Silicon: The First Five Monolayers, Phys. Rev. Lett. 81 (1998) 3014–3017. https://doi.org/10.1103/PhysRevLett.81.3014.

[4] K. Kikuta, K. Noda, S. Okumura, T. Yamaguchi, S. Hirano, Orientation control of perovskite thin films on glass substrates by the application of a seed layer prepared from oxide nanosheets, J. Sol-Gel Sci. Technol. 42 (2007) 381–387. https://doi.org/10.1007/s10971-006-0200-z.

[5] T. Shibata, K. Fukuda, Y. Ebina, T. Kogure, T. Sasaki, One-Nanometer-Thick Seed Layer of Unilamellar Nanosheets Promotes Oriented Growth of Oxide Crystal Films, Adv. Mater. 20 (2008) 231–235. https://doi.org/10.1002/adma.200701381.

[6] T. Shibata, H. Takano, Y. Ebina, D.S. Kim, T.C. Ozawa, K. Akatsuka, T. Ohnishi, K. Takada, T. Kogure, T. Sasaki, Versatile van der Waals epitaxy-like growth of crystal films using two-dimensional nanosheets as a seed layer: orientation tuning of $SrTiO_3$ films along three important axes on glass substrates, J Mater Chem C. 2 (2014) 441–449. https://doi.org/10.1039/C3TC31787K.

Chapter 1: State of art

Introduction

This first chapter describes the state of art concerning the 2-dimensional (2D) oxide nanosheets. First of all, a brief history of the emergence of nanosheets will be exposed. Afterward, the generality of the preparation of 2-dimensional oxides nanosheets will be developed. The third part focuses on different examples of layered phases, their oxides nanosheets, and their different properties. The last part of this chapter is an overview of the nanosheets deposition techniques.

1. Nanosheets: a recent class of materials

The discovery of the exceptional electronic properties of graphene in 2004 by K. Novoselov *et al.* opened the path of a new class of materials: the 2D-materials [1,2]. Research on nanosheets is recent (around 25 years old), and graphene has enhanced researchers' interest in this type of material. In 15 years (2005-2020), the number of publications using the term "nanosheets" has increased about a hundred times (Figure 1.1), reaching a total of around 80.000 publications in 2021. This can be explained by the exceptional properties obtained with nanosheets at a very low thickness (< 10 nm), opening new opportunities for nanotechnologies: nanoelectronic devices, sensors, photocatalysis, optical devices, … [3]. Van der Waals heterostructures made of different nanosheets multilayers can also be imagined to obtain unusual and/or controlled properties [4].

Different types of nanosheets have been synthesized and studied. The dichalcogenide nanosheets of formula MX_2 with M a transition metal and X a chalcogen (S, Se, Te) have centered a lot of attention, particularly with the widely studied MoS_2 [5,6]. Their tunability allows them to have a wide range of properties that can be used for energy storage and optoelectronic applications [7].

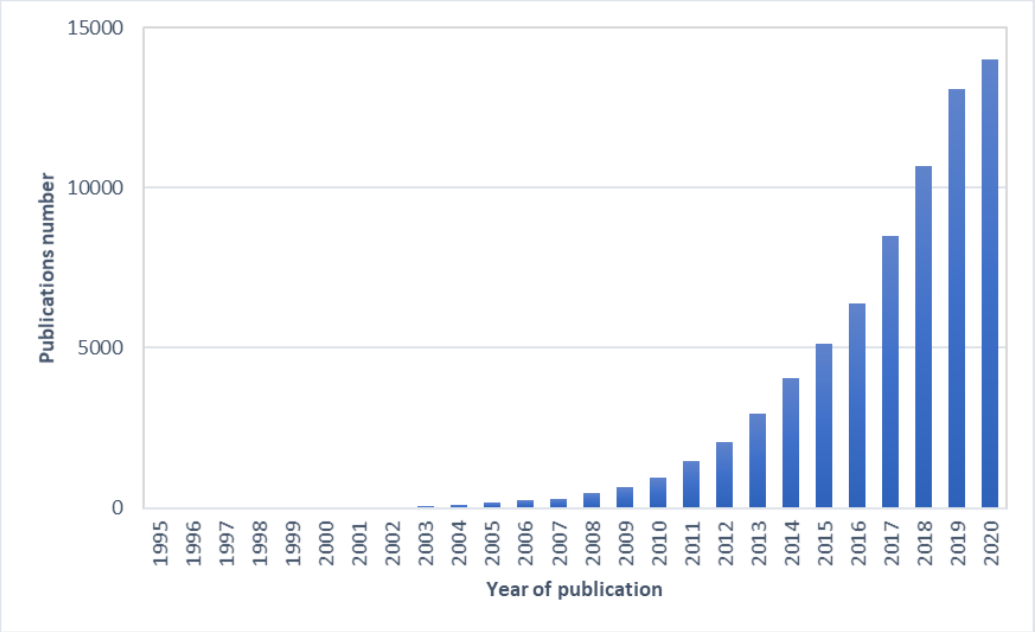

Figure 1.1. Number of publications using the term "nanosheets" as a function of the publication year (source: Scifinder^n ®).

Nitride nanosheets are also a family of nanosheets showing interesting properties. The hexagonal boron nitride, isostructural to graphene, is probably the most studied. Its insulating properties may be interesting for photocatalysis, electronic, and magnetic applications [8–10]. These nanosheets are obtained from the delamination of layered nitride materials or by the nitridation of layered oxide phases [11].

Another type of nanosheets are the Mxenes (carbides) of formula $M_{1+n}X_n$, with M a transition metal and X = C, N. They have shown to exhibit good electronic conductivities which could make it promising for electrode materials, hybrid cells, and supercapacitors applications [12,13].

The double hydroxides nanosheets of formula $[M^{2+}_{1-x}M^{3+}_x(OH)_2][A^{n-}]_{x/n}\cdot zH_2O$, where M^{2+} and M^{3+} are transition metal and A^{n-} an inorganic or organic anion, is a class of nanosheets widely studied for supercapacitors, lithium-ion batteries, and solar cells applications [14–17].

Finally, there are the oxides nanosheets [18] that constitute the purpose of this thesis. The present work is focused on the synthesis and deposition of oxides nanosheets on various substrates for microelectronic applications, using them as a seed layer to allow the preferentially oriented growth of complex oxides thin films on low-cost and large substrates. Regarding this objective, a large lateral size of the nanosheets is desired.

2. Exfoliation of the oxide nanosheets

The exfoliation of layered phases consists in separating the sheets slabs of the material. Different ways of exfoliation exist for oxide nanosheets: the mechanical exfoliation, the chemical intercalation, and bottom-up synthesis [19]. The mechanical exfoliation (commonly ultrasounds) and the bottom-up growth in solution are generally used for the exfoliation of transition metal oxides with a layered structure [20,21], while the liquid exfoliation (chemical intercalation) is used for materials composed of metal oxides layers separated by alkali/alkaline earth ions. This work is based on nanosheets obtained by liquid exfoliation. The method consists of three different steps, which are summarized in Figure 1.2: (a) the synthesis of the layered phase made of metal oxide layers separated by alkali or alkaline earth ions, (b) the exchange of the alkali ions by protons in the structure by treatment in an aqueous acidic solution, and (c) the liquid exfoliation of the layers using an organic exfoliant to delaminate and stabilize the obtained colloidal solution of nanosheets.

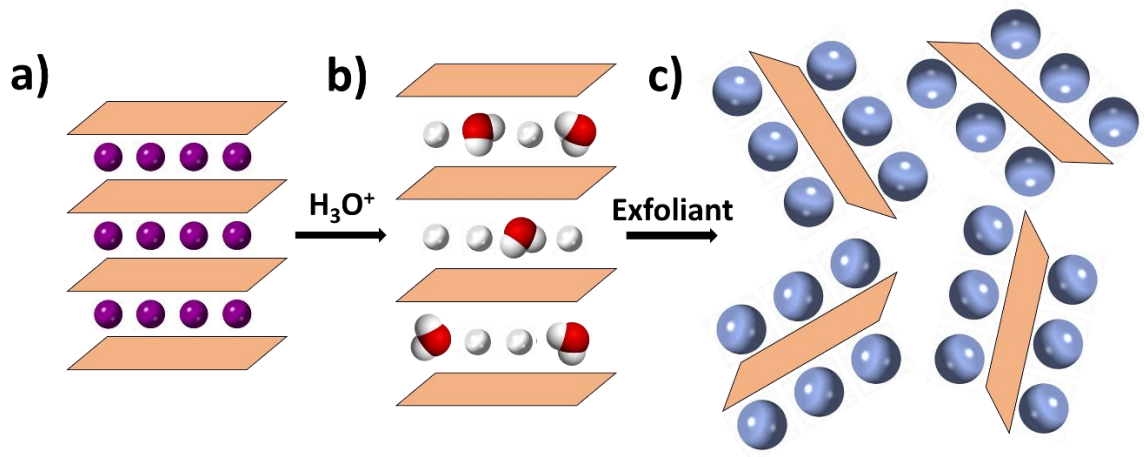

Figure 1.2. The different steps of the delamination of a layered oxide phase: the layers of oxides are in orange; the alkali/alkali earth ions are in purple; protons are in white; oxygens are in red; exfoliant molecules are in grey. (a) The layered oxide is composed of metal oxides layers separated by alkali/alkaline earth ions. (b) The alkali/alkaline earth ions have been exchanged by protons. Water can be intercalated between the layers. (c) The layers are separated by the exfoliant, forming nanosheets in solution.

2.1. Protonation

The protonation is realized by treating the powder with an acidic solution. HNO_3 and HCl are the most commonly used acids for exfoliation. The acid-base reaction leads to the replacement of the alkali ions by protons ions and water molecules [22]. The

alkali/alkaline earth salt formed is eliminated by washing the powder several times with distilled water. The interlayered space of the protonated material uses to be modified due to the intercalation of water in the structure (Figure 1.2b).

2.2. Exfoliation

The exfoliation is carried out by mixing the protonated powder with an exfoliant in the same molar ratio, in aqueous solution. The exfoliants are amphiphile molecules, *i. e.* they are composed of a hydrophilic part, which is positively charged, and hydrophobic part(s) made of alkyl chain(s). A counter ion, usually OH^-, brings neutrality to these molecules. The exfoliants used in this work are shown in figure 1.3. When the exfoliant and the protonated layered phase are mixed, an acid-base reaction occurs: the OH^- and the H^+ present in the layered structure react to form water, while the exfoliant plays the role of the counter ion in the layered structure, delaminating the layered oxides thanks to their long alkyl chains, leading to negatively charged nanosheets, with their charge being balanced by the positively charged exfoliant. It has been proved that the exfoliation occurs instantaneously [22].

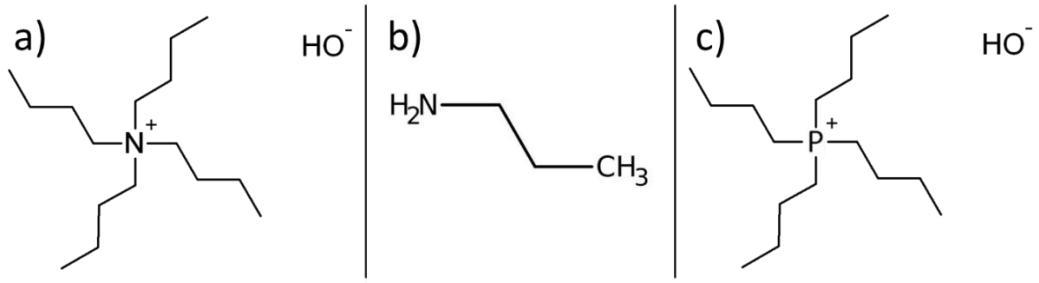

Figure 1.3. The list of the different exfoliants which have been used in this PhD thesis. (a) Tetrabutylammonium hydroxide (TBAOH). (b) Propylamine (PA), which hydrolyzes in solution. (c) Tetrabutylphosphonium hydroxide (TBPOH).

The most commonly used exfoliants are the family of the tetraalkylammonium hydroxides (figure 1.3a). Different studies have been performed by varying the length of their chains: Yuan *et al.* showed that the tetramethylammonium was the most efficient for the exfoliation of titania oxide nanosheets, but this exfoliant leads to smaller size of nanosheets compared to the tetrabutylammonium (TBAOH) [23]. For this reason, TBAOH is the most commonly used exfoliant for oxide nanosheets formation.

The tetrabutylphosphonium hydroxide (TBPOH) is relatively comparable with TBAOH, but the larger size of P and its smaller electronegativity leads to fast exfoliation but smaller nanosheets [24]. However, TBPOH can be useful in some situations, for example, the exfoliation of tantalum oxide nanosheets, which considerably reduce its exfoliation time from 3 weeks with TBAOH to 3 days with TBPOH [25].

n-propylamine and *n*-butylamine are also commonly used exfoliants, which have shown to be particularly efficient for the exfoliation of asymmetric nanosheets, which tend to roll when TBAOH is used, due to the strains engendered by their structures [26]. However, no explanations of why those exfoliants make the nanosheets more stable have been made. This behavior will be discussed in Chapter 3.

3. From layered oxides to oxide nanosheets

A wide variety of nanosheets (NS) can be obtained by the protonation and the exfoliation of layered phases. Table 1.1 displays a summary of the non-exhaustive list of the different nanosheets presented in this chapter, their properties, and the thin films deposited on these nanosheets that show an induced preferential growth.

Table 1.1. Library of some nanosheets described hereafter [51,60-77,89,90,116,117,178].

Layered phase	Nanosheets (NS)	Properties of the NS	2D lattice	Thin films deposited on the NS
$KCa_2Nb_3O_{10}$	$[Ca_2Nb_3O_{10}]^-$	Dielectricity Photocatalysis Photoluminescence	Square	$LaNiO_3$ $BaTiO_3$ $(K,Na)NbO_3$ $Pb(Zr,Ti)O_3$ $BiFeO_3$ $SrRuO_3$ $(Ba,Sr)TiO_3$ $SrTiO_3$ $(Ca,Sr)Bi_4Ti_4O_{15}$ $Pr(Ca,Sr)TiO_3$ $(Sr,Eu)_2(Sn,Ti)O_4$
$Sr_2Nb_3O_{10}$	$[Sr_2Nb_3O_{10}]^-$	Dielectricity	Square	$(K,Na)NbO_3$
$KCa_2Na_3Nb_6O_{19}$	$[Ca_2Na_3Nb_6O_{19}]^-$	Dielectricity	Square	None
α-$LiNbWO_6$	$[NbWO_6]^-$	Catalysis Photocatalysis	Square	VO_2
$K_4Nb_6O_{17}$	$[K_xNb_6O_{17}]^{4-x}$	Catalysis Photocatalysis Photoluminescence	Rectangle	None
$K_{0.8}Ti_{1.73}Li_{0.27}O_4$	$[Ti_{0.87}O_2]^{0.52-}$	Dielectricity Photocatalysis Piezoelectricity	Rectangle	$SrRuO_3$ $Pb(Zr,Ti)O_3$ $SrTiO_3$ VO_2
$Cs_{0.7}Ti_{1.825}\square_{0.175}O_4$	$[Ti_{0.91}O_2]^{0.36-}$	Dielectricity Photocatalysis Photoluminescence	Rectangle	None
$K_zTi_{1-x-y}Fe_xCo_yO_2$	$[Ti_{1-x-y}Fe_xCo_yO_2]^{z-}$	Ferromagnetism	Rectangle	None
$Cs_6W_{11}O_{36}$	$[Cs_4W_{11}O_{36}]^{2-}$	Photochromism Redoxable	Hexagonal	ZnO
$K_{0.45}MnO_2$	$[MnO_2]^{0.45-}$	Redoxable	Hexagonal	ZnO
$Na_{0.2}RuO_2 \bullet 0.45H_2O$	$[Ru_{0.95}O_2]^{0.2-}$	Conductive Redoxable	Hexagonal	None
$Na_{0.9}MoO_2$	$[MoO_2]^{\delta-}$	Redoxable	Hexagonal	$SrTiO_3$
$RbTaO_3$	$[TaO_3]^-$	Photocatalysis	Parallelogram	None
KNb_3O_8	$[Nb_3O_8]^-$	Catalysis Photocatalysis	Rectangle	None

3.1. Layered perovskites

3.1.1. Dion-Jacobson phases and their nanosheets

The Dion-Jacobson (DJ) phases are a family of layered perovskites of formula $AA'_{n-1}B_nO_{3n+1}$ (with A: alkali metal, A': alkaline earth metal, and B: transition metal), which have been discovered by M. Dion *et al.* in 1981 [27]. A DJ phase is constituted of perovskites layers, composed of corner-shared BO_6 octahedra, separated by layers of A cations. The thickness of each perovskite layer is given by the value of *n* which determines the number of BO_6 corner-shared octahedra in the layer (Figure 1.4a).

The most commonly DJ phase studied is $KCa_2Nb_3O_{10}$ (KCN). KCN is monoclinic (space group $P2_1/m$), with a = 7.741 Å, b = 7.707 Å, c = 14.859 Å, β = 97.51°, and can also be described in a larger tetragonal lattice with a = 7.727 Å et b = 29.466 Å (Figure 1.4a) [28].

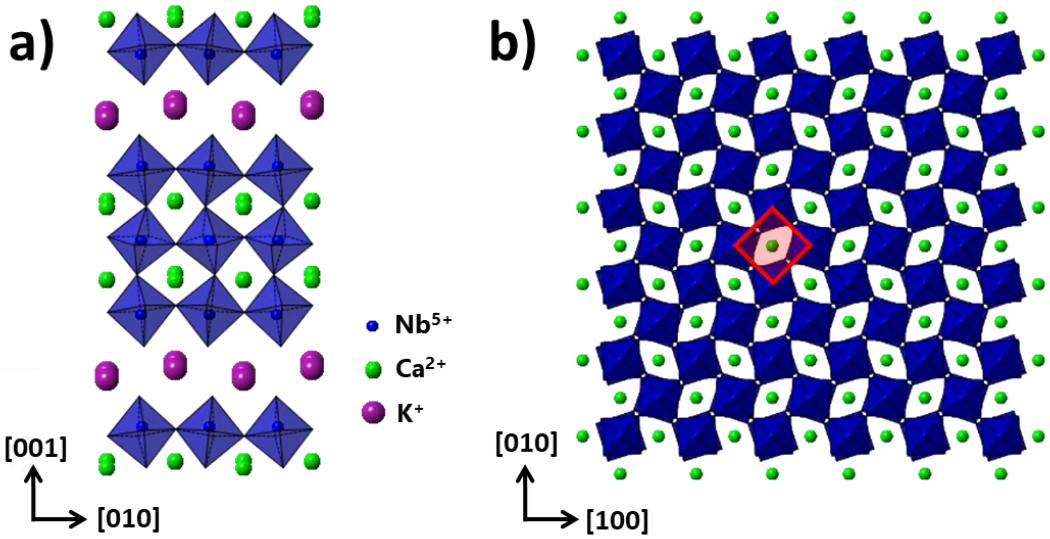

Figure 1.4. (a) $KCa_2Nb_3O_{10}$ DJ structure along the [100] direction. (b) $[Ca_2Nb_3O_{10}]^-$ nanosheet structure along the [001] direction. The 2D square lattice a = 3.854 Å is depicted in red.

KCN has a band gap of 3.2 eV [29] and shows photocatalytic properties for hydrogen production, luminescence properties with rare earth doping, and is a good H_2 sensor due to its high protonic conductivity [4–6]. The K^+ ions located in the interlayers' regions can be exchanged by protons in acid solution, forming the solid $HCa_2Nb_3O_{10}$ (HCN) [33]. HCN also presents photocatalytic properties [8–10] and interesting ion-exchange properties for cations removal [11, 12]. This phase can be delaminated using

alkylammonium ions, such as TBAOH which is the most commonly used for this phase [39]. The exfoliation leads to $(TBA)^+[Ca_2Nb_3O_{10}]^-$ colloid solution. The band gap measured by STEM-VEELS of these nanosheets is 2.9 eV [40], which makes $[Ca_2Nb_3O_{10}]^-$ interesting for various applications, such as photocatalysis [13–21] and as UV photodetector [50]. It can also be used as an insulator for memories, capacitor, and gate dielectric for nanoelectronics thanks to its huge dielectric constant ($\varepsilon_r \simeq 210$) [24–32], or as a seed layer for the oriented growth of complex oxides thin films. For the latter, as the $[Ca_2Nb_3O_{10}]^-$ nanosheets have a 2D-square lattice along the [001] direction, with a lattice constant a = 3.854 Å (Figure 1.4b), it is possible to obtain preferentially oriented growth of complex oxides which present a close 2D-square lattice mismatch with $[Ca_2Nb_3O_{10}]^-$. The nanosheets can be deposited on any substrates using the Langmuir-Blodgett, layer-by-layer, dip coating, spin coating, or drop casting techniques, which allow the deposition of oriented thin films on amorphous and low-cost materials. A wide range of oriented oxides have been obtained using $[Ca_2Nb_3O_{10}]^-$ nanosheets: ferroelectric films ($BaTiO_3$) [60], piezoelectric films ($(K,Na)NbO_3$, $Pb(Zr,Ti)O_3$) [61–69], multiferroic films ($BiFeO_3$) [70], magnetic films ($SrRuO_3$) [71], dielectric films ($(Ba,Sr)TiO_3$, $SrTiO_3$, $CaBi_4Ti_4O_{15}$) [72–75], and luminescent films ($Pr(Ca,Sr)TiO_3$, $(Sr,Eu)_2(Sn,Ti)O_4$) [76,77], deposited by various techniques, such as Pulsed Laser Deposition (PLD), Chemical Solution Deposition (CSD), and sputtering.

It is possible to diversify the $KCa_2Nb_3O_{10}$ phase by adding Na atoms, leading to $KCa_2Na_{n-3}Nb_nO_{3n+1}$ (n = 4–6) phases. The layers are n octahedra thick and contain n – 1 cations (Na and K ions) occupying the same sites in a disordered way [78]. They can be exfoliated using TBAOH to obtain $[Ca_2Na_{n-3}Nb_nO_{3n+1}]^-$, as presented in Figure 1.5 [79,80]. Their bandgap energy depends on their thicknesses and composition: 3.95, 3.80, and 3.77 eV for n = 4, 5, and 6, respectively [80,81], which is higher than the one of the $[Ca_2Nb_3O_{10}]^-$ nanosheets (2.9 eV).

These nanosheets are interesting for various applications such as photocatalytic and photoelectrocatalytic water oxidation (water splitting) [81–83]. $[Ca_2Na_3Nb_6O_{19}]^-$ nanosheets have the highest dielectric constant (ε_r = 470) in the 2D materials family [84], and can be used as high-κ dielectrics to make nanocapacitor devices or multilayer/superlattice assemblies [85,86].

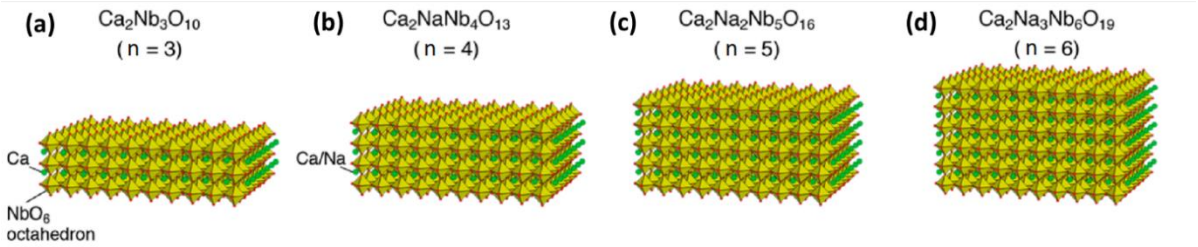

Figure 1.5. Structures of $Ca_2Na_{n-3}Nb_nO_{3n+1}$ nanosheets: (a) $[Ca_2Nb_3O_{10}]^-$, (b) $[Ca_2NaNb_4O_{13}]^-$, (c) $[Ca_2Na_2Nb_5O_{16}]^-$, (d) $[Ca_2Na_3Nb_6O_{19}]^-$ [55].

Otherwise, $[Sr_2Nb_3O_{10}]^-$ nanosheets, far less used than $[Ca_2Nb_3O_{10}]^-$, obtained from the $KSr_2Nb_3O_{10}$ phase, also present interesting properties. It exhibits excellent UV detecting performance [87], high dielectric properties ($\varepsilon_r \simeq 240$), with a dielectric constant which is higher than the one of the $[Ca_2Nb_3O_{10}]^-$ nanosheets ($\varepsilon_r \simeq 210$), which makes it a good candidate as pseudocapacitor [56,88].

The piezoelectric (K,Na)NbO_3 (KNN) (a_{pc} = 3.95 Å) is the only material which has been deposited on $[Sr_2Nb_3O_{10}]^-$ (a = 3.90 Å) nanosheets up to now [89,90]. (001)KNN was grown on $[Ca_2Nb_3O_{10}]^-$ nanosheets by PLD, and high film quality at 400°C was obtained, avoiding K_2O and Na_2O evaporation that occurs at higher temperature [62]. On the other hand, KNN has a lower lattice mismatch with $[Sr_2Nb_3O_{10}]^-$ than $[Ca_2Nb_3O_{10}]^-$, leading to a reduction of the energy requested to obtain the oriented film. High quality (001)KNN films have also been obtained at 350°C, opening the deposition on flexible substrates as polyimide.

A wide variety of other nanosheets from the DJ phases have been synthesized, such as $[Ba_2Nb_3O_{10}]^-$ or $[(Ca,Sr,Ba)_2Ta_3O_{10}]^-$ [91–93], and many other compositions are possible, showing the large possibilities of this type of materials.

3.1.2. Aurivillius and Ruddlesden-Popper phases

The $A_{n+1}B_nO_{3n+1}$ Ruddlesden-Popper (RP) and $(Bi_2O_2)(A_{n-1}B_nO_{3n+1})$ Aurivillius oxides (with A: alkaline earth metal and B: transition metal) are two types of layered perovskites, composed of perovskite layers made of corner-shared BO_6 octahedra, separated by layers of A_2 or Bi_2O_2 cations, respectively, with a thickness of n BO_6 octahedra [94–96]. The perovskite slabs are made of $B^{4+}O_6$ octahedra in these compounds, while they are made of $B^{5+}O_6$ octahedra in the DJ phases (Figure 1.6).

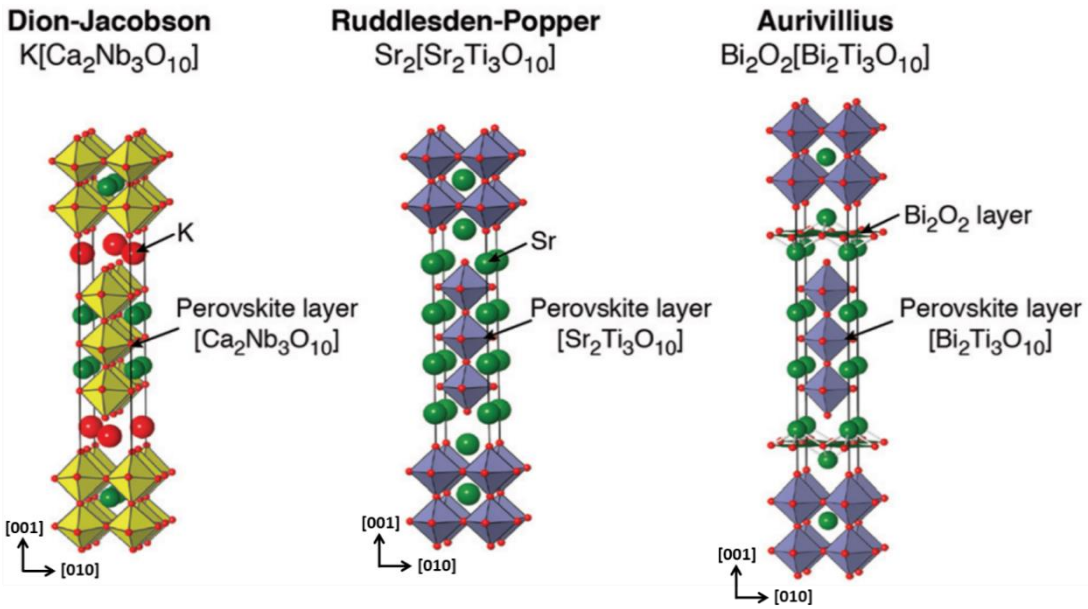

Figure 1.6. Structure of layered perovskites $KCa_2Nb_3O_{10}$ Dion-Jacobson phase, $Sr_4Ti_3O_{10}$ Ruddlesden-Popper phase, and $Bi_4Ti_3O_{10}$ Aurivillius phase [97].

RP and Aurivillius phases have been widely studied for their dielectric and their fatigue-free ferroelectric properties, respectively [98–100]. RP phases are also promising in the halide perovskites field for solar cells, optoelectronic or semiconductors applications [101–103]. As the DJ phases, they can be protonated and exfoliated. Schaak and Mallouk were able to obtain different RP nanosheets using TBAOH and *n*-butylamine, such as $[CaNaTa_3O_{10}]^{2-}$, $[La_2Ti_3O_{10}]^{2-}$, $[Ca_2(Nb,Ta)_2TiO_{10}]^{2-}$ or $[(Ca,Sr)LaTi_2TaO_{10}]^{2-}$ [104,105]. For the Aurivillius phases, various nanosheets have been synthesized, showing interesting behaviors: for example $[Bi_2Ti_3O_{10}]^{2-}$ nanosheets present ferroelectric properties [106], $[Bi_2MoO_6]^{2-}$ and $[Sb_2WO_6]^{2-}$ nanosheets display photocatalytic properties [107,108], and $[SrTa_2O_7]^{2-}$ nanosheets exhibit blue luminescence [109].

RP and Aurivillius nanosheets have not been widely described in the literature compared to the DJ nanosheets. However, they could potentially present high dielectric and ferroelectric properties, as exhibited by the parent compounds, which could be also interesting for multilayer building block devices.

3.2. Other layered oxide and nanosheets with 2D-square lattices

α-$LiNbWO_6$ crystallizes in a tetragonal lattice with the space group $P\bar{4}2_1m$, which corresponds to a trirutile structure, with a = 4.682 Å and c = 9.275 Å [110]. The structure is made of corner and edge-shared WO_6 and NbO_6 octahedra, separated by Li^+ ions (Figure 1.7a). It has recently been shown that this phase could be promising for lithium storage applications [111].

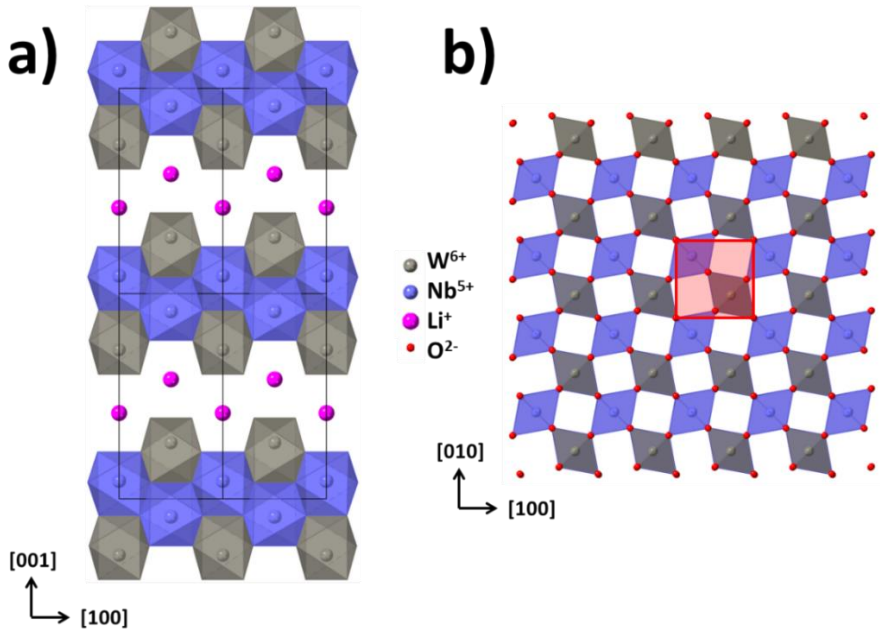

Figure 1.7. (a) The α-$LiNbWO_6$ structure along the [010] direction. (b) $[NbWO_6]^-$ nanosheet structure along the [001] direction. The 2D square lattice with a = 4.682 Å is depicted in red.

The Li^+ ions can be exchanged in the structure by protonation, leading to the $HNbWO_6.xH_2O$ compound [112]. The latter can be exfoliated using propylamine (PA) or TBAOH, to obtain $[NbWO_6]^-$ nanosheets in solutions. It is possible to restack the nanosheets using acid to obtain $HNbWO_6$ nanosheets. Protonated nanosheets show good photocatalytic properties for hydrogen production from water splitting [113] and are solid Brønsted acid for catalysis for reactions such as the formation of 5-hydroxymethylfurfural from glucose [114,115]. The 2D lattice of the niobium tungstate nanosheets are squares of parameter a = 4.682 Å (Figure 1.7b). $[NbWO_6]^-$ nanosheets have recently been used for the (-402) monoclinic/(002) tetragonal orientation growth of the metal-insulator transition VO_2 thin film [116,117]. The nanosheets have a lattice mismatch of 3.6 % and 7.9 % for the (-402) monoclinic orientation and 3.2 % mismatch

for the (002) tetragonal orientation of VO_2, leading to highly oriented films on arbitrary substrates.

3.3. Nanosheets with 2D-rectangle lattice

3.3.1. $[K_xNb_6O_{17}]^{4-x}$ nanosheets from the $K_4Nb_6O_{17}$ phase

$K_4Nb_6O_{17}$ is a layered compound crystallizing in an orthorhombic lattice. Its space group is $P2_1nb$, with a = 7.83 Å, b = 33.21 Å and c = 6.46 Å [118]. The structure is composed of corner and edge-shared NbO_6 octahedra layers, separated by two different potassium ions layers (Figure 1.8a). The potassium ions in the type I layer are weakly linked to the NbO_6 octahedra and thus can be easily exchanged with other mono or bivalent cations [63], [64]. Water molecules can also integrate the type I layer, forming the tri-hydrated $K_4Nb_6O_{17}.3H_2O$ or the pentahydrated $K_4Nb_6O_{17}.5H_2O$ phases [118,121].

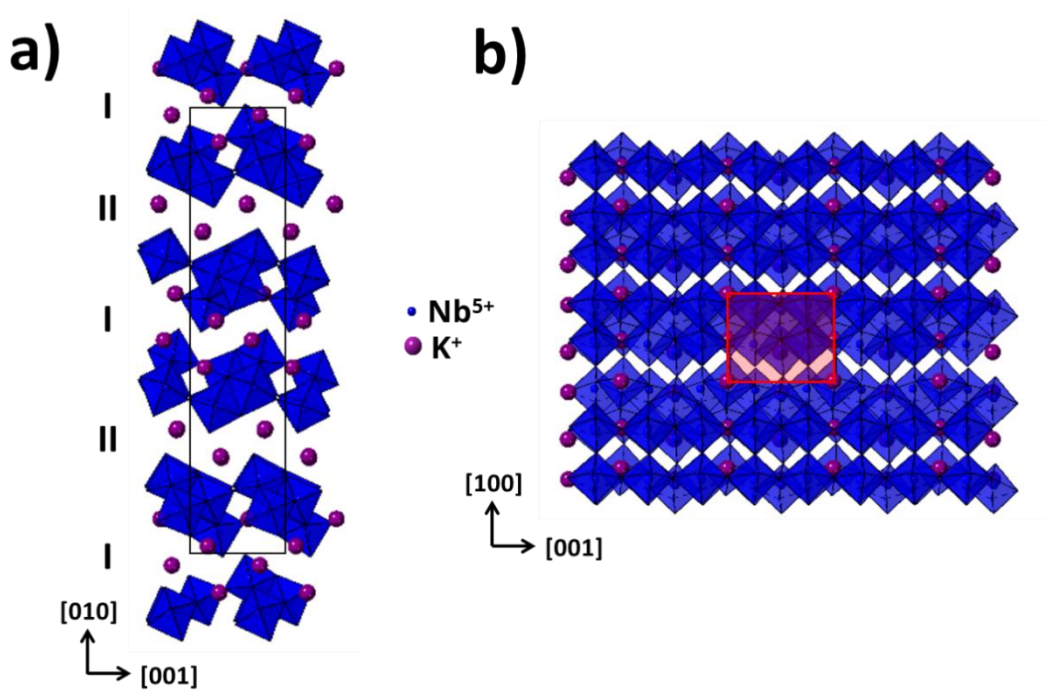

Figure 1.8. (a) $K_4Nb_6O_{17}$ structure along the [100] direction. (b) $[K_2Nb_6O_{17}]^{2-}$ nanosheet structure along the [010] direction. The 2D rectangle lattice with a = 7.83 Å and c = 6.46 Å is displayed in red.

$K_4Nb_6O_{17}$ has a wide band gap of 3.3 eV [122], which makes it a good candidate for photocatalytic applications as water splitting [122,123], H_2 production [124], or the reduction of the hazardous Cr^{6+} ions in safe Cr^{3+} ions [84]. The potassium ions can be easily exchanged in the structure by protons, leading to $H_xK_{4-x}Nb_6O_{17}$ ($0 \leq x \leq 4$), which

also has interesting photocatalytic properties in bulk [126] and nanosheets form [36,127]. Some authors report a protonation only in the interlayer I while other authors report a protonation in the two interlayers. However, EDS reported in several publications clearly shows that the protonation is total in the first interlayer and inexistent or partially done in the second interlayer [128–130]. Other cations, for example Ni^{2+} [131], Sn^{2+} [132], or Eu^{3+} [133], can be inserted into the structure, modifying the photocatalytic properties and luminescence of the material.

The regular exfoliation with TBAOH using the protonated phase leads to monolayer nanosheets, which tend to form nanoscrolls (Figure 1.9) [128]. Saupe *et al.* showed that during the first 30 seconds of the exfoliation, only bilayers nanosheets are obtained. When the exfoliation time increases, the bilayers nanosheets become monolayer nanosheets. No potassium ions were detected in the nanoscrolls by EDS, showing that nanoscrolls come from $[Nb_6O_{17}]^{4-}$ nanosheets [26,134]. Du *et al.* explained the phenomenon by the existence of an intrinsic tension due to the asymmetric structure of the $[Nb_6O_{17}]^{4-}$ nanosheets, which could tend to curve to release the strain energy, leading to nanoscrolls [26]. On the other hand, $[K_2Nb_6O_{17}]^{2-}$ nanosheets have a double layer structure, increasing the rigidity of the nanosheets, and symmetric structure, limiting the strain forces.

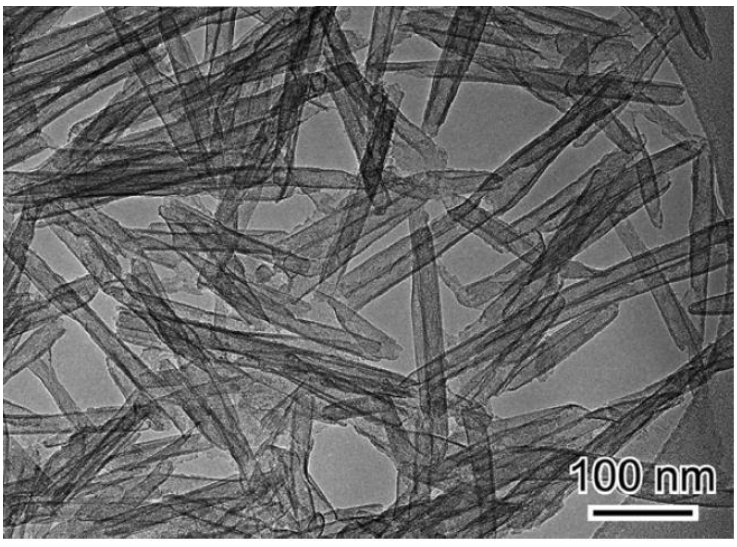

Figure 1.9. Transmission electron microscopy (TEM) micrography of the $[Nb_6O_{17}]^{4-}$ nanoscrolls [134].

Otherwise, nanosheets can be exfoliated from the parent phase or the protonated phase, using *n*-propyl/*n*-butylamine [119,135–137], or *n*-propylammonium chloride [138–140]. The latter has the disadvantage to require centrifugation and washing to get

rid of chloride anions. Both exfoliants only give nanosheets in solution, reported in the literature to be either $[K_2Nb_6O_{17}]^{2-}$ or $[Nb_6O_{17}]^{4-}$ nanosheets. However, the results of the different protonations realized in the literature as discussed above show that the exfoliation would lead to a mix of these two nanosheets in solution. These niobate nanosheets are mostly used for photocatalytic applications [136,139,141,142].

It has to be noted that the $[K_xNb_6O_{17}]^{4-x}$ nanosheets have never been deposited as a dense monolayer on a substrate and have never been used for the oriented growth of complex oxides thin films. The 2D lattice of the niobium nanosheets is made of a rectangle with a = 7.83 Å and c = 6.46 Å (Figure 1.8b), which could probably be used as a template for (011) perovskites growth.

3.3.2. $[Ti_{0.87}O_2]^{0.52-}$ nanosheets from the $K_{0.8}Ti_{1.73}Li_{0.27}O_4$ phase

$K_{0.8}Ti_{1.73}Li_{0.27}O_4$ (KTLO) is a layered oxide with a lepidocrocite structure of lattice constants a = 3.824 Å, b = 15.532 Å and c = 2.973 Å (space group *Cmcm*) [143]. It is made of edge-shared TiO_6 octahedra layers, separated by K^+ ions layers. The Li^+ ions are randomly placed in the Ti^{4+} positions (Figure 1.10a,b).

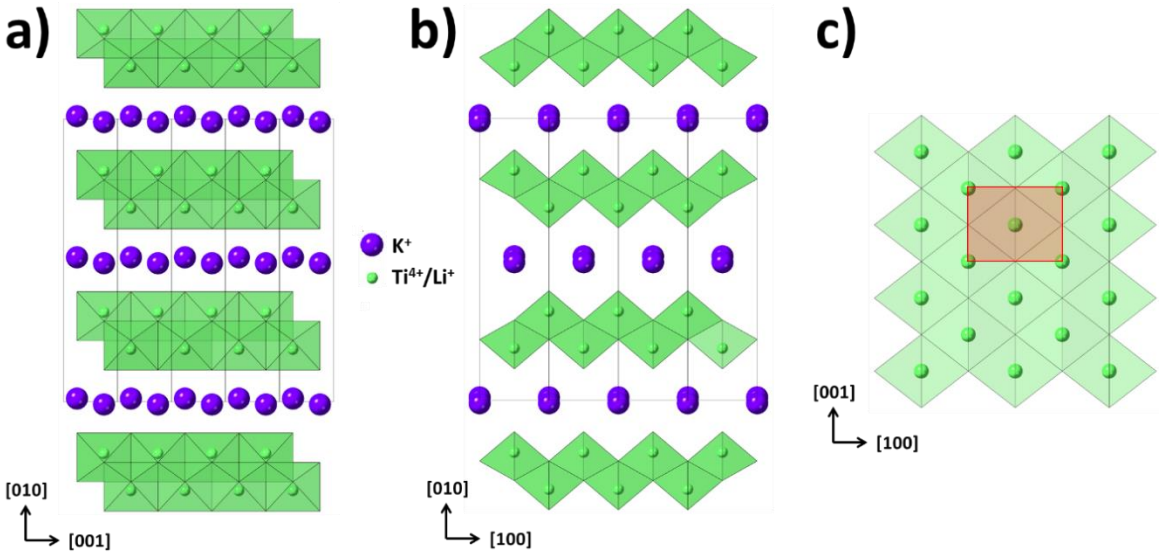

Figure 1.10. (a) $K_{0.8}Ti_{1.73}Li_{0.27}O_4$ structure along the [100] direction and (b) along the [001] direction. (c) $[Ti_{0.87}O_2]^{0.52-}$ nanosheet structure along the [010] direction. The 2D rectangle lattice with a = 3.824 Å and c = 2.973 Å is depicted in red.

The protonation of this phase leads to the exchange of the Li^+ and K^+ ions by protons, forming the $H_{1.07}Ti_{1.73}O_4$ (HTO) phase. Very few studies have been performed on

the properties of KTLO and HTO even if it has been shown that both have good exchange properties for lithium or sodium batteries [144,145], and HTO shows interesting catalytic properties for water splitting [146].

In contact with TBAOH, the protonated phase delaminates into $[Ti_{0.87}O_2]^{0.52-}$ nanosheets, which present Ti vacancies due to the elimination of Li^+ [143]. $[Ti_{0.87}O_2]^{0.52-}$ nanosheets have a large band gap of 3.8 eV and exhibit properties close to those of TiO_2 rutile: the nanosheets have a dielectric constant of $\varepsilon_r = 125$ [147], which is slightly higher than the one of the bulk rutile ($\varepsilon_r = 80–100$) [57,148]. Large size nanosheets (> 100 µm) can be obtained from this phase using the molten salt synthesis with K_2MoO_4 as salt (Figure 1.11) [149].

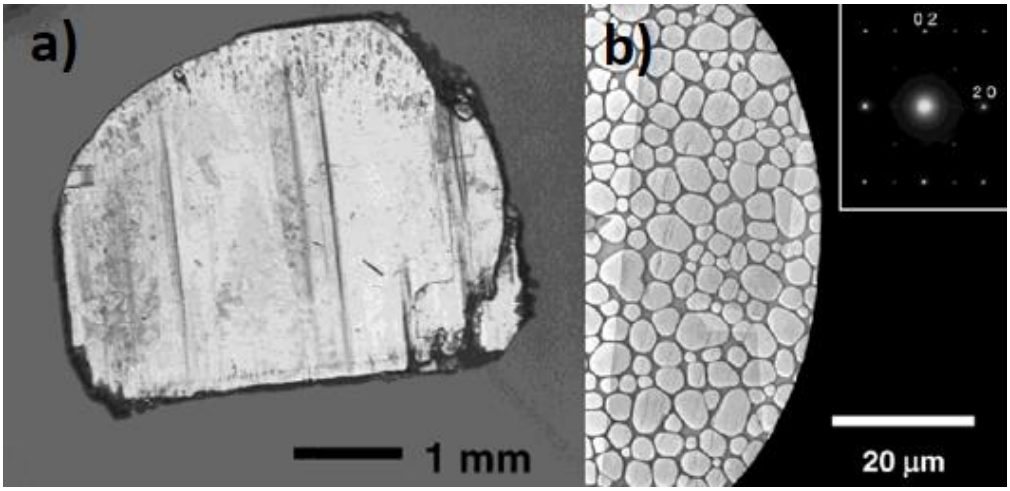

Figure 1.11. (a) Large single crystal of the potassium and lithium titanate. (b) TEM micrography of a large $[Ti_{0.87}O_2]^{0.52-}$ nanosheet [149].

Titanate nanosheets show catalytic properties for decomposition of 2-propanol and organic dyes under UV light [150,151] or the H_2 generation from water splitting [152]. It has also been shown recently that they can be used as ultrathin pressure sensors [153]. $[Ti_{0.87}O_2]^{0.52-}$ can be deposited by the Langmuir-Blodgett technique to obtain dense monolayer on various substrates. Multilayers assemblies can be made to form high-κ nanofilms [154], a ferroelectric device made of $[Ti_{0.87}O_2]^{0.52-}/[Ca_2Nb_3O_{10}]^-/[Ti_{0.87}O_2]^{0.52-}$ multilayers [155], or superlattices with nitrogen-doped graphene for high-rate sodium ion energy storage [156].

$[Ti_{0.87}O_2]^{0.52-}$ nanosheets have a 2D-rectangle lattice in the [010] plane with the following parameter: $a = 3.824$ Å and $c = 2.973$ Å (Figure 1.10c). They can also be used as a seed layer for the oxide growth, especially for the (011) growth orientation of

perovskites, considering an in-plane cell of a and $2c$ = 5.956 Å constants which are close to a and $\sqrt{2}a$ constants of the in-plane lattice of (011) oriented perovskites. Ferromagnetic material $SrRuO_3$ [71,157], piezoelectric $Pb(Zr,Ti)O_3$ films [63,64,66], dielectric $SrTiO_3$ film [74], and metal-insulator VO_2 film [116], have been deposited on various substrates (Pt/Si, Si, glass), leading to highly oriented (011) thin films.

3.3.3. $[Ti_{0.91}O_2]^{0.36-}$ nanosheets from the $Cs_{0.7}Ti_{1.825}\square_{0.175}O_4$ phase

$Cs_{0.7}Ti_{1.825}\square_{0.175}O_4$ phase is also a material with a lepidocrocite structure, crystallizing in orthorhombic lattice (space group *Immm*, with a = 3.831 Å, b = 17.021 Å, c = 2.964 Å) [158]. It is constituted of edge-shared TiO_6 octahedra, separated by Cs^+ ions, which are centered in the lattice (Figure 1.12). The vacancies are located in the octahedral sites.

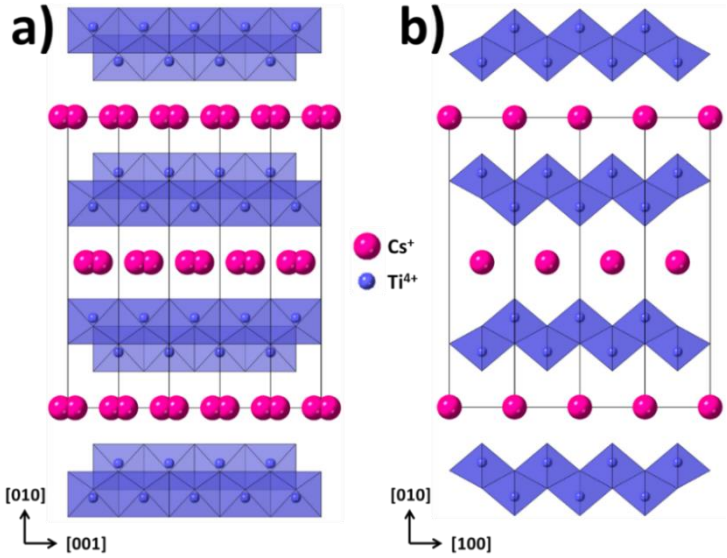

Figure 1.12. (a) $Cs_{0.7}Ti_{1.825}\square_{0.175}O_4$ structure along the [100] direction and (b) along the [001] direction.

The acid-base reaction between K^+ and H^+ ions leads to $H_{0.7}Ti_{1.825}\square_{0.175}O_4$ compound [120], [121]. The protonated phase can be exfoliated with TBAOH to form $[Ti_{0.91}O_2]^{0.36-}$ nanosheets [161]. These nanosheets present a band gap of 3.15 eV [162], which is lower than the one of $[Ti_{0.87}O_2]^{0.52}$ nanosheets (3.8 eV). Otherwise, $[Ti_{0.91}O_2]^{0.36-}$ nanosheets present interesting photocatalytic properties for Prussian blue and methylene blue reduction [163,164], CO_2 conversion into CO and CH_4 [165], and photoluminescence properties when it is doped with Eu^{3+} or Tb^{3+} for optoelectronic

devices applications [166]. It can also be used as a capacitive sensor, associated with bacterial cellulose for wearable electronics [167], and as a fuel cell material.

These titanate nanosheets have a 2D rectangle lattice with a = 3.831 Å and c = 2.964 Å, which are the same as the parameters of the $[Ti_{0.87}O_2]^{0.52-}$ nanosheets. The latter is more suitable for oriented oxides growth thanks to the average lateral size of the obtained nanosheets (10-100 µm), while $[Ti_{0.91}O_2]^{0.36-}$ nanosheets are a hundred times smaller [23,149,168].

3.3.4. Doped Co/Fe titanate nanosheets

Titania nanosheets can be doped with Fe^{3+} or Co^{2+} ions in order to obtain magnetic nanosheets. As Co-doped anatase has shown to exhibit ferromagnetism at room temperature, Osada *et al.* decided to Co/Fe doped the titanate nanosheets in order to see if the same properties are observed [169,170]. These nanosheets can be obtained from the cesium titanate or the potassium titanate by adding iron and/or cobalt oxides precursors in the synthesis process, leading to the substitution of Ti^{4+} by Fe^{3+} and Co^{2+}. Different nanosheets have been synthesized: $[Ti_{0.8}Co_{0.2}O_2]^{0.4-}$, $[Ti_{0.8}Fe_{0.2}O_2]^{0.2-}$, and $[Ti_{1-x-y}Fe_xCo_yO_2]^{z-}$ (with $0 \leq x \leq 0.4$ and $0 \leq y \leq 0.2$), as shown in Figure 1.13 [171].

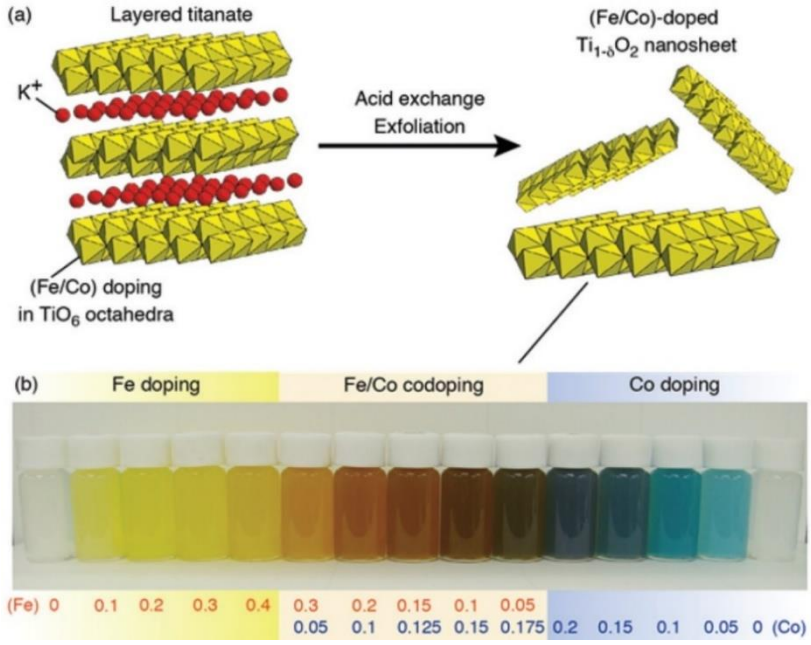

Figure 1.13. (a) Exfoliation process of the Fe/Co-doped $[Ti_{1-\delta}O_2]^{4\delta-}$ nanosheets. (b) Photograph of the nanosheets colloidal solutions with different Fe/Co ratio [171].

The results show that ferromagnetism at room temperature and strong magneto-optical effect (~ 10^4 deg.cm^{-1} at a wavelength of 330 nm) are obtained for 10 layers of $[Ti_{0.8}Co_{0.2}O_2]^{0.4-}$ nanosheets [170]. The same order of magnitude of the magneto-optical effect is obtained at 300 nm for 10 layers of $[Ti_{0.8}Fe_{0.2}O_2]^{0.2-}$ nanosheets, and an even stronger magneto-optical effect is obtained for 10 layers of the Fe/Co mixed $[Ti_{1.5}Fe_{0.2}Co_{0.3}O_4]^{0.4-}$ nanosheets (~ 10^5 deg.cm^{-1}) between 400 and 750 nm [172]. These nanosheets give the possibility to build nanospintronic devices and their properties can be adapted by controlling Fe/Co doping [171]. New nanodevices can also be made by assembling different types of nanosheets. For example, Li *et al.* realized an artificial multiferroic coupling with the $[Ti_{0.8}Fe_{0.2}O_2]^{0.2}$/$[Ca_2Nb_3O_{10}]^-$/$[Ti_{0.8}Fe_{0.2}O_2]^{0.2-}$ superlattices, showing ferroelectricity and magnetic order at room temperature [173].

3.4. Nanosheets with 2D hexagonal lattices

3.4.1. $[Cs_4W_{11}O_{36}]^{2-}$ nanosheets from the $Cs_6W_{11}O_{36}$ phase

$Cs_6W_{11}O_{36}$ is a layered material, crystallizing in a trigonal cell ($R\bar{3}c$, a = 7.261 Å, c = 110.580 Å), with a 2D-pyrochlore structure [174]. It is made of corner shared WO_6 octahedra, forming hexagonal rings where two Cs atoms are inserted (Figure 1.14a). The layers are separated by Cs^+ ions which can be easily exchanged. A slight excess of Cs^+ ions is observed, which could lead to a partial reduction of W^{6+} ions in the sample, explaining the blue color of the crystals [175]. No studies of the properties of this phase have been realized yet.

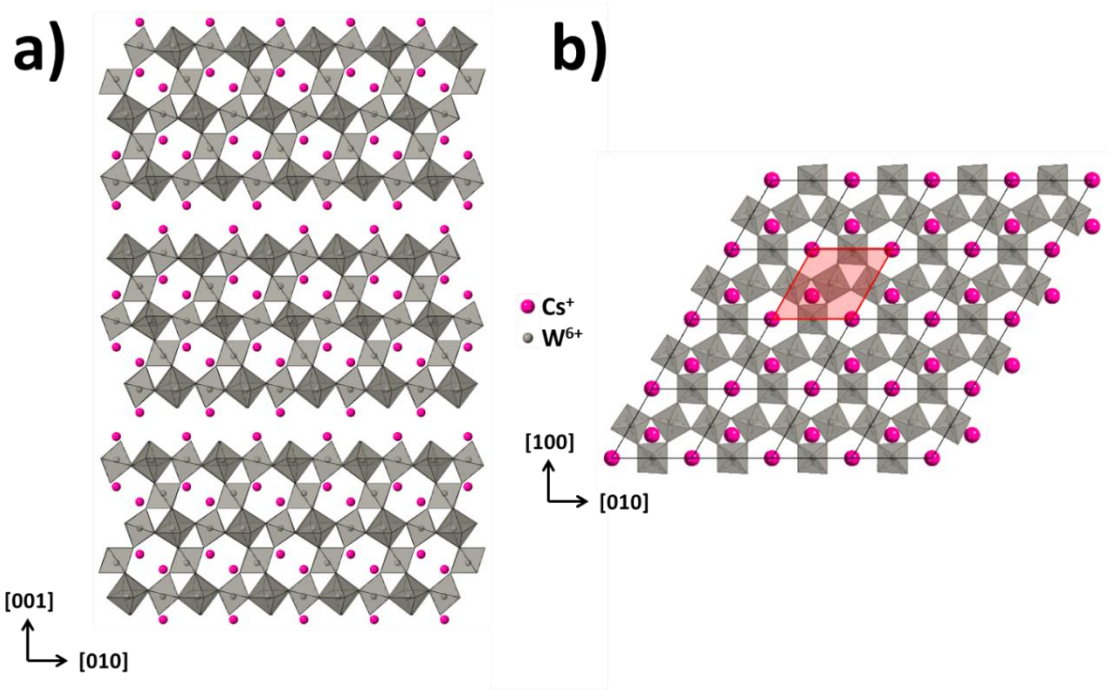

Figure 1.14. (a) $Cs_6W_{11}O_{36}$ structure along the [100] direction. (b) $[Cs_4W_{11}O_{36}]^{2-}$ nanosheet structure along the [001] direction. The 2D hexagonal lattice with a = 7.261 Å is depicted in red.

The phase can be protonated to obtain $H_2Cs_4W_{11}O_{36}{\cdot}6H_2O$ and exfoliated with TBAOH, leading to $[Cs_4W_{11}O_{36}]^{2-}$ nanosheets [176]. These nanosheets present photochromism [176], which can be suitable to make displays, data storages devices, and sensors [177].

$[Cs_4W_{11}O_{36}]^{2-}$ have also been used as a seed layer for the oriented growth of (001)ZnO deposited by PLD on glass and polymer substrates (polyethylene terephthalate) [178]. These cesium tungstate nanosheets have a 2D-hexagonal structure with a = 7.261 Å, which is close to the double of the ZnO hexagonal lattice constant, $2a_{ZnO}$ = 7.50 Å, allowing the oriented growth along the [001] direction.

3.4.2. $[MnO_2]^{\delta-}$ nanosheets from the $(K, Na)_xMnO_2$ birnessite phase

$(K, Na)_xMnO_2$ birnessite is a layered compound with a structure that depends on the synthesis and the amount of K^+ ions in the compound: for x = 0.31, the lattice is orthorhombic (*Ccmm*, a = 5.114 Å, b = 2.840 Å, c = 12.787 Å) [179], while for x = 0.45 the lattice is trigonal ($R\bar{3}c$, a = 2.879 Å, c = 19.071 Å) [180]. Both phases are constituted of side-shared MnO_6 octahedra (Figure 1.15a).

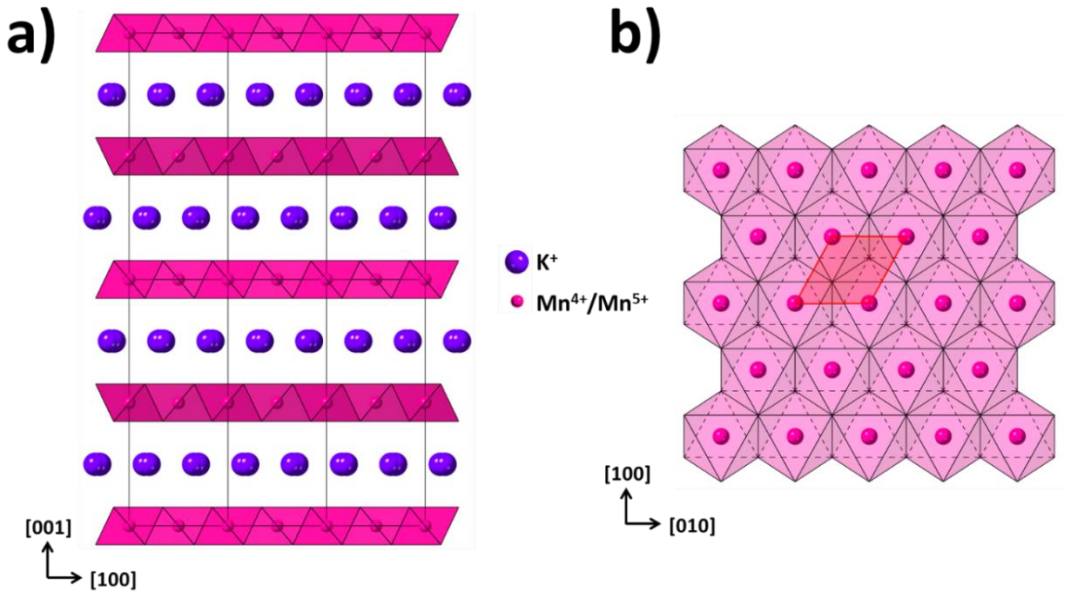

Figure 1.15. (a) $(K,Na)_xMnO_2$ (x = 0.45) structure along the [010] direction. (b) $[MnO_2]^{0.13-}$ nanosheet structure along the [001] direction. The 2D hexagonal lattice with a = 2.88 Å is depicted in red.

The protonation of the $(K,Na)_{0.45}MnO_2$ phase by acidic solution leads to the compound $H_{0.13}MnO_2$, which can be exfoliated with TBAOH to obtain $[MnO_2]^{0.13-}$ nanosheets [180], which are negatively charged due to the presence of a small amount of Mn^{3+} ions [181]. $[MnO_2]^{\delta-}$ nanosheets can also be obtained by a one-step reaction (bottom-up synthesis) by oxidizing $MnCl_2$ with H_2O_2 with tetramethylammonium hydroxide (TMAOH) [182]. The latter is fast (2 minutes reaction) compared to the multistep synthesis from the layered phase.

The MnO_2 nanosheets have been widely used for many applications: supercapacitors [183,184], photovoltaic [185], for the storage of Li/Na ions for battery applications [186–188], photocatalysis for the degradation of organic compounds [189,190], or as absorbent for Cd^{2+} in water [191].

$[MnO_2]^{0.45-}$ nanosheets have a 2D hexagonal lattice of parameter a = 2.88 Å (Figure 1.15b). Shibata *et al.* have used these nanosheets as a seed layer for the oriented growth of (001)ZnO thin film on glass [73]. The (001)ZnO 2D-hexagonal lattice constants are $a = b$ = 3.25 Å, which are close to those of $[MnO_2]^{0.45-}$ nanosheets.

3.4.3. $[Ru_{0.95}O_2]^{0.2-}$ nanosheets from the (K, Na)RuO_2 phase

$Na_{0.2}RuO_2 \cdot 0.45H_2O$ is a layered ruthenate crystallizing in a trigonal space group $R\bar{3}m$ with a = 2.930 Å and c = 21.913 Å [192]. This phase is obtained by the hydration of $NaRuO_2$ in water for several days. The structure is composed of layers of edge-shared RuO_6 octahedra, separated by Na^+/H_2O layers (Figure 1.16a). The protonation of this material leads to the compound $H_{0.2}RuO_2 \cdot 0.5H_2O$, which can be exfoliated using TBAOH in $[Ru_{0.95}O_2]^{0.2-}$ nanosheets [193]. Two different ruthenate nanosheets are described in the literature: $[Ru_{0.95}^{3.8+}O_2]^{0.2-}$ and $[Ru^{4+}O_{2.1}]^{0.2-}$ [193,194], the latter is obtained from $K_{0.2}RuO_{2.1} \cdot xH_2O$. However, the difference between these two nanosheets is not very clear. In fact, even if Fukuda *et al.* published two different structures for the two compounds, *i.e.* the 2D-hexagonal $[Ru_{0.95}^{3.8+}O_2]^{0.2-}$ (a = 2.930 Å) and the 2D-oblique cell $[Ru^{4+}O_{2.1}]^{0.2-}$ (a = 5.611 Å, b = 5.122 Å, γ = 109.4°) , the same group recently published different papers using the potassium precursor to obtain $[Ru_{0.95}^{3.8+}O_2]^{0.2-}$ nanosheets [58,85].

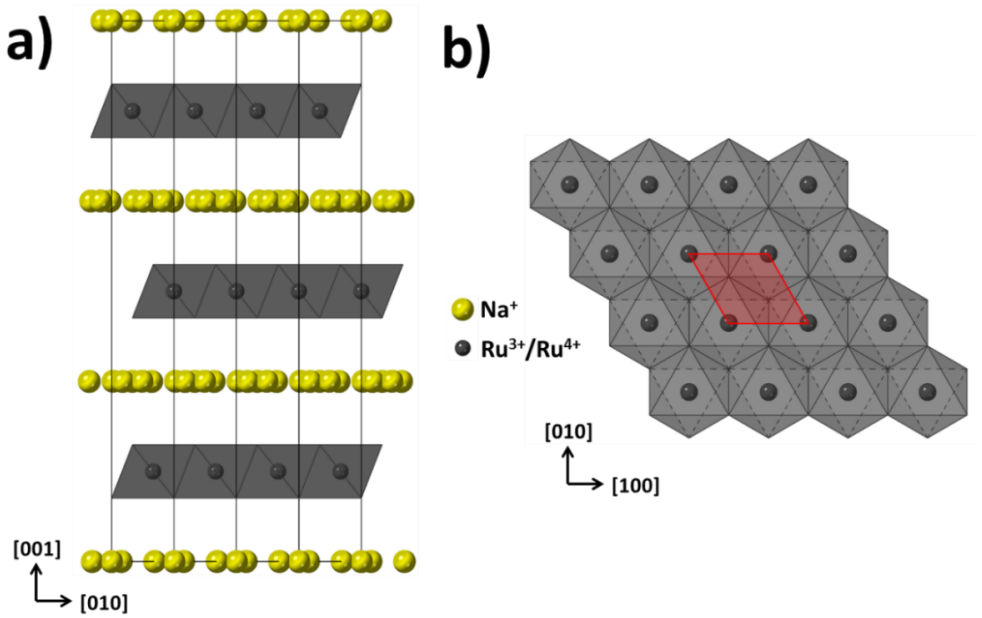

Figure 1.16. (a) $Na_{0.2}RuO_2 \cdot 0.45H_2O$ structure along the [100] direction. (b) $[Ru_{0.95}O_2]^{0.2-}$ nanosheet structure along the [001] direction. The 2D hexagonal lattice with a = 2.930 Å is depicted in red.

Otherwise, these nanosheets exhibit a high capacitance (~700 $F.g^{-1}$) and a high conductivity [193,195]. Thus, the metallic transparent conductive $[Ru_{0.95}O_2]^{0.2-}$ nanosheets can be used to make nanocapacitors by intercalating them with dielectric nanosheets as $[Ca_2Nb_3O_{10}]^-$ or $[Ca_2NaNb_4O_{13}]^-$ nanosheets [58,85]. Very high capacitances (27.5 and 40-52 $\mu F.cm^{-2}$, respectively) and low leakage currents have been obtained for

these devices. Furthermore, $[Ru_{0.95}O_2]^{0.2-}$ nanosheets exhibit the highest catalytic activity known for the electrocatalytic oxygen evolution reaction from water oxidation in acid medium [196].

These nanosheets have never been deposited for the oriented growth of complex oxides thin films. However, the 2D lattice of the ruthenium nanosheets is a hexagonal lattice with a = 2.93 Å (Figure 1.16b), which could theoretically be used as a template for (111) perovskites growth.

3.4.4. $[MoO_2]^{x-}$ nanosheets from the $Na_{0.9}MoO_2$ phase

$Na_{0.9}MoO_2$ is a layered compound crystallizing in a monoclinic lattice ($C2/m$ with a = 12.454 Å, b = 2.889 Å, c = 4.935 Å, and β = 103.98°) [197]. The structure consists of layers of edge-shared MoO_6 octahedra separated by Na^+ layers (Figure 1.17a). The nanosheets $[MoO_2]^{\delta-}$ are obtained by the protonation and the exfoliation of the parent phase. These nanosheets have not been widely described in the literature, but it has been shown that they can be used as electrode material for Li-storage capacity [198,199].

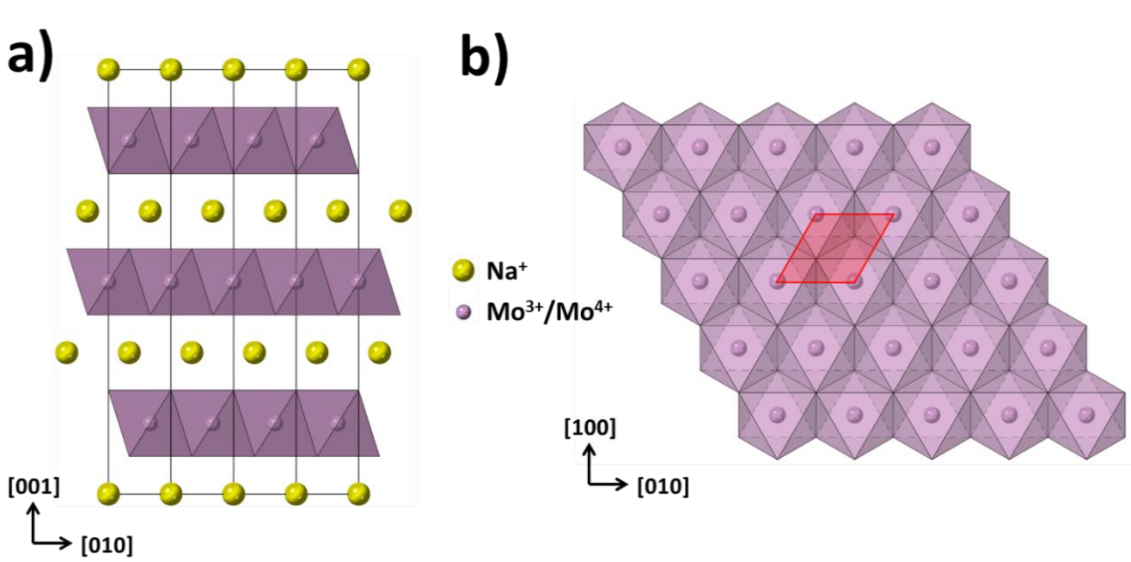

Figure 1.17. (a) Na_xMoO_2 structure along the [100] direction. (b) $[MoO_2]^{x-}$ nanosheet structure along the [001] direction. The 2D hexagonal lattice with a = 2.90 Å is depicted in red.

$[MoO_2]^{\delta-}$ nanosheets have a 2D rectangular lattice with b = 2.90 Å and c = 5.02 Å, which can be described a 2D ortho-hexagonal lattice of parameter $a = b$ = 2.90 Å (Figure 1.17b). Shibata *et al.* have used these nanosheets as a seed layer for the oriented growth of (111)$SrTiO_3$ thin film on glass [51]. The (111)$SrTiO_3$ hexagonal in-plane lattice

distance are equal to 5.52 Å, which are close to those of $[MoO_2]^{\delta-}$ nanosheets when the lattice is doubled ($2a = 2b$ = 5.80 Å), which allows the oriented growth.

3.5. Other oxide nanosheets

3.5.1. $[TaO_3]^-$ nanosheets from the $RbTaO_3$ phase

$RbTaO_3$ is a layered compound isostructural to $CsNbO_3$, crystallizing in a monoclinic lattice ($C2/m$, a = 9.589 Å, b = 8.505 Å, c = 8.135 Å, β = 94.87°) [200]. This structure is composed of two types of TaO_6 distorted octahedra: $Ta^{I}O_6$ which are edge-shared between each other, and $Ta^{II}O_6$ edge-shared and corner-shared with the $Ta^{I}O_6$ octahedra (Figure 1.18).

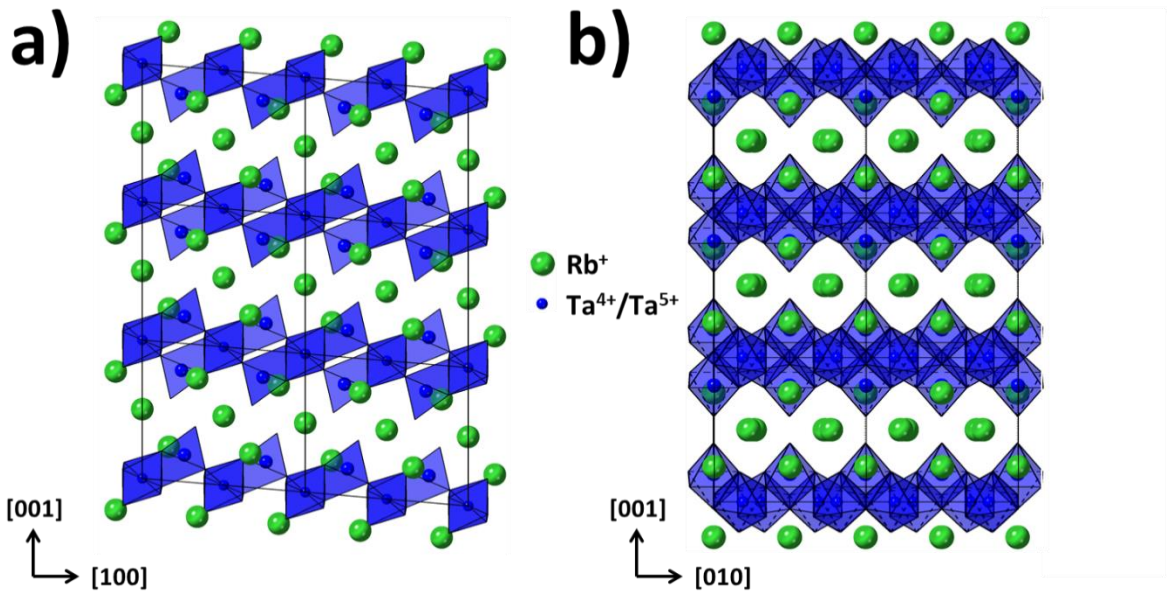

Figure 1.18. (a) $RbTaO_3$ structure along the [010] direction and (b) along the [100] direction.

$RbTaO_3$ has a theoretical band gap of ~3.5 eV [13] and has interesting ferroelectric properties in its perovskite structure (T > 520K) [202]. The Rb^+ ions in the structure can be exchanged by protons to form the $HTaO_3$ phase, which can be exfoliated using TBAOH or TBPOH [25,203]. The latter has the advantage to decrease the exfoliation time from 3 weeks to 36 hours. $[TaO_3]^-$ nanosheets present photocatalytic properties, by decomposing organic compounds under UV radiation [204]. They also have been used as an effective electrode reducer for solid-state lithium batteries [205]. More recently, the

$[TaO_3]^-$ band gap has been measured by scanning tunneling microscopy and was found to be around 5 eV [25], showing the high potential of these exfoliated nanosheets.

3.5.2. $[Nb_3O_8]^-$ nanosheets from the KNb_3O_8 phase

The layered triniobate KNb_3O_8 is orthorhombic (*Amam*, a = 8.903 Å, b = 21.160 Å, c = 3.799 Å) [206], and made of NbO_6 corner and edge shared octahedra (Figure 1.19), forming $[Nb_3O_8]^-$ nanosheets, separated by K^+ ions. KNb_3O_8 presents a band gap of 3.7 eV, which is higher than the one of the $K_4Nb_6O_{17}$ phase. KNb_3O_8 presents luminescence properties [207] and an excellent photocatalytic activity, which can be used for colorants degradation [73,74], ethylene glycol catalysis [210], or the photocatalytic reduction of CO_2 to methane [211].

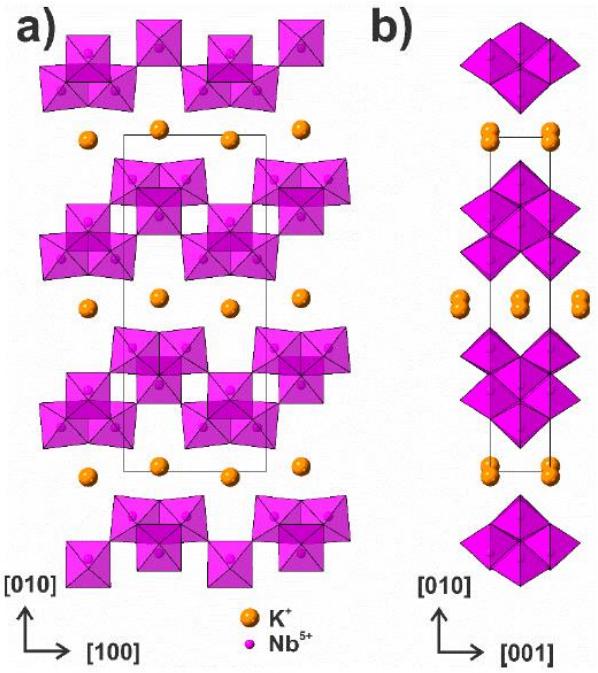

Figure 1.19. (a) KNb_3O_8 structure along the [001] direction and (b) along the [100] direction.

KNb_3O_8 can be protonated to obtain HNb_3O_8 by acid-base reaction. The protonated phase also shows photocatalytic and catalytic properties [211,212]. The exfoliation with TBAOH leads to $[Nb_3O_8]^-$ nanosheets, which present a high photoinduced hydrophilic conversion under UV (50 to 60 times greater than anatase), which make it a good candidate for catalytic coating (self-cleaning glass) [78–81].

4. Nanosheets deposition techniques

For the transfer of the nanosheets on substrates, different techniques can be used, depending on the aimed application. Here is reported a non-exhaustive list of commonly used or promising nanosheets deposition techniques.

4.1. Langmuir-Blodgett technique

The Langmuir-Blodgett technique (LB) is the most commonly used technique for nanosheets deposition. The method consists of forming a monolayer of molecular thickness at the surface of a liquid (Langmuir film) to then deposit it on a substrate. The history of LB films begins in 1774 when Benjamin Franklin described for the first time the formation of an oil layer after accidentally dropped it in a lake. A hundred years later, Agnes Pockles published with Lord Rayleigh in 1891 the bases of water/air interface monolayers characterization [217]. Irving Langmuir, inspired by her work, made the first systematic study on organic monolayers (called Langmuir films nowadays) [218], leading him to the Nobel prize in 1932. The first Langmuir-Blodgett film deposition was made by Katherine Blodgett (I. Langmuir's PhD student) in 1934, depositing several monolayers of stearic acid on various metal substrates [219]. This technique, firstly used to obtain organic thin films, was extended to inorganic nanomaterials, with the development of hybrid materials.

The LB method enables a precise thickness control of the nanosheets layer as well as a homogenous and dense deposition. However, an important inconvenience is that the deposition is time-consuming: an experiment can take between 1 and 2 hours. Furthermore, LB depositions are sensitive to temperature variation, humidity, and vibrations which make them delicate to use with reproducibility. Despite these inconveniences, all the nanosheets presented in this chapter have been deposited by the Langmuir-Blodgett method, except $[K_2Nb_6O_{17}]^{2-}$ and $[Nb_3O_8]^-$ nanosheets [23,25,74,85,116,178], showing that LB is up to now the reference method for monolayer deposition. The operation of the Langmuir-Blodgett used in this work will be detailed in Chapter 2.

4.2. Spin coating deposition

Spin coating is a classic method for thin films deposition. It consists of injecting material in solution onto a spinning substrate in order to obtain a thin film of this material. The thickness and the quality of the film will depend on the viscosity, the concentration of the solution, the speed and acceleration of spinning of the substrate. The deposition is driven by the centrifugal force which pushes the particles (here the nanosheets) on the sides of the substrates, which leads to a thin layer (Figure 1.20) [220].

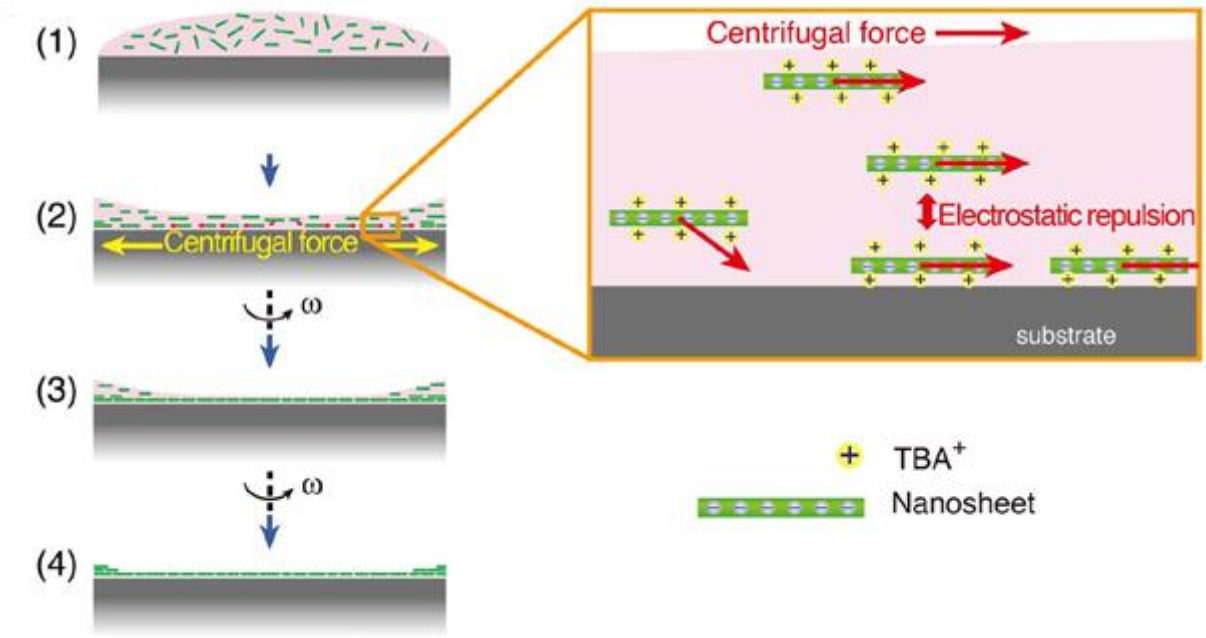

Figure 1.20. Schematic description of the spin coating deposition of nanosheets. (1) The solution is deposited on the substrate. (2), (3), (4) The nanosheets form a monolayer driven by the centrifugal force and the electrostatic repulsion between each other [220].

Spin coating has been used to deposit the following oxide nanosheets on various substrates: $[TaO_3]^-$, $[Ca_2Nb_3O_{10}]^-$, $[Nb_3O_8]^-$, $[Ti_{0.87}O_2]^{0.52-}$, and $[Ti_{0,91}O_2]^{0.36-}$ [205,215,220–222]. However, the obtained films were relatively thick (from 15 to 200 nm) or were presenting low surface coverage. Nevertheless, Kim *et al.* succeeded to deposit graphene oxide (GO) nanosheets in an aqueous solution using spin coating. A dense monolayer was obtained on a 10 x 10 mm SiO_2 substrate [223]. Furthermore, Mastuba *et al.* managed to deposit a dense monolayer of different oxide nanosheets ($[Ca_2Nb_3O_{10}]^-$, $[Ti_{0.87}O_2]^{0.52-}$, GO) in a dimethyl sulfoxide (DMSO) solution on various substrates [220]. The deposition was made on relatively large substrates (30 mm of diameter), with a homogenous nanosheets layer, but only in the center of the substrate.

There is an increase of nanosheets overlapping which accumulates on the sides, as shown in Figure 1.21.

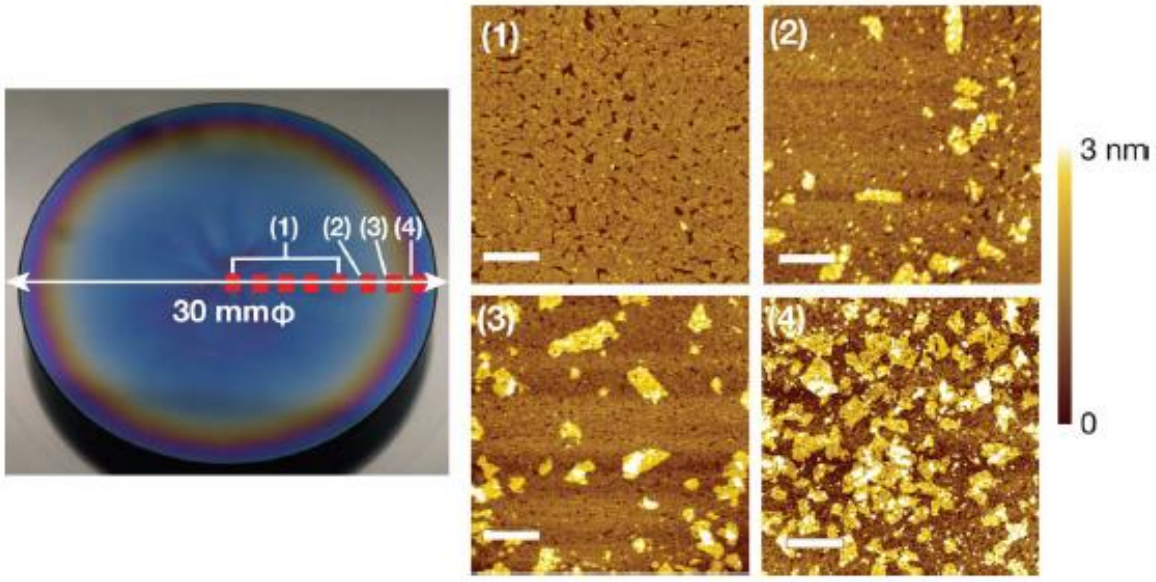

Figure 1.21. On the left, photography of a $[Ti_{0.87}O_2]^{0.52-}$ deposited by spin coating on a 30 mm of diameter Si substrate. (1-4) AFM image of the nanosheet layer. On the first half of the substrate, a dense and homogenous nanosheets film is obtained. (2), (3), (4) Stacked nanosheets are observed on the sides of the substrate [220].

Spin coating deposition is very fast (< 1 mn), but the solutions are quite long to prepare and material-consuming as 95 % of the solution is being wasted for each deposition and therefore cannot be reused [214]. To conclude, the spin coating seems more adapted for a nanosheets thick layer.

4.3. Electrophoretic deposition

The electrophoretic deposition (EPD) technique has been discovered for the first time by the Russian scientist Ruess in 1808, by observing the movement of clay particles in water when an electric field was applied in the solution. In 1933, the first material deposition was performed with this technique with W and ThO_2 particles deposited on a platinum cathode as an emitter for electron tube application [224], and the first theoretical explanations have been made in 1940 [225]. This method consists of two electrode cells dived in a colloidal solution of the material to deposit. An electric current is applied, inducing the movement of particles toward the oppositely charged electrode until they drop off on it, forming a film on the electrode. It is therefore well-adapted for large-scale depositions (Figure 1.22). The particles in solution can be positively charged

and the deposition will then occur on the cathode (cathodic EPD) or can be negatively charged and the deposition will happen on the anode (anodic EPD) [226].

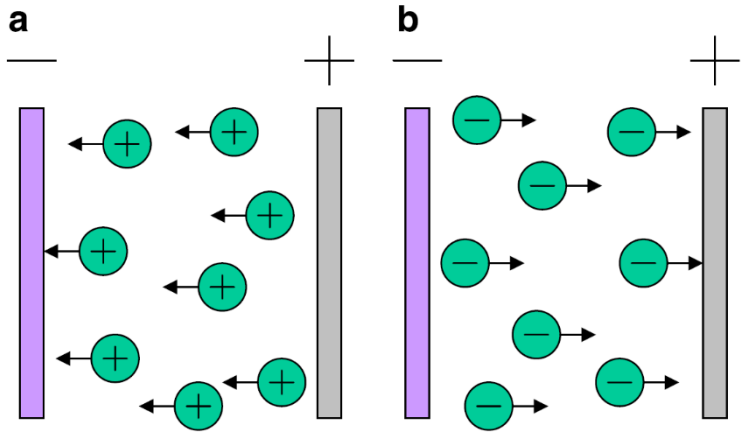

Figure 1.22. Schematic illustration of the electrophoretic deposition process: (a) cathodic EPD and (b) anodic EPD [226].

This technique is different from the electrolytic deposition process (ELD), which is based on a solution of salts (ionic species), while EPD is based on the suspension of particles in a solvent [227]. EPD has been shown to be an efficient technique for oxide nanosheets deposition. Their negative charges make the method convenient for their deposition on conductor substrates. For example, $[Ti_{0.87}O_2]^{0.52-}$ and $[Ti_{0.91}O_2]^{0.36-}$ were deposited on Pt and indium tin oxide (ITO) substrates respectively, by using directly the aqueous colloidal solution [228,229]. The $[Ca_2Nb_3O_{10}]^-$ and $[Sr_2Nb_3O_{10}]^-$ DJ nanosheets also have been deposited by EPD on Pt/Ti/SiO_2/Si substrates using colloidal nanosheets solution in acetone [230,231]. Other oxides nanosheets have been deposited by this method, like GO, $[MnO_2]^{\delta-}$, and $[Sr_2NaNb_4O_{13}]^-$ [232–234].

The advantage of the EPD technique is to provide nanosheets multilayers in a short time, compared to the LB technique which is time-consuming. However, it seems very complicated to get one monolayer of nanosheets by the method. Moreover, the crystalline quality of thin films grown by this method is not very good compared to those deposited by the LB method, due to the impossibility to decompose TBA^+ ions completely with UV and annealing treatments.

4.4. The drop casting method

Drop casting (DC) is the easiest technique for nanomaterials deposition. It consists of dropping a colloidal solution on a substrate. After evaporation of the solvent, a film

made of particles is formed on the substrate in a very short time. The film thickness depends on the volume dropped on the substrate and the particle concentration. It is a rapid technique, but with which it is complicated to get a uniform coating, a well-controlled thickness, and large area coverage. Some parameters can affect the deposition, as the substrate wettability, the solvent used (volatility, surface tension), the variation of concentration during the solvent evaporation, which make DC difficult to apply for dense nanoparticles or large area depositions [235]. However, recent work by Y. Shi *et al.* has shown that it is actually possible to make nanosheets deposition by this technique on large substrates with a dense covering and a high reproductive rate [236]. Using a dilute nanosheets solution in a water/ethanol solvent mixture, the drop deposition is made on a substrate heated at 100-120°C on a hot plate. The liquid is then drained back in 30 seconds and a dense nanosheets monolayer is obtained (Figure 1.23). The deposition is driven by a balance between the Marangoni effect and the capillary flow. The Marangoni effect corresponds to the differences of surface tension induced by two different fluids or one fluid with different temperature gradients.

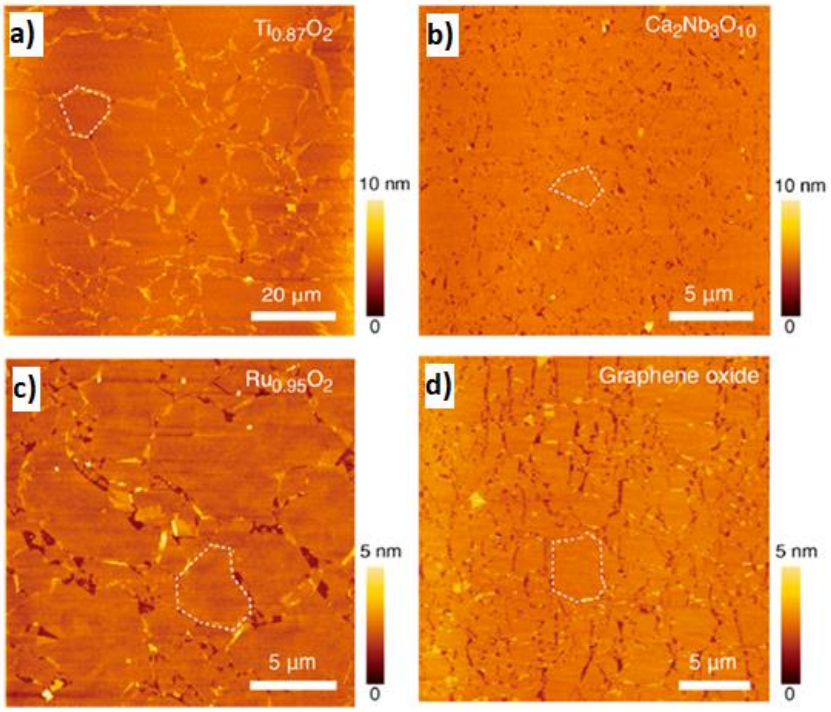

Figure 1.23. Atomic Force Microscopy (AFM) micrographies of different nanosheets deposited by the drop casting technique: (a) $[Ti_{0.87}O_2]^{0.52-}$ nanosheets, (b) $[Ca_2Nb_3O_{10}]^-$ nanosheets, (c) $[Ru_{0.95}O_2]^{0.2-}$ nanosheets, (d) graphene oxide [236].

Usually, colloidal suspensions with an organic solvent are used for drop casting deposition for their high volatility and low surface tension. As seen before, the nanosheets

are obtained by exfoliation in a water solution, which has high surface tension and low Marangoni flow. Ethanol is added to decrease the water surface tension of water and to enhance the Marangoni flow [237] while the substrate is heated to enhance the volatility and increase the Marangoni flow. When the colloidal solution is deposited on the substrate, the capillary flow moves the nanosheets to the edges of the drop, to compensate for the matter losses due to the solvent evaporation (*i.e.* coffee-ring effect) [238]. At the same time, the temperature gap between the substrate/droplet and the droplet/air interface induces a surface tension gradient, which leads to strong Marangoni convection. These phenomena lead to a cycling flow that carries the nanosheets from the inside of the droplet to the surface (Figure 1.24a,e). When the liquid removal begins, the contact angle between the liquid and the substrate decreased and the Marangoni flow/heat convection cycling movement gets confined on the edges part of the droplet (Figure 1.24b,f). As the nanosheets are covered with hydrophobic TBA^+ ions, they get stacked at the air/water interface, accumulating and forming a homogeneous and dense layer (Figure 1.24c,f) that would be rapidly deposited as a function of the liquid draining (Figure 1.24d,h).

DC deposition only needs a tiny amount of solution. Depending on the substrate type and size, it needs between 0.1 and 5 mL of solution at a relatively low concentration (0.007 wt %). Compared to the amount of solution used for LB deposition, it is theoretically possible to make 2000 times more depositions with the DC technique than with the LB technique. Thus, it is an economical deposition technique, with no material waste. DC can also be considered as the fastest technique known to obtain nanosheets layer on substrates (around 30 seconds), compared to CSD (1 minute) or LB (between 1 and 2 hours). Nevertheless, the deposition principle described previously does not apply to the pipet deposition zone, as the pipet draining induces a turbulent flow. It is thus observed that the pipet deposition zone is not covered by the nanosheets layer.

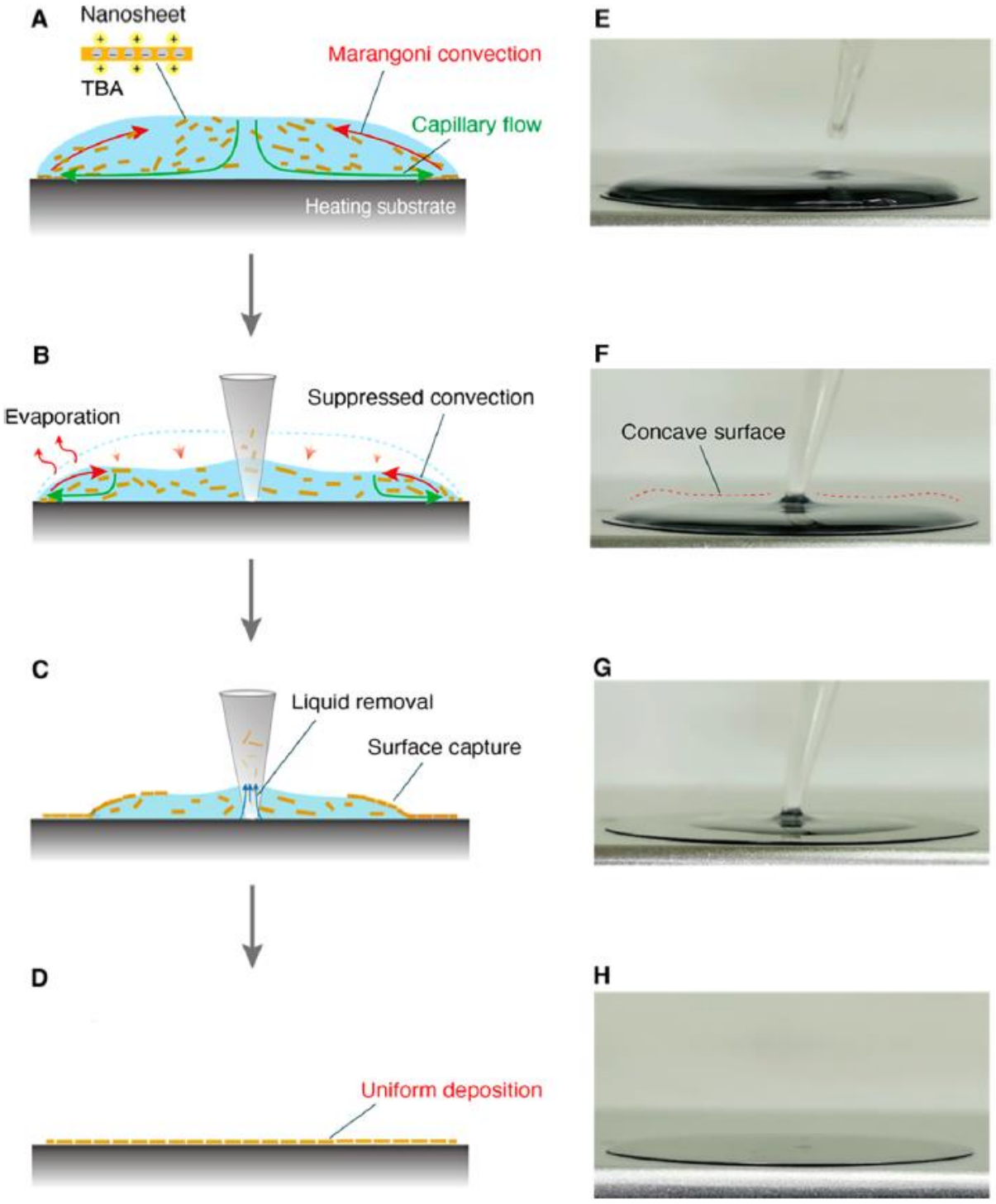

Figure 1.24. (a-d) Schematic description of the drop casting deposition process. (e-h) Experimental process of the nanosheets deposition by the drop casting technique [236].

Conclusions

In this chapter, an overview of the wide field of the oxide nanosheets was exposed. A brief introduction was made on the different types of nanosheets: graphene, silicates, oxides, and chalcogenides. The chapter was then focusing on the 2D oxides and their synthesis. Oxide nanosheets are usually obtained by liquid exfoliation of the layered materials previously protonated with an acid solution. Several nanosheets have been presented.

The properties of bulk materials and nanosheets have been described. Nanosheets are known to exhibit interesting properties for photocatalysis, photovoltaics, batteries, or supercapacitors. They can also be used as a seed layer for the oriented growth of oxide thin films, offering the possibility to obtain oriented films on large surfaces and any substrates.

Different techniques have been exposed for nanosheets deposition. Each of them is well-adapted depending on the aimed application. The LB deposition is perfect for dense monolayer but not efficient for multilayer deposition due to the time deposition needed, while the spin coating method allows to obtain a dense nanosheets layer in a short time but with less control on the quality of the layer. Electrophoretic deposition is a fast but imprecise deposition that leads to a thick film made of randomly stacked nanosheets. The DC deposition is fast, material saving, efficient on large substrates, with the same film quality as LB films. All those arguments show that DC is probably the most promising deposition method for industrial applications whereas LB is a method leading to a high control of monolayers of a large variety of nanosheets.

References

[1] K.S. Novoselov, Electric Field Effect in Atomically Thin Carbon Films, Science. 306 (2004) 666–669. https://doi.org/10.1126/science.1102896.

[2] A.K. Geim, K.S. Novoselov, The rise of graphene, Nat. Mater. 6 (2007) 183–191. https://doi.org/10.1038/nmat1849.

[3] M. Xu, T. Liang, M. Shi, H. Chen, Graphene-Like Two-Dimensional Materials, Chem. Rev. 113 (2013) 3766–3798. https://doi.org/10.1021/cr300263a.

[4] A.K. Geim, I.V. Grigorieva, Van der Waals heterostructures, Nature. 499 (2013) 419–425. https://doi.org/10.1038/nature12385.

[5] K.F. Mak, C. Lee, J. Hone, J. Shan, T.F. Heinz, Atomically Thin MoS 2 : A New Direct-Gap Semiconductor, Phys. Rev. Lett. 105 (2010) 136805. https://doi.org/10.1103/PhysRevLett.105.136805.

[6] B. Radisavljevic, A. Radenovic, J. Brivio, V. Giacometti, A. Kis, Single-layer MoS_2 transistors, Nat. Nanotechnol. 6 (2011) 147–150. https://doi.org/10.1038/nnano.2010.279.

[7] M. Chhowalla, H.S. Shin, G. Eda, L.-J. Li, K.P. Loh, H. Zhang, The chemistry of two-dimensional layered transition metal dichalcogenide nanosheets, Nat. Chem. 5 (2013) 263–275. https://doi.org/10.1038/nchem.1589.

[8] W. Lei, D. Portehault, D. Liu, S. Qin, Y. Chen, Porous boron nitride nanosheets for effective water cleaning, Nat. Commun. 4 (2013) 1777. https://doi.org/10.1038/ncomms2818.

[9] J. Choi, Y.-H. Kim, K.J. Chang, D. Tománek, Itinerant ferromagnetism in heterostructured C/BN nanotubes, Phys. Rev. B. 67 (2003) 125421. https://doi.org/10.1103/PhysRevB.67.125421.

[10] D. Golberg, Y. Bando, Y. Huang, T. Terao, M. Mitome, C. Tang, C. Zhi, Boron Nitride Nanotubes and Nanosheets, ACS Nano. 4 (2010) 2979–2993. https://doi.org/10.1021/nn1006495.

[11] A. da Silva Maia, F. Cheviré, V. Demange, V. Bouquet, M. Pasturel, S. Députier, R. Lebullenger, M. Guilloux-Viry, F. Tessier, Preparation of niobium based oxynitride nanosheets by exfoliation of Ruddlesden-Popper phase precursor, Solid State Sci. 54 (2016) 17–21. https://doi.org/10.1016/j.solidstatesciences.2015.11.013.

[12] M. Naguib, V.N. Mochalin, M.W. Barsoum, Y. Gogotsi, 25th Anniversary Article: MXenes: A New Family of Two-Dimensional Materials, Adv. Mater. 26 (2014) 992–1005. https://doi.org/10.1002/adma.201304138.

[13] B. Anasori, M.R. Lukatskaya, Y. Gogotsi, 2D metal carbides and nitrides (MXenes) for energy storage, Nat. Rev. Mater. 2 (2017) 16098. https://doi.org/10.1038/natrevmats.2016.98.

[14] J. Yu, Q. Wang, D. O'Hare, L. Sun, Preparation of two dimensional layered double hydroxide nanosheets and their applications, Chem. Soc. Rev. 46 (2017) 5950–5974. https://doi.org/10.1039/C7CS00318H.

[15] Y. Wang, W. Yang, J. Yang, A Co–Al Layered Double Hydroxides Nanosheets Thin-Film Electrode, Electrochem. Solid-State Lett. 10 (2007) A233. https://doi.org/10.1149/1.2768166.

[16] X.D. Li, W.S. Yang, F. Li, D.G. Evans, X. Duan, Stoichiometric synthesis of pure $NiFe_2O_4$ spinel from layered double hydroxide precursors for use as the anode material in lithium-ion batteries, J. Phys. Chem. Solids. 67 (2006) 1286–1290. https://doi.org/10.1016/j.jpcs.2006.01.096.

[17] J.H. Lee, J. Chang, J.-H. Cha, D.-Y. Jung, S.S. Kim, J.M. Kim, Anthraquinone Sulfonate Modified, Layered Double Hydroxide Nanosheets for Dye-Sensitized Solar Cells, Chem. - Eur. J. 16 (2010) 8296–8299. https://doi.org/10.1002/chem.201000703.

[18] R. Ma, T. Sasaki, Nanosheets of Oxides and Hydroxides: Ultimate 2D Charge-Bearing Functional Crystallites, Adv. Mater. 22 (2010) 5082–5104. https://doi.org/10.1002/adma.201001722.

[19] Z. Sun, T. Liao, L. Kou, Strategies for designing metal oxide nanostructures, Sci. China Mater. 60 (2017) 1–24. https://doi.org/10.1007/s40843-016-5117-0.

[20] N. Mahmood, I.A. De Castro, K. Pramoda, K. Khoshmanesh, S.K. Bhargava, K. Kalantar-Zadeh, Atomically thin two-dimensional metal oxide nanosheets and their heterostructures for energy storage, Energy Storage Mater. 16 (2019) 455–480. https://doi.org/10.1016/j.ensm.2018.10.013.

[21] Z. Sun, T. Liao, Y. Dou, S.M. Hwang, M.-S. Park, L. Jiang, J.H. Kim, S.X. Dou, Generalized self-assembly of scalable two-dimensional transition metal oxide nanosheets, Nat. Commun. 5 (2014) 3813. https://doi.org/10.1038/ncomms4813.

[22] H. Yuan, D. Dubbink, R. Besselink, J.E. ten Elshof, The Rapid Exfoliation and Subsequent Restacking of Layered Titanates Driven by an Acid-Base Reaction, Angew. Chem. Int. Ed. 54 (2015) 9239–9243. https://doi.org/10.1002/anie.201502539.

[23] H. Yuan, R. Lubbers, R. Besselink, M. Nijland, J.E. ten Elshof, Improved Langmuir–Blodgett Titanate Films via in Situ Exfoliation Study and Optimization of Deposition Parameters, ACS Appl. Mater. Interfaces. 6 (2014) 8567–8574. https://doi.org/10.1021/am501380d.

[24] F. Geng, R. Ma, Y. Yamauchi, T. Sasaki, Tetrabutylphosphonium ions as a new swelling/delamination agent for layered compounds, Chem. Commun. 50 (2014) 9977. https://doi.org/10.1039/C4CC03736G.

[25] M.A. Timmerman, R. Xia, Y. Wang, K. Sotthewes, M. Huijben, J.E. ten Elshof, Long-range ordering of two-dimensional wide bandgap tantalum oxide nanosheets in printed films, J. Mater. Chem. C. (2021) 10.1039.D1TC00801C. https://doi.org/10.1039/D1TC00801C.

[26] G. Du, Q. Chen, Y. Yu, S. Zhang, W. Zhou, L.-M. Peng, Synthesis, modification and characterization of $K_4Nb_6O_{17}$-type nanotubes, J. Mater. Chem. 14 (2004) 1437. https://doi.org/10.1039/b317095k.

[27] M. Dion, M. Ganne, M. Tournoux, Nouvelles familles de phases $M^{I}M^{II}_2Nb_3O_{10}$ a feuillets "perovskites," Mater. Res. Bull. 16 (1981) 1429–1435. https://doi.org/10.1016/0025-5408(81)90063-5.

[28] T. Tokumitsu, K. Toda, T. Aoyagi, D. Sakuraba, K. Uematsu, M. Sato, Powder Neutron Diffraction Study of Layered Perovskite, $KCa_2Nb_3O_{10}$, J. Ceram. Soc. Jpn. 114 (2006) 795–797. https://doi.org/10.2109/jcersj.114.795.

[29] K.S. Virdi, Y. Kauffmann, C. Ziegler, P. Ganter, B.V. Lotsch, W.D. Kaplan, P. Blaha, C. Scheu, Electronic structure of $KCa_2Nb_3O_{10}$ as envisaged by density functional theory and valence electron energy loss spectroscopy, Phys. Rev. B. 87 (2013) 115108. https://doi.org/10.1103/PhysRevB.87.115108.

[30] N. Kulischow, C. Ladasiu, R. Marschall, Layered Dion-Jacobson type niobium oxides for photocatalytic hydrogen production prepared via molten salt synthesis, Catal. Today. 287 (2017) 65–69. https://doi.org/10.1016/j.cattod.2016.10.009.

[31] M.A. Bizeto, V.R.L. Constantino, H.F. Brito, Luminescence properties of the layered niobate $KCa_2Nb_3O_{10}$ doped with Eu^{3+} and La^{3+} ions, J. Alloys Compd. 311 (2000) 159–168. https://doi.org/10.1016/S0925-8388(00)01086-0.

[32] M. Sakthivel, W. Weppner, Application of layered perovskite type proton conducting $KCa_2Nb_3O_{10}$ in H_2 sensors: Pt particle size and temperature dependence, Sens. Actuators B Chem. 125 (2007) 435–440. https://doi.org/10.1016/j.snb.2007.02.054.

[33] A.J. Jacobson, J.T. Lewandowski, J.W. Johnson, Ion exchange of the layered perovskite $KCa_2Nb_3O_{10}$ by protons, J. Common Met. 116 (1986) 137–146. https://doi.org/10.1016/0022-5088(86)90224-9.

[34] T. Nakato, K. Ito, K. Kuroda, C. Kato, Photochemical behavior of perovskite-related layered niobates $HA_2Nb_3O_{10}$ (A = Ca, Sr) intercalated with methylviologen, Microporous Mater. 1 (1993) 283–286. https://doi.org/10.1016/0927-6513(93)80071-2.

[35] Y. Yamashita, K. Hyuga, V. Petrykin, M. Kakihana, M. Yoshimura, K. Domen, H. Kato, A. Kudo, Photocatalytic Properties of $HCa_2Nb_3O_{10}$ Prepared by Polymerizable Complex Method, J. Ceram. Soc. Jpn. 115 (2007) 511–513. https://doi.org/10.2109/jcersj2.115.511.

[36] K. Maeda, T.E. Mallouk, Comparison of two- and three-layer restacked Dion–Jacobson phase niobate nanosheets as catalysts for photochemical hydrogen evolution, J. Mater. Chem. 19 (2009) 4813. https://doi.org/10.1039/b903692j.

[37] R. Chitrakar, S. Tezuka, A. Sonoda, H. Kakita, K. Sakane, K. Ooi, T. Hirotsu, $HCa_2Nb_3O_{10}\cdot 1.5H_2O$ as an Ion Exchanger for NH_4^+ Ion Removal, Ind. Eng. Chem. Res. 47 (2008) 176–179. https://doi.org/10.1021/ie0704389.

[38] R. Chitrakar, Y. Makita, A. Sonoda, Cesium Ion Decontamination by Layered Perovskite $HCa_2Nb_3O_{10}\cdot 1.5H_2O$, Bull. Chem. Soc. Jpn. 86 (2013) 1419–1425. https://doi.org/10.1246/bcsj.20130201.

[39] Y. Ebina, Study on exfoliation of layered perovskite-type niobates, Solid State Ion. 151 (2002) 177–182. https://doi.org/10.1016/S0167-2738(02)00707-5.

[40] K.S. Virdi, Y. Kauffmann, C. Ziegler, P. Ganter, P. Blaha, B.V. Lotsch, W.D. Kaplan, C. Scheu, Band Gap Extraction from Individual Two-Dimensional Perovskite Nanosheets Using Valence Electron Energy Loss Spectroscopy, J. Phys. Chem. C. 120 (2016) 11170–11179. https://doi.org/10.1021/acs.jpcc.6b00142.

[41] Y. Ebina, N. Sakai, T. Sasaki, Photocatalyst of Lamellar Aggregates of RuO_x-Loaded Perovskite Nanosheets for Overall Water Splitting, J. Phys. Chem. B. 109 (2005) 17212–17216. https://doi.org/10.1021/jp051823j.

[42] K. Izawa, T. Yamada, U. Unal, S. Ida, O. Altuntasoglu, M. Koinuma, Y. Matsumoto, Photoelectrochemical Oxidation of Methanol on Oxide Nanosheets, J. Phys. Chem. B. 110 (2006) 4645–4650. https://doi.org/10.1021/jp056210l.

[43] O.C. Compton, F.E. Osterloh, Niobate Nanosheets as Catalysts for Photochemical Water Splitting into Hydrogen and Hydrogen Peroxide, J. Phys. Chem. C. 113 (2009) 479–485. https://doi.org/10.1021/jp807839b.
[44] H. Zhou, E.M. Sabio, T.K. Townsend, T. Fan, D. Zhang, F.E. Osterloh, Assembly of Core–Shell Structures for Photocatalytic Hydrogen Evolution from Aqueous Methanol, Chem. Mater. 22 (2010) 3362–3368. https://doi.org/10.1021/cm903839t.
[45] E.M. Sabio, M. Chi, N.D. Browning, F.E. Osterloh, Charge Separation in a Niobate Nanosheet Photocatalyst Studied with Photochemical Labeling, Langmuir. 26 (2010) 7254–7261. https://doi.org/10.1021/la904377f.
[46] E.M. Sabio, R.L. Chamousis, N.D. Browning, F.E. Osterloh, Photocatalytic Water Splitting with Suspended Calcium Niobium Oxides: Why Nanoscale is Better than Bulk – A Kinetic Analysis, J. Phys. Chem. C. 116 (2012) 3161–3170. https://doi.org/10.1021/jp209006n.
[47] S. Igarashi, S. Sato, T. Takashima, M. Ogawa, Preparation of Finite Particles of Layered Niobate ($KCa_2Nb_3O_{10}$) for Improved Materials Performance, Ind. Eng. Chem. Res. 52 (2013) 3329–3333. https://doi.org/10.1021/ie303243h.
[48] Y. Zhou, T. Wen, Y. Guo, B. Yang, Y. Wang, Controllable doping of nitrogen and tetravalent niobium affords yellow and black calcium niobate nanosheets for enhanced photocatalytic hydrogen evolution, RSC Adv. 6 (2016) 64930–64936. https://doi.org/10.1039/C6RA11407E.
[49] P. Ganter, B.V. Lotsch, Photocatalytic Nanosheet Lithography: Photolithography based on Organically Modified Photoactive 2D Nanosheets, Angew. Chem. Int. Ed. 56 (2017) 8389–8392. https://doi.org/10.1002/anie.201703149.
[50] Y. Zhang, S. Li, Z. Li, H. Liu, X. Liu, J. Chen, X. Fang, High-Performance Two-Dimensional Perovskite $Ca_2Nb_3O_{10}$ UV Photodetectors, Nano Lett. 21 (2021) 382–388. https://doi.org/10.1021/acs.nanolett.0c03759.
[51] Y.-H. Kim, H.-J. Kim, M. Osada, B.-W. Li, Y. Ebina, T. Sasaki, 2D Perovskite Nanosheets with Thermally-Stable High-κ Response: A New Platform for High-Temperature Capacitors, ACS Appl. Mater. Interfaces. 6 (2014) 19510–19514. https://doi.org/10.1021/am506629g.
[52] B.-W. Li, M. Osada, T.C. Ozawa, Y. Ebina, K. Akatsuka, R. Ma, H. Funakubo, T. Sasaki, Engineered Interfaces of Artificial Perovskite Oxide Superlattices *via* Nanosheet Deposition Process, ACS Nano. 4 (2010) 6673–6680. https://doi.org/10.1021/nn102144s.
[53] B.-W. Li, M. Osada, K. Akatsuka, Y. Ebina, T.C. Ozawa, T. Sasaki, Solution-Based Fabrication of Perovskite Multilayers and Superlattices Using Nanosheet Process, Jpn. J. Appl. Phys. 50 (2011) 09NA10. https://doi.org/10.1143/JJAP.50.09NA10.
[54] B.-W. Li, M. Osada, Y. Ebina, K. Akatsuka, K. Fukuda, T. Sasaki, High Thermal Robustness of Molecularly Thin Perovskite Nanosheets and Implications for Superior Dielectric Properties, ACS Nano. 8 (2014) 5449–5461. https://doi.org/10.1021/nn502014c.
[55] B.-W. Li, M. Osada, Y.-H. Kim, Y. Ebina, K. Akatsuka, T. Sasaki, Atomic Layer Engineering of High-κ Ferroelectricity in 2D Perovskites, J. Am. Chem. Soc. 139 (2017) 10868–10874. https://doi.org/10.1021/jacs.7b05665.
[56] M. Osada, K. Akatsuka, Y. Ebina, H. Funakubo, K. Ono, K. Takada, T. Sasaki, Robust High-κ Response in Molecularly Thin Perovskite Nanosheets, ACS Nano. 4 (2010) 5225–5232. https://doi.org/10.1021/nn101453v.
[57] M. Osada, T. Sasaki, Two-Dimensional Dielectric Nanosheets: Novel Nanoelectronics From Nanocrystal Building Blocks, Adv. Mater. 24 (2012) 210–228. https://doi.org/10.1002/adma.201103241.
[58] C. Wang, M. Osada, Y. Ebina, B.-W. Li, K. Akatsuka, K. Fukuda, W. Sugimoto, R. Ma, T. Sasaki, All-Nanosheet Ultrathin Capacitors Assembled Layer-by-Layer *via* Solution-Based Processes, ACS Nano. 8 (2014) 2658–2666. https://doi.org/10.1021/nn406367p.
[59] M.S. Khan, H.-J. Kim, T. Taniguchi, Y. Ebina, T. Sasaki, M. Osada, Layer-by-layer engineering of two-dimensional perovskite nanosheets for tailored microwave dielectrics, Appl. Phys. Express. 10 (2017) 091501. https://doi.org/10.7567/APEX.10.091501.
[60] H. Uchida, T. Oi, K. Noguchi, S. Moki, J.W. Kim, H. Shima, K. Nishida, T. Kiguchi, A. Akama, T.J. Konno, H. Funakubo, Orientation control of barium titanate films using metal oxide nanosheet layer, Jpn. J. Appl. Phys. 55 (2016) 10TA15. https://doi.org/10.7567/JJAP.55.10TA15.
[61] K. Kikuta, K. Noda, S. Okumura, T. Yamaguchi, S. Hirano, Orientation control of perovskite thin films on glass substrates by the application of a seed layer prepared from oxide nanosheets, J. Sol-Gel Sci. Technol. 42 (2007) 381–387. https://doi.org/10.1007/s10971-006-0200-z.

[62] S.H. Kweon, J.-H. Kim, M. Im, W.H. Lee, S. Nahm, Physical Properties of $(Na_{1-x}K_x)NbO_3$ Thin Film Grown at Low Temperature Using Two-Dimensional $Ca_2Nb_3O_{10}$ Nanosheet Seed Layer, ACS Appl. Mater. Interfaces. 10 (2018) 25536–25546. https://doi.org/10.1021/acsami.8b09482.

[63] M. Bayraktar, A. Chopra, F. Bijkerk, G. Rijnders, Nanosheet controlled epitaxial growth of $PbZr_{0.52}Ti_{0.48}O_3$ thin films on glass substrates, Appl. Phys. Lett. 105 (2014) 132904. https://doi.org/10.1063/1.4896991.

[64] A. Chopra, M. Bayraktar, F. Bijkerk, G. Rijnders, Controlled growth of $PbZr_{0.52}Ti_{0.48}O_3$ using nanosheet coated Si (001), Thin Solid Films. 589 (2015) 13–16. https://doi.org/10.1016/j.tsf.2015.04.039.

[65] Y. Minemura, D. Ichinose, K. Nagasaka, J.W. Kim, H. Shima, K. Nishida, T. Kiguchi, T.J. Konno, N. Oshima, H. Funakubo, H. Uchida, Polar-axis-oriented crystal growth of tetragonal PZT films on stainless steel substrate using pseudo-perovskite nanosheet buffer layer, AIP Adv. 5 (2015) 077139. https://doi.org/10.1063/1.4927208.

[66] M.D. Nguyen, H. Yuan, E.P. Houwman, M. Dekkers, G. Koster, J.E. ten Elshof, G. Rijnders, Highly Oriented Growth of Piezoelectric Thin Films on Silicon Using Two-Dimensional Nanosheets as Growth Template Layer, ACS Appl. Mater. Interfaces. 8 (2016) 31120–31127. https://doi.org/10.1021/acsami.6b09470.

[67] A. Chopra, M. Bayraktar, M. Nijland, J.E. ten Elshof, F. Bijkerk, G. Rijnders, Polarization recovery in lead zirconate titanate thin films deposited on nanosheets-buffered Si (001), AIP Adv. 6 (2016) 125209. https://doi.org/10.1063/1.4971373.

[68] A. Chopra, M. Bayraktar, M. Nijland, J.E. ten Elshof, F. Bijkerk, G. Rijnders, Tuning of large piezoelectric response in nanosheet-buffered lead zirconate titanate films on glass substrates, Sci. Rep. 7 (2017) 251. https://doi.org/10.1038/s41598-017-00333-2.

[69] M.D. Nguyen, E.P. Houwman, H. Yuan, B.J. Wylie-van Eerd, M. Dekkers, G. Koster, J.E. ten Elshof, G. Rijnders, Controlling Piezoelectric Responses in $Pb(Zr_{0.52}Ti_{0.48})O_3$ Films through Deposition Conditions and Nanosheet Buffer Layers on Glass, ACS Appl. Mater. Interfaces. 9 (2017) 35947–35957. https://doi.org/10.1021/acsami.7b07428.

[70] K. Nagasaka, N. Oshima, J.W. Kim, H. Shima, A. Akama, T. Kiguchi, K. Nishida, T.J. Konno, H. Funakubo, H. Uchida, Fabrication of $(100)_c$-oriented Mn-doped bismuth ferrite films on silicon and stainless steel substrates using calcium niobate nanosheets, J. Ceram. Soc. Jpn. 123 (2015) 322–328. https://doi.org/10.2109/jcersj2.123.322.

[71] M. Nijland, S. Kumar, R. Lubbers, D.H.A. Blank, G. Rijnders, G. Koster, J.E. ten Elshof, Local Control over Nucleation of Epitaxial Thin Films by Seed Layers of Inorganic Nanosheets, ACS Appl. Mater. Interfaces. 6 (2014) 2777–2785. https://doi.org/10.1021/am4052624.

[72] C. Jung, T. Ohnishi, M. Osada, K. Takada, T. Sasaki, Oriented Film Growth of $Ba_{1-x}Sr_xTiO_3$ Dielectrics on Glass Substrates Using 2D Nanosheet Seed Layer, ACS Appl. Mater. Interfaces. 5 (2013) 4592–4596. https://doi.org/10.1021/am400849z.

[73] T. Shibata, K. Fukuda, Y. Ebina, T. Kogure, T. Sasaki, One-Nanometer-Thick Seed Layer of Unilamellar Nanosheets Promotes Oriented Growth of Oxide Crystal Films, Adv. Mater. 20 (2008) 231–235. https://doi.org/10.1002/adma.200701381.

[74] T. Shibata, H. Takano, Y. Ebina, D.S. Kim, T.C. Ozawa, K. Akatsuka, T. Ohnishi, K. Takada, T. Kogure, T. Sasaki, Versatile van der Waals epitaxy-like growth of crystal films using two-dimensional nanosheets as a seed layer: orientation tuning of SrTiO3 films along three important axes on glass substrates, J Mater Chem C. 2 (2014) 441–449. https://doi.org/10.1039/C3TC31787K.

[75] Y. Kondoh, S. Ogawa, J. Kimura, T. Kiguchi, T.J. Konno, H. Funakubo, H. Uchida, Dielectric property of (001) one-axis oriented $CaBi_4Ti_4O_{15}$-based thin films and their temperature dependence, J. Ceram. Soc. Jpn. 122 (2014) 477–482. https://doi.org/10.2109/jcersj2.122.477.

[76] H. Tetsuka, H. Takashima, K. Ikegami, H. Nanjo, T. Ebina, F. Mizukami, Nanosheet Seed-Layer Assists Oriented Growth of Highly Luminescent Perovskite Films, Chem. Mater. 21 (2009) 21–26. https://doi.org/10.1021/cm8027912.

[77] H. Tetsuka, H. Takashima, K. Ikegami, H. Nanjo, T. Ebina, F. Mizukami, Oriented growth of luminescent strontium stannate films using a unilamellar nanosheet seed-layer, Thin Solid Films. 522 (2012) 100–103. https://doi.org/10.1016/j.tsf.2012.09.004.

[78] A.J. Jacobson, J.W. Johnson, J.T. Lewandowski, Interlayer chemistry between thick transition-metal oxide layers: synthesis and intercalation reactions of $K[Ca_2Na_{n-3}Nb_nO_{3n+1}]$ $(3 \le n \le 7)$, Inorg. Chem. 24 (1985) 3727–3729. https://doi.org/10.1021/ic00217a006.

[79] M.M.J. Treacy, S.B. Rice, A.J. Jacobson, J.T. Lewandowski, Electron microscopy study of delamination in dispersions of the perovskite-related layered phases $K[Ca_2Na_{n-3}Nb_nO_{3n-1}]$: evidence for single-layer formation, Chem. Mater. 2 (1990) 279–286. https://doi.org/10.1021/cm00009a018.

[80] Y. Ebina, K. Akatsuka, K. Fukuda, T. Sasaki, Synthesis and In Situ X-ray Diffraction Characterization of Two-Dimensional Perovskite-Type Oxide Colloids with a Controlled Molecular Thickness, Chem. Mater. 24 (2012) 4201–4208. https://doi.org/10.1021/cm302480h.

[81] M.R. Aziza, C.-W. Chang, A. Mohapatra, C.-W. Chu, C.-C. Kaun, Y.-H. Su, Dion–Jacobson Phase Perovskite $Ca_2Na_{n-3}Nb_nO_{3n+1}$ (n = 4–6) Nanosheets as High-κ Photovoltaic Electrode Materials in a Solar Water-Splitting Cell, ACS Appl. Nano Mater. 3 (2020) 6367–6375. https://doi.org/10.1021/acsanm.0c00747.

[82] Y. Zhou, T. Wen, X. Zhang, B. Chang, W. Kong, Y. Guo, B. Yang, Y. Wang, A Multiple Structure-Design Strategy towards Ultrathin Niobate Perovskite Nanosheets with Thickness-Dependent Photocatalytic Hydrogen-Evolution Performance, Chem. - Asian J. 12 (2017) 2727–2733. https://doi.org/10.1002/asia.201701001.

[83] M.S. Khan, Z. Diao, M. Osada, S. Shen, Nitrogen doped ultrathin calcium/sodium niobate perovskite nanosheets for photocatalytic water oxidation, Sol. Energy Mater. Sol. Cells. 205 (2020) 110283. https://doi.org/10.1016/j.solmat.2019.110283.

[84] B.-W. Li, M. Osada, Y.-H. Kim, Y. Ebina, K. Akatsuka, T. Sasaki, Atomic Layer Engineering of High-κ Ferroelectricity in 2D Perovskites, J. Am. Chem. Soc. 139 (2017) 10868–10874. https://doi.org/10.1021/jacs.7b05665.

[85] M.S. Khan, H. Kim, Y. Kim, Y. Ebina, W. Sugimoto, T. Sasaki, M. Osada, Scalable Design of Two-Dimensional Oxide Nanosheets for Construction of Ultrathin Multilayer Nanocapacitor, Small. 16 (2020) 2003485. https://doi.org/10.1002/smll.202003485.

[86] M.S. Khan, M. Osada, L. Dong, Y.-H. Kim, Y. Ebina, T. Sasaki, Rational Assembly of Two-Dimensional Perovskite Nanosheets as Building Blocks for New Ferroelectrics, ACS Appl. Mater. Interfaces. 13 (2021) 1783–1790. https://doi.org/10.1021/acsami.0c16967.

[87] S. Li, Y. Zhang, W. Yang, H. Liu, X. Fang, 2D Perovskite $Sr_2Nb_3O_{10}$ for High-Performance UV Photodetectors, Adv. Mater. 32 (2020) 1905443. https://doi.org/10.1002/adma.201905443.

[88] W.-H. Lee, J.-U. Woo, H.-G. Hwang, S. Nahm, G. Lee, J.-W. Choi, $Sr_2Nb_3O_{10}$ nanosheet thin film grown via LB method for high-performance planar-type pseudocapacitor, Appl. Surf. Sci. 525 (2020) 146640. https://doi.org/10.1016/j.apsusc.2020.146640.

[89] J.-H. Kim, S.H. Kweon, S. Nahm, Low-temperature crystalline lead-free piezoelectric thin films grown on 2D perovskite nanosheet for flexible electronic device applications, Nano Res. 12 (2019) 2559–2567. https://doi.org/10.1007/s12274-019-2486-5.

[90] J.-H. Kim, J.-U. Woo, Y.-J. Yee, I.-S. Kim, H.-S. Shin, H.-G. Hwang, S.H. Kweon, H.-J. Choi, S. Nahm, [001]-oriented crystalline Potassium-Sodium Niobate thin film fabricated at low temperature for use in piezoelectric energy harvester, Appl. Surf. Sci. 537 (2021) 147871. https://doi.org/10.1016/j.apsusc.2020.147871.

[91] M. Osada, T. Sasaki, A- and B-Site Modified Perovskite Nanosheets and Their Integrations into High-k Dielectric Thin Films, Int. J. Appl. Ceram. Technol. 9 (2012) 29–36. https://doi.org/10.1111/j.1744-7402.2011.00713.x.

[92] W. Wan, Y.-Y. Zhou, L. Yan, B. Su, S. Ye, In Situ Compositing $CsPbBr_3$ with Exfoliated Layered-Perovskite $CsCa_2Ta_3O_{10}$: Interfacial Interaction and Enhanced Stability, ACS Appl. Mater. Interfaces. 11 (2019) 47227–47236. https://doi.org/10.1021/acsami.9b15990.

[93] M. Hojamberdiev, M.F. Bekheet, E. Zahedi, H. Wagata, Y. Kamei, K. Yubuta, A. Gurlo, N. Matsushita, K. Domen, K. Teshima, New Dion–Jacobson Phase Three-Layer Perovskite $CsBa_2Ta_3O_{10}$ and Its Conversion to Nitrided $Ba_2Ta_3O_{10}$ Nanosheets via a Nitridation–Protonation–Intercalation–Exfoliation Route for Water Splitting, Cryst. Growth Des. 16 (2016) 2302–2308. https://doi.org/10.1021/acs.cgd.6b00081.

[94] S.N. Ruddlesden, P. Popper, New compounds of the K_2NiF_4 type, Acta Crystallogr. 10 (1957) 538–539. https://doi.org/10.1107/S0365110X57001929.

[95] S.N. Ruddlesden, P. Popper, The compound $Sr_3Ti_2O_7$ and its structure, Acta Crystallogr. 11 (1958) 54–55. https://doi.org/10.1107/S0365110X58000128.

[96] B. Aurivillius, Mixed Bismuth Oxides with Layer Lattices. 1. The Structure Type of $CaNb_2Bi_2O_9$, Arki Kemi. 1 (1949) 463–480.

[97] M. Osada, T. Sasaki, Nanoarchitectonics in dielectric/ferroelectric layered perovskites: from bulk 3D systems to 2D nanosheets, Dalton Trans. 47 (2018) 2841–2851. https://doi.org/10.1039/C7DT03719H.

[98] C.-H. Lee, N.D. Orloff, T. Birol, Y. Zhu, V. Goian, E. Rocas, R. Haislmaier, E. Vlahos, J.A. Mundy, L.F. Kourkoutis, Y. Nie, M.D. Biegalski, J. Zhang, M. Bernhagen, N.A. Benedek, Y. Kim, J.D. Brock, R. Uecker, X.X. Xi, V. Gopalan, D. Nuzhnyy, S. Kamba, D.A. Muller, I. Takeuchi, J.C. Booth, C.J. Fennie, D.G. Schlom, Exploiting dimensionality and defect mitigation to create tunable microwave dielectrics, Nature. 502 (2013) 532–536. https://doi.org/10.1038/nature12582.

[99] C.A.-P. de Araujo, J.D. Cuchiaro, L.D. McMillan, M.C. Scott, J.F. Scott, Fatigue-free ferroelectric capacitors with platinum electrodes, Nature. 374 (1995) 627–629. https://doi.org/10.1038/374627a0.

[100] B.H. Park, B.S. Kang, S.D. Bu, T.W. Noh, J. Lee, W. Jo, Lanthanum-substituted bismuth titanate for use in non-volatile memories, Nature. 401 (1999) 682–684. https://doi.org/10.1038/44352.

[101] H. Tsai, W. Nie, J.-C. Blancon, C.C. Stoumpos, R. Asadpour, B. Harutyunyan, A.J. Neukirch, R. Verduzco, J.J. Crochet, S. Tretiak, L. Pedesseau, J. Even, M.A. Alam, G. Gupta, J. Lou, P.M. Ajayan, M.J. Bedzyk, M.G. Kanatzidis, A.D. Mohite, High-efficiency two-dimensional Ruddlesden–Popper perovskite solar cells, Nature. 536 (2016) 312–316. https://doi.org/10.1038/nature18306.

[102] Y. Chen, Y. Sun, J. Peng, J. Tang, K. Zheng, Z. Liang, 2D Ruddlesden-Popper Perovskites for Optoelectronics, Adv. Mater. 30 (2018) 1703487. https://doi.org/10.1002/adma.201703487.

[103] C.C. Stoumpos, D.H. Cao, D.J. Clark, J. Young, J.M. Rondinelli, J.I. Jang, J.T. Hupp, M.G. Kanatzidis, Ruddlesden–Popper Hybrid Lead Iodide Perovskite 2D Homologous Semiconductors, Chem. Mater. 28 (2016) 2852–2867. https://doi.org/10.1021/acs.chemmater.6b00847.

[104] R.E. Schaak, T.E. Mallouk, Prying Apart Ruddlesden−Popper Phases: Exfoliation into Sheets and Nanotubes for Assembly of Perovskite Thin Films, Chem. Mater. 12 (2000) 3427–3434. https://doi.org/10.1021/cm000495r.

[105] R.E. Schaak, T.E. Mallouk, Perovskites by Design: A Toolbox of Solid-State Reactions, Chem. Mater. 14 (2002) 1455–1471. https://doi.org/10.1021/cm010689m.

[106] J.-Y. Kim, I. Chung, J.-H. Choy, G.-S. Park, Macromolecular Nanoplatelet of Aurivillius-type Layered Perovskite Oxide, $Bi_4Ti_3O_{12}$, Chem. Mater. 13 (2001) 2759–2761. https://doi.org/10.1021/cm0102436.

[107] C. Guo, J. Xu, S. Wang, L. Li, Y. Zhang, X. Li, Facile synthesis and photocatalytic application of hierarchical mesoporous Bi_2MoO_6 nanosheet-based microspheres, CrystEngComm. 14 (2012) 3602. https://doi.org/10.1039/c2ce06757a.

[108] S.-P. Hu, C.-Y. Xu, F.-X. Ma, L. Cao, L. Zhen, Solvothermal synthesis of orthorhombic Sb_2WO_6 hierarchical structures and their visible-light-driven photocatalytic activity, Dalton Trans. 43 (2014) 8439–8445. https://doi.org/10.1039/C3DT53561D.

[109] S. Ida, C. Ogata, U. Unal, K. Izawa, T. Inoue, O. Altuntasoglu, Y. Matsumoto, Preparation of a Blue Luminescent Nanosheet Derived from Layered Perovskite $Bi_2SrTa_2O_9$, J. Am. Chem. Soc. 129 (2007) 8956–8957. https://doi.org/10.1021/ja073105b.

[110] J.L. Fourquet, A. Le Bail, P.A. Gillet, $LiNbWO_6$: Crystal structure of its two allotropic forms, Mater. Res. Bull. 23 (1988) 1163–1170. https://doi.org/10.1016/0025-5408(88)90207-3.

[111] X. Cheng, T. Liu, H. Yu, F. Ran, W. Ye, H. Zhu, M. Shui, Y. Xie, J. Shu, Polymorphism-Controlled Electrochemical Energy Storage Performance of $LiNbWO_6$, Chem. Mater. 32 (2020) 3376–3384. https://doi.org/10.1021/acs.chemmater.9b04898.

[112] V. Bhat, J. Gopalakrishnan, $HNbWO_6$ and $HTaWO_6$: Novel oxides related to ReO_3 formed by ion exchange of rutile-type $LiNbWO_6$ and $LiTaWO_6$, J. Solid State Chem. 63 (1986) 278–283. https://doi.org/10.1016/0022-4596(86)90178-7.

[113] Y. Liu, J. Xiong, S. Luo, R. Liang, N. Qin, S. Liang, L. Wu, Ultrathin $HNbWO_6$ nanosheets: facile synthesis and enhanced hydrogen evolution performance from photocatalytic water splitting, Chem. Commun. 51 (2015) 15125–15128. https://doi.org/10.1039/C5CC05788D.

[114] C. Tagusagawa, A. Takagaki, S. Hayashi, K. Domen, Characterization of $HNbWO_6$ and $HTaWO_6$ Metal Oxide Nanosheet Aggregates As Solid Acid Catalysts, J. Phys. Chem. C. 113 (2009) 7831–7837. https://doi.org/10.1021/jp900525a.

[115] A. Takagaki, Production of 5-Hydroxymethylfurfural from Glucose in Water by Using Transition Metal-Oxide Nanosheet Aggregates, Catalysts. 9 (2019) 818. https://doi.org/10.3390/catal9100818.

[116] P.T.P. Le, K. Hofhuis, A. Rana, M. Huijben, H. Hilgenkamp, G.A.J.H.M. Rijnders, J.E. ten Elshof, G. Koster, N. Gauquelin, G. Lumbeeck, C. Schüßler-Langeheine, H. Popescu, F. Fortuna, S. Smit, X.H. Verbeek, G. Araizi-Kanoutas, S. Mishra, I. Vaskivskyi, H.A. Dürr, M.S. Golden, Tailoring Vanadium Dioxide Film Orientation Using Nanosheets: a Combined Microscopy, Diffraction, Transport, and Soft X-Ray in Transmission Study, Adv. Funct. Mater. 30 (2020) 1900028. https://doi.org/10.1002/adfm.201900028.

[117] P.T.P. Le, S. Huang, M.D. Nguyen, J.E. ten Elshof, G. Koster, Tuning the metal insulator transition of vanadium dioxide on oxide nanosheets, Appl. Phys. Lett. 119 (2021) 081601. https://doi.org/10.1063/5.0059174.
[118] M. Gasperin, M.T. Le Bihan, Mecanisme d'hydratation des niobates alcalins lamellaires de formule $A_4Nb_4O_{17}$ (A = K, Rb, Cs), J. Solid State Chem. 43 (1982) 346–353. https://doi.org/10.1016/0022-4596(82)90251-1.
[119] M.A. Bizeto, V.R.L. Constantino, Layered $H_2K_2Nb_6O_{17}$ exfoliation promoted by n-butylamine, Mater. Res. Bull. 39 (2004) 1811–1820. https://doi.org/10.1016/j.materresbull.2004.07.001.
[120] N. Kinomura, N. Kumada, F. Muto, Ion exchange of $K_4Nb_6O_{17}{\cdot}3H_2O$, J Chem Soc Dalton Trans. (1985) 2349–2351. https://doi.org/10.1039/DT9850002349.
[121] S.K. Sahu, L.A. Boatner, A. Navrotsky, Formation and Dehydration Enthalpy of Potassium Hexaniobate, J. Am. Ceram. Soc. 100 (2017) 304–311. https://doi.org/10.1111/jace.14465.
[122] K. Domen, J.N. Kondo, M. Hara, T. Takata, Photo- and Mechano-Catalytic Overall Water Splitting Reactions to Form Hydrogen and Oxygen on Heterogeneous Catalysts, Bull. Chem. Soc. Jpn. 73 (2000) 1307–1331. https://doi.org/10.1246/bcsj.73.1307.
[123] H. Hayashi, Y. Hakuta, Y. Kurata, Hydrothermal synthesis of potassium niobate photocatalysts under subcritical and supercritical water conditions, J. Mater. Chem. 14 (2004) 2046. https://doi.org/10.1039/b400130n.
[124] H.-L. Chou, C.-C. Lee, H.-M. Chen, W.-N. Su, B.-J. Hwang, Characterization of $K_4Nb_6O_{17}$ synthesized by a sol–gel method for H_2 evolution, J. Chin. Inst. Eng. 34 (2011) 3–9. https://doi.org/10.1080/02533839.2011.552961.
[125] Y. Ma, X. Liu, Y. Li, Y. Su, Z. Chai, X. Wang, $K_4Nb_6O_{17}{\cdot}4.5H_2O$: A novel dual functional material with quick photoreduction of Cr(VI) and high adsorptive capacity of Cr(III), J. Hazard. Mater. 279 (2014) 537–545. https://doi.org/10.1016/j.jhazmat.2014.07.046.
[126] R. Abe, K. Shinmei, N. Koumura, K. Hara, B. Ohtani, Visible-Light-Induced Water Splitting Based on Two-Step Photoexcitation between Dye-Sensitized Layered Niobate and Tungsten Oxide Photocatalysts in the Presence of a Triiodide/Iodide Shuttle Redox Mediator, J. Am. Chem. Soc. 135 (2013) 16872–16884. https://doi.org/10.1021/ja4048637.
[127] C. Hu, L. Zhang, L. Cheng, J. Chen, W. Hou, W. Ding, A comparison of H+-restacked nanosheets and nanoscrolls derived from $K_4Nb_6O_{17}$ for visible-light degradation of dyes, J. Energy Chem. 23 (2014) 136–144. https://doi.org/10.1016/S2095-4956(14)60128-5.
[128] G.B. Saupe, C.C. Waraksa, H.-N. Kim, Y.J. Han, D.M. Kaschak, D.M. Skinner, T.E. Mallouk, Nanoscale Tubules Formed by Exfoliation of Potassium Hexaniobate, Chem. Mater. 12 (2000) 1556–1562. https://doi.org/10.1021/cm981136n.
[129] M.A. Bizeto, D.L.A. De Faria, V.R.L. Constantino, Porphyrin intercalation into a layered niobate derived from $K_4Nb_6O_{17}$, J. Mater. Sci. 37 (2002) 265–270. https://doi.org/10.1023/A:1013687825874.
[130] X. Liu, W. Que, P. Chen, Y. Tian, J. Liu, Z. He, H. Zhou, L. Bing Kong, Facile preparation of protonated hexaniobate nanosheets and its enhanced photocatalytic activity, Nanotechnology. 28 (2017) 235702. https://doi.org/10.1088/1361-6528/aa6b4f.
[131] A. Furube, T. Shiozawa, A. Ishikawa, A. Wada, C. Hirose, K. Domen, Primary process of photogenerated carriers in ion-exchanged $K_4Nb_6O_{17}$ thin films investigated by femtosecond transient absorption spectroscopy, Chem. Phys. 285 (2002) 31–37. https://doi.org/10.1016/S0301-0104(02)00686-9.
[132] Y. Hosogi, H. Kato, A. Kudo, Photocatalytic Activities of Layered Titanates and Niobates Ion-Exchanged with Sn^{2+} under Visible Light Irradiation, J. Phys. Chem. C. 112 (2008) 17678–17682. https://doi.org/10.1021/jp805693j.
[133] V.R.L. Constantino, M.A. Bizeto, H.F. Brito, Photoluminescence study of layered niobates intercalated with Eu^{3+} ions, J. Alloys Compd. 278 (1998) 142–148. https://doi.org/10.1016/S0925-8388(98)00588-X.
[134] S. Lee, K. Teshima, Y. Niina, S. Suzuki, K. Yubuta, T. Shishido, M. Endo, S. Oishi, Highly crystalline niobium oxide converted from flux-grown $K_4Nb_6O_{17}$ crystals, CrystEngComm. 11 (2009) 2326. https://doi.org/10.1039/b905870b.
[135] X. Liu, W. Que, P. Chen, Y. Tian, J. Liu, Z. He, H. Zhou, L. Bing Kong, Facile preparation of protonated hexaniobate nanosheets and its enhanced photocatalytic activity, Nanotechnology. 28 (2017) 235702. https://doi.org/10.1088/1361-6528/aa6b4f

.

[136] G. Yan, H. Shi, H. Tan, W. Zhu, Y. Wang, H. Zang, Y. Li, Coupling with a narrow-band-gap semiconductor for the enhancement of visible-light photocatalytic activity: preparation of $Bi_2O_xS_{3-x}/Nb_6O_{17}$ and application to the degradation of methyl orange, Dalton Trans. 45 (2016) 13944–13950. https://doi.org/10.1039/C6DT02338J.
[137] N. Miyamoto, H. Yamamoto, R. Kaito, K. Kuroda, Formation of extraordinarily large nanosheets from $K_4Nb_6O_{17}$, Chem. Commun. (2002) 2378–2379. https://doi.org/10.1039/b206998a.
[138] T. Nakato, N. Miyamoto, A. Harada, H. Ushiki, Sol–Gel Transition of Niobium Oxide Nanosheet Colloids: Hierarchical Aspect of a Novel Macroscopic Property Appearing in Colloidally Dispersed States of Layered Niobate $K_4Nb_6O_{17}$, Langmuir. 19 (2003) 3157–3163. https://doi.org/10.1021/la0265474.
[139] M.C. Sarahan, E.C. Carroll, M. Allen, D.S. Larsen, N.D. Browning, F.E. Osterloh, $K_4Nb_6O_{17}$-derived photocatalysts for hydrogen evolution from water: Nanoscrolls versus nanosheets, J. Solid State Chem. 181 (2008) 1678–1683. https://doi.org/10.1016/j.jssc.2008.06.021.
[140] B.P. Bastakoti, Y. Li, M. Imura, N. Miyamoto, T. Nakato, T. Sasaki, Y. Yamauchi, Polymeric Micelle Assembly with Inorganic Nanosheets for Construction of Mesoporous Architectures with Crystallized Walls, Angew. Chem. Int. Ed. 54 (2015) 4222–4225. https://doi.org/10.1002/anie.201410942.
[141] T. Nakato, T. Fujita, E. Mouri, Synergistic photocatalytic hydrogen evolution over oxide nanosheets combined with photochemically inert additives, Phys. Chem. Chem. Phys. 17 (2015) 5547–5550. https://doi.org/10.1039/C4CP06083K.
[142] X. Wang, Y. Zhai, C. Kuang, H. Liu, L. Li, Simple Synthesis of $K_4Nb_6O_{17}$/C Nanosheets for High-Power Lithium-Ion Batteries with Good Stability, Materials. 12 (2019) 262. https://doi.org/10.3390/ma12020262.
[143] T. Sasaki, F. Kooli, M. Iida, Y. Michiue, S. Takenouchi, Y. Yajima, F. Izumi, B.C. Chakoumakos, M. Watanabe, A mixed alkali metal titanate with the lepidocrocite-like layered structure. Preparation, crystal structure, protonic form, and acid-base intercalation properties, Chem. Mater. 10 (1998) 4123–4128. https://doi.org/10.1021/cm980535f.
[144] M. Shirpour, J. Cabana, M. Doeff, Lepidocrocite-type Layered Titanate Structures: New Lithium and Sodium Ion Intercalation Anode Materials, Chem. Mater. 26 (2014) 2502–2512. https://doi.org/10.1021/cm500342m.
[145] L.-J. Hou, R.-C. Liu, H.-Y. Yuan, D.-Z. Kong, W.-X. Shen, J.-H. Zang, J. Guo, S.-G. Dai, M.-L. Wang, T.-T. Xu, X.-J. Li, Y. Wang, Micro-structured lepidocrocite-type $H_{1.07}Ti_{1.73}O_4$ as anode for lithium-ion batteries with an ultrahigh rate and long-term cycling performance, Rare Met. 40 (2021) 1391–1401. https://doi.org/10.1007/s12598-020-01618-8.
[146] Y. Song, H. Wang, J. Xiong, B. Guo, S. Liang, L. Wu, Photocatalytic hydrogen evolution over monolayer H1.07Ti1.73O4·H2O nanosheets: Roles of metal defects and greatly enhanced performances, Appl. Catal. B Environ. 221 (2018) 473–481. https://doi.org/10.1016/j.apcatb.2017.09.009.
[147] K. Akatsuka, M. Haga, Y. Ebina, M. Osada, K. Fukuda, T. Sasaki, Construction of Highly Ordered Lamellar Nanostructures through Langmuir–Blodgett Deposition of Molecularly Thin Titania Nanosheets Tens of Micrometers Wide and Their Excellent Dielectric Properties, ACS Nano. 3 (2009) 1097–1106. https://doi.org/10.1021/nn900104u.
[148] A. Kumar, S.K.C. Palanisamy, J.M. Boter, C. Hellenthal, J.E. ten Elshof, H.J.W. Zandvliet, Imaging of Ti0.87O2 nanosheets using scanning tunneling spectroscopy, Appl. Surf. Sci. 265 (2013) 201–204. https://doi.org/10.1016/j.apsusc.2012.10.169.
[149] T. Tanaka, Y. Ebina, K. Takada, K. Kurashima, T. Sasaki, Oversized Titania Nanosheet Crystallites Derived from Flux-Grown Layered Titanate Single Crystals, Chem. Mater. 15 (2003) 3564–3568. https://doi.org/10.1021/cm034307j.
[150] T. Shibata, N. Sakai, K. Fukuda, Y. Ebina, T. Sasaki, Photocatalytic properties of titania nanostructured films fabricated from titania nanosheets, Phys. Chem. Chem. Phys. 9 (2007) 2413. https://doi.org/10.1039/b618448k.
[151] C. Zhou, J. Luo, Q. Chen, Y. Jiang, X. Dong, F. Cui, Titanate nanosheets as highly efficient non-light-driven catalysts for degradation of organic dyes, Chem. Commun. 51 (2015) 10847–10849. https://doi.org/10.1039/C5CC03279B.
[152] H. Yuan, K. Han, D. Dubbink, G. Mul, J.E. ten Elshof, Modulating the External Facets of Functional Nanocrystals Enabled by Two-Dimensional Oxide Crystal Templates, ACS Catal. 7 (2017) 6858–6863. https://doi.org/10.1021/acscatal.7b02605.
[153] H. Liu, B. Feng, X. Bai, T. Qi, Z. Wei, R. Liu, K. Yin, J. Gao, D. Yang, G. Zheng, J.E. ten Elshof, C. Shan, Q. Sun, H. Yuan, Two-dimensional oxide based pressure sensors with high sensitivity, Nano Sel. (2021) nano.202100053. https://doi.org/10.1002/nano.202100053.

[154] M. Osada, Y. Ebina, H. Funakubo, S. Yokoyama, T. Kiguchi, K. Takada, T. Sasaki, High-κ Dielectric Nanofilms Fabricated from Titania Nanosheets, Adv. Mater. 18 (2006) 1023–1027. https://doi.org/10.1002/adma.200501224.
[155] Y.-H. Kim, L. Dong, M. Osada, B.-W. Li, Y. Ebina, T. Sasaki, Artificial design for new ferroelectrics using nanosheet-architectonics concept, Nanotechnology. 26 (2015) 244001. https://doi.org/10.1088/0957-4484/26/24/244001.
[156] P. Xiong, X. Zhang, F. Zhang, D. Yi, J. Zhang, B. Sun, H. Tian, D. Shanmukaraj, T. Rojo, M. Armand, R. Ma, T. Sasaki, G. Wang, Two-Dimensional Unilamellar Cation-Deficient Metal Oxide Nanosheet Superlattices for High-Rate Sodium Ion Energy Storage, ACS Nano. 12 (2018) 12337–12346. https://doi.org/10.1021/acsnano.8b06206.
[157] M. Nijland, S. Thomas, M.A. Smithers, N. Banerjee, D.H.A. Blank, G. Rijnders, J. Xia, G. Koster, J.E. ten Elshof, Epitaxy on Demand, Adv. Funct. Mater. 25 (2015) 5140–5148. https://doi.org/10.1002/adfm.201501483.
[158] I.E. Grey, C. Li, I.C. Madsen, J.A. Watts, The stability and structure of $Cs_x[Ti_{2-x/4}\_x/4]O_4$, 0.61 < x < 0.65, J. Solid State Chem. 66 (1987) 7–19. https://doi.org/10.1016/0022-4596(87)90215-5.
[159] T. Sasaki, Y. Komatsu, Y. Fujiki, A new layered hydrous titanium dioxide $H_xTi_{2-x/4}O_4 \cdot H_2O$, J Chem Soc Chem Commun. (1991) 817–818. https://doi.org/10.1039/C39910000817.
[160] T. Sasaki, M. Watanabe, Y. Michiue, Y. Komatsu, F. Izumi, S. Takenouchi, Preparation and Acid-Base Properties of a Protonated Titanate with the Lepidocrocite-like Layer Structure, Chem. Mater. 7 (1995) 1001–1007. https://doi.org/10.1021/cm00053a029.
[161] T. Sasaki, M. Watanabe, H. Hashizume, H. Yamada, H. Nakazawa, Macromolecule-like Aspects for a Colloidal Suspension of an Exfoliated Titanate. Pairwise Association of Nanosheets and Dynamic Reassembling Process Initiated from It, J. Am. Chem. Soc. 118 (1996) 8329–8335. https://doi.org/10.1021/ja960073b.
[162] H. Sato, K. Ono, T. Sasaki, A. Yamagishi, First-Principles Study of Two-Dimensional Titanium Dioxides, J. Phys. Chem. B. 107 (2003) 9824–9828. https://doi.org/10.1021/jp035017t.
[163] T. Yamamoto, N. Saso, Y. Umemura, Y. Einaga, Photoreduction of Prussian Blue Intercalated into Titania Nanosheet Ultrathin Films, J. Am. Chem. Soc. 131 (2009) 13196–13197. https://doi.org/10.1021/ja9041274.
[164] X. Luan, M.T. Gutierrez Wing, Y. Wang, Enhanced photocatalytic activity of graphene oxide/titania nanosheets composites for methylene blue degradation, Mater. Sci. Semicond. Process. 30 (2015) 592–598. https://doi.org/10.1016/j.mssp.2014.10.032.
[165] W. Tu, Y. Zhou, Q. Liu, Z. Tian, J. Gao, X. Chen, H. Zhang, J. Liu, Z. Zou, Robust Hollow Spheres Consisting of Alternating Titania Nanosheets and Graphene Nanosheets with High Photocatalytic Activity for CO_2 Conversion into Renewable Fuels, Adv. Funct. Mater. 22 (2012) 1215–1221. https://doi.org/10.1002/adfm.201102566.
[166] H. Xin, R. Ma, L. Wang, Y. Ebina, K. Takada, T. Sasaki, Photoluminescence properties of lamellar aggregates of titania nanosheets accommodating rare earth ions, Appl. Phys. Lett. 85 (2004) 4187–4189. https://doi.org/10.1063/1.1812811.
[167] S. Sriphan, T. Charoonsuk, S. Khaisaat, O. Sawanakarn, U. Pharino, S. Phunpruch, T. Maluangnont, N. Vittayakorn, Flexible capacitive sensor based on 2D-titanium dioxide nanosheets/bacterial cellulose composite film, Nanotechnology. 32 (2021) 155502. https://doi.org/10.1088/1361-6528/abd8ae.
[168] T. Sasaki, Y. Ebina, T. Tanaka, M. Harada, M. Watanabe, G. Decher, Layer-by-Layer Assembly of Titania Nanosheet/Polycation Composite Films, Chem. Mater. 13 (2001) 4661–4667. https://doi.org/10.1021/cm010478h.
[169] Y. Matsumoto, Room-Temperature Ferromagnetism in Transparent Transition Metal-Doped Titanium Dioxide, Science. 291 (2001) 854–856. https://doi.org/10.1126/science.1056186.
[170] M. Osada, Y. Ebina, K. Takada, T. Sasaki, Gigantic Magneto–Optical Effects in Multilayer Assemblies of Two-Dimensional Titania Nanosheets, Adv. Mater. 18 (2006) 295–299 . https://doi.org/10.1002/adma.200501810.
[171] M. Osada, S. Yoguchi, M. Itose, B.-W. Li, Y. Ebina, K. Fukuda, Y. Kotani, K. Ono, S. Ueda, T. Sasaki, Controlled doping of semiconducting titania nanosheets for tailored spinelectronic materials, Nanoscale. 6 (2014) 14227–14236. https://doi.org/10.1039/C4NR04465G.
[172] M. Osada, M. Itose, Y. Ebina, K. Ono, S. Ueda, K. Kobayashi, T. Sasaki, Gigantic magneto-optical effects induced by (Fe⁄Co)-cosubstitution in titania nanosheets, Appl. Phys. Lett. 92 (2008) 253110. https://doi.org/10.1063/1.2937094.
[173] B.-W. Li, M. Osada, Y. Ebina, S. Ueda, T. Sasaki, Coexistence of Magnetic Order and Ferroelectricity at 2D Nanosheet Interfaces, J. Am. Chem. Soc. 138 (2016) 7621–7625. https://doi.org/10.1021/jacs.6b02722.

[174] R.E. Marsh, I. Bernal, More space-group changes, Acta Crystallogr. B. 51 (1995) 300–307. https://doi.org/10.1107/S0108768194011857.
[175] S.F. Solodovnikov, N.V. Ivannikova, Synthesis and X-Ray Diffraction Study of Potassium, Rubidium, and Cesium Polytungstates with Defect Pyrochlore and Hexagonal Tungsten Bronze Structures, Inorg Mater. (1998) 845–853.
[176] K. Fukuda, K. Akatsuka, Y. Ebina, R. Ma, K. Takada, I. Nakai, T. Sasaki, Exfoliated Nanosheet Crystallite of Cesium Tungstate with 2D Pyrochlore Structure: Synthesis, Characterization, and Photochromic Properties, ACS Nano. 2 (2008) 1689–1695. https://doi.org/10.1021/nn800184w.
[177] M. Miyauchi, A. Kondo, D. Atarashi, E. Sakai, Tungstate nanosheet ink as a photonless and electroless chromic device, J Mater Chem C. 2 (2014) 3732–3737. https://doi.org/10.1039/C3TC32513J.
[178] T. Shibata, T. Ohnishi, I. Sakaguchi, M. Osada, K. Takada, T. Kogure, T. Sasaki, Well-Controlled Crystal Growth of Zinc Oxide Films on Plastics at Room Temperature Using 2D Nanosheet Seed Layer, J. Phys. Chem. C. 113 (2009) 19096–19101. https://doi.org/10.1021/jp9074288.
[179] A.-C. Gaillot, V.A. Drits, A. Manceau, B. Lanson, Structure of the synthetic K-rich phyllomanganate birnessite obtained by high-temperature decomposition of $KMnO_4$, Microporous Mesoporous Mater. 98 (2007) 267–282. https://doi.org/10.1016/j.micromeso.2006.09.010.
[180] Y. Omomo, T. Sasaki, Wang, M. Watanabe, Redoxable Nanosheet Crystallites of MnO_2 Derived via Delamination of a Layered Manganese Oxide, J. Am. Chem. Soc. 125 (2003) 3568–3575. https://doi.org/10.1021/ja021364p.
[181] Y. Wang, Y.-Z. Zhang, D. Dubbink, J.E. ten Elshof, Inkjet printing of δ-MnO_2 nanosheets for flexible solid-state micro-supercapacitor, Nano Energy. 49 (2018) 481–488. https://doi.org/10.1016/j.nanoen.2018.05.002.
[182] K. Kai, Y. Yoshida, H. Kageyama, G. Saito, T. Ishigaki, Y. Furukawa, J. Kawamata, Room-Temperature Synthesis of Manganese Oxide Monosheets, J. Am. Chem. Soc. 130 (2008) 15938–15943. https://doi.org/10.1021/ja804503f.
[183] Z. Liu, K. Xu, H. Sun, S. Yin, One-Step Synthesis of Single-Layer MnO_2 Nanosheets with Multi-Role Sodium Dodecyl Sulfate for High-Performance Pseudocapacitors, Small. 11 (2015) 2182–2191. https://doi.org/10.1002/smll.201402222.
[184] J. Qian, H. Jin, B. Chen, M. Lin, W. Lu, W.M. Tang, W. Xiong, L.W.H. Chan, S.P. Lau, J. Yuan, Aqueous Manganese Dioxide Ink for Paper-Based Capacitive Energy Storage Devices, Angew. Chem. Int. Ed. 54 (2015) 6800–6803. https://doi.org/10.1002/anie.201501261.
[185] N. Sakai, Y. Ebina, K. Takada, T. Sasaki, Photocurrent Generation from Semiconducting Manganese Oxide Nanosheets in Response to Visible Light, J. Phys. Chem. B. 109 (2005) 9651–9655. https://doi.org/10.1021/jp0500485.
[186] S. Ida, A.K. Thapa, Y. Hidaka, Y. Okamoto, M. Matsuka, H. Hagiwara, T. Ishihara, Manganese oxide with a card-house-like structure reassembled from nanosheets for rechargeable Li-air battery, J. Power Sources. 203 (2012) 159–164. https://doi.org/10.1016/j.jpowsour.2011.11.042.
[187] J.-H. Kang, S.-M. Paek, S.-J. Hwang, J.-H. Choy, Pre-swelled nanostructured electrode for lithium ion battery: TiO_2-pillared layered MnO_2, J. Mater. Chem. 20 (2010) 2033. https://doi.org/10.1039/b918363a.
[188] P. Xiong, R. Ma, N. Sakai, T. Sasaki, Genuine Unilamellar Metal Oxide Nanosheets Confined in a Superlattice-like Structure for Superior Energy Storage, ACS Nano. 12 (2018) 1768–1777. https://doi.org/10.1021/acsnano.7b08522.
[189] H. Sun, K. Xu, M. Huang, Y. Shang, P. She, S. Yin, Z. Liu, One-pot synthesis of ultrathin manganese dioxide nanosheets and their efficient oxidative degradation of Rhodamine B, Appl. Surf. Sci. 357 (2015) 69–73. https://doi.org/10.1016/j.apsusc.2015.08.258.
[190] J. Wang, G. Zhang, P. Zhang, Layered birnessite-type MnO_2 with surface pits for enhanced catalytic formaldehyde oxidation activity, J. Mater. Chem. A. 5 (2017) 5719–5725. https://doi.org/10.1039/C6TA09793F.
[191] L. Peng, Q. Zeng, B. Tie, M. Lei, J. Yang, S. Luo, Z. Song, Manganese Dioxide nanosheet suspension: A novel absorbent for Cadmium(II) contamination in waterbody, J. Colloid Interface Sci. 456 (2015) 108–115. https://doi.org/10.1016/j.jcis.2015.06.017.
[192] M. Shikano, C. Delmas, J. Darriet, $NaRuO_2$ and $Na_xRuO_2{\cdot}yH_2O$: New Oxide and Oxyhydrate with Two Dimensional RuO_2 Layers, Inorg. Chem. 43 (2004) 1214–1216. https://doi.org/10.1021/ic035324d.
[193] K. Fukuda, T. Saida, J. Sato, M. Yonezawa, Y. Takasu, W. Sugimoto, Synthesis of Nanosheet Crystallites of Ruthenate with an α-$NaFeO_2$-Related Structure and Its Electrochemical Supercapacitor Property, Inorg. Chem. 49 (2010) 4391–4393. https://doi.org/10.1021/ic100176d.

[194] K. Fukuda, H. Kato, J. Sato, W. Sugimoto, Y. Takasu, Swelling, intercalation, and exfoliation behavior of layered ruthenate derived from layered potassium ruthenate, J. Solid State Chem. 182 (2009) 2997–3002. https://doi.org/10.1016/j.jssc.2009.08.012.
[195] J. Sato, H. Kato, M. Kimura, K. Fukuda, W. Sugimoto, Conductivity of Ruthenate Nanosheets Prepared via Electrostatic Self-Assembly: Characterization of Isolated Single Nanosheet Crystallite to Mono- and Multilayer Electrodes, Langmuir. 26 (2010) 18049–18054. https://doi.org/10.1021/la103848f.
[196] S. Laha, Y. Lee, F. Podjaski, D. Weber, V. Duppel, L.M. Schoop, F. Pielnhofer, C. Scheurer, K. Müller, U. Starke, K. Reuter, B.V. Lotsch, Ruthenium Oxide Nanosheets for Enhanced Oxygen Evolution Catalysis in Acidic Medium, Adv. Energy Mater. 9 (2019) 1803795. https://doi.org/10.1002/aenm.201803795.
[197] R.E. McCarley, K.-H. Lii, P.A. Edwards, L.F. Brough, New extended clusters in ternary molybdenum oxides, J. Solid State Chem. 57 (1985) 17–24. https://doi.org/10.1016/S0022-4596(85)80056-6.
[198] H. Sugaya, K. Fukuda, M. Morita, H. Murayama, E. Matsubara, T. Kume, Y. Uchimoto, High-capacity Lithium-ion Storage System Using Unilamellar Crystallites of Exfoliated MoO_2 Nanosheets, Chem. Lett. 44 (2015) 1595–1597. https://doi.org/10.1246/cl.150706.
[199] Y. Zhou, C. Geng, A MoO_2 sheet as a promising electrode material: ultrafast Li-diffusion and astonishing Li-storage capacity, Nanotechnology. 28 (2017) 105402. https://doi.org/10.1088/1361-6528/aa56d0.
[200] M. Serafin, R. Hoppe, Coordination number 5 and 6 in $RbTaO_3$: $Rb_4{}^{\infty 2}[Ta_4O_{12}]$, Angew. Chem.-Int. Ed. Engl. 17 (1978) 354–355. https://doi.org/10.1002/anie.197803541.
[201] Materials Data on $RbTaO_3$ by Materials Project, (2020). https://doi.org/10.17188/1204746.
[202] A.I. Lebedev, Ferroelectric properties of RbNbO3 and $RbTaO_3$, Phys. Solid State. 57 (2015) 331–336. https://doi.org/10.1134/S1063783415020237.
[203] K. Fukuda, I. Nakai, Y. Ebina, R. Ma, T. Sasaki, Colloidal unilamellar layers of tantalum oxide with open channels, Inorg. Chem. 46 (2007) 4787–4789. https://doi.org/10.1021/ic7004002.
[204] J. Huang, R. Ma, Y. Ebina, K. Fukuda, K. Takada, T. Sasaki, Layer-by-Layer Assembly of TaO_3 Nanosheet/Polycation Composite Nanostructures: Multilayer Film, Hollow Sphere, and Its Photocatalytic Activity for Hydrogen Evolution, Chem. Mater. 22 (2010) 2582–2587. https://doi.org/10.1021/cm903733s.
[205] X. Xu, K. Takada, K. Fukuda, T. Ohnishi, K. Akatsuka, M. Osada, B.T. Hang, K. Kumagai, T. Sekiguchi, T. Sasaki, Tantalum oxide nanomesh as self-standing one nanometre thick electrolyte, Energy Environ. Sci. 4 (2011) 3509. https://doi.org/10.1039/c1ee01389k.
[206] M. Gasperin, Structure du triniobate(V) de potassium KNb_3O_8 , un niobate lamellaire, Acta Crystallogr. B. 38 (1982) 2024–2026. https://doi.org/10.1107/S056774088200781X.
[207] G. Blasse, F. van Tol, Luminescence of KNb_3O_8, Solid State Commun. 95 (1995) 465–468. https://doi.org/10.1016/0038-1098(95)00300-2.
[208] G. Zhang, J. Gong, X. Zou, F. He, H. zhang, Q. Zhang, Y. Liu, X. Yang, B. Hu, Photocatalytic degradation of azo dye acid red G by KNb_3O_8 and the role of potassium in the photocatalysis, Chem. Eng. J. 123 (2006) 59–64. https://doi.org/10.1016/j.cej.2006.06.021.
[209] X. Liu, W. Que, L.B. Kong, Hydrothermal synthesis of bamboo-shaped nanosheet KNb_3O_8 with enhanced photocatalytic activity, J. Alloys Compd. 627 (2015) 117–122. https://doi.org/10.1016/j.jallcom.2014.12.115.
[210] Z.-J. Yang, Y.-F. Li, Q.-B. Wu, N. Ren, Y.-H. Zhang, Z.-P. Liu, Y. Tang, Layered niobic acid with self-exfoliatable nanosheets and adjustable acidity for catalytic hydration of ethylene oxide, J. Catal. 280 (2011) 247–254. https://doi.org/10.1016/j.jcat.2011.03.026.
[211] X. Li, H. Pan, W. Li, Z. Zhuang, Photocatalytic reduction of CO_2 to methane over HNb_3O_8 nanobelts, Appl. Catal. Gen. 413–414 (2012) 103–108. https://doi.org/10.1016/j.apcata.2011.10.044.
[212] P. Zhou, Q. Li, J. He, D. Li, Z. Li, Structural features of HNb_3O_8 nanosheets and their catalytic performance in toluene nitration, Russ. J. Phys. Chem. A. 89 (2015) 2097–2104. https://doi.org/10.1134/S0036024415110254.
[213] K. Katsumata, S. Okazaki, C.E.J. Cordonier, T. Shichi, T. Sasaki, A. Fujishima, Preparation and Characterization of Self-Cleaning Glass for Vehicle with Niobia Nanosheets, ACS Appl. Mater. Interfaces. 2 (2010) 1236–1241. https://doi.org/10.1021/am100091f.
[214] T. Shibata, G. Takanashi, T. Nakamura, K. Fukuda, Y. Ebina, T. Sasaki, Titanoniobate and niobate nanosheet photocatalysts: superior photoinduced hydrophilicity and enhanced thermal stability of unilamellar Nb_3O_8 nanosheet, Energy Env. Sci. 4 (2011) 535–542. https://doi.org/10.1039/C0EE00437E.

[215] S. Suzuki, K. Teshima, A. Yamaguchi, K. Yubuta, T. Shishido, S. Oishi, Fabrication and photocatalytic performance of highly crystalline nanosheets derived from flux-grown KNb_3O_8 crystals, CrystEngComm. 14 (2012) 987–992. https://doi.org/10.1039/C1CE06035J.
[216] Y. Zhou, T. Wen, W. Kong, B. Yang, Y. Wang, The impact of nitrogen doping and reduced-niobium self-doping on the photocatalytic activity of ultra-thin $Nb_3O_8^-$ nanosheets, Dalton Trans. 46 (2017) 13854–13861. https://doi.org/10.1039/C7DT03006A.
[217] Rayleigh, Surface Tension, Nature. 43 (1891) 437–439. https://doi.org/10.1038/043437c0.
[218] I. Langmuir, The constitution and fundamental properties of solids and liquids. II. Liquids, J. Am. Chem. Soc. 39 (1917) 1848–1906. https://doi.org/10.1021/ja02254a006.
[219] K.B. Blodgett, Films Built by Depositing Successive Monomolecular Layers on a Solid Surface, J. Am. Chem. Soc. 57 (1935) 1007–1022. https://doi.org/10.1021/ja01309a011.
[220] K. Matsuba, C. Wang, K. Saruwatari, Y. Uesusuki, K. Akatsuka, M. Osada, Y. Ebina, R. Ma, T. Sasaki, Neat monolayer tiling of molecularly thin two-dimensional materials in 1 min, Sci. Adv. 3 (2017) e1700414. https://doi.org/10.1126/sciadv.1700414.
[221] L. Chang, M.A. Holmes, M. Waller, F.E. Osterloh, A.J. Moulé, Calcium niobate nanosheets as a novel electron transport material for solution-processed multi-junction polymer solar cells, J. Mater. Chem. 22 (2012) 20443. https://doi.org/10.1039/c2jm33351a.
[222] K. Awaya, S. Ida, A perfectly oriented, free-standing and transparent titania nanosheet film with the band gap of a monolayer, Chem. Commun. 56 (2020) 9811–9814. https://doi.org/10.1039/D0CC04158K.
[223] J.W. Kim, D. Kang, T.H. Kim, S.G. Lee, N. Byun, D.W. Lee, B.H. Seo, R.S. Ruoff, H.S. Shin, Mosaic-like Monolayer of Graphene Oxide Sheets Decorated with Tetrabutylammonium Ions, ACS Nano. 7 (2013) 8082–8088. https://doi.org/10.1021/nn403363s.
[224] E. Harsanyi, (1933).
[225] H.C. Hamaker, E.J.W. Verwey, Part II.—(C) Colloid stability. The role of the forces between the particles in electrodeposition and other phenomena, Trans Faraday Soc. 35 (1940) 180–185. https://doi.org/10.1039/TF9403500180.
[226] L. Besra, M. Liu, A review on fundamentals and applications of electrophoretic deposition (EPD), Prog. Mater. Sci. 52 (2007) 1–61. https://doi.org/10.1016/j.pmatsci.2006.07.001.
[227] I. Zhitomirsky, Cathodic electrodeposition of ceramic and organoceramic materials. Fundamental aspects, Adv. Colloid Interface Sci. 97 (2002) 279–317. https://doi.org/10.1016/S0001-8686(01)00068-9.
[228] L. Xue, K. Kajiyoshi, Y. Yan, Preparation of highly oriented titania nanosheet thin films by electrophoretic deposition, Thin Solid Films. 518 (2009) 10–15. https://doi.org/10.1016/j.tsf.2009.05.058.
[229] T. Yui, Y. Mori, T. Tsuchino, T. Itoh, T. Hattori, Y. Fukushima, K. Takagi, Synthesis of Photofunctional Titania Nanosheets by Electrophoretic Deposition, Chem. Mater. 17 (2005) 206–211. https://doi.org/10.1021/cm0491882.
[230] S.-H. Kweon, M. Im, W.-H. Lee, S. Nahm, J.-W. Choi, S.-J. Hwang, Electrophoretic deposition of $Ca_2Nb_3O_{10}^-$ nanosheets synthesized by soft-chemical exfoliation, J. Mater. Chem. C. 4 (2016) 178–184. https://doi.org/10.1039/C5TC03815D.
[231] Y.-S. Lee, H. Yim, S.-Y. Yoo, B.-K. Ju, J.-W. Choi, Dielectric properties of single crystal Sr2Nb3O10 dielectric nanosheet thin films by electrophoretic deposition (EPD) and post deposition treatments, J. Alloys Compd. 711 (2017) 51–57. https://doi.org/10.1016/j.jallcom.2017.03.342.
[232] M. Diba, D.W.H. Fam, A.R. Boccaccini, M.S.P. Shaffer, Electrophoretic deposition of graphene-related materials: A review of the fundamentals, Prog. Mater. Sci. 82 (2016) 83–117. https://doi.org/10.1016/j.pmatsci.2016.03.002.
[233] M. Cheong, I. Zhitomirsky, Electrophoretic deposition of manganese oxide films, Surf. Eng. 25 (2009) 346–352. https://doi.org/10.1179/174329408X281786.
[234] M. Im, S.-H. Kweon, D.-H. Kim, W.-H. Lee, S. Nahm, J.-W. Choi, S.-J. Hwang, Structural and electrical properties of $Sr_2NaNb_4O_{13}$ thin film grown by electrophoretic method using nanosheets synthesized from $K(Sr_2Na)Nb_4O_{13}$ compound, J. Eur. Ceram. Soc. 37 (2017) 2407–2413. https://doi.org/10.1016/j.jeurceramsoc.2017.02.012.
[235] T.G. Dane, J.E. Bartenstein, B. Sironi, B.M. Mills, O. Alexander Bell, J. Emyr Macdonald, T. Arnold, C.F.J. Faul, W.H. Briscoe, Influence of solvent polarity on the structure of drop-cast electroactive tetra(aniline)-surfactant thin films, Phys. Chem. Chem. Phys. 18 (2016) 24498–24505. https://doi.org/10.1039/C6CP05221E.
[236] Y. Shi, M. Osada, Y. Ebina, T. Sasaki, Single Droplet Assembly for Two-Dimensional Nanosheet Tiling, ACS Nano. 14 (2020) 15216–15226. https://doi.org/10.1021/acsnano.0c05434.

[237] C. Diddens, H. Tan, P. Lv, M. Versluis, J.G.M. Kuerten, X. Zhang, D. Lohse, Evaporating pure, binary and ternary droplets: thermal effects and axial symmetry breaking, J. Fluid Mech. 823 (2017) 470–497. https://doi.org/10.1017/jfm.2017.312.
[238] R.D. Deegan, O. Bakajin, T.F. Dupont, G. Huber, S.R. Nagel, T.A. Witten, Capillary flow as the cause of ring stains from dried liquid drops, Nature. 389 (1997) 827–829. https://doi.org/10.1038/39827.

Chapter 2: Syntheses, depositions, and characterization methods

Introduction

This chapter introduces the different experimental techniques for the materials syntheses, deposition, and characterizations used in this work. The first part details the crystal growth methods used to obtain large crystals of the layered phases. The second part describes the nanosheets deposition techniques. Afterward, the morphological and structural characterizations will be presented. Finally, the thin films deposition techniques will be detailed.

1. Powders syntheses, protonation, and exfoliation

1.1. The solid state reaction

The solid state reaction is the most classic technique for material synthesis. The method consists in mixing elements precursors and treating them at high temperature to engender their diffusions to form the desired phase. Many factors can influence the reaction: the chemical and physical properties of the precursors, how they are mixed, their contact surface area, and the reaction conditions [1]. In the case of the layered phases syntheses, the physic properties of the precursors can be problematic, especially for the alkali precursors, which can be very hygroscopic and usually decompose into volatile components below the maximum stage synthesis temperature (between 600 and 900°C for carbonates precursors) [2–4]. It is then important to work with dry chemicals and to add an excess of alkali precursors to allow the reaction to be total and without secondary phases. Intimate mixing of the precursors by manual grinding or ball milling is also needed to avoid the formation of secondary phases. Moreover, it is possible to increase the contact surface area of the precursors to improve the diffusion of the elements by pelletizing the mixed powder. The syntheses were realized in alumina and platinum crucibles. The choice of the crucible is very important as it should remain chemically and thermally stable during the synthesis. The syntheses were realized under

air atmosphere at temperature between 900 and 1200°C [5–8]. The reactivity of the precursors strongly depends on the synthesis temperature. It is thus necessary to make a full study of the reaction as a function of the temperature to find the optimal synthesis temperature to obtain the expected phase.

1.2. The molten salt synthesis

The molten salt synthesis is a type of flux synthesis, which is a method of crystal growth where the reactants are dissolved in a solvent (flux). The molten salt, which has a lower melting temperature than the reactants, is used here as the solvent. The molten salt aims to increase the reaction rate, the homogeneity level between the reactants in the solid solution, to decrease the synthesis temperature, and to control the size and shape of the crystals. During the cooling, particles homogenously nucleate in the liquid and large crystals can be obtained by limiting the nuclei number [9,10]. The molten salts are generally alkali materials (NaCl, KCl, K_2SO_4, KNO_3, …), which can be easily eliminated by dissolution in water after synthesis. These salts are also well known to be very aggressive for crucibles [11]. Therefore, suitable crucibles, generally in platinum, are needed for this type of synthesis. In this work, molten salt syntheses using K_2SO_4 and K_2MoO_4 [12,13], which are detailed in Chapter 3, were realized.

1.3. Protonation of the layered phases

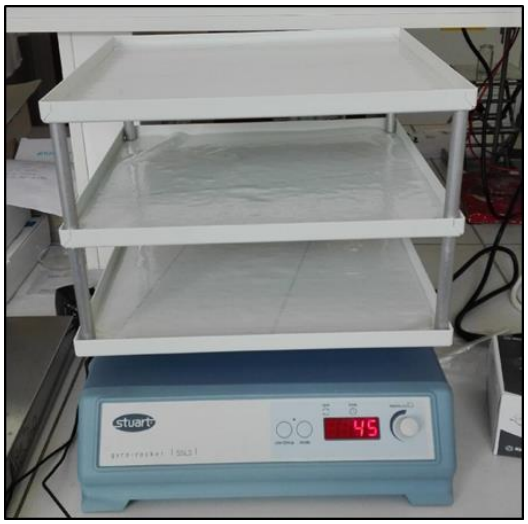

Figure 1.1. Oscillating plate used for the protonation and the exfoliation of the powders.

The protonations of the powders were realized by using 6 M nitric acid. The samples were then agitated 24 hours using an oscillating plate (Figure 2.1). The powder was then decanted and the acid was replaced by fresh one. This step was repeated 3 times. The protonated powder was then filtered and dried in an oven. Specific informations concerning the protonation will be detailed in Chapter 3.

1.4. Liquid exfoliation of the protonated powders

The exfoliations of the protonated phases were realized using tetrabutylammonium hydroxide (TBAOH), *n*-propylamine, and *n*-butylamine. Powder and exfoliant were mixed in a molar ratio 1:1 for an exfoliation with TBAOH and 1:10 for an exfoliation with *n*-propylamine and *n*-butylamine. The conditions will be detailed in Chapter 3.

2. Nanosheets depositions techniques

2.1. The Langmuir-Blodgett technique

The depositions of nanosheets were realized by the Langmuir-Blodgett (LB) technique using a Langmuir-Blodgett KSV Nima trough device. It is composed of a trough filled with the nanosheets solution, with a dipper cavity to fully dive the substrate into the solution. On the sides, two barriers compress the air/liquid interface and densify all the nanosheets together to form a monolayer. A Wilhelmy plate in platinum (tensiometer) measures the surface pressure produced by the nanosheets (Figure 2.2a). The surface pressure Π is obtained by measuring the difference between γ the surface tension of the solvent and γ_0 the surface tension with the nanosheets monolayer:

$$\Pi = \gamma - \gamma_0$$

The surface tension corresponds to the force engendered by the molecular interactions (cohesive forces) at the air/liquid interface to minimize the energy of the system. The high surface tension of water (~73 mN/m at 20°C) makes it the best candidate as a subphase. For a rectangular Wilhelmy plate (Figure 2.2b), the downward force can be calculated using the equation [14]:

$$F = w_p t_p (g\rho_p l_p - g\rho_l h_l + 2\gamma \cos\theta)$$

with l_p, w_p, t_p, and ρ_p the length, width, thickness, and material density of the Wilhelmy plate, immersed to a height h_l in a liquid of density ρ_l, γ the liquid surface tension, θ the contact angle between the liquid phase and the plate, and g the gravitational constant. The surface pressure can then be calculated with the Wilhelmy equation [15], by measuring the variation of F between the clean surface and the surface with a monolayer:

$$\Pi = -\Delta\gamma = \frac{-\Delta F}{2(t_p + w_p)\cos\theta}$$

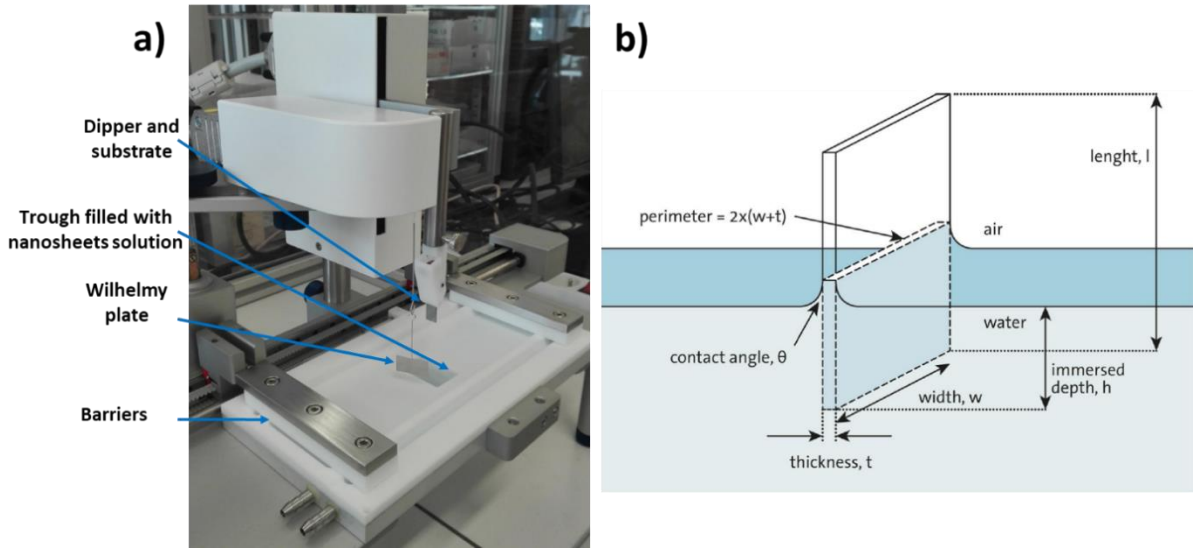

Figure 1.2. (a) Photography of a Langmuir-Blodgett KSV Nima trough device. (b) Wilhelmy plate (figure Biolin Scientific®).

When the solution is poured into the trough, the surface pressure is weakly affected due to too few nanosheets interactions. The substrate is then dipped in the solution. After waiting for 15 mn the balance state of the solution, the barriers movements start to reduce the trough area and the nanosheets at the air/liquid interface get closer, increasing the repulsive forces. The densification of the nanosheets layer can be followed by drawing the surface pressure as a function of the liquid area (isotherm graph, Figure 2.3a). The surface pressure increases when the trough area decreases, until an inflection point which is synonymous with a highly dense layer at the air/liquid interface. When the compression continues after this point, the surface pressure remains constant until a collapse occurs due to nanosheets overlapping [16]. The limit value is thus set on the inflection point, and the barrier will keep that value stable during the process. Then the substrate is lifted up with the nanosheets layer transferred on its surface

(Figure 2.3b). Subsequent heating and/or UV treatments of the samples are necessary to decompose tetrabutylammonium residues [17,18].

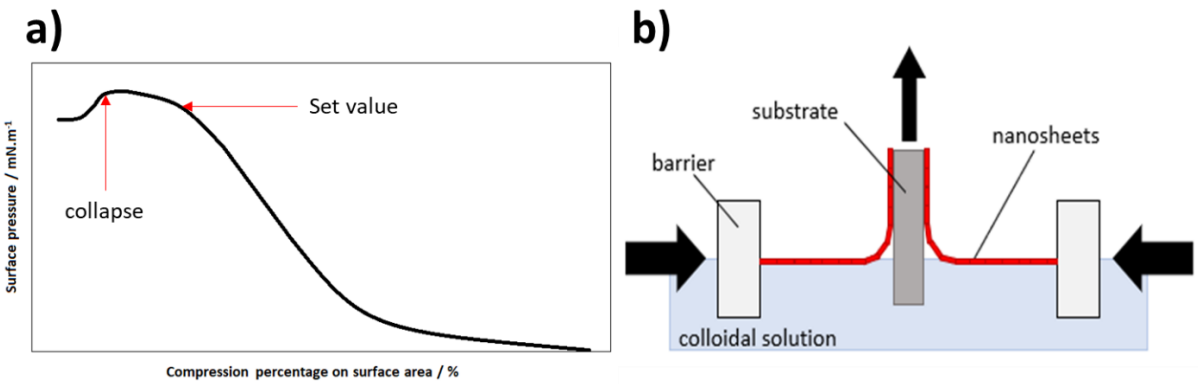

Figure 1.3. (a) LB isotherm (surface pressure as a function of the compression rate on surface area) of $[Ca_2Nb_3O_{10}]^-$ nanosheets. The pressure increase with the compression until a bowing point synonym of a highly dense monolayer of nanosheets. (b) LB deposition process: the substrate goes up with the nanosheets monolayer adsorbed on the surface and the barrier keeps the surface pressure constant during the process.

The LB process is a very sensitive technique. Different parameters can affect the quality of the deposited film. First, it is important to keep the temperature of the subphase constant during the deposition as the viscosity and the surface tension of water are directly related to the temperature. Therefore, the variation of temperature during the deposition directly affects the surface pressure, which is the key parameter of the deposition. Variation of humidity also seems to be an important parameter as it may affect the surface pressure. Some studies on LB organic films show that variation of humidity can affect the properties of the films, and that high humidity decreases the surface pressure [19,20]. This behavior has not been studied on inorganic LB films. However, our experiences have shown that high humidity leads to complicated LB deposition. The LB device also needs to be placed on an antivibration device, to avoid any vibrations which could be caused by the operator or nearby experiments.

2.2. The drop casting method

The drop casting depositions of nanosheets were realized following the method of Shi *et al.* presented in chapter 1 [21]. The depositions were realized using a diluted solution of nanosheets mixed with ethanol, whose parameters are detailed in Chapter 3. The solutions were deposited with a propette on various substrates beforehand heated at 100-120°C on a heating plate. The solutions were deposited and reabsorbed on the

substrate within a low and continuous flow. The substrate is then let on the hot plate for a minute to be completely dried. A UV treatment is also needed for this type of deposition.

3. Morphological and structural characterizations

3.1. X-ray diffraction

X-ray diffraction (XRD) is an essential characterization technique for powders and thin films. XRD characterizations were carried out using a θ–2θ Bragg-Brentano diffractometer (Bruker AXS D8 Advanced, Figure 2.4b) working with a monochromatized Cu $K\alpha_1$ radiation and equipped with a 1D detector LynxEye (192 channels).

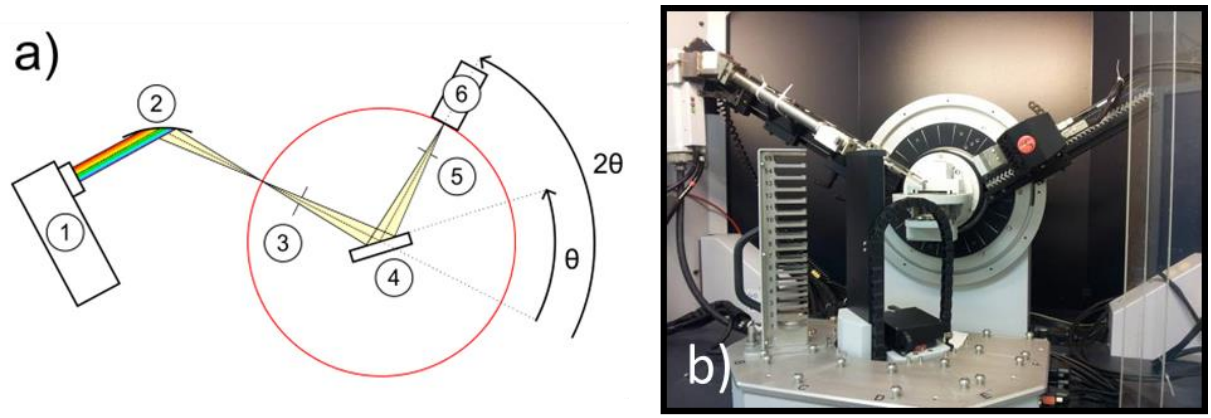

Figure 1.4. (a) Schematic representation of a X-ray diffractometer in Bragg-Brentano geometry. 1) Cu X-ray tube, 2) curved Ge(111) monochromator, 3) divergence slits, 4) sample, 5) divergence slit, and 6) detector. (b) Photography of the Bruker AXS D8 Advanced diffractometer.

The method in θ–2θ configuration consists in measuring the XRD of the *hkl* plans parallel to the sample surface by tilting the sample by an angle θ and the detector by 2θ, while the X-ray tube stays fixed. XRD is based on the constructive interference of X-rays waves emitted from the crystals, determined by the Bragg's law:

$$2.d_{hkl}.\sin\theta = n.\lambda$$

where d_{hkl} is the interplanar spacing of the crystal, θ the diffraction angle, λ the X-ray wavelength, and n an integer.

The technique enables to obtain a diffractogram which is characteristic of the crystallography of the analyzed materials. It is then possible to identify the phases present

in the analyzed powder or the thin film, as well as the preferential orientations of thin films depending on the present peaks.

The preparation and the position of the samples in the diffractometer are primordial. For the powders, the preparation is generally made with cyclohexane to stick the powder on the mount. The height and the flatness of the sample need to be precise to avoid shifts of the diffraction peaks. However, in the case of powders, it is experimentally complicated. Therefore, benchmark materials, which are materials of which the positions of the peaks do not vary, can be used. In this work, hexatriacontane and silicon were used, and the position of the peaks was corrected with the DIFFRAC.EVA software by shifting the diffractogram thanks to the peak of the benchmark material.

3.2. In-plane X-ray diffraction

The in-plane diffraction has been realized at the OSIRIX platform (UMS 2001 CNRS – Rennes 1 University ScanMAT) by Dr Valérie Demange. The experiments were performed with a 5-circles SmartLab Rigaku with Cu $K\alpha_{1,2}$ radiation (λ = 1.5418 Å) and equipped with a HyPix-3000 detector (Figure 2.5).

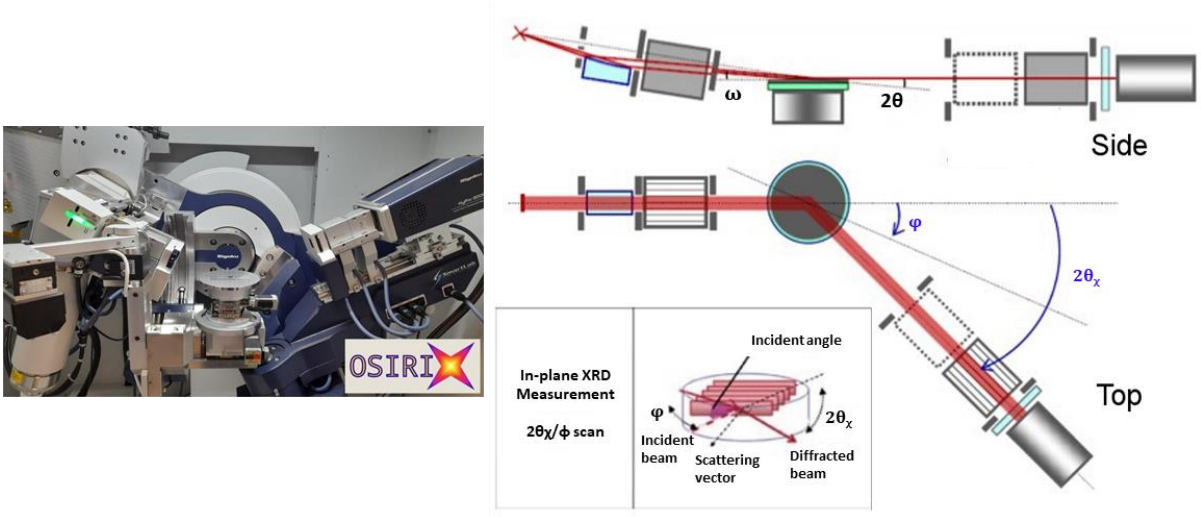

Figure 1.5. On the left, photography of the 5-circles SmartLab Rigaku from the OSIRIX platform. On the right, schematic representation of in-plane diffraction (figure Rigaku®).

The Bragg-Brentano configuration is unadapted for the observation of very low thickness materials (few nanometers). In this work, the in-plane XRD technique has been used to characterize the nanosheets layers deposited on a substrate. In-plane X-ray diffraction is made by positioning the X-ray tube and the detector in such a way that

the incident and diffracted beams are both nearly parallel to the sample surface (Figure 2.5). This position allows the diffraction of the planes nearly perpendicular to the sample surface, which enables to deduce the in-plane lattice parameters of the thin material. The detector is rotated by a $2\theta_\chi$ angle (Figure 2.5), while the substrate is rotated by a φ angle. The diffraction is thus realized in a $2\theta_\chi/\varphi$ configuration and, as the nanosheets are 2D-materials, only 2 Miller indices are attributed to each diffraction peak.

3.3. Scanning electron microscopy

Scanning electron microscopy (SEM) has been realized at the scanning electron microscopy and microanalysis center (CMEBA, UMS 2001 CNRS – Rennes 1 University ScanMAT) by Francis Gouttefangeas and Loïc Joanny. SEM analyses have been performed generally with a field emission gun Jeol JSM 7100F instrument (Figure 2.6a). The technique consists in detecting the secondary electrons produced by the interaction between the electrons beam and the sample surface. This technique enables to observe the morphology and size of the crystals and thin films. The microscope is also equipped with a SDD X-Max 50 mm^2 Oxford Instruments detector to realize energy dispersive X-ray spectroscopy (EDXS). This type of analysis allows the quantification of elements present in the material, with an error percentage from 2 to 10%. EDXS is not precise for light element quantification (below sodium).

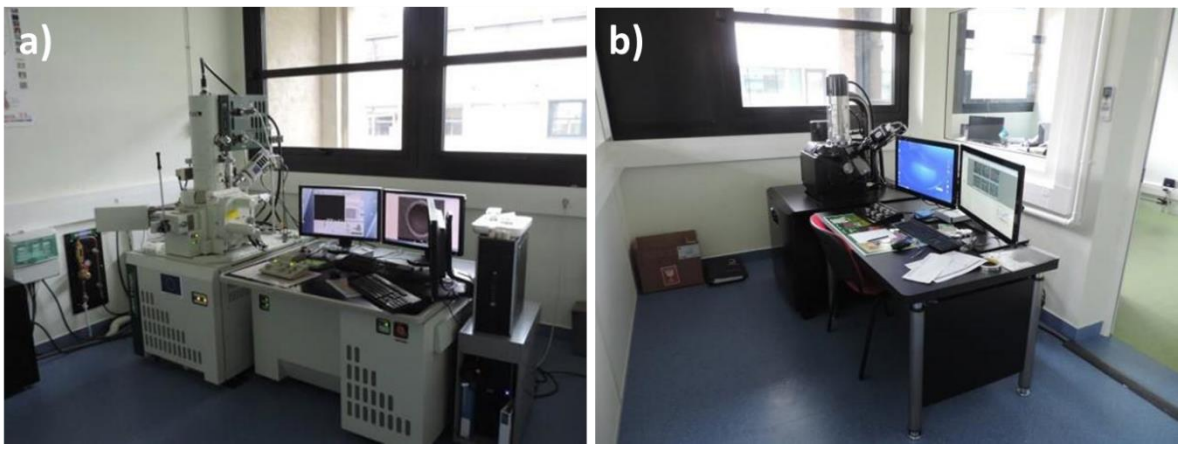

Figure 1.6. Photographs of (a) Jeol JSM 7100 F instrument, (b) Jeol IT 300.

For the observation of powders, metallization has been realized to improve the contrast and the quality of the experiences. For the observation of the nanosheets deposited on insulating substrates such as glass, SEM Jeol IT 300 (Figure 2.6b), can be

used as the sample observation does not need any metallization thanks to low vaccum conditions. This instrument is equipped with a conventional filament electron source.

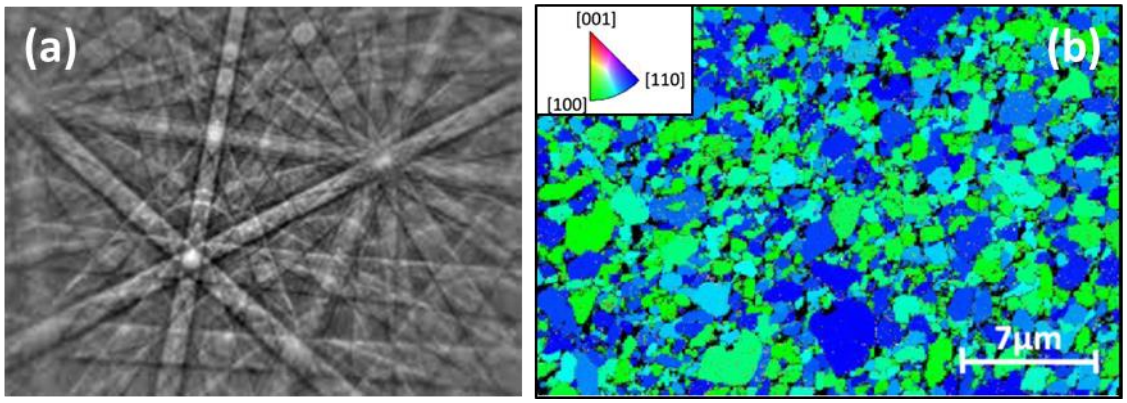

Figure 1.7. (a) Example of Kikuchi bands [22]. Example of an in-plane EBSD map of a $La_{0.67}Sr_{0.33}MnO_3$ thin film deposited on $[Ca_2Nb_3O_{10}]^-$ nanosheets (see Chapter 4) [23].

Electron backscatter diffraction (EBSD) analyses have also been realized on the oxide thin films deposited on the nanosheets. The experiments were realized at the CRISMAT laboratory by Marie Dallochio during her PhD, with a Zeiss Supra 55 (FEG source) SEM equipped with an ultra-sensitive high-resolution detector from Bruker at an accelerating voltage of 15 kV. For this type of experiment, the sample is tilted at an angle of 70°, and the crystallographic planes are diffracted forming Kikuchi bands (Figure 2.7a), characteristics of each plan. The Kikuchi bands can then be indexed using crystallographic databases to deduce the crystal orientations of the films (Figure 2.7b). EBSD is a useful tool as it enables to complete XRD analyses by visualizing the in-plane orientation of the film.

3.4. Transmission electron microscopy

Transmission electron microscopy (TEM) analyses have been realized at the THEMIS platform (UMS 2001 CNRS – Rennes 1 University ScanMAT). The experiments were performed by using a LaB_6 Jeol 2100 instrument (Figure 2.8b). The method consists in passing an electron beam through the sample. The electrons interact with the material and the obtained image is magnified by lens and observed thanks to a fluorescent screen. This technique enables high resolution observations with a precision from 0.2 to 2 Å depending on the microscope resolution. However, the observations are limited to thin samples (< 100 nm) as the absorption of the electrons is strongly correlated to the thickness of the sample.

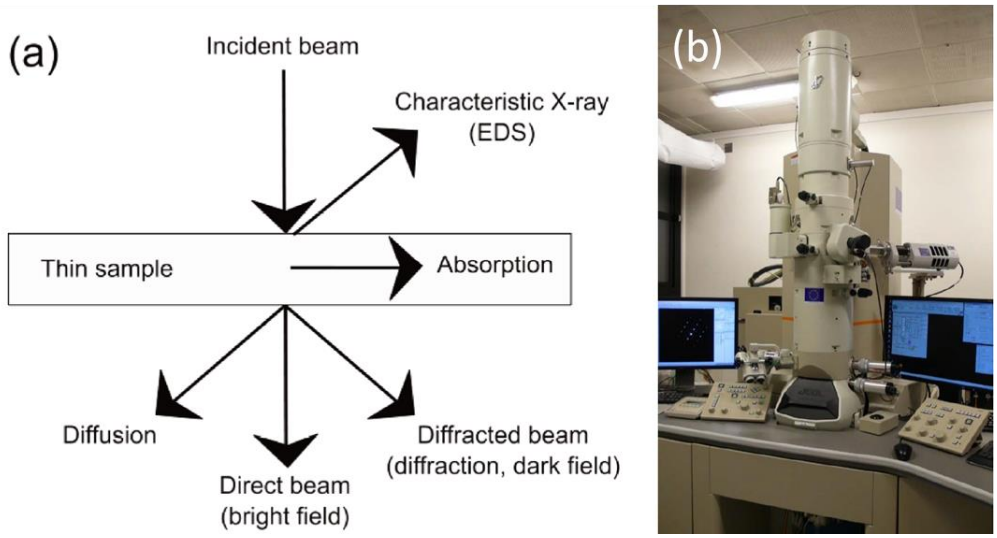

Figure 1.8. (a) Presentation of the different signals induced by the interaction between the electron beam and the sample. (b) Photograph of the LaB_6 Jeol 2100 instrument at ScanMAT UMS.

Bright field mode consists in observing the direct beam through the sample, which induces a contrasted image thanks to the absorption, the scattering of the electrons, and the use of an aperture. This observation mode is the most widely used. It enables to obtain clear images in a short time. High resolution transmission electron microscopy (HRTEM) can also be performed to observe the sample at very high magnification. HRTEM is generally used for lattice structure imaging and to study the homogeneity of the sample (phase transitions, twinning).

TEM can also be used in electron diffraction mode. It enables the determination of the crystal symmetry and the lattice parameters of the material. The images and electron diffraction patterns were recorded using a GATAN Orius SC200D charge coupled device camera and an Ultrascan 1000 camera for HRTEM.

As for SEM, EDXS analysis can also be realized by TEM. TEM-EDXS enables higher precision analyses compared to SEM. This is due to the difference of the electron interaction volume which is correlated to the thickness of the analyzed sample. Therefore, local elemental analysis (areas of 10-20 nm^2) can be realized by TEM-EDXS. EDXS were performed using an Oxford Aztec 80 mm^2 SDD device.

TEM is perfectly adapted for the observation and analysis of nanosheets thanks to their nanometric thicknesses. Nanosheets samples were prepared by dropping a droplet of the diluted colloidal suspensions on an amorphous carbon copper grid (Agar). Powder

samples were prepared by crushing the powder in a mortar in ethanol. Then, a droplet of the obtained suspension was deposited on a TEM grid.

3.5. Atomic force microscopy

The atomic force microscopy (AFM) has been used for the observation of the nanosheets layer on the substrate surface. The experiments were realized by Sophie Ollivier, with a NT-MDT Ntegra microscope equipped with an antivibration device. The technique aims to measure the interaction forces between the sample surface and a tip to generate the topography of the sample. Figure 2.9 shows a simplified schematic representation of AFM. The sample is placed on a support connected to a piezoelectric tube. A tip in silicon with a low stiffness constant and an apex of some nanometers was used for the experiments. This tip is connected to a cantilever which scans the surface of the material. A laser beam measures the vertical movement of the cantilever induced by the interaction between the tip and the surface. The laser signal is then analyzed by a photodetector and the topography of the substrate surface is obtained.

AFM was used in tapping mode, where the tip is vibrating at its resonance frequency. When the tip interacts with the surface, the tip oscillation will decrease depending on the topography. The micrograph is then obtained by measuring the frequency differences of the tip during the scan.

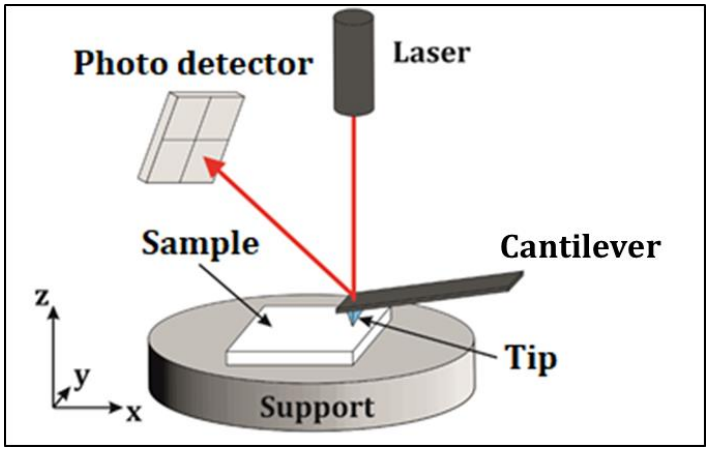

Figure 1.9. Simplified schematic representation of AFM.

This method was used to observe nanosheets deposited on substrates. As the nanosheets are few nanometers thick, the technique is perfectly adapted to their

observation. AFM allows us to measure the thickness and shape of the nanosheets, and the local coverage of the nanosheets layer. It is also useful for the study of the thin films deposited on the nanosheets, to measure the crystal size and their root-mean-square roughness R_{rms}.

3.6. Scanning tunneling microscopy

Scanning tunneling microscopy (STM) is a technique based on the measurement of tunneling current on the material surface. The STM experiments (Figure 2.10) have been realized by Dr Pascal Turban at the Rennes Institute of Physic (IPR). The method consists in placing a metallic tip close to the surface of the material. A voltage is then applied between the tip and the sample which induces tunneling effect. The topography is then obtained by mapping the current intensity as a function of the tip position. A homemade tungsten tip obtained by alkaline attack of a tungsten wire by a sodium hydroxide solution was used for the experiments. The obtained tip is then heated at 900°C to evaporate the tungsten hydroxide at its surface.

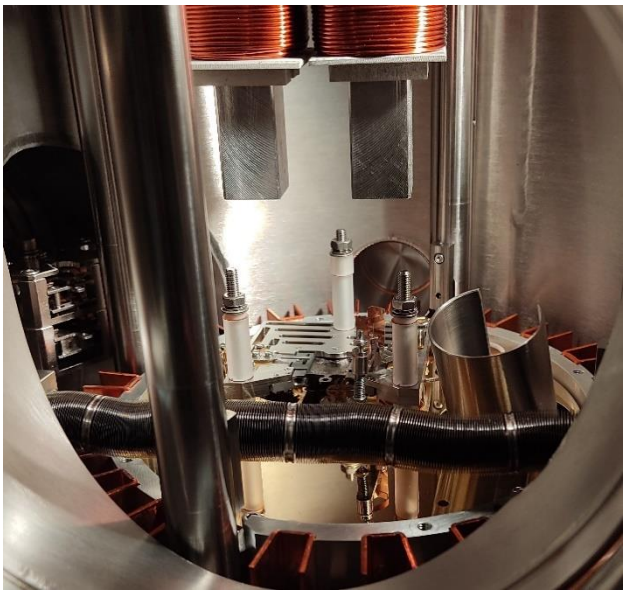

Figure 1.10. Photograph of the STM device of the IPR laboratory.

This technique enables to observe the sample surface with a precision until 0.1 Å. STM was used in this work to observe the evolution of the surface structure of the nanosheets after heating treatment under ultra-high vacuum.

3.7. X-ray photoelectron spectroscopy

X-ray photoelectron spectroscopy (XPS) is a surface analysis technique, where photoelectrons produced by the X-ray irradiation of the material are analyzed. The XPS experiments described in this thesis were realized by Dr Bruno Lépine, Haley Glavina (master trainee), and Dr Pascal Turban from the Rennes Institute of Physic (IPR). A caption photograph is presented Figure 2.11. The surface irradiation leads to the formation of electrons in an excited state, which travel through the material until the surface. The mean free path of an electron until the surface depends on the electron kinetic energy and the nature of the crossed environment. The photoelectrons are then separated depending on their kinetic energy through an electron energy analyzer. An electron detector will then count the electrons of given energy and an energy spectrum is obtained as a function of the detected elements. XPS enables to get the elemental composition of the surface of the material and the oxidation degree of the elements.

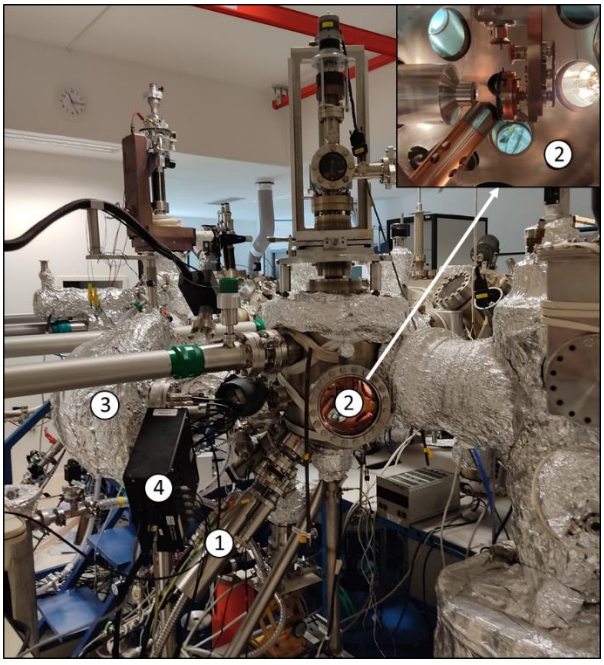

Figure 1.11. Photograph of the XPS device of the IPR laboratory. (1) X-ray tube Mg/Al source, (2) analysis chamber, (3) electron energy analyzer, and (4) electron detector.

XPS is well-adapted for the analysis of nanosheets seed layers as their thicknesses are around some nanometers which is of the order of magnitude of the XPS analysis depth. Studies on the influence of chemical or heat treatments on elements oxidation and nanosheets degradation can be realized.

4. Thin films depositions

4.1. Pulsed laser deposition

The pulsed laser deposition (PLD) is a thin film deposition technique that consists in stricking a ceramic target, containing the elements to deposit, with a high energy laser inside a vacuum chamber. The elements are then vaporized with a high energy, forming a plasma with a plume shape, which will be deposited on a heated substrate placed in front of the target (Figure 2.12). The latter is obtained by solid state reaction and densified by cold uniaxial pressure followed by a heating treatment. Different parameters can affect the quality and the composition of the films: the laser energy, the fluence (energy of the pulse per target surface unit), the pulse frequency of the laser, the target density and composition, the distance between the target and the substrate, the substrate (nature and thickness), the substrate temperature, and the background gas partial pressure.

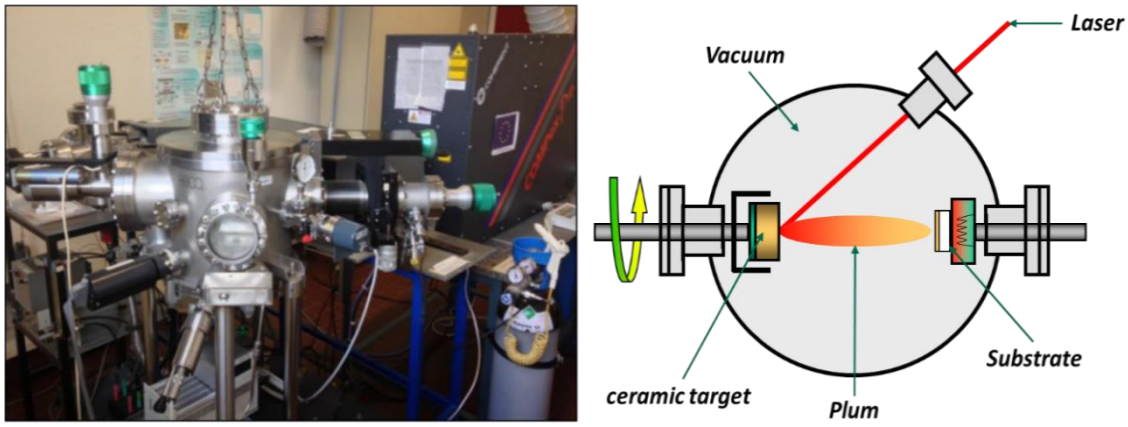

Figure 1.12. Photograph of the PLD device and illustration of the technique.

The technique offers a high deposition reproducibility. The PLD is also perfectly adapted for the deposition of complex materials thanks to a precise control of the composition. However, for volatile elements (alkaline, alkaline earth), an excess is needed in the target to counterbalance their loss during the deposition.

The $KNbO_3$ thin films deposited at the ISCR laboratory were prepared by ablating the ceramic target with a KrF excimer laser (Figure 2.12, Coherent company, pulse duration 20 ns, λ = 248 nm) set at energy: 225 mJ, fluence: 2–3 $J.cm^{-2}$, and a 2 Hz frequency. The films were grown at a substrate-target distance from 50 to 60 mm under 30 Pa oxygen partial pressure. A K-enriched $KNbO_3$ target was used for the deposition.

The PLD depositions of $La_{0.67}Sr_{0.33}MnO_3$ (LSMO), $SrVO_3$ (SVO), and $CaVO_3$ (CVO) at the CRISMAT and GEMaC laboratories were realized by Prof. Bernard Mercey and Dr Bruno Bérini with a KrF excimer laser (λ = 248 nm) with a repetition rate between 2 Hz for LSMO and 3 Hz for SVO and CVO. The laser fluence was adjusted at 1.6 $J.cm^{-2}$ to obtain a deposition rate close to 0.1 Å per laser pulse. The LSMO deposition was carried out under oxygen–ozone mixture conditions [24], with a deposition pressure of 5×10^{-4} mbar. For SVO and CVO, $Sr_2V_2O_7$ and $Ca_2V_2O_7$ polycrystalline targets, prepared by standard solid-state reaction, were used. As the perovskite structure is not the most stable one in the Ca(Sr)-V-O system [25,26], the depositions were carried out under vacuum, *i.e.* in reductive conditions, to reach the perovskite phase of the vanadate films.

4.2. Radio frequency magnetron sputtering

Radio frequency (RF) magnetron sputtering depositions were realized by Jacques Manguele (PhD student) at the CRISMAT laboratory in Caen. The method consists in accelerating argon (Ar) ions by applying an RF electric field. A plasma composed of Ar^+ is then created and to hit the negatively charged target of the material to deposit. The atoms of the target are then sputtered on a substrate placed in front of the target.

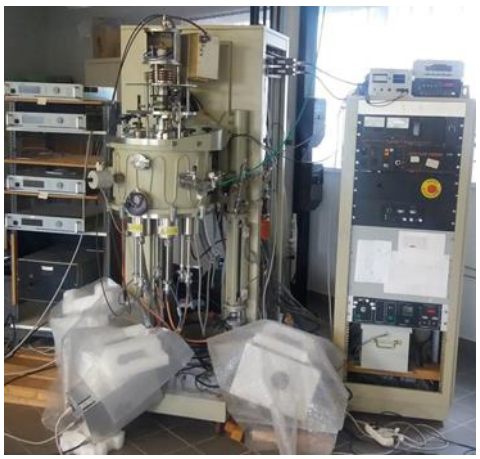

Figure 1.13. RF magnetron sputtering device of the CRISMAT laboratory.

Magnetron sputtering is generally used for the deposition of metals or conductive materials. However, it is also possible to deposit other materials such as insulators thanks to the RF voltage which greatly decreases the deposition time in association with a magnetron. This technique is widely used in industry as it allows uniform deposition on large areas.

4.3. Chemical solution deposition

The chemical solution deposition (CSD) consists of the deposition of a chemical solution (so-called a resin) on a substrate prior to heating treatments at high temperature to create a crystallized homogenous film. The CSD depositions presented in this thesis were performed by Dr Valérie Bouquet. The solutions were synthesized by the Pechini process, which is a related sol-gel synthesis [27]. The synthesis of the gel consists in mixing citric acid with metallic precursor(s) to obtain the metallic citrate (Figure 2.14). The solution is then mixed with ethylene glycol and a reaction of polycondensation occurs leading to a polymer with an ester function. The viscosity of the obtained polymeric resin needs to be adjusted by controlling the water content (by addition or evaporation of water). The solutions were then spin coated using a Spin 150 SPS Europe (Figure 2.14) to obtain thin and homogenous films on the desired substrate. The films were then thermally treated: a first treatment is needed to eliminate the organic resin (pyrolysis), and a final one to crystallize the deposited film (calcination).

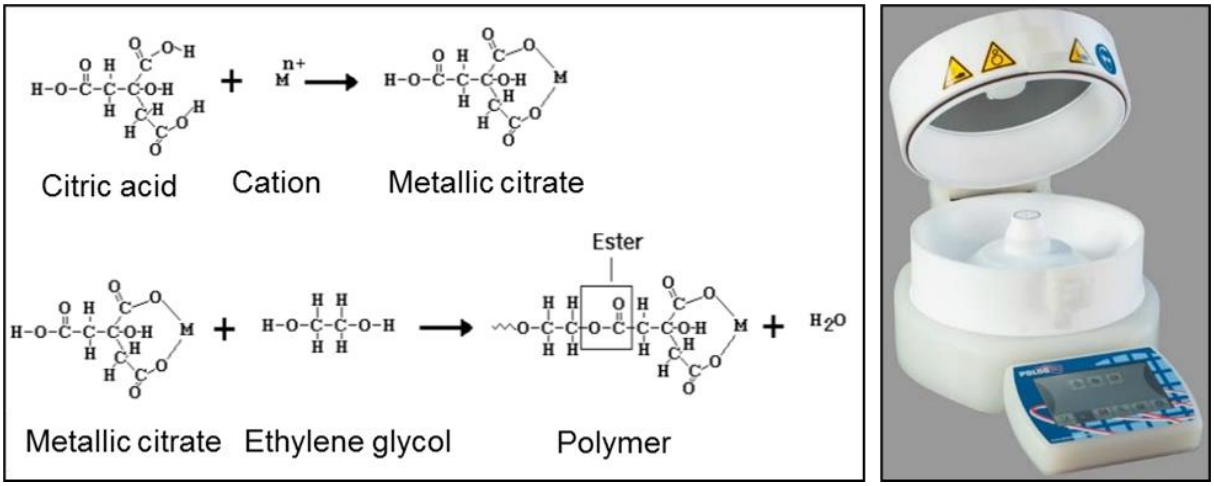

Figure 1.14. On the left, a summary of the Pechini reaction, and on the right is a photograph of the Spin 150 SPS Europe spin coater.

This method enables direct and precise control of the stoichiometry of complex systems at relatively low temperature. Furthermore, this technique has shown to provide great reproducibility and homogeneity for thin films deposition.

References

[1] S.-J. Cho, M.-J. Uddin, P. Alaboina, Review of Nanotechnology for Cathode Materials in Batteries, in: Emerg. Nanotechnologies Recharg. Energy Storage Syst., Elsevier, 2017: pp. 83–129. https://doi.org/10.1016/B978-0-323-42977-1.00003-0.

[2] R.L. Lehman, J.S. Gentry, N.G. Glumac, Thermal stability of potassium carbonate near its melting point, Thermochim. Acta. 316 (1998) 1–9. https://doi.org/10.1016/S0040-6031(98)00289-5.

[3] H.-H. Liao, L.-M. Chen, Z. Xu, G. Li, Y. Yang, Highly efficient inverted polymer solar cell by low temperature annealing of Cs_2CO_3 interlayer, Appl. Phys. Lett. 92 (2008) 173303. https://doi.org/10.1063/1.2918983.

[4] T. Yoon, M.S. Milien, B.S. Parimalam, B.L. Lucht, Thermal Decomposition of the Solid Electrolyte Interphase (SEI) on Silicon Electrodes for Lithium Ion Batteries, Chem. Mater. 29 (2017) 3237–3245. https://doi.org/10.1021/acs.chemmater.7b00454.

[5] T. Sasaki, F. Kooli, M. Iida, Y. Michiue, S. Takenouchi, Y. Yajima, F. Izumi, B.C. Chakoumakos, M. Watanabe, A mixed alkali metal titanate with the lepidocrocite-like layered structure. Preparation, crystal structure, protonic form, and acid-base intercalation properties, Chem. Mater. 10 (1998) 4123–4128. https://doi.org/10.1021/cm980535f.

[6] Y. Ebina, Study on exfoliation of layered perovskite-type niobates, Solid State Ion. 151 (2002) 177–182. https://doi.org/10.1016/S0167-2738(02)00707-5.

[7] M.A. Bizeto, D.L.A. De Faria, V.R.L. Constantino, Porphyrin intercalation into a layered niobate derived from K4Nb6O17, J. Mater. Sci. 37 (2002) 265–270. https://doi.org/10.1023/A:1013687825874.

[8] K. Fukuda, K. Akatsuka, Y. Ebina, R. Ma, K. Takada, I. Nakai, T. Sasaki, Exfoliated Nanosheet Crystallite of Cesium Tungstate with 2D Pyrochlore Structure: Synthesis, Characterization, and Photochromic Properties, ACS Nano. 2 (2008) 1689–1695. https://doi.org/10.1021/nn800184w.

[9] K.H. Yoon, Y.S. Cho, D.H. Kang, Molten salt synthesis of lead-based relaxors, J. Mater. Sci. 33 (1998) 2977–2984. https://doi.org/10.1023/A:1004310931643.

[10] E. A., Y. S., V. V., Advanced Ceramic Target Materials Produced by Self-Propagating High-Temperature Synthesis for Deposition of Functional Nanostructured Coatings - Part 1: Four Elements and Less Systems, in: C. Sikalidis (Ed.), Adv. Ceram. - Synth. Charact. Process. Specif. Appl., InTech, 2011. https://doi.org/10.5772/38904.

[11] K. Sridharan, T.R. Allen, Corrosion in Molten Salts, in: Molten Salts Chem., Elsevier, 2013: pp. 241–267. https://doi.org/10.1016/B978-0-12-398538-5.00012-3.

[12] T. Tanaka, K. Fukuda, Y. Ebina, K. Takada, T. Sasaki, Highly Organized Self-Assembled Monolayer and Multilayer Films of Titania Nanosheets, Adv. Mater. 16 (2004) 872–875. https://doi.org/10.1002/adma.200306470.

[13] H. Yuan, M. Nguyen, T. Hammer, G. Koster, G. Rijnders, J.E. ten Elshof, Synthesis of $KCa_2Nb_3O_{10}$ Crystals with Varying Grain Sizes and Their Nanosheet Monolayer Films As Seed Layers for PiezoMEMS Applications, ACS Appl. Mater. Interfaces. 7 (2015) 27473–27478. https://doi.org/10.1021/acsami.5b09456.

[14] C.D. Volpe, S. Siboni, The Wilhelmy method: a critical and practical review, Surf. Innov. 6 (2018) 120–132. https://doi.org/10.1680/jsuin.17.00059.

[15] L. Wilhelmy, Ueber die Abhängigkeit der Capillaritäts-Constanten des Alkohols von Substanz und Gestalt des benetzten festen Körpers, Ann. Phys. Chem. 195 (1863) 177–217. https://doi.org/10.1002/andp.18631950602.

[16] H. Yuan, M. Timmerman, M. van de Putte, P. Gonzalez Rodriguez, S. Veldhuis, J.E. ten Elshof, Self-Assembly of Metal Oxide Nanosheets at Liquid–Air Interfaces in Colloidal Solutions, J. Phys. Chem. C. 120 (2016) 25411–25417. https://doi.org/10.1021/acs.jpcc.6b07961.

[17] A.P. Dral, D. Dubbink, M. Nijland, J.E. ten Elshof, G. Rijnders, G. Koster, Atomically Defined Templates for Epitaxial Growth of Complex Oxide Thin Films, J. Vis. Exp. (2014) 52209 . https://doi.org/10.3791/52209.

[18] B.-W. Li, M. Osada, T.C. Ozawa, Y. Ebina, K. Akatsuka, R. Ma, H. Funakubo, T. Sasaki, Engineered Interfaces of Artificial Perovskite Oxide Superlattices *via* Nanosheet Deposition Process, ACS Nano. 4 (2010) 6673–6680. https://doi.org/10.1021/nn102144s.

[19] W. Fatani, R.A. Fouracre, The effect of humidity on Langmuir-Blodgett films of phosphatidic acid (DPPA) and stearic acid (SA), in: IEEE 1997 Annu. Rep. Conf. Electr. Insul. Dielectr. Phenom., IEEE, Minneapolis, MN, USA, 1997: pp. 263–266. https://doi.org/10.1109/CEIDP.1997.634609.

[20] H.C. Kim, Y.H. Choi, W. Bu, M. Meron, B. Lin, Y.-Y. Won, Increased humidity can soften glassy Langmuir polymer films by two mechanisms: plasticization of the polymer material, and suppression of the evaporation cooling effect, Phys. Chem. Chem. Phys. 19 (2017) 10663–10675. https://doi.org/10.1039/C7CP00785J.
[21] Y. Shi, M. Osada, Y. Ebina, T. Sasaki, Single Droplet Assembly for Two-Dimensional Nanosheet Tiling, ACS Nano. 14 (2020) 15216–15226. https://doi.org/10.1021/acsnano.0c05434.
[22] A. Winkelmann, T.B. Britton, G. Nolze, Constraints on the effective electron energy spectrum in backscatter Kikuchi diffraction, Phys. Rev. B. 99 (2019) 064115. https://doi.org/10.1103/PhysRevB.99.064115.
[23] A. Boileau, M. Dallocchio, F. Baudouin, A. David, U. Lüders, B. Mercey, A. Pautrat, V. Demange, M. Guilloux-Viry, W. Prellier, A. Fouchet, Textured Manganite Films Anywhere, ACS Appl. Mater. Interfaces. 11 (2019) 37302–37312. https://doi.org/10.1021/acsami.9b12209.
[24] B. Mercey, A. David, O. Copie, W. Prellier, Monitoring the growth of $SrTiO_3$ and $La_{0.66}Sr_{0.33}MnO_3$ thin films using a low-pressure Reflection High Energy Electron Diffraction system, Phys. B Condens. Matter. 503 (2016) 100–105. https://doi.org/10.1016/j.physb.2016.09.023.
[25] J. Macías, A.A. Yaremchenko, J.R. Frade, Redox transitions in strontium vanadates: Electrical conductivity and dimensional changes, J. Alloys Compd. 601 (2014) 186–194. https://doi.org/10.1016/j.jallcom.2014.02.148.
[26] B. Bérini, V. Demange, M. Bouttemy, E. Popova, N. Keller, Y. Dumont, A. Fouchet, Control of High Quality $SrVO_3$ Electrode in Oxidizing Atmosphere, Adv. Mater. Interfaces. 3 (2016) 1600274. https://doi.org/10.1002/admi.201600274.
[27] L. Dimesso, Pechini Processes: An Alternate Approach of the Sol–Gel Method, Preparation, Properties, and Applications, in: L. Klein, M. Aparicio, A. Jitianu (Eds.), Handb. Sol-Gel Sci. Technol., Springer International Publishing, Cham, 2016: pp. 1–22. https://doi.org/10.1007/978-3-319-19454-7_123-1.

Chapter 3: Syntheses, depositions, and characterization of nanosheets

Introduction

This chapter presents the different syntheses, depositions, and characterizations of nanosheets realized during this thesis. The nanosheets were picked as a function of their 2D lattice, to allow the growth of perovskites along their (100), (110), and (111) orientations: $[Ca_2Nb_3O_{10}]^-$ (2D square lattice) for the (100) orientation, $[K_{4-x}Nb_6O_{17}]^{x-}$ and $[Ti_{0.87}O_2]^{0.52-}$ (2D rectangular lattice) for the (110) orientation, and $[Cs_4W_{11}O_{36}]^{2-}$ (2D hexagonal lattice) for the (111) orientation. XRD, SEM, and TEM analyses were systematically realized after synthesis, protonation, and exfoliation of the lamellar phases. AFM was also systematically used for the observation of the nanosheets on substrates.

The first part describes the synthesis of the $[Ca_2Nb_3O_{10}]^-$ nanosheets, obtained by the protonation and the exfoliation of $KCa_2Nb_3O_{10}$, synthesized by solid state reaction and molten salt synthesis. The nanosheets were then deposited on various substrates by the Langmuir-Blodgett method and by the drop casting technique. XPS and STM experiments have been realized on these nanosheets to study the crystalline surface structure stability after thermal and HF treatments.

The next part develops the synthesis of the $[K_{4-x}Nb_6O_{17}]^{x-}$ nanosheets, obtained by the protonation and exfoliation of $K_4Nb_6O_{17}$, synthesized by solid state reaction. Different exfoliants have been used to obtain the nanosheets and to avoid the formation of nanoscrolls. The nanosheets were then deposited on various substrates by the Langmuir-Blodgett method and by the drop casting technique.

Then, the syntheses of the $[Ti_{0.87}O_2]^{0.52-}$ nanosheets will be detailed. These nanosheets were obtained by the protonation and the exfoliation of the $K_{0.8}Ti_{1.73}Li_{0.27}O_4$ phase, synthesized by solid state reaction and molten salt synthesis. The nanosheets were then deposited on various substrates by the drop casting technique.

The last part of the chapter reports the synthesis of the $[Cs_4W_{11}O_{36}]^{2-}$ nanosheets, obtained by the protonation and the exfoliation of the $Cs_6W_{11}O_{36}$ phase, synthesized by solid state reaction. The nanosheets were then deposited on various substrates by the Langmuir-Blodgett method and by the drop casting technique. STM experiments have been realized to study the thermal stability of the crystalline surface structure of this type of nanosheets.

Some attempts of $[MnO_2]^{\delta-}$ syntheses have also been realized during this thesis. A brief description of the syntheses realized will be presented.

1. Synthesis, deposition, and characterizations of $[Ca_2Nb_3O_{10}]^-$ nanosheets

1.1. Synthesis of $KCa_2Nb_3O_{10}$ Dion-Jacobson phase

1.1.1. Synthesis of $KCa_2Nb_3O_{10}$ by solid state reaction

The $KCa_2Nb_3O_{10}$ powder (KCN) was firstly synthesized by solid-state reaction(SRR). K_2CO_3 (Acros Organics, 99%), $CaCO_3$ (R.P. Normapur, 99.5%) and Nb_2O_5 (Alfa Aesar, 99.5%) precursors (K:Ca:Nb = 1.15:4:3) were ball-milled in ethanol for 5 h. An excess of K_2CO_3 was needed in order to counterbalance the potassium loss caused by the volatility of K_2O formed at high temperature. 15% of excess was found to give the best result without any secondary phases. After ball milling, the powder was uniaxially pressed and treated for 10 h at 1100°C. The obtained pellet was placed in distilled water and softly crushed. The powder was filtered and dried resulting in a yellowish $KCa_2Nb_3O_{10}$ powder. The XRD patterns are shown in Figure 3.1.

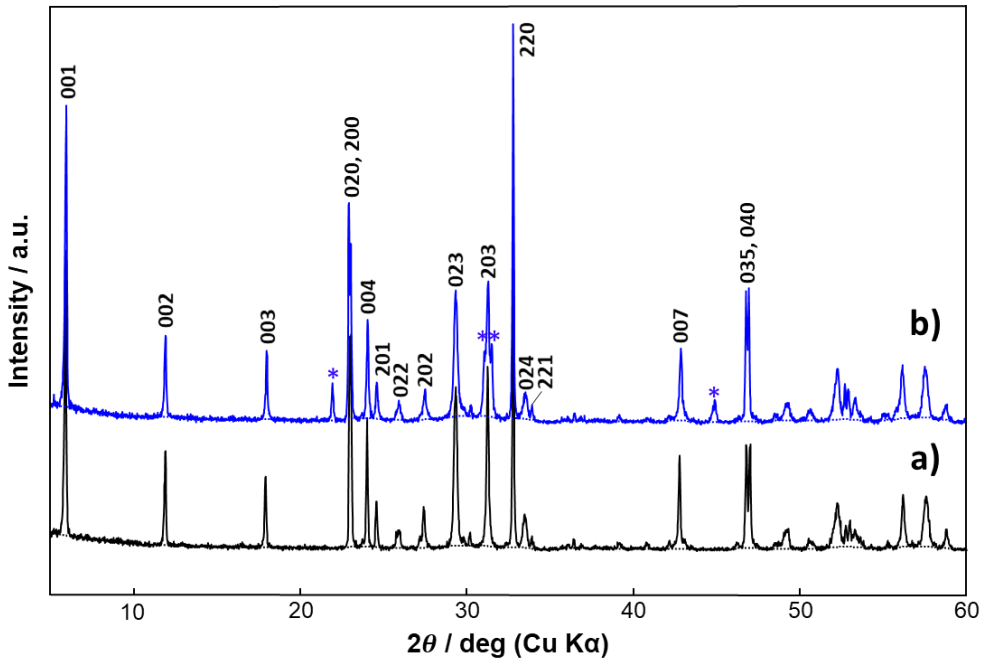

Figure 3.1. XRD diagrams of the KCN powder: (a) synthesis with an excess of 15% of K_2CO_3. (b) Synthesis with an excess of 30% of K_2CO_3. *: $KNbO_3$ phase.

The XRD pattern Figure3.1a shows KCN synthesized with an excess of 15% of K_2CO_3. Pure KCN has been obtained (Powder Diffraction Standards (JCPDS) card N°01–075–9853, Annexe A p.187) for this synthesis. A too large excess of K_2CO_3 leads to the formation of $KNbO_3$, as shown in Figure3.1b with an excess of 30% of K_2CO_3.

Figure 3.2 displays the SEM micrographs of the pure KCN powder. Layered crystals with a lateral size between 1 to 5 µm have been obtained. SEM-EDXS analyses show a crystals composition of $K_{1\pm0.2}Ca_{2\pm0.2}Nb_{3\pm0.3}O_x$.

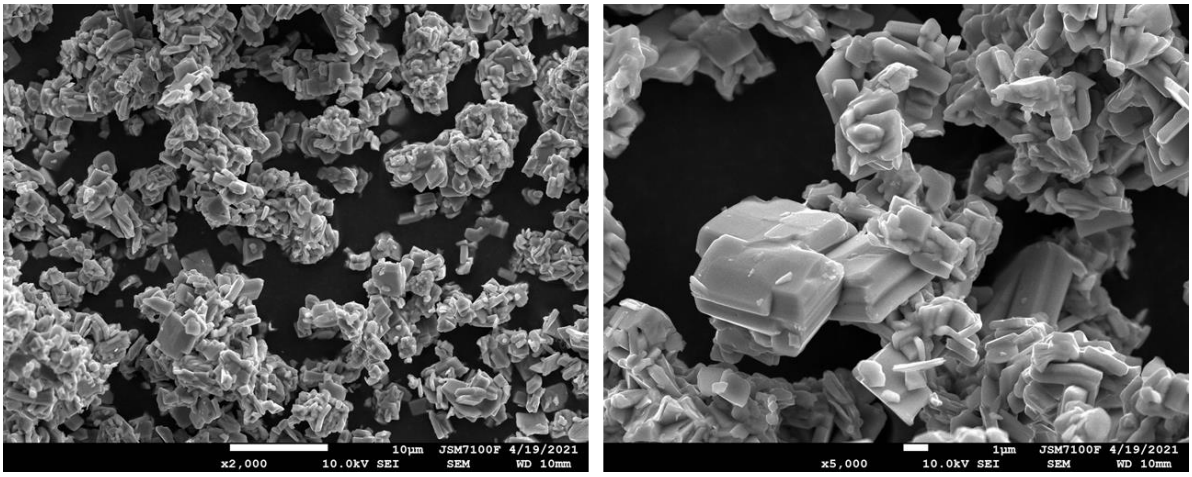

Figure 3.2. SEM micrographs of the KCN phase. Crystals with lateral sizes between 1 and 5 µm are obtained.

TEM experiments have also been realized on KCN crystals. Figure 3.3a shows the [001] zone axis selected-area electron diffraction pattern (EDP), which corresponds to the normal of the NS surface of two crystals plates of KCN. In the first EDP, the {*h*00} and {0*k*0} reflections, with odd *h* and *k* (labeled by arrows in the figure), are present with a weak intensity as expected for the monoclinic structure [1]. Most of the analyzed crystals present a similar EDP. In the second EDP (Figure 3.3b), these reflections are absent indicating a change of octahedral tilt for some crystals, which results in either a large ($a \simeq 7.8$ Å, with extinctions) or a smaller ($a \simeq 3.9$ Å) tetragonal cell. These results confirm that the structure of KCN is monoclinic and not orthorhombic as it is usually presented in the majority of the publications on this phase [2,3]. The composition of KCN powder was found to be around $K_{1.1\pm0.1}Ca_{2.1\pm0.2}Nb_{3\pm0.3}O_x$ by TEM-EDXS, which is consistent with SEM-EDXS analyses results.

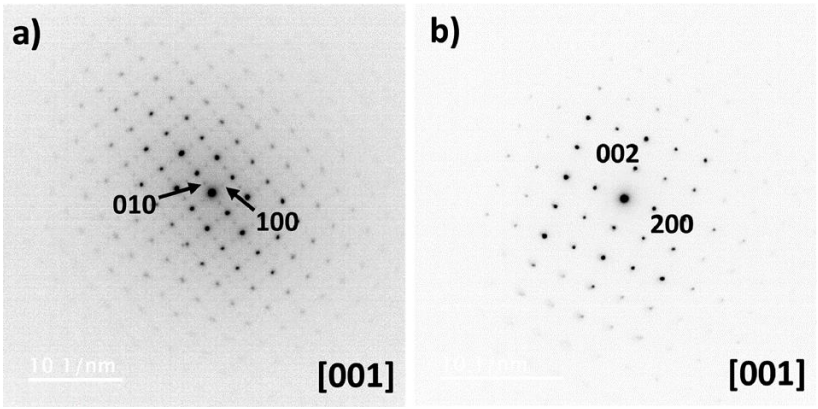

Figure 3.3. (a) EDP along the [001] zone axis of the monoclinic KCN phase. (b) EDP of the KCN phase along the [001] zone axis of a second crystal.

1.1.2. Synthesis of $KCa_2Nb_3O_{10}$ by molten salt synthesis

As described previously, the solid-state reaction of KCN leads to crystals with a maximum lateral size of 5 µm, which is also limiting the size of the nanosheets after exfoliation and may affect the properties of the subsequently grown film. As described in Chapter 2, the molten salt synthesis (MSS) is an efficient method to grow large crystals. The MSS of KCN has been developed by Yuan *et al.* [4,5], based on the work of Tanaka *et al*. who used the K_2MoO_4 salt for the growth of layered titanate phase (see Chapter 1, Figure 1.11.a), obtaining millimetric crystals [6]. Yuan *et al.* have used in their work the K_2SO_4 and K_2MoO_4 molten salts, which lead to an average crystals size of 8 µm (up to 20 µm) and 20 µm (up to 100 µm) respectively.

The general equations of these reactions are detailed below:

$$K_2CO_3 + 4CaCO_3 + 3Nb_2O_5 + 10K_2SO_4 \rightarrow 2KCa_2Nb_3O_{10} + 4CO_2 + 10K_2SO_4 \quad (1)$$

$$11K_2CO_3 + 4CaCO_3 + 3Nb_2O_5 + 10MoO_3 \rightarrow 2KCa_2Nb_3O_{10} + 15CO_2 + 10K_2MoO_4 \quad (2)$$

For these syntheses, K_2CO_3 (Acros Organics, 99%), $CaCO_3$ (R.P. Normapur, 99.5%), and Nb_2O_5 (Alfa Aesar, 99.5%) precursors (K:Ca:Nb = 1.1:4:3) were ball-milled in ethanol for 5 h. The resulting powder was dried and the flux material K_2SO_4 (Alfa Aesar, 99%) or K_2MoO_4 (formed *in situ* by the reaction of K_2CO_3 + MoO_3 (Alfa Aesar, 99.95%)) were added in a molar ratio 10:1. The powders were mixed softly together in a mortar for 5 mn and were then placed in an alumina crucible. As the heating treatment was not fully detailed in the literature, many syntheses have been realized 1) to obtain the expected phase without any secondary phases, 2) to obtain large and homogenous KCN crystals. Good results were obtained by heating the mixture at 1150°C for 30 min, and then slowly cooled down to 950°C at a speed of 4°C/hour for 37h30. The powders were then naturally cooled at room temperature and were washed 3 times in 250 mL of water to remove the flux salts.

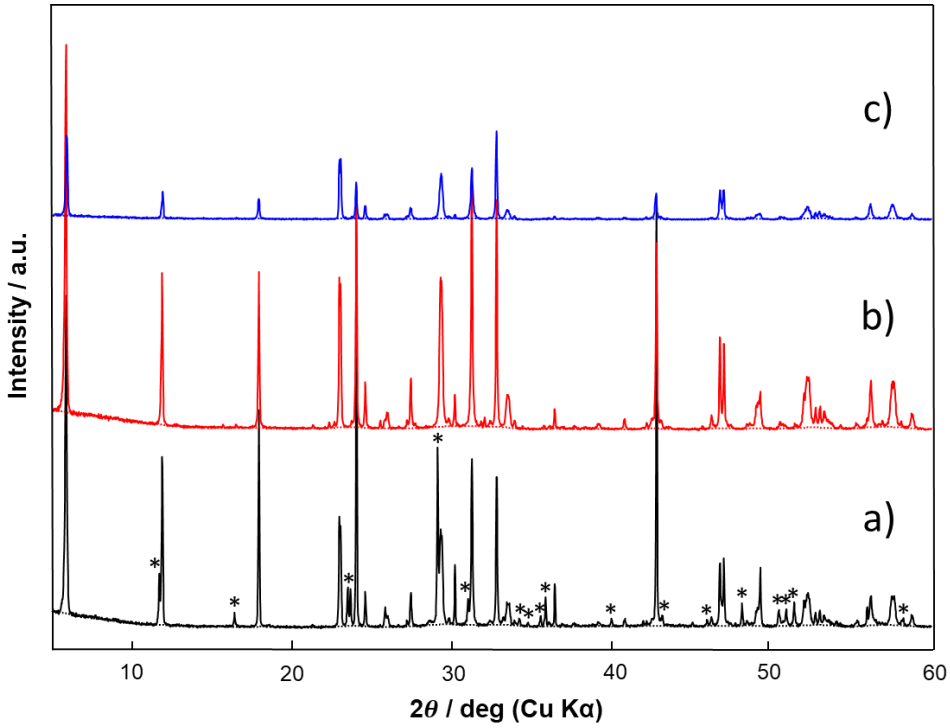

Figure 3.4. XRD diagram of KCN obtained by (a) K_2MoO_4 molten salt synthesis, (b) K_2SO_4 molten salt synthesis, (c) solid-state reaction for comparison. *: $CaNb_2O_6$ phase.

The XRD patterns of KCN synthesized by MSS are displayed in figure 3.4. The first results show that KCN obtained by the two MSS have a higher crystallinity than KCN obtained by solid-state reaction. However, a secondary phase, $CaNb_2O_6$ (JCPDS card N°00–039–1392, Annexe A, p. 188), was also obtained with the K_2MoO_4 MSS, showing a lack of potassium in the reaction. $CaNb_2O_6$ is only present in trace in the K_2SO_4 MSS.

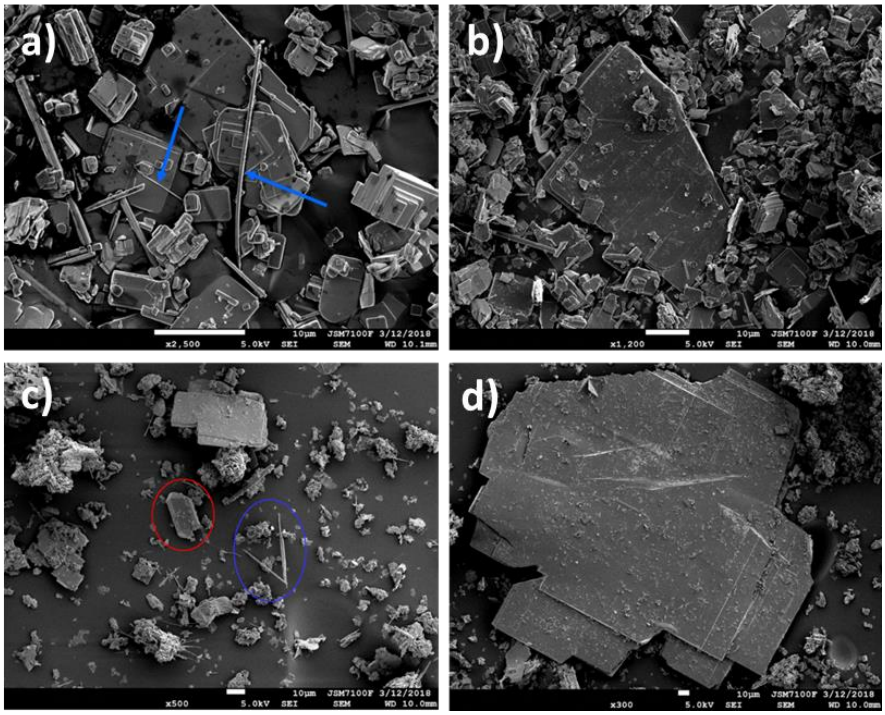

Figure 3.5. SEM micrographs of KCN obtained by MSS. (a-b) KCN crystals obtained by K_2SO_4 MSS. In (a), the blue arrows show the supposed $K_6Nb_{10.8}O_{30}$ crystals. The crystals have an average size of 10 µm, up to 50 µm for the largest crystals, as shown in micrograph (b). (c-d) KCN crystals obtained by K_2MoO_4 MSS. In (c), a $CaNb_2O_6$ crystal is circled in red and $K_6Nb_{10.8}O_{30}$ crystals are circled in blue. The KCN crystals have an average size of 10-20 µm, up to 500 µm for the largest crystals, as shown in micrograph (d).

SEM micrographs of these powders are displayed in Figure 3.5. For the K_2SO_4 MSS (Figure 3.5a), it can be observed well-formed KCN crystals of homogenous lateral size with an average of 10 µm. Figure 3.5b shows a large KCN crystal of 50 µm obtained with K_2SO_4 salt, which is the biggest size obtained for this synthesis. The blue arrows on micrograph 3.5a show very thin needle-like crystals, which could correspond to the $K_6Nb_{10.8}O_{30}$ phase [7,8]. This phase has also been observed by XRD in some samples, with very low-intensity peaks (JCPDS N°01-070–5051, Annexe A, p. 190), while on SEM images, the samples were full of needles. It can be explained by the fact that these needles are so thin (0.1 to 1 µm large) that their diffraction is limited. However, their presence in the presented samples is very limited. In Figure 3.5c is displayed the micrograph of the powder obtained with K_2MoO_4 salt. A $CaNb_2O_6$ crystal is shown in red, while some

$K_6Nb_{10.8}O_{30}$ crystals are shown in blue. $CaNb_2O_6$ crystals can reach dozens of micrometers. EDXS measurements confirm that the red circled crystal corresponds to the $CaNb_2O_6$ phase, while it is more difficult to confirm that the needle crystals correspond to the $K_6Nb_{10.8}O_{30}$ phase, due to their thin thickness. Otherwise, heterogenous crystal size is obtained with this salt, from some micrometers to hundreds of micrometers, as shown in Figure 3.5d.

To summary, larger KCN crystals have been obtained from the MSS. However, secondary phases have been obtained. A study (not described in this thesis) to determine the ideal excess of potassium needed to obtain the pure phase has been realized. The pure KCN phase was obtained with 13% of K_2CO_3 excess. With an excess higher than 13%, $KNbO_3$ is obtained as secondary phase. The secondary phases obtained by varying the excess of potassium in the MSS are summarized in Table 3.1. Otherwise, KCN crystals obtained with K_2SO_4 salt have shown to be homogenous in size and well-crystallized, but reaching a limited crystal size of 50 µm, while KCN crystals obtained with K_2MoO_4 salt have shown to be heterogeneous in size but reaching much higher crystal size (> 500 µm).

Table 3.1. Summary of the secondary phases obtained by varying the excess of potassium in the molten salt syntheses.

Amount of potassium (K)	**Lack of K**	**Ideal amount of K (± 13 %)**	**Excess of K**
Secondary phases obtained	$CaNb_2O_6$ $K_6Nb_{10.8}O_{30}$	$K_6Nb_{10.8}O_{30}$ (SEM) not detectable by XRD	$KNbO_3$ $K_6Nb_{10.8}O_{30}$

In order to get the advantages of the two molten salt syntheses, *i.e.* size homogenous and large crystals, new methods of synthesis were developed in this thesis. The two syntheses have been done one after the other: K_2SO_4 MSS to get uniform and well-crystallized crystals and then K_2MoO_4 MSS to increase their size. Another double synthesis has also been realized using firstly the SSR and then K_2MoO_4 salt synthesis, in the same conditions as those described above, one after the other. The powders were washed several times with 250 mL of distilled water after each MSS and filtered. The XRD patterns of the best obtained results are displayed in Figure 3.6.

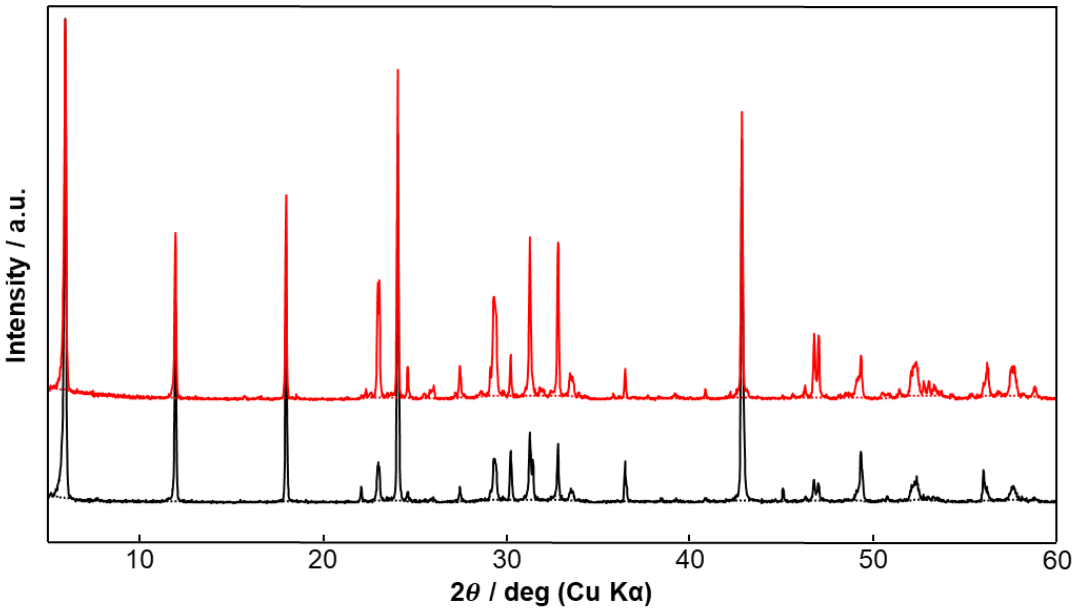

Figure 3.6. XRD powder patterns of the double flux syntheses. In black, the XRD pattern of the synthesis by K_2SO_4 and K_2MoO_4 molten salts. In red, the XRD pattern of the synthesis by SSR and K_2MoO_4 molten salts.

Both patterns show that the powders are highly well-crystallized, with a very small amount of $KNbO_3$ and $K_6Nb_{10.8}O_{30}$ as secondary phases. Figure 3.7a,b show SEM and optical micrographs of KCN crystals obtained by the double synthesis MSS K_2SO_4 and MSS K_2MoO_4. Homogenous and large crystals of KCN have been obtained, with an average size of ~100 µm. Some crystals have a size up to 1 mm (Figure 3.7b). On the other hand, Figure 3.7c-d shows crystals of KCN obtained by the double synthesis SSR and MSS K_2MoO_4. Homogenous and large crystals of KCN are also obtained, with an average size similar to the double MSS, and some crystals obtained were also up to 1 mm (Figure 3.7d).

The obtained results are promising. We proved that it is possible to obtain larger crystals from MSS, with a high average size. Furthermore, it has been shown that it is possible to obtain these crystals characteristics by combining SSR and K_2MoO_4 MSS. It is a real advantage to use SSR because the reaction time is clearly shorter than the MSS reaction (30 hours difference). However, the results are difficult to reproduce, probably due to the highly corrosive power of the molten salts. In fact, there is obviously a diffusion of the molten salt inside the alumina crucible, changing its color, making it fragile, and modifying the stoichiometry of the mixture. The use of a Pt crucible that we have very recently acquired would be more suitable in the future for this MSS method to avoid diffusion problems.

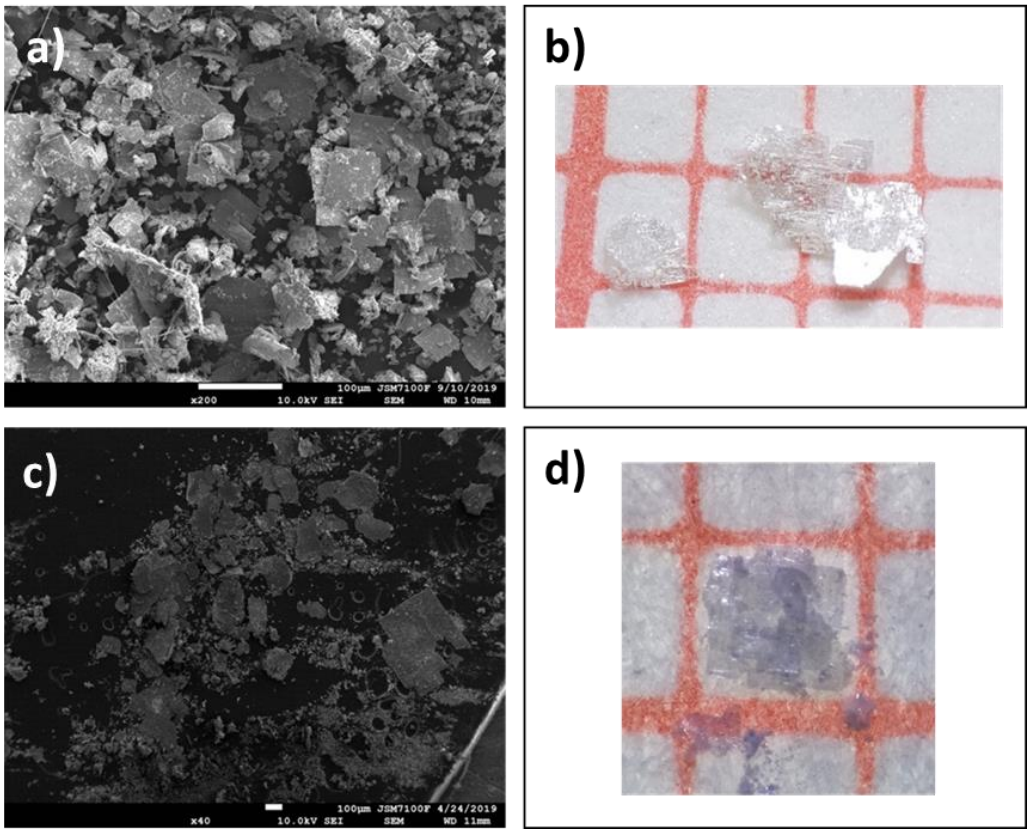

Figure 3.7. SEM and optical micrographs of the crystals obtained by double syntheses. (a-b) Synthesis by K_2SO_4 and K_2MoO_4 molten salts. Higher homogeneity of the crystal size has been obtained, up to 1 mm. (c-d) Synthesis by SSR and K_2MoO_4 molten salts. Higher homogeneity of the crystal size has also been obtained, up to 1 mm. 1 square = 1 mm^2.

1.2. Protonation of the $KCa_2Nb_3O_{10}$ phase

Following Ebina *et al.*'s method [9], the protonated phase is obtained by treating 1 g of KCN powder in 20 mL of 6 M nitric acid for 3 days. The acid is replaced every 24 h by fresh acid to obtain a full protonation of the powder. The powder is then filtered and washed several times with distilled water and dried. The XRD patterns of KCN and $HCa_2Nb_3O_{10}$ (HCN) powders are shown in Figure 3.8. The pattern of the protonated powder, after 72 h in acid, displays the peaks of the $HCN.1.5H_2O$ phase (a = 3.854 Å, c = 16.225 Å, JCPDS card N°00–39–0915, Annexe A, p. 192) [10]). Compared to the parent phase, the (00l) peaks of HCN are shifted toward lower angles, due to the increase of the interlamellar space induced by the K^+ exchange by H^+ ions and the insertion of water, from $d_{KCN}(001)$ = 14.73 Å to $d_{HCN.1.5}(001)$ = 16.22 Å.

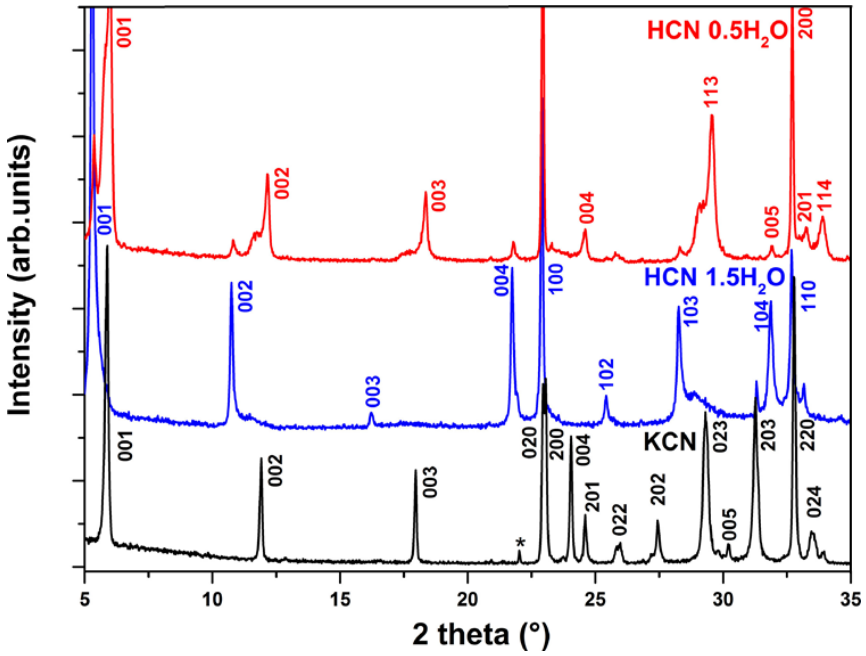

Figure 3.8. XRD powder pattern of (a) the KCN phase (*: $KNbO_3$ phase). (b) the HCN.1.5H_2O (HCN1.5) phase. c) of HCN1.5 after a few hours in a dry atmosphere corresponding to the HCN.0.5H_2O phase.

After drying the powder at 80°C for 2 h, two dehydrated phases are obtained, namely HCN.0.5H_2O (a = 5.452 Å, c = 14.414 Å, $P4/mbm$, JCPDS card N°01–077–4249, Annexe A, p. 193, interlamellar space $d_{HCN.0.5}(001)$ = 14.41 Å [10,11]) with an intermediately hydrated phase, HCN.$x$$H_2O$ (interlamellar space $d_{HCN.x}(001)$ = 15.14 Å) which corresponds to the insertion of approximatively one molecule of water. In fact, the insertion of water molecules inside the lamellar compound induces shifts of perovskite sheets that involve changes of coordination number for the molecules and modifying the value of the lattice constant c. Interestingly, the dehydration and hydration phenomena are perfectly reversible; the dehydrated powder was set under a moist atmosphere in an oven; consequently, the peaks shift again to a lower angle as displayed in Figure 3.8. This phenomenon is similar to the one observed by Jacobson *et al.* [10].

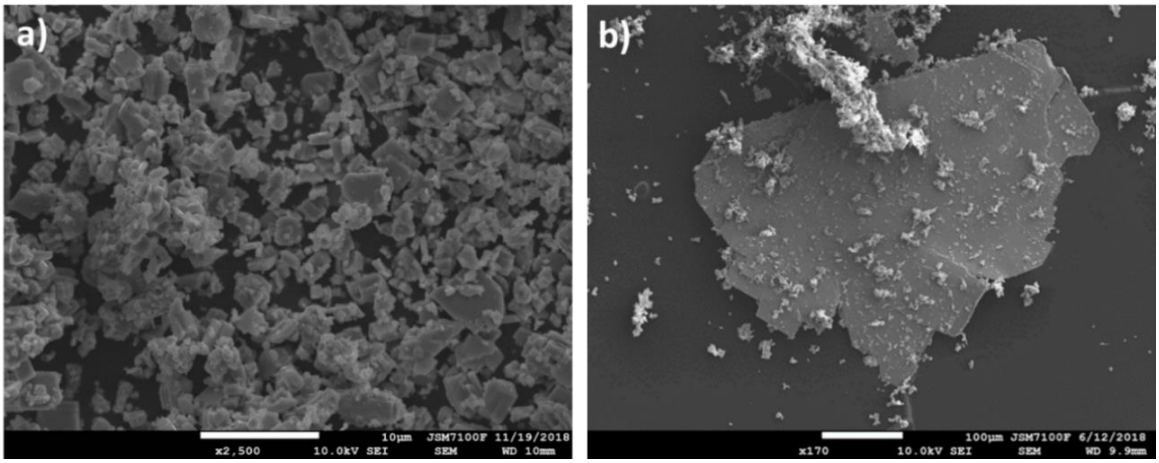

Figure 3.9. SEM micrographs of the HCN phase obtained by (a) solid stage reaction and (b) by molten salt synthesis.

Figure 3.9 shows the SEM micrographs of protonated crystals obtained by SSR and MMS. The crystal shapes and sizes are kept after the protonation. TEM experiments have also been carried out for the protonated phase (Figure 3.10).

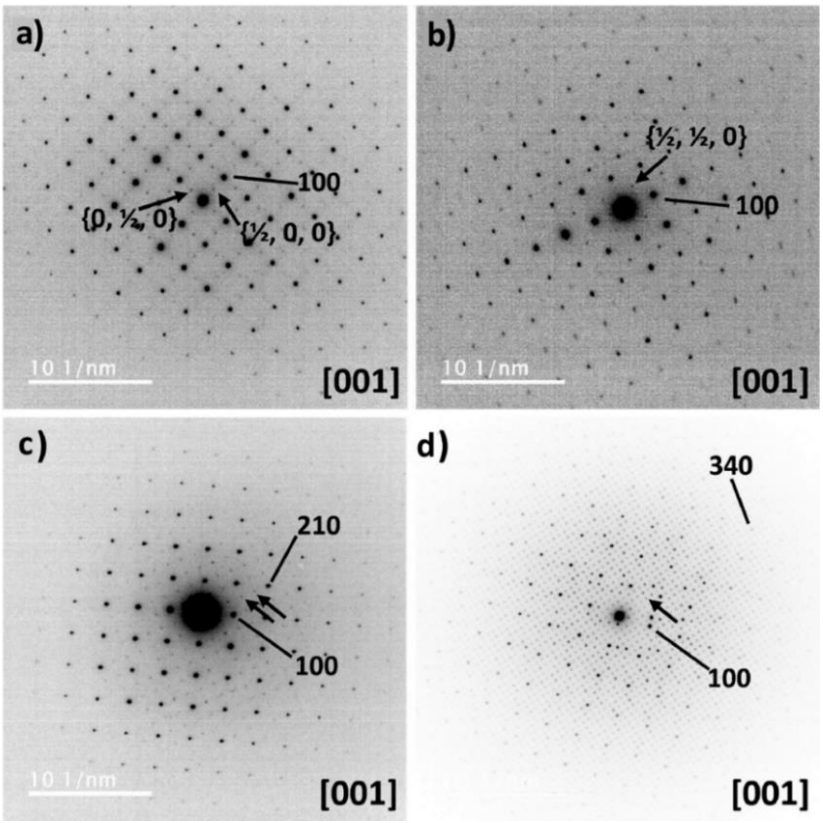

Figure 3.10. (a) EDP of the HCN.1.5H_2O phase showing weak superlattice reflections indicated by the arrows. (b) EDP of the HCN.0.5H_2O phase showing weak reflections that should be forbidden, indicated by the arrows. (c) EDP of the HCN.1.5H_2O phase showing weak superlattice reflections indicated by the arrows. These reflections are aligned along the [210]* row. (d) EDP of the HCN.1.5H_2O phase showing weak superlattice reflections indicated by the arrows. These reflections are aligned along the [430]* row.

Different patterns along the [001] zone axis were recorded. In Figure 3.10a, the presence of weak superlattice reflections at {½, 0, 0} and {0, ½, 0} positions (labeled by arrows in the figure) indicates that the lattice constants *a* and *b* are actually double that was that determined by XRD. The fact that these reflections are detected only by electron diffraction and not by XRD was already reported by Jacobson *et al*. [10]. In Figure 3.10b, the EDP is different with the presence of weak reflections at {½, ½, 0} positions (labeled by an arrow in the figure), but no longer along *a** and *b** axes. In both cases, these superlattice reflections result from the tilting of NbO_6 octahedra along [100], [010], and [001] axis [10,12]. EDPs in Figure 3.10c,d display two other superstructures with five extra reflections along the [210]* direction, and twenty-five extra reflections along the [430]* direction (labeled by arrows in the figure); these reflections correspond to lattice distances of about 8.6 Å and 19.3 Å, respectively. These particular superstructures can arise from octahedral tilts or oxygen vacancies ordering. The composition of HCN powder was found to be around $K_{0.15\pm0.1}Ca_{2.1\pm0.2}Nb_{3\pm0.3}O_x$ by TEM-EDXS and SEM-EDXS analysis showing therefore that a slight amount of potassium is still present in the exchanged phase, as previously observed [3,13].

1.3. Exfoliation of the $HCa_2Nb_3O_{10}$ phase

The protonated phase HCN was exfoliated using TBAOH in a molar ratio 1:1 in 50 mL of pure water. The solution is softly agitated for 24 hours using an oscillating device. A white colloidal solution of $[Ca_2Nb_3O_{10}]^-$ nanosheets is obtained.

In the literature, most of the publications mention that the exfoliation takes from 1 to 2 weeks to be completed [14,15]. This very long process is time-consuming and needs a lot of anticipation to allow fluent work. However, as mentioned in Chapter 1 2.2., the exfoliation (with $[Ti_{0.91}O_2]^{0.36-}$ nanosheets) has been proved to be much faster than expected (some seconds) [16]. After 1 to 2 weeks of agitation, the solution is trouble, characteristic of its colloidal nature.

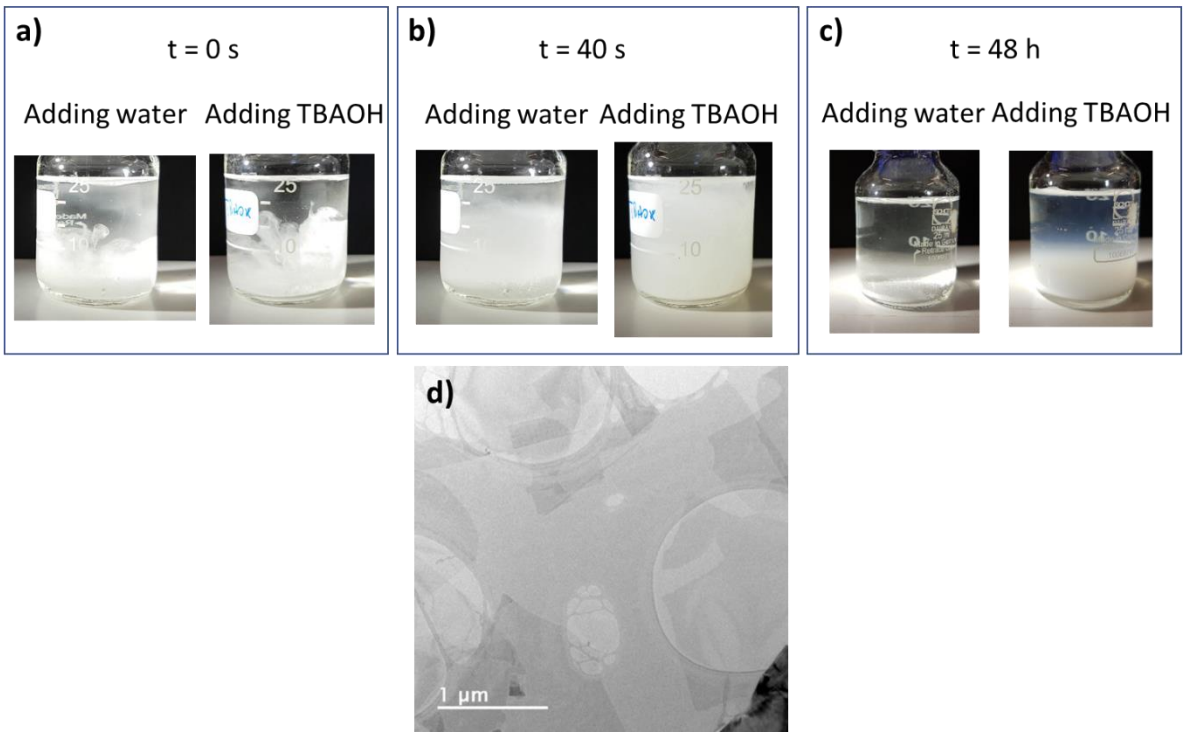

Figure 3.11. (a) At t = 0 s, water in the left flask and TBAOH in the right flask are added in the same amount and softly agitated. (b) At t = 40 s, both solutions become murky. The protonated powder already begins to decant in the flask with water (c). At t = 48 h, the protonated phase has totally decanted in the left flask while a colloidal solution has been obtained to the right flask containing TBAOH. (d) TEM micrograph of the sample obtained after 40 s of exfoliation. Nanosheets have been obtained.

In order to verify that the exfoliation occurs instantly with $[Ca_2Nb_3O_{10}]^-$ nanosheets, a simple experience has been made. It consists in considering two different flasks containing HCN and distilled water respectively (Figure 3.11). In the first flask, water is added to the solution while in the second flask, TBAOH is added in the solution, both in the same amount and without agitation. In both cases, the adding of liquid leads to a turbid solution, as seen in Figure 3.11a,b. Therefore, it is difficult to distinguish between the effect of drop agitation and the effective exfoliation of HCN. At t = 40 s, it is already possible to see that the left flask with water already begins to decant, while the right one with TBAOH does not decant, showing that the exfoliation is already occurring. At the same time, drops of the liquid have been taken at different moments of the exfoliation process (from 40 s to 48 h), deposited on TEM grids, and observed by TEM to give a general idea about when the exfoliation occurs. Figure 3.11d shows a micrograph of nanosheets obtained after 40 s of exfoliation, confirming that the exfoliation is instantaneous.

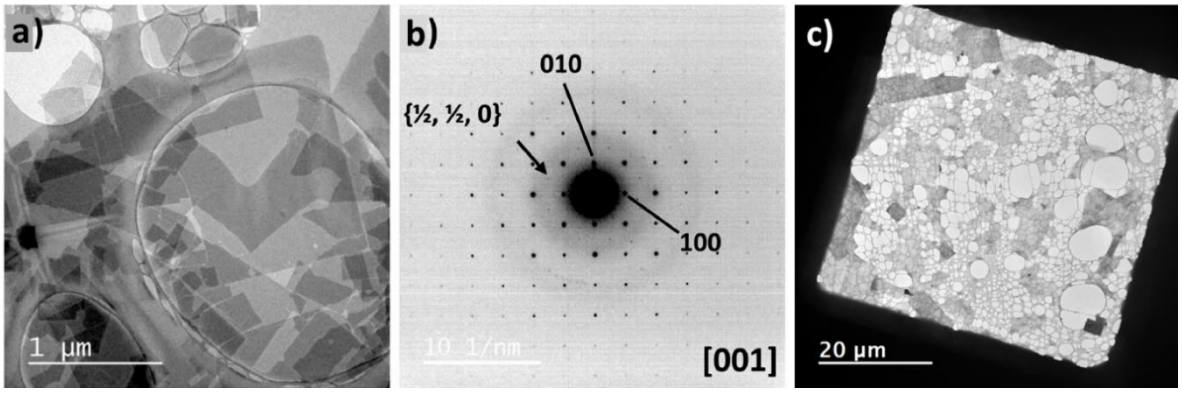

Figure 3.12. (a) Bright field micrograph of the $[Ca_2Nb_3O_{10}]^-$ nanosheets obtained by the protonation and exfoliation of KCN obtained by solid-state reaction. (b) EDP of a single $[Ca_2Nb_3O_{10}]^-$nanosheets along the [001] axis. A weak reflection is indicated by the arrow. (c) Bright field micrograph of the $[Ca_2Nb_3O_{10}]^-$ nanosheets obtained by the protonation and exfoliation of KCN obtained by MSS.

Figure 3.12a shows a brightfield TEM micrograph of several nanosheets collected from the colloidal solution, showing the different dimensions (from about 0.1 µm to 5 µm) obtained after several days of exfoliation. Figure 3.12b is a [001] zone axis EDP of a single nanosheet. The comparison between brightfield micrographs and EDP shows that the [100]* and [010]* directions are parallel to the nanosheets edges. In addition to the fundamental reflections (corresponding to lattice parameters $a \simeq b \simeq 3.88$ Å), all the recorded EDPs on nanosheets exhibit very weak superlattice {½, ½, 0} reflections, due to a tilt of octahedra, indicating that a $\sqrt{2a}$ lattice constant should be used to describe the tetragonal lattice [25]. The composition of NS was found to be $Ca_{2.4\pm0.7}Nb_{3\pm0.7}O_x$ by TEM-EDXS. In Figure 3.12c is displayed a micrograph of the first result of the exfoliation which has been realized from crystals obtained by the MSS method. Nanosheets from 5 to 20 µm have been obtained.

1.4. Deposition of the $[Ca_2Nb_3O_{10}]^-$ nanosheets on substrates

1.4.1. Deposition on substrates using the Langmuir-Blodgett technique

$[Ca_2Nb_3O_{10}]^-$ nanosheets have been deposited on various substrates by the Langmuir-Blodgett technique. As described in Chapter 2, the Langmuir-Blodgett has been acquired in the framework of the PolyNash project. Therefore, all the parameters and conditions to drive an efficient deposition were studied in this PhD thesis. The first work was to determine the optimal concentration of the $[Ca_2Nb_3O_{10}]^-$ colloidal solution. Different dilutions (from 2 to 10 times in volume) have been realized and depositions on

substrates with these solutions have been analyzed by AFM and/or SEM. The results have shown that the solution diluted 2.5 times gave the best result, which is different from reported dilutions of the literature [17]. Then, depositions were realized on different substrates such as silicon, silica, Pt/Si, and mica. The depositions were realized as described in the previous chapter. The value of surface pressure to obtain a good covering was between 9 and 15 mN/m depending on the substrate and the depositions conditions. High coverages were obtained on the different substrates, as shown in Figure 3.13, where nanosheets monolayers on Si, SiO_2, and mica are displayed.

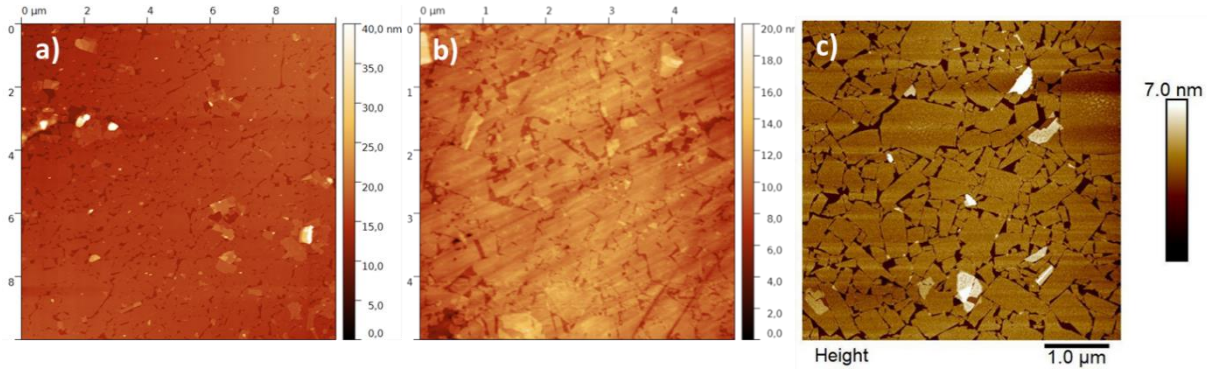

Figure 3.13. AFM images of the $[Ca_2Nb_3O_{10}]^-$ nanosheets dense monolayer deposited by Langmuir-Blodgett on (a) silicon, (b) silica, and (c) on mica (B. Bérini, GEMaC).

The nanosheets can also be observed by SEM if the substrate is conductive, or if the SEM is set up for non-conductive observations (low voltage). The micrographs in Figure 3.14 are examples of observations of a nanosheets monolayer on Si and Pt/Si substrates. AFM is time-consuming compared to SEM, and the latter has the great advantage to catch large areas compared to AFM which is local.

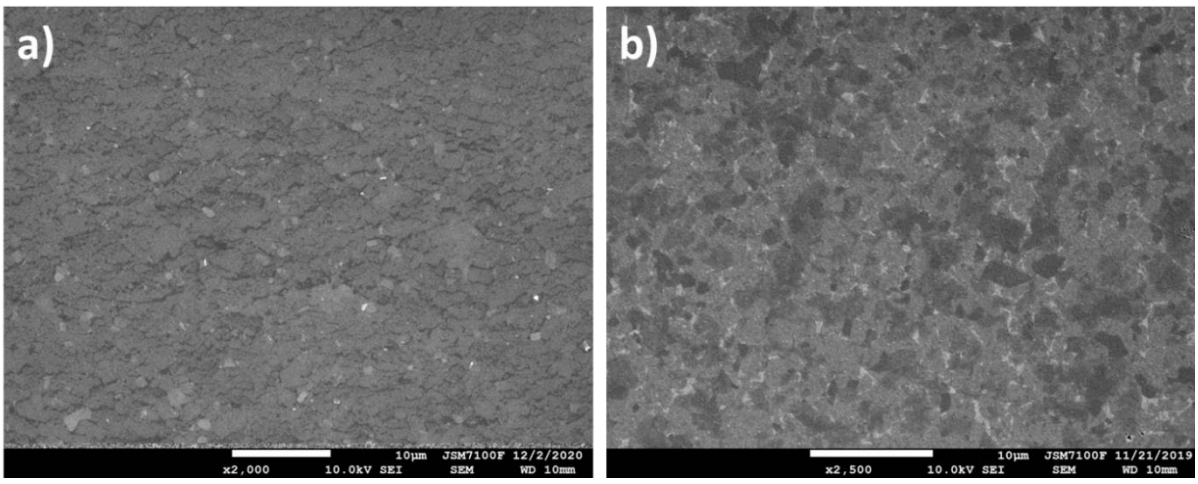

Figure 3.14. SEM micrographs of the $[Ca_2Nb_3O_{10}]^-$ nanosheets dense monolayer deposited on (a) silicon, (b) platinum.

Even if it is possible to obtain good results of covering with the Langmuir-Blodgett technique, it is complicated for some types of substrates to have good reproducibility, due to the sensibility of the Langmuir-Blodgett technique (strongly dependent on temperature and humidity variations), and depending on the wettability of the substrate.

1.4.2. Deposition of the $[Ca_2Nb_3O_{10}]^-$ nanosheets on substrates using the drop casting technique

Table 3.2. Deposition conditions of the $[Ca_2Nb_3O_{10}]^-$ (CNO) nanosheets on various substrates.

Substrates	Amount of CNO parent phase	Ultrapure water volume	Absolute ethanol amount	Heating temperature	Amount of solution deposited/Substrate size
Silica (Eagle glass)	100 µL	5 mL	60 µL	120°C	150 µL 10x10 mm
Mica	100 µL	5 mL	200 µL	120°C	600 µL 25x25 mm
Pt/Si	80 µL	10 mL	200 µL	100°C	180 µL 10x7 mm
Silicon	80 µL	10 mL	400 µL	100°C	200 µL 10x10 mm

Following the recent work of Shi *et al.* [18], it has been possible to use the drop casting technique for the deposition of $[Ca_2Nb_3O_{10}]^-$ nanosheets on various substrates. Although the parameters of the deposition on Si substrate were already reported, we have determined or adapted the deposition conditions for silica, mica, and Pt/Si substrates. The conditions used for the $[Ca_2Nb_3O_{10}]^-$ depositions are reported in Table 3.2. The AFM results displayed in Figure 3.15 show highly densified nanosheets monolayers on Si, SiO_2, mica, and platinum giving the same quality as a Langmuir-Blodgett deposition in a very short time. However, it can be observed some nanosheets overlapping and/or nanosheets that are not totally exfoliated. This behavior is not problematic for oxide growth application as the 2D lattice will still remain, but it will bring a higher roughness to the film. It is possible to carefully remove the overlapping crystals by cleaning the surface with a cotton tip.

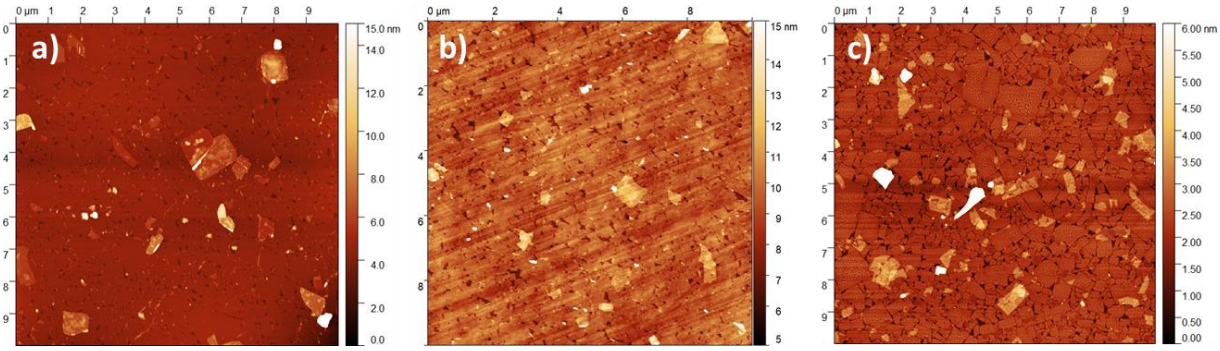

Figure 3.15. AFM images of the $[Ca_2Nb_3O_{10}]^-$ nanosheets dense monolayer deposited by drop casting on (a) silicon, (b) silica, and (c) on mica.

SEM micrographs were also performed on nanosheets deposited on Si and Pt/Si. Figure 3.16a shows a large zone of the Si substrate covered by nanosheets, and an uncovered part in the middle. This 1 mm^2 zone is the mark of the pipette when the solution was injected at the surface of the liquid. This phenomenon was reported by Shi *et al.* [18]. It is then important to try to inject the solution on one of the sides of the substrate to avoid this uncovered zone in the middle of the substrate. Figure 3.16b shows the dense mosaic-like nanosheets monolayer on a large surface of a Pt/Si substrate.

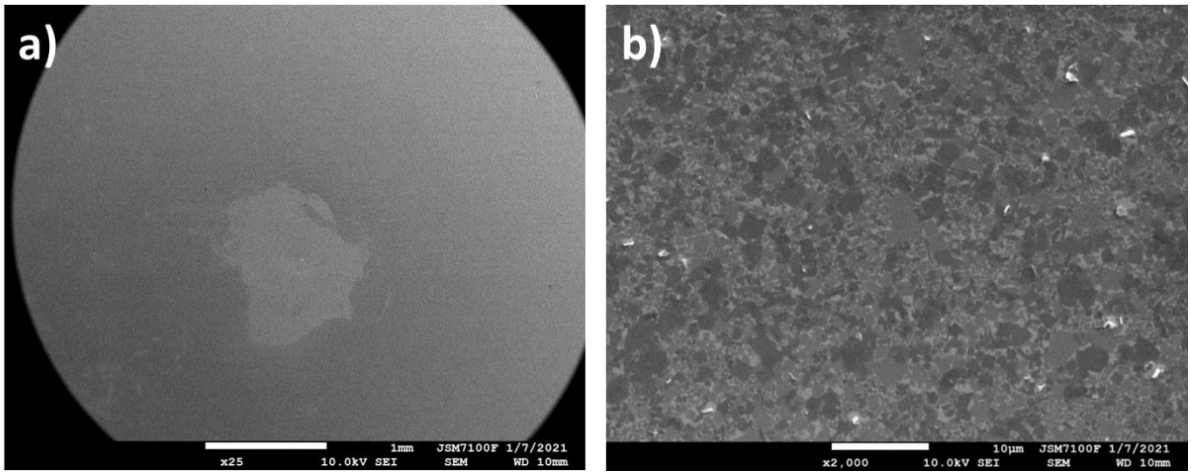

Figure 3.16. SEM micrographs of $[Ca_2Nb_3O_{10}]^-$ nanosheets deposited on Si substrate: (a) Large SEM field of the nanosheets layer on Si, showing a mark without nanosheets due to the pipette. (b) SEM micrograph of a dense monolayer of calcium niobate nanosheets on Pt/Si.

Nanosheets obtained from the exfoliation of KCN crystals synthesized by MSS have also been recently deposited on Si substrate (Figure 3.17). A dense monolayer of quite large nanosheets has been obtained (nanosheets from 5 to 10 µm).

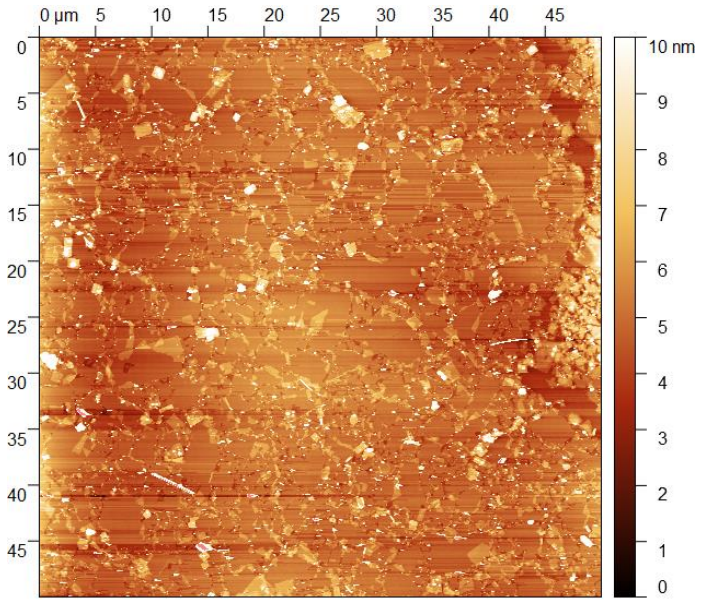

Figure 3.17. AFM images of the $[Ca_2Nb_3O_{10}]^-$ nanosheets dense monolayer deposited by drop casting on silicon.

The drop casting method offers the possibility to get highly reproducible nanosheets covering in a shorter time than the Langmuir-Blodgett technique. The method was widely used to deposit $[Ca_2Nb_3O_{10}]^-$ nanosheets during the last year of this thesis.

1.5. In-plane diffraction of the $[Ca_2Nb_3O_{10}]^-$ nanosheets

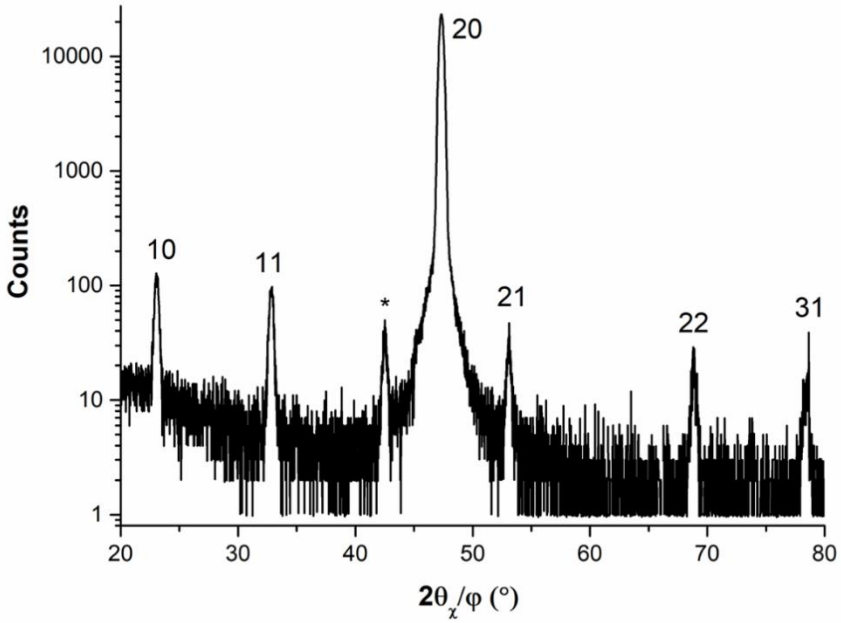

Figure 3.18. In-plane XRD diagram of $[Ca_2Nb_3O_{10}]^-$ nanosheets deposited on Si substrate. *: K_β line of the 20 reflections.

In-plane X-ray diffraction experiments have been performed on $[Ca_2Nb_3O_{10}]^-$ nanosheets deposited on a Si substrate to measure their lattice parameters (Figure 3.18). The sample was prepared by drop casting and 3 layers were deposited on the substrate. The diffraction pattern obtained shows the reflections of the vertical plans. The nanosheets lattice parameters have been measured to be $a \simeq 3.84$ Å for the 20 reflection and $b \simeq 3.87$ Å for the 11 reflection, which is in good agreement with the theoretical values ($a = 3.854$ Å and $b = 3.871$ Å). These values are also closed to those obtained by Li *et al.* ($a \simeq b \simeq 3.85$ Å) [19].

1.6. XPS experiments on $[Ca_2Nb_3O_{10}]^-$ nanosheets

XPS experiments have been realized by Dr. Bruno Lépine, Haley Glavina (master trainee), and Dr. Pascal Turban, from the Rennes Institute of Physic (IPR). Two different experiments were realized and then analyzed by XPS: HF treatment and annealing treatment of a Si substrate covered by a monolayer of nanosheets.

1.6.1. HF treatment on $[Ca_2Nb_3O_{10}]^-$/Si substrate followed by XPS

HF treatment is commonly used in microelectronic to eliminate native silica on the surface of silicon. The experiment aims to see if the nanosheets resist to HF and if it is still possible to eliminate the silica at the surface of the silicon underneath the nanosheets layer. Taking into account that the presence of silica on Si substrate cannot be avoided because of the deposition conditions of the nanosheets, this method could be useful for future preparation of metal/oxide/semiconductor (MOS) structures integrating a nanosheets layer with high dielectric permittivity. A silicon substrate covered by $[Ca_2Nb_3O_{10}]^-$ nanosheets were treated with HF 2 % for 1 mn, cleaned, dried and, placed in the XPS chamber. In Figure 3.19 is displayed the XPS spectra of Si2p and O1s signals. The peaks Si2p and O1s of SiO_2, present in the spectra of the substrate "as deposited", disappear after HF treatment, showing that the HF has successfully deoxidized the silicon substrate, leaving only the contribution of the hydrogenated Si substrate for the Si2p signal and the NS signal for the O1s signal.

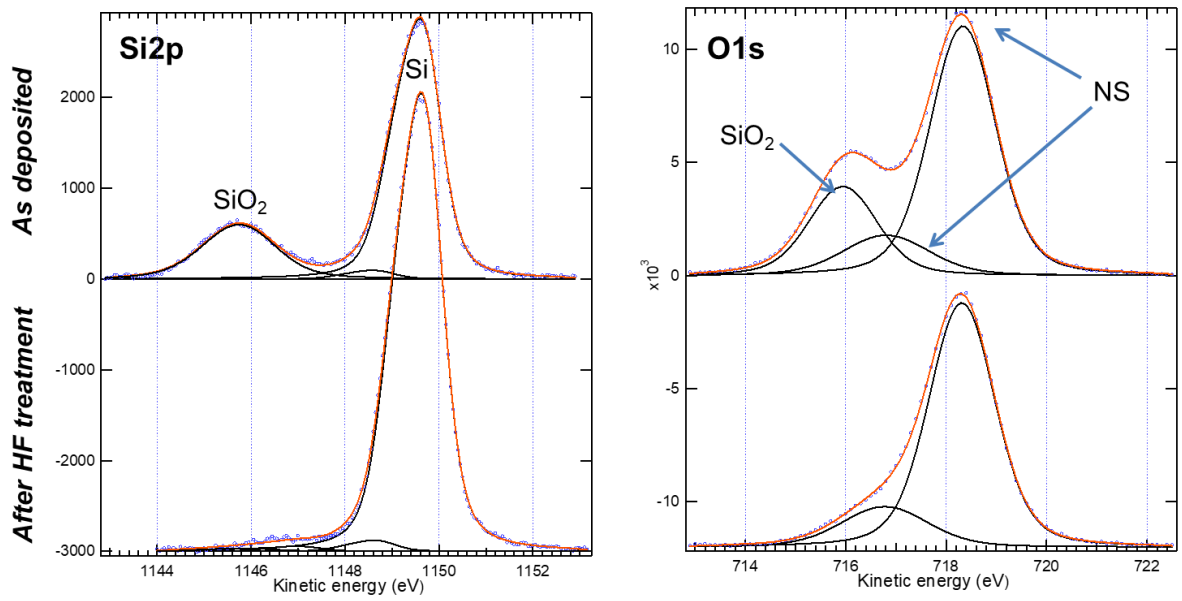

Figure 3.19. Results of the XPS analysis: on the left the XPS spectra of the Si2p signal, and on the right the XPS spectra of the O1s signal, before and after HF treatment.

The effect of HF on the nanosheets can be observed by looking at the Nb3d and Ca2p signals (Figure 3.20). For the Nb3d signal, a few minor modifications are observed: there is a minor broadening of the Nb3d levels, and a new weak component with chemical shift appeared, which represents 4% of the total Nb signal. For the Ca2p signal, no change on the core level (inner atomic planes of the nanosheets) is observed. As the Ca atoms are not affected, the inner Nb atoms of the nanosheets placed in between the two CaO planes should also not be affected. Thus, 1/3 of the Nb3d signal should not be modified, while a part of the 2/3 left of the signal, which corresponds to the Nb atoms in the outer NbO_2 planes, are modified (change of chemical environment). The new component formed corresponds to a partial reduction of Nb^{5+} in Nb^{4+} due to a light deoxidation of the outer NbO_2 layers. Otherwise, no loss of elemental Nb or Ca has been observed which confirms that the nanosheets resist to HF treatment.

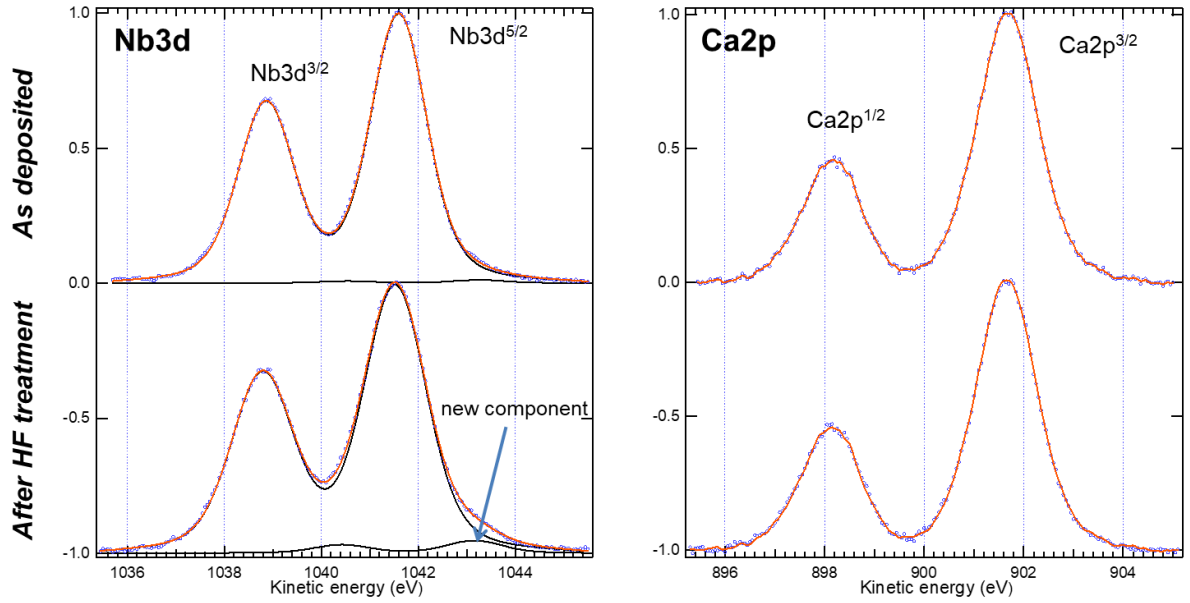

Figure 3.20. Results of the XPS analysis: on the left the XPS spectra of the Nb3d signal, and on the right the XPS spectra of the Ca2p signal, before and after HF treatment.

To conclude, it has been experimentally shown that the native SiO_2 layer formed on a Si substrate covered by $[Ca_2Nb_3O_{10}]^-$ nanosheets can be eliminated by HF treatment, without modifying the nanosheets layer.

1.6.2. XPS experiments on $[Ca_2Nb_3O_{10}]^-$/Si substrates at different annealing temperatures

The $[Ca_2Nb_3O_{10}]^-$/Si substrates were annealed under ultra high vacuum (UHV) at different temperatures to study the thermal stability of the nanosheets under vacuum. The knowledge of the stability or evolution of nanosheets at high temperature is an important point for further use as for the later deposition of thin films. The XPS experiments were made after 30 s annealing at 160°C and 370°C and the results of the Nb3d and Ca2p signals are shown in Figure 3.21. For the annealing temperature of 160°C, no difference on the Nb3d and Ca2p signals are observed compared to the results obtained on the $[Ca_2Nb_3O_{10}]^-$/Si substrates after HF treatment. Thus, the $[Ca_2Nb_3O_{10}]^-$ nanosheets are thermally stable at 160°C. For the annealing temperature of 370°C, there is an increase of the Nb3d secondary component and a widening of the Ca2p signal (or a secondary component). The results obtained are consistent with the appearance of oxygen vacancies.

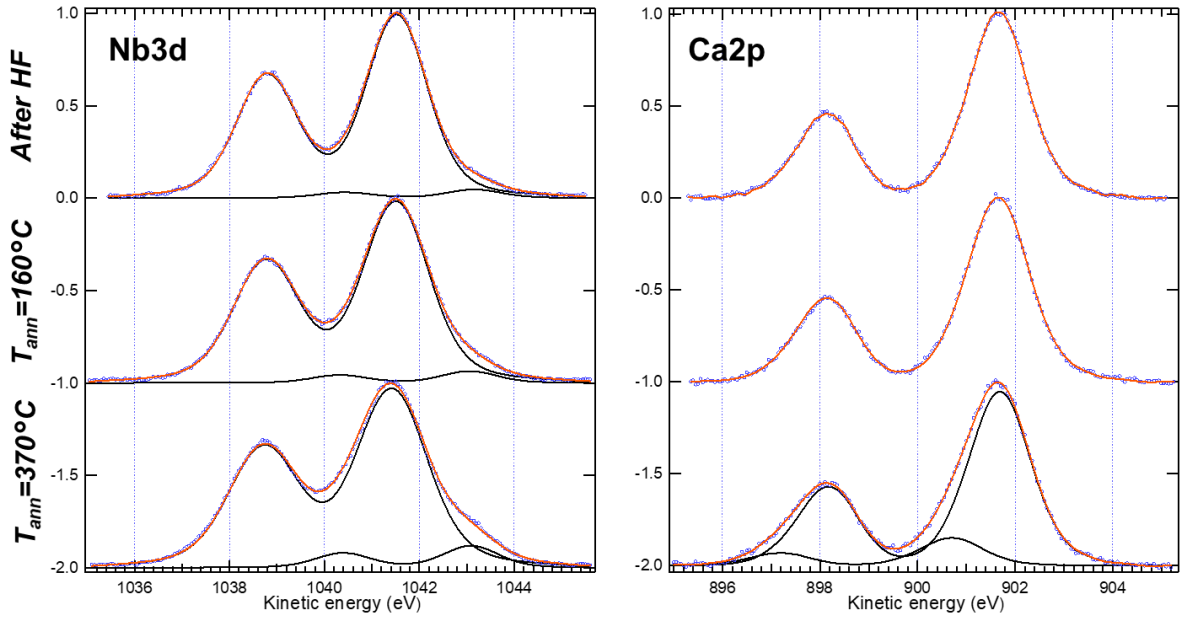

Figure 3.21. Results of the XPS analysis: on the left is displayed the XPS spectra of the Nb3d signal, and on the right, the XPS spectra of the Ca2p signal, at annealing temperatures of 160°C and 370°C compared with the sample treated by HF.

A second experiment was made with a $[Ca_2Nb_3O_{10}]^-$/Si sample, annealed at 370°C under UHV, and then annealed at 110°C in air. The XPS spectra show a return to initial chemical states of Nb and Ca after *ex situ* annealing (Figure 3.22), which could correspond to the healing of oxygen vacancies in nanosheets.

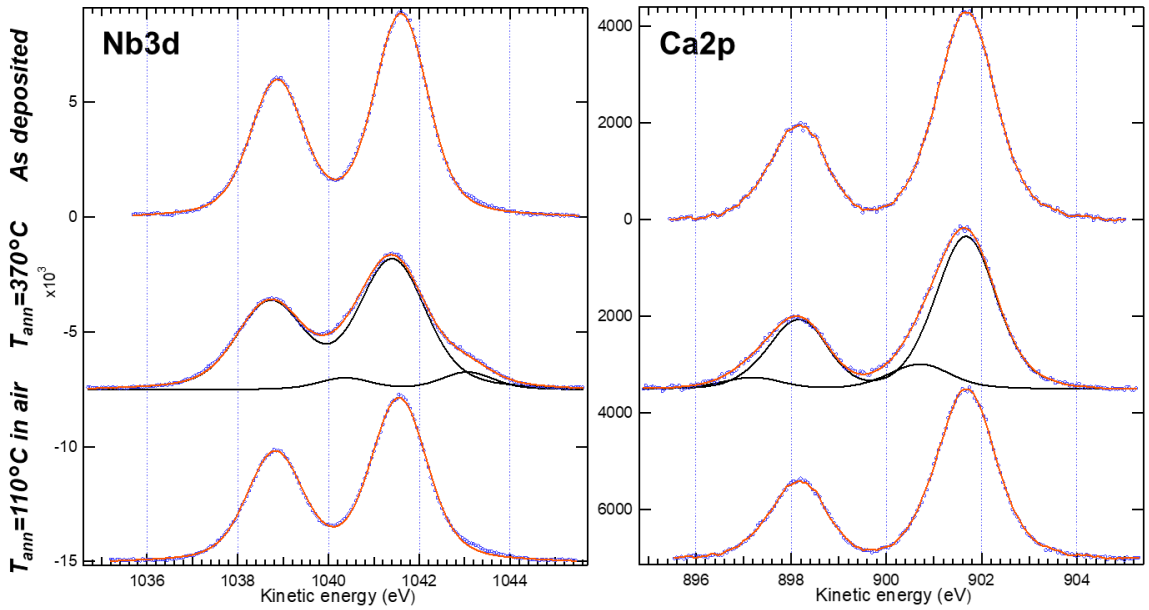

Figure 3.22. Results of the XPS analysis: on the left the XPS spectra of the Nb3d signal, and on the right the XPS spectra of the Ca2p signal, at an annealing temperature of 370°C under UHV, after annealing at 110°C in air, compared to the initial sample.

To conclude, the $[Ca_2Nb_3O_{10}]^-$ nanosheets are stable to temperature up to 160°C under UHV. At 370°C, the nanosheets are subjected to important modifications, probably induced by the appearance of oxygen vacancies. The phenomenon is reversible. STM experiments were then performed to verify if the phenomena observed in XPS are due to oxygen vacancies.

1.7. STM experiments on $[Ca_2Nb_3O_{10}]^-$ nanosheets

Scanning tunneling microscopy (STM) has been used to further characterize the nanosheets layers and especially their evolution during heat treatment. The STM experiments have been realized by Dr. Pascal Turban, from the Rennes Institute of Physics (IPR). Highly oriented pyrolytic graphite (HOPG) was used as substrate and the nanosheets were deposited by dipping the substrate in the colloidal nanosheets solution. The sample was then annealed for 20 mn at 110°C in air to eliminate water residues and 30 mn under UV to photochemically decompose TBAOH molecules to stick the nanosheets on the substrate. Then, the sample was annealed at 160°C under UHV. In Figure 3.23a, it is possible to see a $[Ca_2Nb_3O_{10}]^-$ nanosheet of more than 1 μm^2 area, with a height of 1.5 nm, which is close to the height reported in the literature [20,21]. At higher magnification (Figure 3.23b,c), it is possible to see a textured surface from 2 to 4 Å. This textured surface seems due to local fluctuations of the surface potential rather than an intrinsic roughness of the nanosheet. The fast Fourier transformation (FFT) displayed in Figure 3.23d shows the square surface lattice of the nanosheets of $\sim$ 16.3 Å, which corresponds to a 4×4 lattice reconstructed surface.

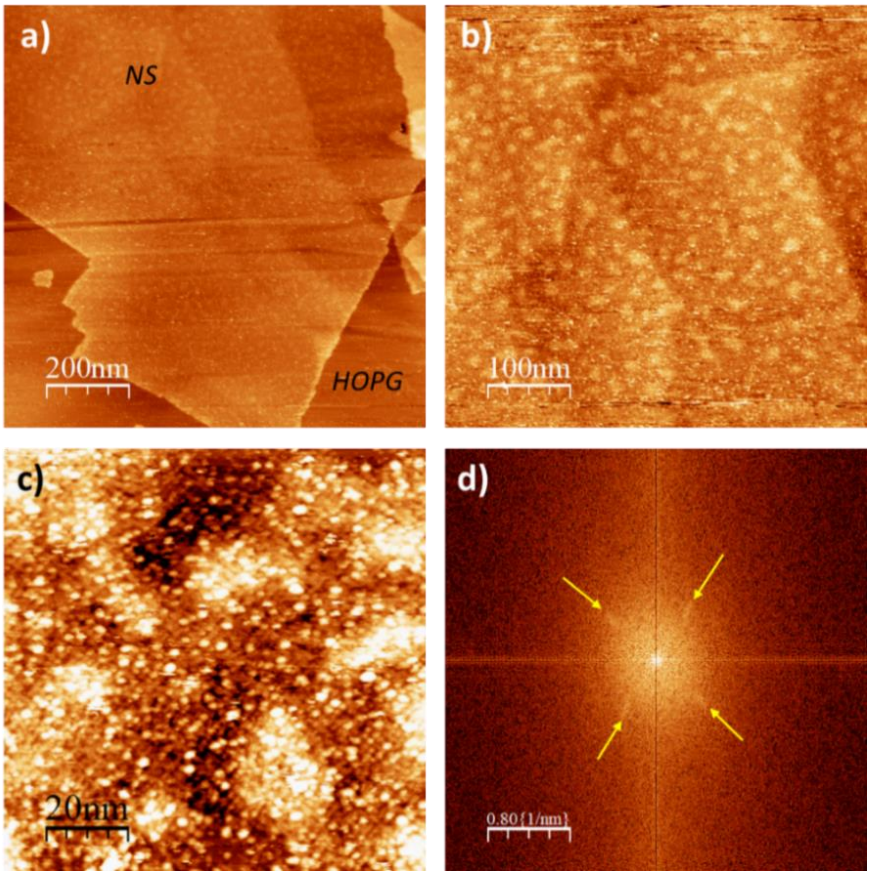

Figure 3.23. STM experiments on a $[Ca_2Nb_3O_{10}]^-$ nanosheet deposited on HOPG substrate annealed 20 mn 110°C in air + 30 mn under UV and then annealed 1 hour at 160°C under UHV. (a) STM image of a $[Ca_2Nb_3O_{10}]^-$ nanosheet. (b) magnification of the surface of the nanosheet showing a textured surface. (c) Image at higher magnification showing a square lattice surface, parallel to the NS edges. (d) FFT of the image c), showing a square lattice.

Another STM experiment was made with a sample annealed at 360°C under UHV. The morphology of the surface has changed (Figure 3.24a): the surface parameters were measured to be ~ 7.8 Å (Figure 3.24b), which corresponds to a 2 × 2 reconstructed ordered lattice. This phenomenon has already been described in the literature on the surface of $SrTiO_3$ substrates, which was attributed to ordered oxygen vacancies on the perovskite surface lattice [22–24]. The formation of these oxygen vacancies is facilitated to compensate the net negative charge of the nanosheets surfaces when the TBA^+ are decomposed.

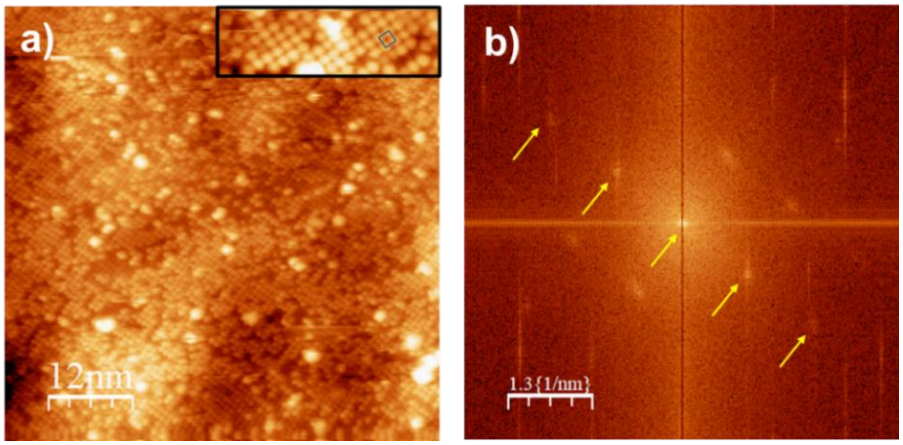

Figure 3.24. STM experiments on a $[Ca_2Nb_3O_{10}]^-$ nanosheet deposited on HOPG substrate annealed 20 mn 110°C in air + 30 mn under UV and then annealed 1 hour at 360°C under UHV. (a) STM image of the surface of a $[Ca_2Nb_3O_{10}]^-$ nanosheet. The magnification window on the top is 15.9 × 4.8 nm^2. (b) FFT of the image (a).

To conclude, the STM experiments complete the measurement of XPS, by confirming the stability of the nanosheets up to 160°C under UHV. They also confirm the hypothesis previously mentioned on the creation of surface oxygen vacancies on the nanosheets at 360°C.

Conclusion

The $[Ca_2Nb_3O_{10}]^-$ nanosheets were successfully obtained by the protonation and exfoliation of the $KCa_2Nb_3O_{10}$ Dion Jacobson phase, synthesized by SSR and MSS. However, the MSS syntheses need to be improved to have homogenous results. The depositions by the Langmuir-Blodgett method and the drop casting technique show high coverage on the surface of various substrates. The XPS experiments demonstrate that it is possible to deoxidize a Si substrate covered by nanosheets with an HF treatment, without affecting the nanosheets. Moreover, the coupled experiments of XPS and STM have demonstrated the stability of the $[Ca_2Nb_3O_{10}]^-$ nanosheets up to 160°C under UHV, and that at high temperature (360°C), oxygen vacancies were formed at the surface of the nanosheets, leading to a reduction of the niobium and compensate the negative charge of the nanosheets surfaces.

2. Synthesis, deposition, and characterizations of $[K_{4-x}Nb_6O_{17}]^{x-}$ nanosheets

2.1. Synthesis of the $K_4Nb_6O_{17}$ phase

The $K_4Nb_6O_{17}$ powder (KN) was synthesized by SSR. K_2CO_3 (Acros Organics, 99%) and Nb_2O_5 (Alfa Aesar, 99.5%) precursors (K:Nb = 2.4:3) were ball-milled in ethanol for 5 h. An excess of 20% of K_2CO_3 was needed in order to counterbalance the potassium loss caused by the volatility of K_2O formed at high temperature. The powder was placed in an alumina crucible and treated for 10 h at 1100°C. The powder was filtered and dried resulting in large shiny greyish crystals. The XRD pattern of the powder is displayed in Figure 3.25. The pure hydrated phase $K_4Nb_6O_{17}.3H_2O$ (JCPDS card N°00-021-1297, completed with calculated indexation, Annexe A, p. 195-197) is obtained without any secondary phase.

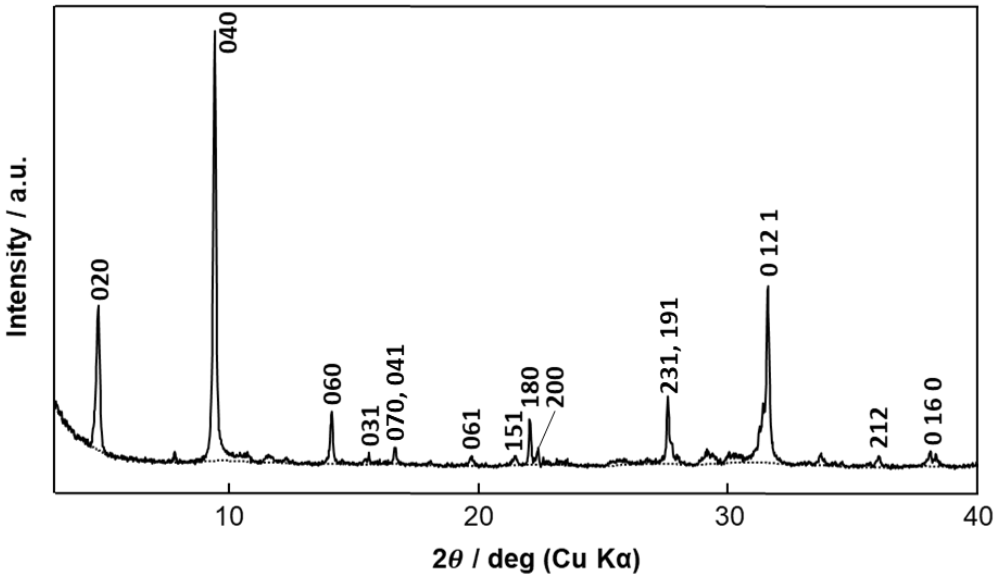

Figure 3.25. XRD diagram of the KN phase obtained by SSR.

The SEM micrograph and photograph of the KN crystals obtained are displayed in Figure 3.26. The crystals size average is 200 µm, with many crystals up to 1 cm. The composition of the crystals was found by SEM-EDXS analyses to be around $K_{4\pm0.3}Nb_{6\pm0.3}O_x$.

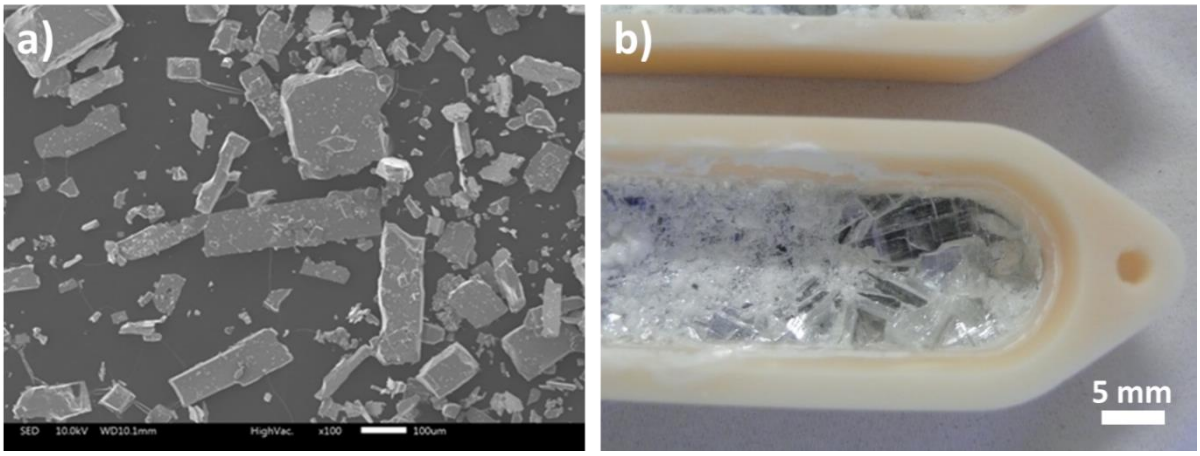

Figure 3.26. (a) SEM micrograph of KN crystals. (b) Photograph of a crucible containing KN crystals after synthesis.

TEM experiments have also been realized on the KN phase. Figure 3.27 shows KN crystals and EDP of a KN crystal along the [010] zone axis. It can be observed that the most intense reflections are {*h*00} and {00*l*} (with h and k even, labeled in the figure). The measured lattice constants are $a \simeq 7.83$ Å and $b \simeq 6.56$ Å, which are close to those of the literature [25], [26]. The composition measured by TEM-EDXS is close to the one previously measured by SEM-EDXS previously.

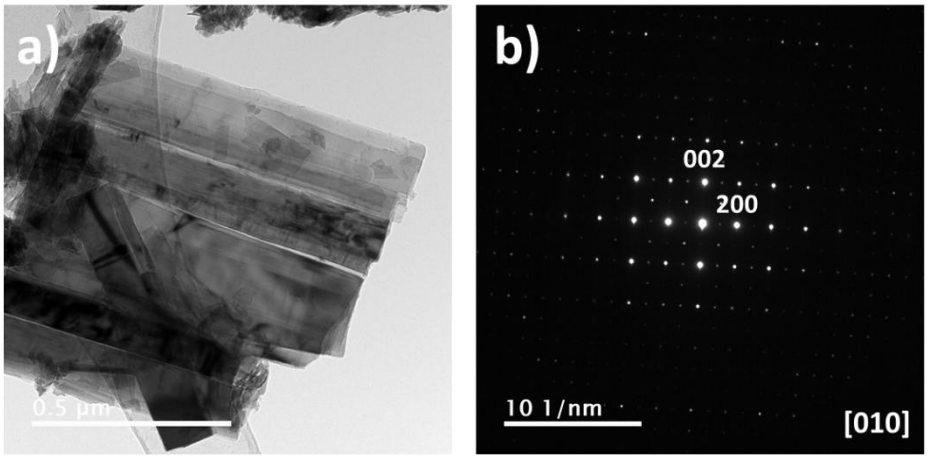

Figure 3.27. (a) Bright field micrograph of KN crystals. (b) EDP of a KN crystal along the [010] zone axis.

2.2. Protonation of the $K_4Nb_6O_{17}$ phase

KN protonation has been realized in the same conditions as for KCN. The protonated phase is obtained by treating 1 g of KN powder in 20 mL of 6 M nitric acid for 3 days. The acid was replaced every 24 h by fresh acid to obtain a full protonation of the powder. After 3 days, the $H_xK_{4-x}Nb_6O_{17}$ (HKN) powder was filtered and washed several times with distilled water and dried. The time of protonation of this phase has not been

described in the literature. In order to get an estimation of the protonation time needed, XRD analyses have been performed after 24h, 48h, and 72h of protonation. The results are displayed in Figure 3.28.

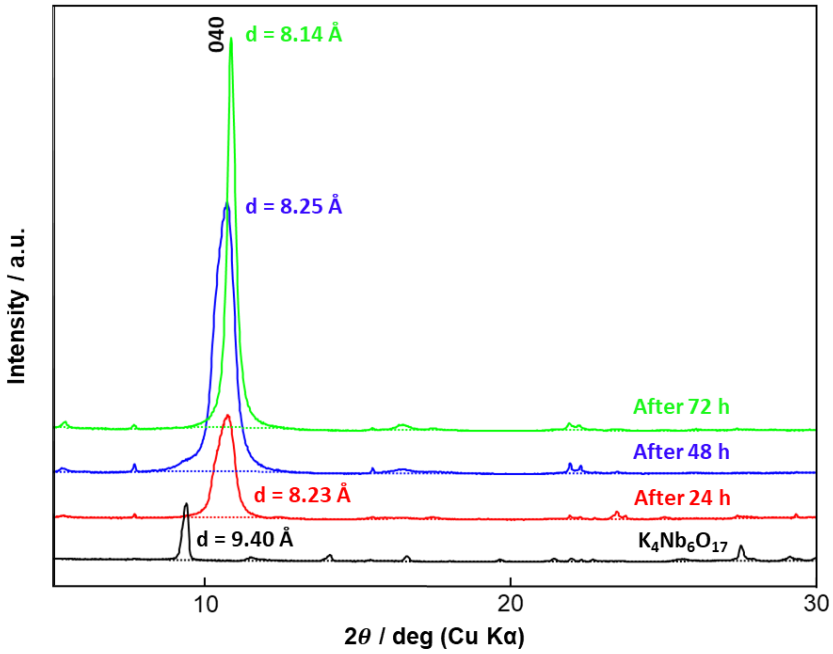

Figure 3.28. XRD patterns of the protonation of the KN phase: KN before protonation (black), after 24 h of protonation (red), after 48 h (blue), and after 72 h (green).

The protonated phase is not referenced in diffraction databases. It can be observed that the 040 peak (d_{040} = 9.40±0.05 Å for $K_4Nb_6O_{17}.3H_2O$, d_{040} = 8.2±0.05 Å for $K_4Nb_6O_{17}$) is shifted to higher diffraction angles, which corresponds to a decrease of the parameter *b*. The shift has stopped progressing after 72 h, demonstrating that the total protonation is achieved for this amount of time. We have measured d_{040} = 8.14±0.05 Å for HKN, which is slightly higher than the value reported in the literature by Bizeto *et al.* (d_{040}= 8.0 Å) [27]. The position of the 040 peak also depends on the hydration rate of the protonated phase. SEM realized on the protonated phase shows large crystals with the same average lateral size as the parent phase (Figure 3.29). It can be noticed that the crystals already begin to delaminate.

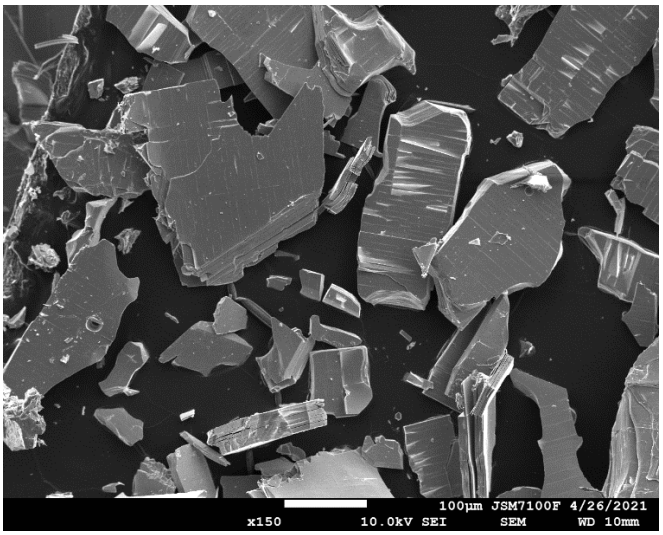

Figure 3.29. SEM micrograph of the protonated HKN phase.

The composition of the crystals was found to be around $H_xK_{1.5\pm0.2}Nb_{6\pm0.3}O_y$ by SEM-EDXS analyses. This result demonstrates that the protonation does not only occur in the interlayer I but also partially in the interlayer II of the KN phase (cf. Chapter 1).

2.3. Exfoliation of the $H_xK_{4-x}Nb_6O_{17}$ phase

2.3.1. Exfoliation with TBAOH

The HKN protonated phase was exfoliated using TBAOH in a molar ratio 1:1 in 50 mL of pure water. The solution is softly agitated for 2 weeks using an oscillating device. A colloidal solution has been obtained and analyzed by TEM. As described in the literature [28,29], the nanosheets tend to become nanoscrolls (Figure 3.30a). The composition of the nanoscrolls measured by TEM-EDXS was found to be Nb_xO_y without any potassium detected within the detection limit of the detector. The EDP realized on a nanoscroll is displayed in Figure 3.30b and shows a pattern with diffraction rings corresponding to the expected phase [28]. It can be concluded that the nanosheets roll into nanoscrolls, with a composition $[Nb_6O_{17}]^{4-}$. However, it is possible to see that some nanosheets are also present in the solution (Figure 3.30c), showing that the rolling process is not total.

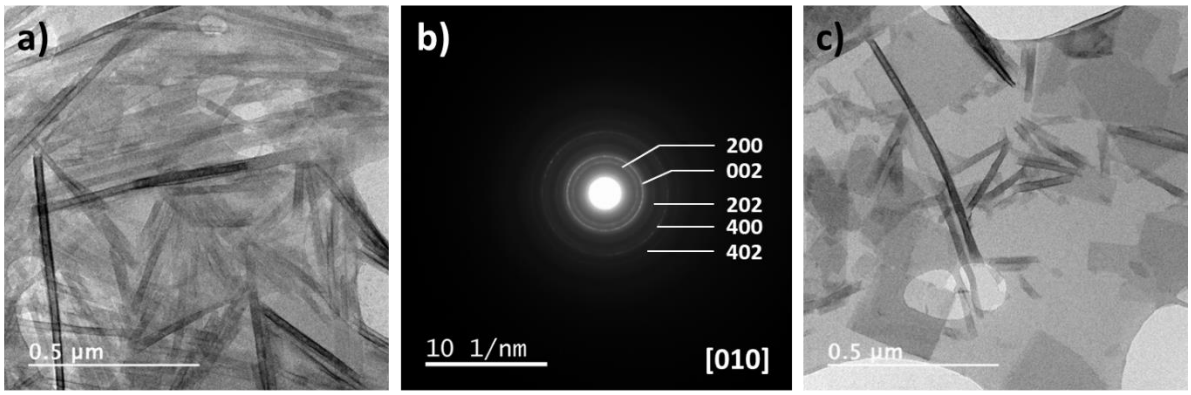

Figure 3.30. (a) Bright field micrograph of the $[Nb_6O_{17}]^{4-}$ nanoscrolls obtained by the protonation and exfoliation of KN. (b) EDP of a $[Nb_6O_{17}]^{4-}$ nanoscroll. (c) Bright field micrograph showing a mix of $[Nb_6O_{17}]^{4-}$ nanoscrolls and $[K_{4-x}Nb_6O_{17}]^{x-}$ nanosheets.

2.3.2. Exfoliation with n-alkylamine

As described in Chapter 1, the niobate nanosheets can be obtained by using propylammonium chloride directly with the KN phase (*i.e.* without protonation) [30,31], as described in the equation below:

$$K_4Nb_6O_{17} + xPA^+ + xCl^- \rightarrow x(PA)^+ [K_{4-x}Nb_6O_{17}]^{x-} + xKCl$$

The problem with this way of exfoliation is that KCl is formed in solution, requiring centrifugations and filtration or dialyze, which tend to decrease the nanosheets size. That is why it has been decided to use another way of exfoliation using the protonated niobate phase with propylamine (PA, C_3H_9N) or butylamine ($C_4H_{11}N$) [27,32]. Alkylamines easily get protonated with water, creating a balance in solution, as shown in equation (1). The formed hydroxides ions will react with the protons of the layered phase, and the alkylammonium ions (AA) will exfoliate and give the counter ion for the negative nanosheets (2).

$$CH_3–(CH_2)_n–NH_2 + H_2O \rightleftharpoons CH_3–(CH_2)_n–NH_3^+ + HO^- \qquad (1)$$

$$H_xK_{4-x}Nb_6O_{17} + x(AA)^+ + xHO^- \rightarrow x(AA)^+ [K_{4-x}Nb_6O_{17}]^{x-} + xH_2O \qquad (2)$$

The great advantage of this method is that no secondary phase is produced. However, due to the equations involved, it can be expected that the exfoliation time is longer than with TBAOH as the PA is a weak base, with a dissociation constant of $K_b = 4.7 \times 10^{-4}$.

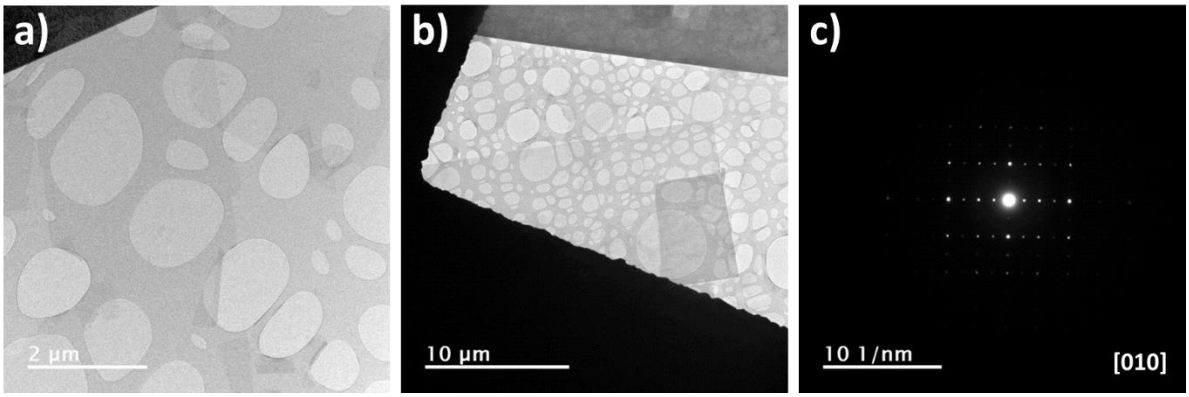

Figure 3.31. (a-b) Bright field micrographs of the $[K_{4-x}Nb_6O_{17}]^{x-}$ nanosheets obtained by the protonation and exfoliation of KN by *n*-alkylamine. (c) EDP of a single $[K_{4-x}Nb_6O_{17}]^{x-}$ nanosheet along the [010] axis.

Therefore, the protonated phase HKN was exfoliated using PA and butylamine, in molar ratios of 1:1, 1:2, 1:10, and 1:20 in 50 mL of pure water. The solutions are softly agitated for 24 hours using an oscillating device. Colloidal solutions of $[K_{4-x}Nb_6O_{17}]^{x-}$ nanosheets were obtained. The molar ratio of 1:10 was found to be optimal by comparing by TEM the different colloidal solutions. The bright field micrographs in Figure 3.31 show large and rectangular shape nanosheets up to 20 µm. The EDP along the [010] zone axis of a single $[K_{4-x}Nb_6O_{17}]^{x-}$ nanosheet is displayed in Figure 3.31c. It shows the [100]* and [001]* directions, corresponding to the measured lattice constants $a \simeq 7.88$ Å and $c \simeq 6.52$ Å. It is possible to observe different thicknesses of the nanosheets from 0.8 to 2 nm. The compositions of the $K_xNb_6O_y$ nanosheets measured by TEM-EDXS were different from one nanosheet to another, with $0 \leq x \leq 1$. The hypothesis which can be made from the composition and observations is that different types of nanosheets are obtained in the solution. Firstly, the interlayer II can be totally exfoliated leading to $[Nb_6O_{17}]^{4-}$ nanosheets ($x = 0$). Secondly, the interlayer II can be exfoliated but with some K^+ ions staying on the surface of the nanosheets ($0 \leq x \leq 1$). The last possibility is that the interlayer II is not exfoliated ($0 < x \leq 1$). The size of the nanosheets has also to be taken into consideration: the larger is the protonated crystal, the harder is the exfoliation.

2.4. Deposition on substrates using the Langmuir-Blodgett technique

The $[K_{4-x}Nb_6O_{17}]^{x-}$ nanosheets have never been deposited by the Langmuir-Blodgett technique according to the literature. Firstly, depositions tests have been performed from the TBAOH exfoliation. As mentioned in Paragraph 2.3.1., a mix of nanoscrolls and nanosheets is obtained in the solution. As a nanoscroll is logically denser

and has a smaller coverage area compared to a nanosheet, it can be expected that the nanosheets have more chance to be at the liquid/air interface than the nanoscrolls, which should tend to sink. Figure 3.32a shows an AFM image of the deposition on a glass substrate. It is clear on the image that the large majority of the deposition is made of nanoscrolls. Therefore, the depositions were focused only on *n*-alkylamine based exfoliations.

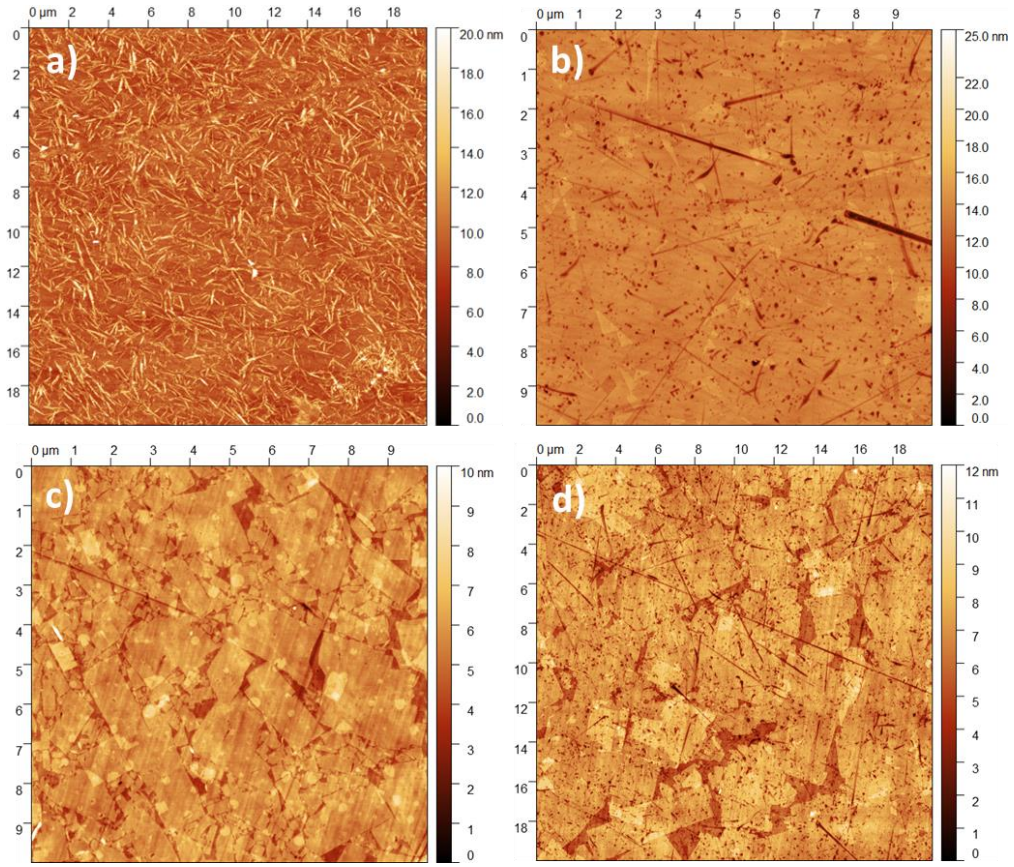

Figure 3.32. AFM images of the Langmuir-Blodgett deposition of $[K_{4-x}Nb_6O_{17}]^{x-}$ nanosheets. (a) Attempt of nanosheets deposition from the TBAOH exfoliation. A film of nanoscrolls is obtained. (b-c) Nanosheets deposition from the *n*-propylamine exfoliation. Both depositions are dense in nanosheets, but the thicknesses of the nanosheets of the two depositions are different. (d) Nanosheets deposition from the *n*-butylamine exfoliation.

Figure 3.32b,c show the depositions of nanosheets from an *n*-propylamine exfoliation. The two samples are made of a dense nanosheets monolayer, with different morphologies. In fig b, the nanosheets are very thin and it is difficult to see them on the substrate. The heights of the nanosheets were found to be between 1 to 1.5 nm. In Figure 3.32c, the nanosheets are thicker and can be seen very well. The heights have been measured from 1.5 to 2 nm. Thus, for the same type of exfoliation, two different thicknesses of nanosheets were obtained. For the exfoliation with *n*-butylamine, nanosheets of 2 nm thickness were also obtained (Figure 3.32d).

2.5. Deposition on substrates using the drop casting technique

Table 3.3. Deposition conditions of the $[K_{4-x}Nb_6O_{17}]^{x-}$ (KN) nanosheets on various substrates.

Substrates	Amount of KN parent phase	Ultrapure water	Absolute ethanol amount	Heating temperature	Amount of solution deposited/Substrate size
Silicon	40 µL	5 mL	200 µL	100°C	200 µL 10x10 mm
Silica (to optimize)	80 µL	5 mL	30 µL	120°C	150 µL 10x10 mm
Silica (Eagle glass) (to optimize)	80 µL	5 mL	30 µL	120°C	150 µL 10x10 mm

The deposition of $[K_{4-x}Nb_6O_{17}]^{x-}$ nanosheets by the drop casting technique has also never been reported before this work. The same deposition parameters as for $[Ca_2Nb_3O_{10}]^-$ nanosheets were used for the first attempts (Table 3.3). The AFM results displayed in Figure 3.33 show large nanosheets on SiO_2. However, important overlapping of the nanosheets is observed.

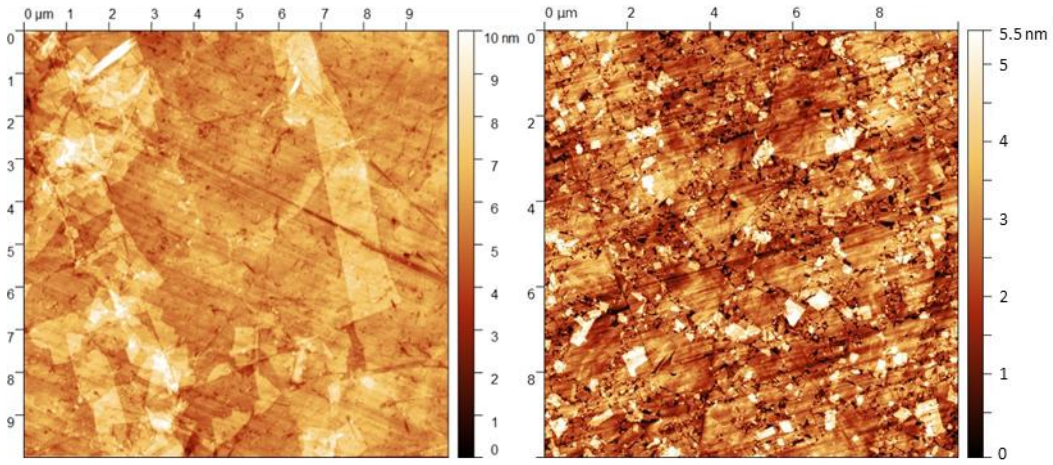

Figure 3.33. AFM images of the $[K_{4-x}Nb_6O_{17}]^{x-}$ nanosheets dense monolayer deposited by drop casting on silica.

As the exfoliant is different from the other nanosheets, the wettability of the liquid on the substrate can be different. Moreover, the concentration of the nanosheets in solution can be different depending on the nature of the nanosheets. Experiments are in progress to find the efficient parameters by varying the concentration of the nanosheets solution and the amount of ethanol in the solution to deposit.

2.6. In-plane diffraction of the $[K_{4-x}Nb_6O_{17}]^{x-}$ nanosheets

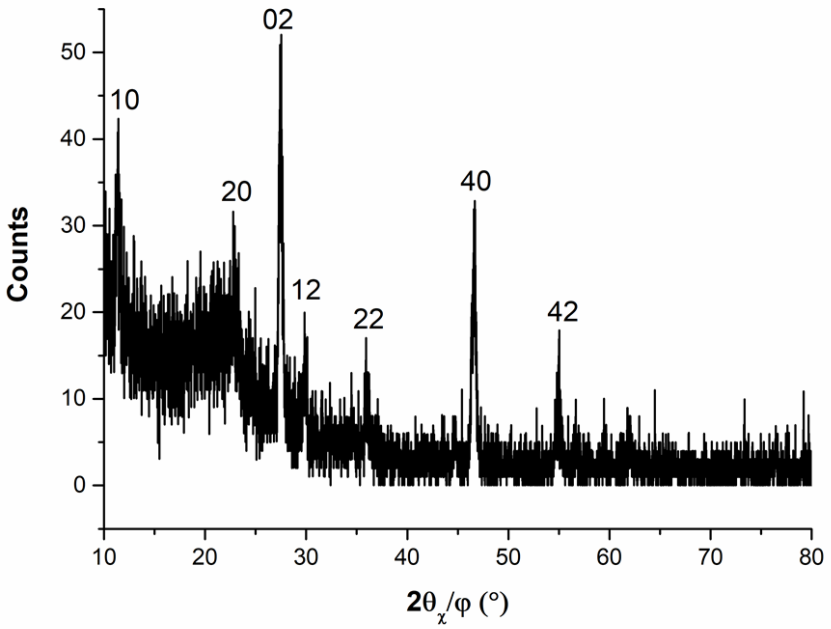

Figure 3.34. In-plane XRD diagram of $[K_{4-x}Nb_6O_{17}]^{x-}$ nanosheets deposited on SiO_2 substrate.

In-plane X-ray diffraction experiments have been performed on $[K_{4-x}Nb_6O_{17}]^{x-}$ nanosheets deposited on a SiO_2 substrate to measure their lattice parameters (Figure 3.34). The sample was prepared by drop casting and 3 layers were deposited on the substrate. The diffraction pattern obtained shows the reflections of the vertical plans. The nanosheets lattice parameters have been measured to be a = 7.76 Å from the 20 reflection and c = 6.45 Å from the 02 reflection, which is in good agreement with the theoretical values (a = 7.83 Å and c = 6.46 Å).

Conclusion

The synthesis of the $[K_{4-x}Nb_6O_{17}]^{x-}$ nanosheets have been successfully realized using *n*-propylammonium and *n*-butylammonium, avoiding the formation of nanoscrolls. These nanosheets have been successfully deposited onto glass substrates by the Langmuir-Blodgett and the drop casting techniques. However, the depositions parameters have to be adjusted to obtain a homogenous deposition and to allow the deposition on other substrates. Further experiments have to be realized to control the nanosheets thicknesses. Depositions of perovskites on these nanosheets are in progress in the CRISMAT laboratory to obtain their (110) orientation.

3. Synthesis, deposition, and characterizations of titanate nanosheets

These results have been obtained within the framework of the internship of Amélia Baucher (master student).

3.1. Synthesis of the titanate nanosheets

3.1.1. Synthesis of $K_{0.8}Ti_{1.73}Li_{0.27}O_4$ by molten salt synthesis

Crystals of potassium titanate $K_{0.8}Ti_{1.73}Li_{0.27}O_4$ (KTLO) were synthesized by K_2MoO_4 MSS, based on the result of Tanaka *et al.* [6]. K_2CO_3 (Acros Organics, 99%), TiO_2 (Acros Organics, 98-100%), Li_2CO_3 (Alfa Aesar, 99%), and MoO_3 (Alfa Aesar, 99.95%) precursors in a molar ratio of 1.73:1.67:0.13:1.27 were ball-milled in ethanol for 5 h, and the powder was placed in a platinum crucible. The powder was treated at 1200°C for 10 h, then slowly cooled at 950°C by decreasing the temperature at a speed of 4°C/h. The powder was then naturally cooled at room temperature and washed 3 times in 250 mL of water to remove the flux salts. The general equations of these reactions are detailed below:

$$1.67K_2CO_3 + 1.73TiO_2 + 0.135Li_2CO_3 + 1.27MoO_3 \rightarrow K_{0.8}Ti_{1.73}Li_{0.27}O_4 + 1.27K_2MoO_4 + 1.805CO_2$$

The XRD pattern of the powder displayed Figure 3.35 confirms that the expected KTLO phase was obtained (JCPDS card N°01–089–5420, Annexe A, p.198), with the lattice parameters a = 3.814 Å, b = 15.594 Å, and c = 2.929 Å. Minor $K_2Li_6O_{13}$ and $Ti_{1.67}Li_{1.33}O_{13}$ secondary phases impoverished in potassium were also obtained, as reported in the literature [6].

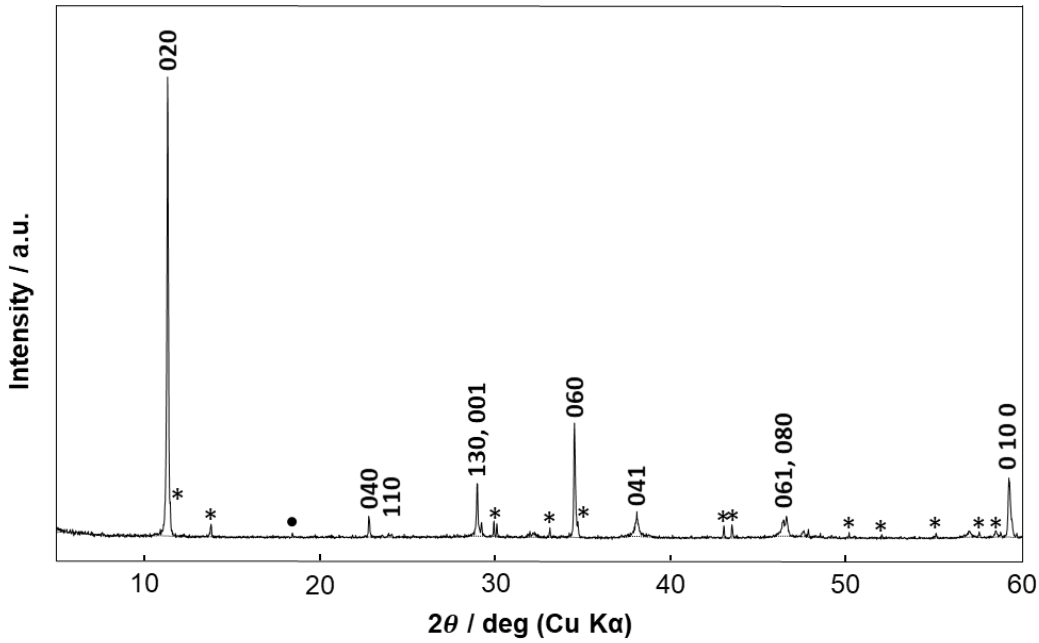

Figure 3.35. XRD pattern of the KTLO powder obtained by MSS. The * symbol corresponds to $K_2Li_6O_{13}$ and • to $Ti_{1.67}Li_{1.33}O_{13}$.

The crystals average lateral size of this compound observed by SEM was from 10 to 100 µm (Figure 3.36), but crystals with a size up to the millimeter were also observed under an optical microscope, as shown in the photography in Figure 3.35b. The SEM-EDXS analyses show a K/Ti ratio of 0.41, which is lighter than the theoretical K/Ti ratio (0.46), and confirm the lack of potassium during the synthesis.

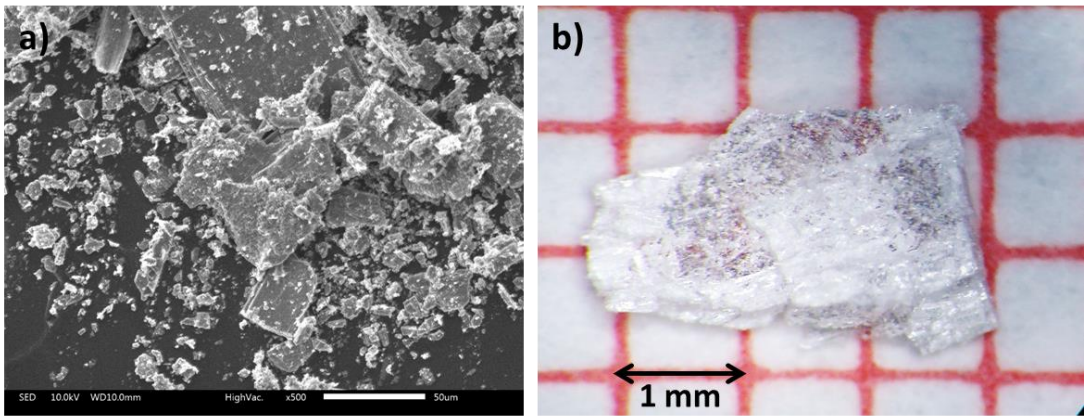

Figure 3.36. (a) SEM image of KTLO crystals. (b) Photography of a KTLO crystal.

3.2. Protonation of the $K_{0.8}Ti_{1.73}Li_{0.27}O_4$ phase

The layered materials obtained were treated with HNO_3 6M. For these phases, the full protonation was obtained after 24 hours, which is much shorter than for $HCa_2Nb_3O_{10}$ and $H_{2+x}K_{2-x}Nb_6O_{17}$. The powders were then filtered and washed several times with

distilled water and dried. The protonated $H_{1.07}Ti_{1.73}O_4$ (HTO) phase was obtained. The results on titanate compounds are similar to those of Tanaka *et al*. [6]. Compared to the parent phase, the (0*k*0) peaks of HTO are shifted toward lower angles, due to the increase of the interlamellar space induced by the K^+ and Li^+ exchanged by H^+ ions and the insertion of water (Figure 3.37).

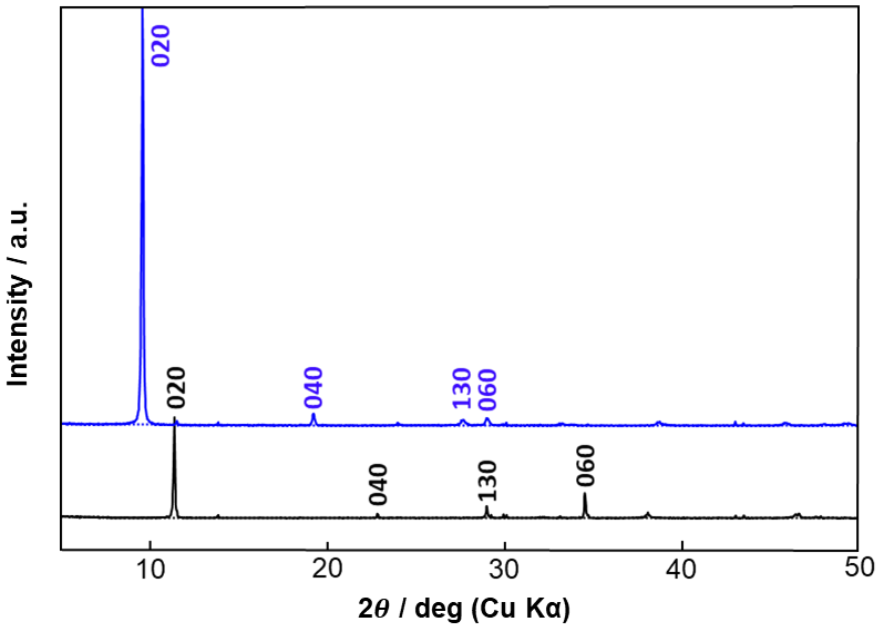

Figure 3.37. Comparison between the XRD powder patterns of the KTLO phase (black) and the HTO phase (blue).

3.3. Exfoliation of the $H_{1.07}Ti_{1.73}O_4$ phase

The exfoliation of $H_{1.07}Ti_{1.73}O_4$ was carried out using TBAOH in a molar ratio 1:1 in 50 mL of pure water. The solution is softly agitated for 1 week using an oscillating device. A colloidal solution of $[Ti_{0.87}O_2]^{0.52-}$ is obtained.

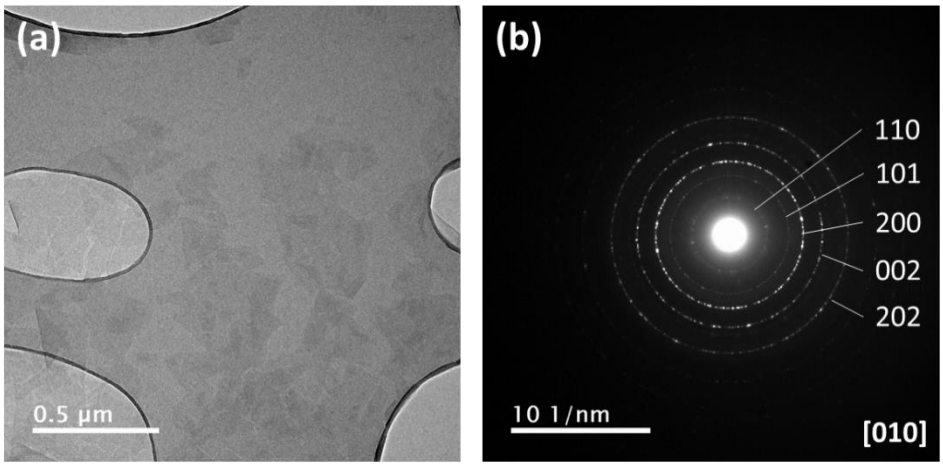

Figure 3.38. (a) Brightfield micrograph of the $[Ti_{0.87}O_2]^{0.52-}$ nanosheets. (b) EDP of superposed nanosheets along the [010] axis.

As shown in the TEM micrograph displayed in Figure 3.38, nanosheets from 0.1 µm to 1 µm were obtained. The electron diffraction pattern (Figure 3.38b) shows the Ewald sphere induced by nanosheets superimposed of each others. The indexation of the rings pattern shows that the good phase is obtained.

3.4. Deposition on substrates using the drop casting technique

3.4.1. Deposition of the $[Ti_{0.87}O_2]^{0.52-}$ nanosheets by drop casting

Table 3.4. Deposition conditions of the $[Ti_{0.87}O_2]^{0.52-}$ nanosheets on various substrates.

Substrates	Amount of $Ti_{0.87}O_2$ parent phase	Ultrapure water	Absolute ethanol amount	Heating temperature	Amount of solution deposited/Substrate size
Silica	100 µL	5 mL	60 µL	120°C	150 µL 10x10 mm
Slicon (Eagle glass)	80 µL	5 mL	60 µL	120°C	150 µL 10x10 mm
Pt/Si	40 µL	5 mL	100 µL	100°C	250 µL 10x10 mm

Drop casting depositions have been realized on silicon and glass substrates, following the conditions of Shi *et al.* [18]. In these attempts, they have shown to present high overlapping of nanosheets, due to a too high concentration of nanosheets in the solution. After corrections, dense nanosheets monolayer have been successfully obtained, as shown in Figure 3.39 The conditions used are detailed in Table 3.4.

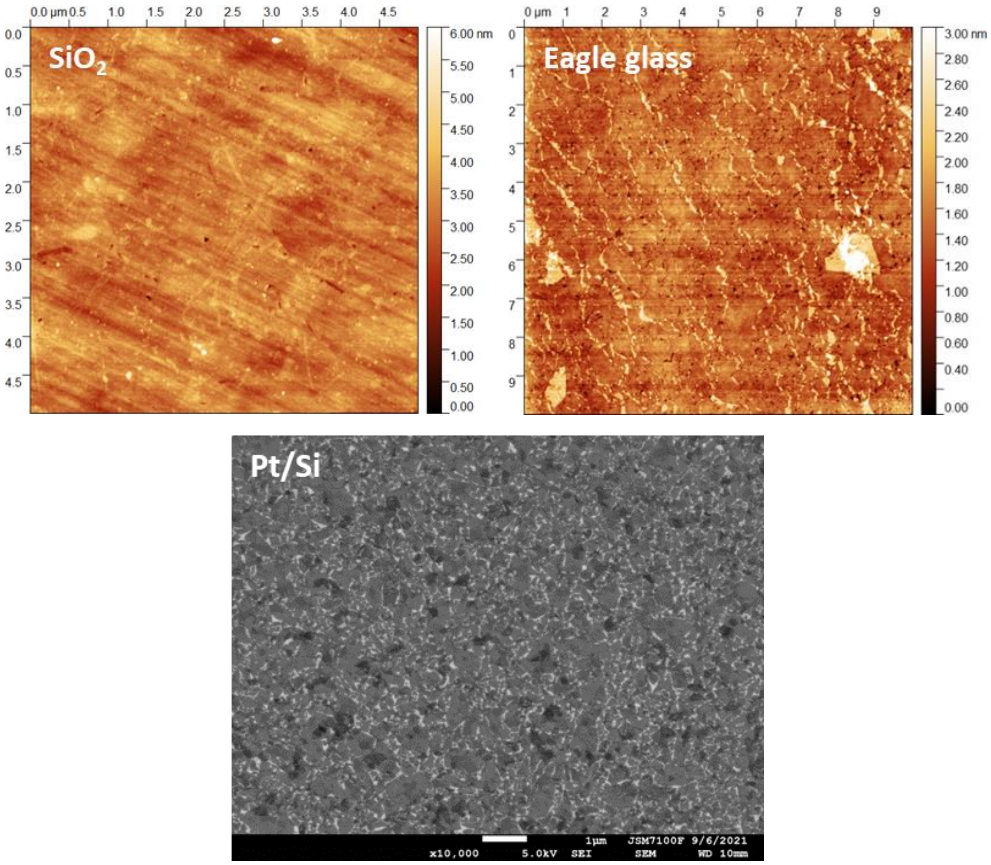

Figure 3.39. AFM and SEM micrographs of $[Ti_{0.87}O_2]^{0.52-}$ nanosheets deposited on different substrates.

3.5. In-plane diffraction of the $[Ti_{0.87}O_2]^{0.52-}$ nanosheets

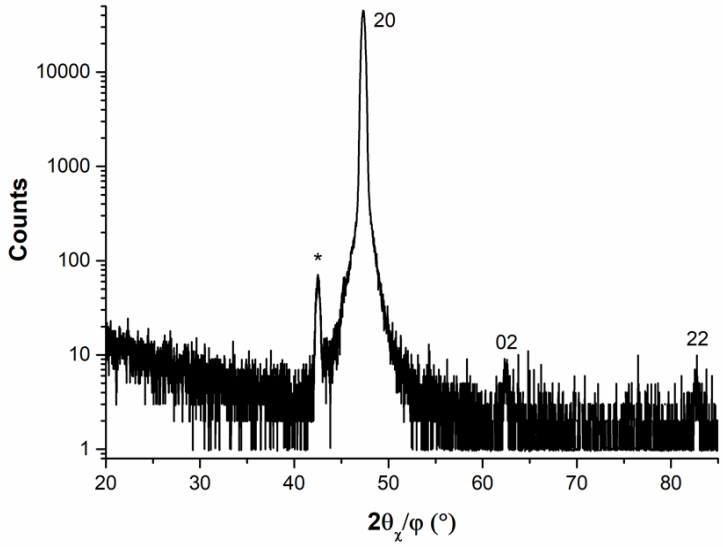

Figure 3.40. In-plane XRD diagram of $[Ti_{0.87}O_2]^{0.52-}$ nanosheets deposited on Si substrate. *: K_β line of the 20 reflections.

In-plane X-ray diffraction experiments have been performed on $[Ti_{0.87}O_2]^{0.52-}$ nanosheets deposited on a Si substrate to measure their lattice parameters (Figure 3.40).

The sample was prepared by drop casting and 3 layers were deposited on the substrate. The diffraction pattern obtained shows the reflections of the vertical plans. The nanosheets lattice parameters have been measured to be a = 3.84 Å from the 20 reflection and c = 2.97 Å from the 02 reflection, which is in good agreement with the theoretical values (a = 3.824 Å and c = 2.973 Å). These values are also closed to those reported in the literature by Fukuda *et al*. ($a \simeq$ 3.760 Å and $c \simeq$ 2.967 Å) [33].

Conclusion

The $[Ti_{0.87}O_2]^{0.52-}$ nanosheets were successfully obtained from the protonation and the exfoliation of the $K_{0.8}Ti_{1.73}Li_{0.27}O_4$ phase. Dense monolayers of nanosheets were obtained by the drop casting technique on various substrates. The $[Ti_{0.87}O_2]^{0.52-}$ nanosheets will be used for the growth of (110) perovskites, in collaboration with the CRISMAT.

4. Synthesis, deposition, and characterizations of $[Cs_4W_{11}O_{36}]^{2-}$ nanosheets

4.1. Synthesis of the $Cs_6W_{11}O_{36}$ phase

The $Cs_6W_{11}O_{36}$ powder (CWO) was synthesized according to the method of Miyauchi *et al.* [34]. Cs_2CO_3 (Sigma Aldrich, 99.9%) and WO_3 (Alfa Aesar, 99.8%) precursors (Cs:W = 3:11) were ball-milled in ethanol for 5 h. The powder was placed in an alumina crucible and treated for 6 h at 900°C. The powder was filtered and dried. The $Cs_4W_{11}O_{35}$ (JCPDS card n° 00-051-1891, Annexe A, p. 200) and $Cs_{0.3}WO_3$ (JCPDS card n° 01-081-1244, Annexe A, p. 201) phases were obtained, which present a deficit of Cs compared to the expected phase. Thus, an excess of Cs_2CO_3 was needed in order to counterbalance the cesium loss caused by the volatility of Cs_2O formed at high temperature. For a ratio of Cs:W = 4:11 [35], the $CsW_{1.6}O_6$ phase (JCPDS card No. n° 01-081-0012, Annexe A, p. 203) was synthesized, which is over in Cs compared to the expected phase. It was then needed to vary the Cs quantity between 3:11 and 4:11, to obtain $Cs_6W_{11}O_{36}$. A ratio of 3.75:11 leads to large bluish and greyish crystals, as expected and described in Chapter 1 3.4.a. The XRD pattern of the powder is displayed in Figure 3.41. The CWO phase (JCPDS card n° 01-083-1021, Annexe A, p. 204) is obtained with the

secondary phase $Cs_4W_{11}O_{35}$. The latter is also a layered oxide phase crystallizing in an orthorhombic lattice with a = 14.669 Å, b = 52.387 Å, and c = 7.736 Å which is possible to protonate and exfoliate [36]. This phase can also be described as a pseudo hexagonal (ph) lattice with a_{ph} = 14.669 Å and b_{ph} = 15.011 Å, which is close to $2a$ = 14.552 Å of $Cs_6W_{11}O_{36}$. Therefore, this phase is not problematic for oxide growth application.

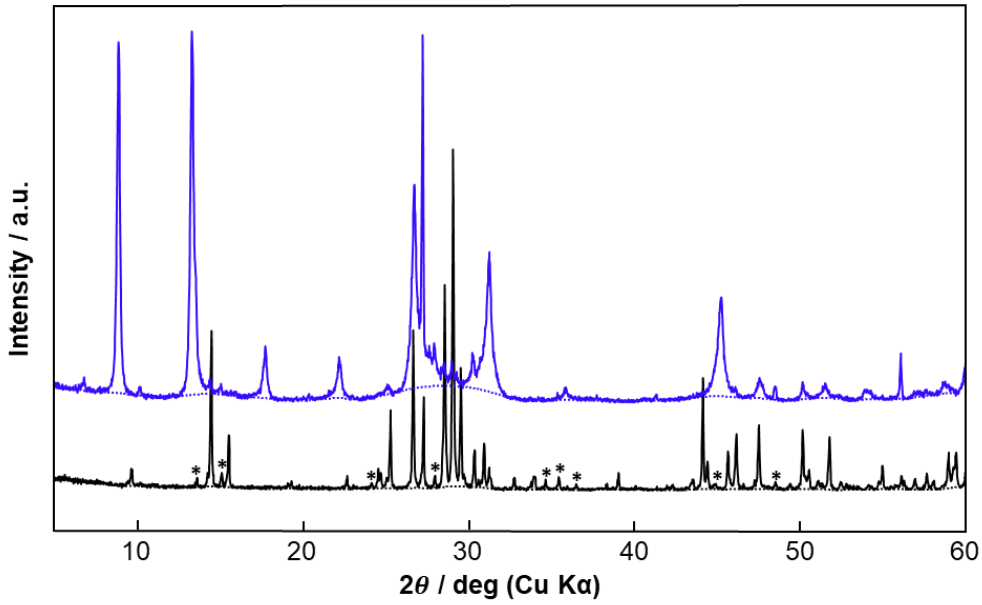

Figure 3.41. XRD diagram of the CWO phase. *: $Cs_4W_{11}O_{35}$ phase.

The SEM micrograph of the powder shows large CWO crystals with a lateral size from 10 µm to 1 mm (Figure 3.42). The composition was found to be $Cs_{6.8\pm0.7}W_{11\pm1.1}O_x$ SEM-EDXS, which is not very representative as the atomic percentages' uncertainties are important. It is thus better to discuss on the composition using the atomic ratio Cs/W. A ratio equal to 0.620 has been obtained, higher than the 0.545 ratio. Higher Cs composition (6.36:11) was also reported in the literature [35,37].

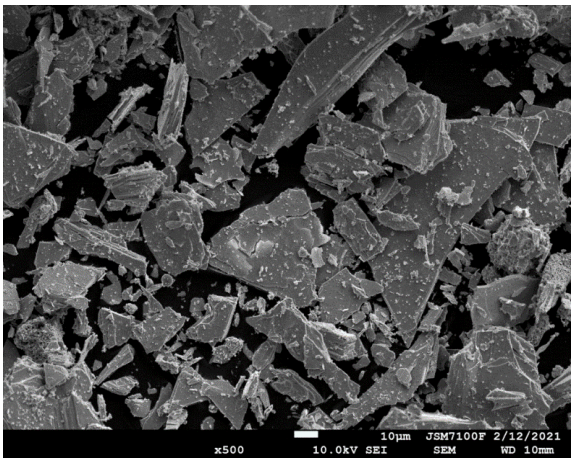

Figure 3.42. SEM micrograph of CWO crystals.

4.2. Protonation of the $Cs_6W_{11}O_{36}$ phase

The protonation of the CWO phase was realized in the same conditions as for KCN and KN phases. The protonated phase was obtained by treating 1 g of CWO powder in 20 mL of 6 M nitric acid for 3 days. The acid was replaced every 24 h by fresh acid to obtain the protonated phase $H_2Cs_4W_{11}O_{36}$ phase (HCWO). After 3 days, the powder was filtered and washed several times with distilled water and dried. The powder has lost its blue color, indicating the exchange of the Cs^+ by proton, and formed a sticky white paste. The XRD pattern of the protonated phase is displayed Figure 3.41. It can be observed a shift of the (00*l*) peaks between the parent and the protonated phase, as observed for KCN with its protonated phase. The insertion of water molecules inside the lamellar compound modifies the value of the lattice constant *c*. Fukuda *et al*. found that the protonated phase was $H_{2.1}Cs_{3.9}W_{11}O_{36}{\cdot}6H_2O$, which also explains the doughy behavior of the powder.

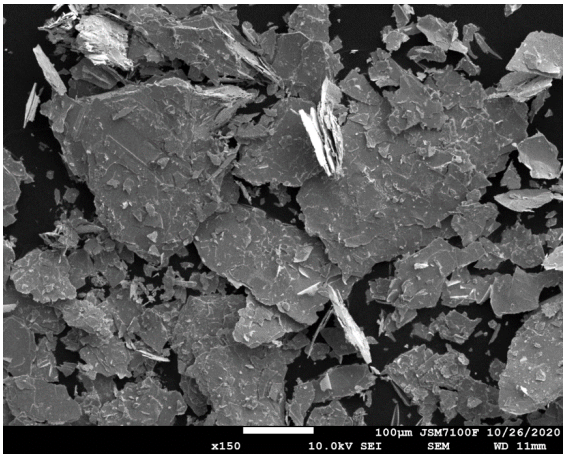

Figure 3.43. SEM micrograph of HCWO crystals.

The SEM micrograph in Figure 3.43. shows large HCWO crystals, which kept the same size as the parent phase. The composition measured by SEM-EDXS was found to be around $H_{1.6}Cs_{4.4\pm0.4}W_{11\pm1.1}O_x$ (Cs:W atomic ratio = 0.403), showing that the protonation might not be total.

4.3. Exfoliation of the $H_2Cs_4W_{11}O_{36}$ phase

The protonated phase HCWO was then exfoliated using TBAOH in a molar ratio 1:2 in 50 mL of pure water. The solution was softly agitated for 24 hours using an oscillating device. A colloidal solution of $[Cs_4W_{11}O_{36}]^{2-}$ nanosheets was obtained. TEM experiments have then been realized on the exfoliated solution. The solution had to be diluted 5 times

because the first sample was too rich in nanosheets. The micrographs and EDP results are shown in Figure 3.44. Even after dilution, as presented in Figure 3.44a,b, the concentration of the cesium tungstate nanosheets is important on the grid. Various lateral sizes of nanosheets are observed: from 0.5 µm up to 20 µm.

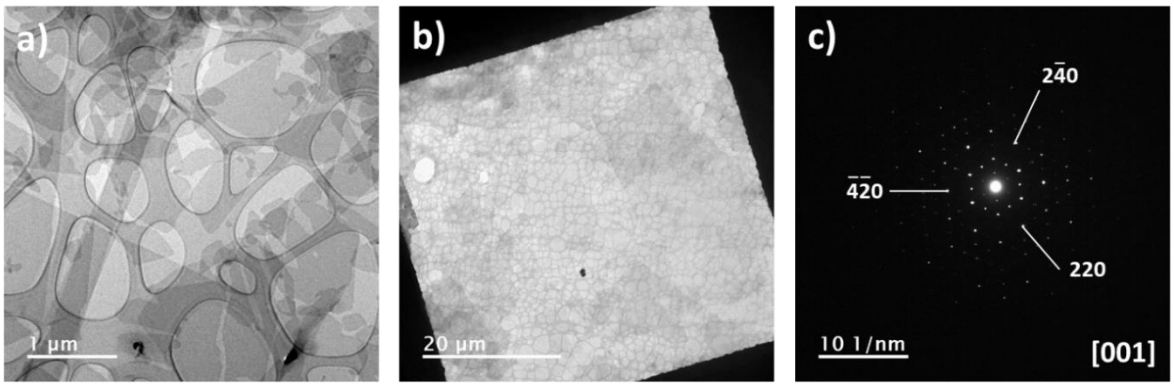

Figure 3.44. (a) Brightfield micrograph of the $[Cs_4W_{11}O_{36}]^{2-}$ nanosheets obtained by the protonation and exfoliation of HCWO by TBAOH. (b) Brightfield micrograph showing large $[Cs_4W_{11}O_{36}]^{2-}$ nanosheets (~20 µm). (c) EDP of a single $[Cs_4W_{11}O_{36}]^{2-}$ nanosheet along the [001] axis.

The TEM-EDXS analysis gave the composition $Cs_{4.4\pm0.4}W_{11\pm1.1}O_x$ for the nanosheets on average, which is consistent with the SEM-EDXS results of the protonated phase. In Figure 3.44c is displayed the EDP of a $[Cs_4W_{11}O_{36}]^{2-}$ nanosheet along the [001] axis. The lattice parameters were found to be $a = b \simeq 7.46$ Å, which is close to its theoretical values. All the results are similar to the literature [35,38].

4.4. Deposition on substrates using the Langmuir-Blodgett technique

Few tries of depositions of the $[Cs_4W_{11}O_{36}]^{2-}$ nanosheets have been realized on SiO_2 substrates by the Langmuir-Blodgett technique. Different dilutions (from 4 to 8 times in volume) have been realized and the covering depositions with these solutions have been analyzed by AFM and/or SEM. The results have shown that the solution diluted 8 times gave the best result, which is different from the reported dilution of the literature. The depositions were realized as described in the previous chapter. The value of surface pressure to obtain a good covering was between 8 and 13 mN/m depending on the depositions conditions. High coverages were obtained for these depositions, even if some overlaps are present (Figure 3.45).

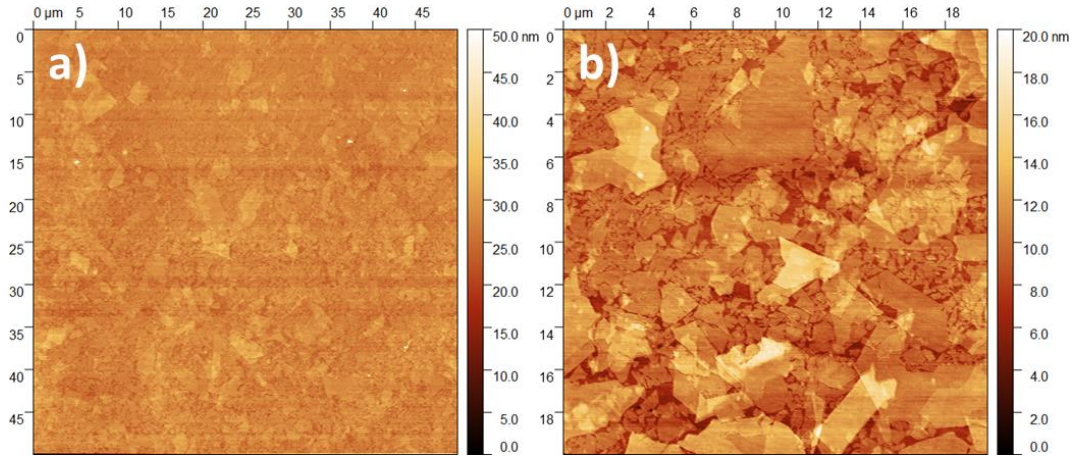

Figure 3.45. AFM images of the Langmuir-Blodgett deposition of $[Cs_4W_{11}O_{36}]^{2-}$ nanosheets. (a) Large AFM image 50 x 50 µm, showing a dense coverage on the surface of the substrate. (b) Magnification 20 x 20 µm of the zone showed in (a).

Only a few depositions have been made using the Langmuir-Blodgett technique because the developments of the cesium tungstate nanosheets were made at the same time as the development of the drop casting technique in the laboratory. Thus, the majority of the depositions of this type of nanosheets have been made by drop casting.

4.5. Deposition on substrates using the drop casting technique

Table 3.5. Deposition conditions of the $[Cs_4W_6O_{36}]^{2-}$ (CWO) nanosheets on various substrates.

Substrates	Amount of CWO parent phase	Ultrapure water volume	Absolute ethanol amount	Heating temperature	Amount of solution deposited/Substrate size
Silica	100 µL	5 mL	60 µL	120°C	150 µL 10x10 mm
Silica (Eagle glass)	90 µL	5 mL	60 µL	120°C	150 µL 10x10 mm
Silicon	40 µL (larger amount needed)	5 mL	200 µL	100°C	150 µL 10x10 mm

The $[Cs_4W_{11}O_{36}]^{2-}$ nanosheets have been deposited on Si and SiO_2 substrates by the drop casting technique (Table 3.5). For the deposition of Si, the parameters have not been reported by Shi *et al.* The parameters of deposition of $[Ca_2Nb_3O_{10}]^-$ on Si were used for the first test. As shown in Figure 3.46a, the substrate is totally covered by nanosheets, even if some overlaps of nanosheets can be observed. The solution has thus to be slightly diluted to obtain a perfect result. For the deposition on SiO_2 substrates, the parameters have been

reported by Shi *et al*. The deposition leads to a highly densified nanosheets film (Figure 3.46), with very few nanosheets overlaps. The transfer of this type of nanosheets on various substrates works very well.

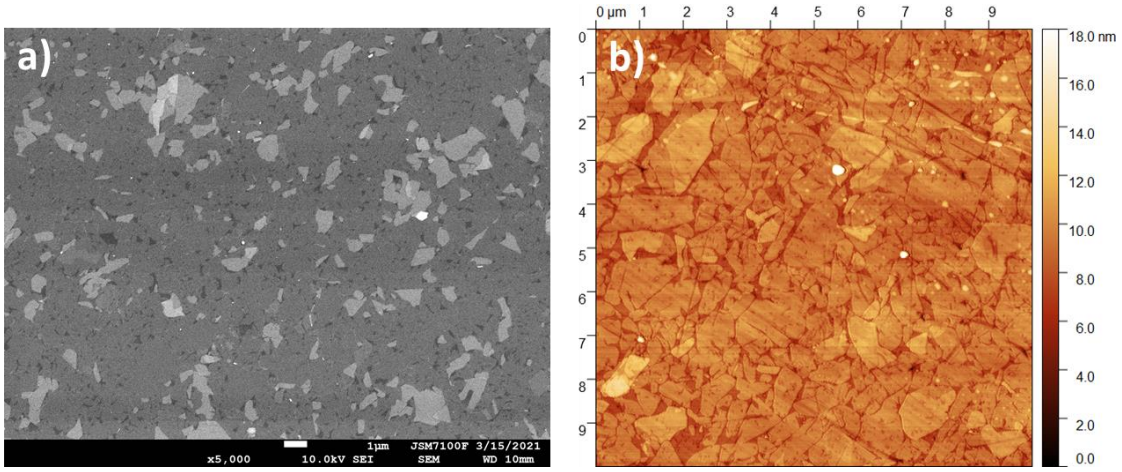

Figure 3.46. Micrographs of the depositions of $[Cs_4W_{11}O_{36}]^{2-}$ nanosheets. (a) SEM micrograph of the nanosheets deposited on Si. (b) AFM micrograph of the nanosheets deposited on SiO_2.

3.6. In-plane diffraction of the $[Cs_4W_{11}O_{36}]^{2-}$ nanosheets

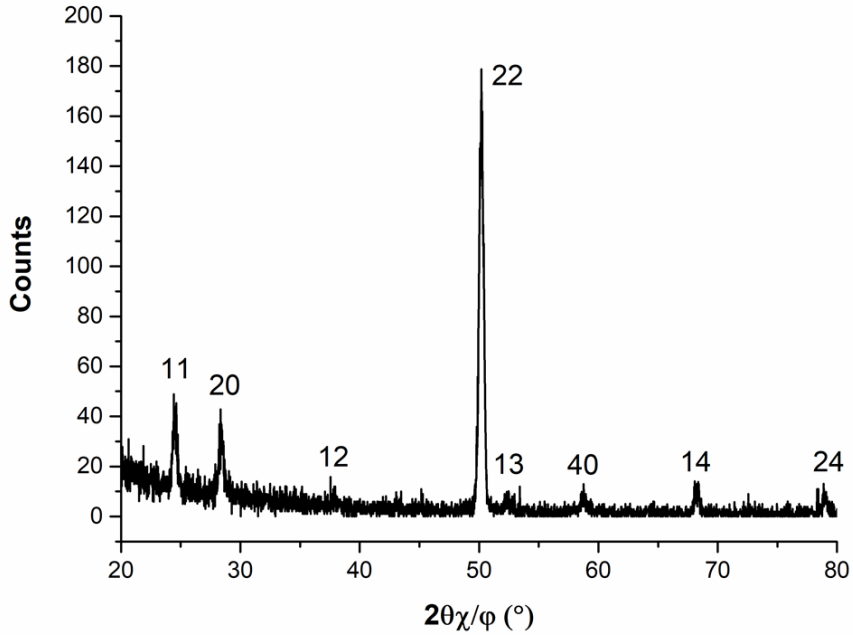

Figure 3.47. In-plane XRD diagram of $[Cs_4W_{11}O_{36}]^{2-}$ nanosheets deposited on Si substrate.

In-plane X-ray diffraction experiments have been performed on $[Cs_4W_{11}O_{36}]^{2-}$ nanosheets deposited on a Si substrate to measure their lattice parameters (Figure 3.47). The sample was prepared by drop casting and 3 layers were deposited on the substrate.

The diffraction pattern obtained shows the reflections of the vertical plans. The nanosheets lattice parameters have been measured to be $a \simeq 7.255$ Å from the 22 reflection, which is in good agreement with the theoretical value ($a \simeq 7.261$ Å). This value is also closed to the one obtained by Fukuda *et al.* (a ≃ 7.269 Å) [35].

Conclusion

The $[Cs_4W_{11}O_{36}]^{2-}$ nanosheets were successfully obtained by the protonation and exfoliation of the $Cs_6W_{11}O_{36}$ phase. The deposition by the Langmuir-Blodgett method and the drop casting technique show high coverage on the surface of various substrates. Depositions of perovskites on these nanosheets are in progress to obtain their (111) orientation, in collaboration with the CRISMAT laboratory.

5. Synthesis and characterizations of $[MnO_2]^{\delta-}$ nanosheets

To obtain MnO_2 nanosheets, several syntheses have been realized during this thesis. In this part, the first results of two methods of synthesis are described: the oxidation of $MnCl_2$ by H_2O_2 and the reduction of $KMnO_4$ by the sodium dodecyl sulfate (SDS).

5.1. Synthesis of MnO_2 nanosheets by the oxidation of $MnCl_2$

The synthesis of MnO_2 nanosheets by the oxidation of $MnCl_2$ has been realized according to the method of Kay *et al.* [39,40]. 20 mL of an aqueous solution of TBAOH 0.6 M and 3 wt% H_2O_2 was added to 0.3 M solution of $MnCl_2$. The red/brown obtained solution was diluted to reach 50 mL and agitated 24 hours on an oscillating plate (Figure 3.48a).

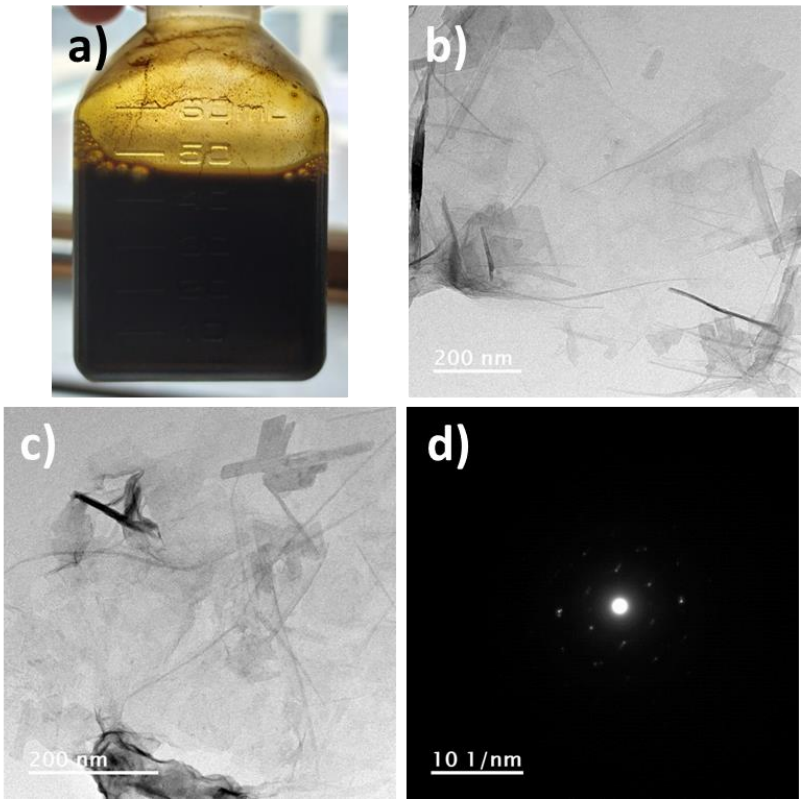

Figure 3.48. (a) The colloidal solution obtained after synthesis. (b-c) TEM micrographs of the colloidal solutions. Nanosheets, nanowires, and nanocrystals are observed. (d) EDP of a MnO_2 nanosheet.

This synthesis has the great advantage to be very fast (some seconds) and remain stable in time. However, the TEM micrographs displayed in Figure 48b,c show a mix of nanosheets, nanowires, and nanocrystals, with a lateral size from 150 to 200 nm, which could be attributed to different allotropic forms of MnO_2. This result is different from those obtained in the literature where only nanosheets were obtained [40]. Furthermore, TEM-EDXS analyses show 98% of Mn, with pollution of 2% by Ca and S atoms, which might be induced by the glassware used. Further investigations are in progress to obtain the nanosheets by this method.

5.2. Synthesis of MnO_2 nanosheets by the reduction of $KMnO_4$

The synthesis of MnO_2 nanosheets by the reduction of $KMnO_4$ has been realized according to the method of Liu *et al* [41]. SDS ($NaC_{12}H_{25}SO_4$) have been used as the reducing agent in acidic solution, following the proposed equations:

$$[C_{12}H_{25}SO_4]^- + H_2O \rightarrow C_{12}H_{25}OH + H^+ + SO_4^{2-} \quad (1)$$

$$3C_{12}H_{25}OH + 4MnO_4^- + 4H^+ \rightarrow 3C_{11}H_{23}COOH + 4MnO_2 + 5H_2O \quad (2)$$

For this synthesis, 16 mL of SDS 0.055 M and 0.8 mL of H_2SO_4 0.1 M were added into 142 mL of distilled water. The solution was heated 15 mn at 95°C. 1.6 mL $KMnO_4$ 0.05 mM was then added and the solution was stirred and heated for 60 min. A dark brown colloidal solution was obtained and cooled in the fridge overnight. 25 mL of the colloidal solution were then centrifuged at 5000 rpm for 20 mn. A red/brown layered solid was obtained (Figure 3.49a). The liquid was removed and distilled water was added before new centrifugation at 10000 rpm for 20 mn. These steps are repeated 4 times: 2 times with ethanol and 2 times with ultrapure water. The obtained solid is finally redissolved in ultrapure water with ultrasounds for 15 mn.

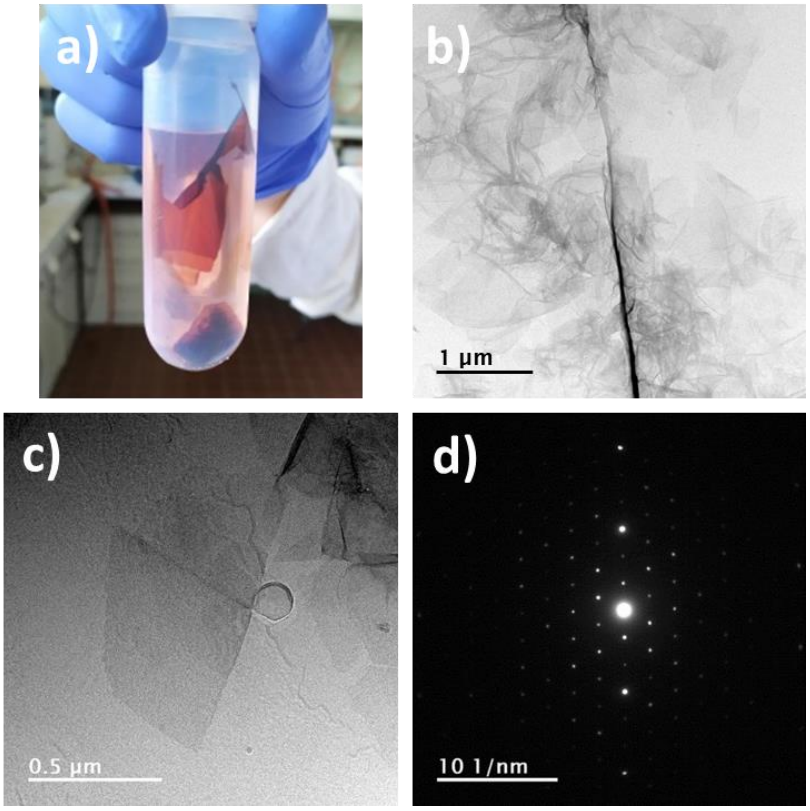

Figure 3.49. (a) Photography of the brown/red solid obtained after centrifugation of the MnO_2 colloidal solution. (b-c) TEM micrographs of the MnO_2 nanosheets. (d) EDP of a MnO_2 crystal.

TEM experiments show $[MnO_2]^{\delta-}$ nanosheets with a lateral size from 0.5 to 5 µm (Figure 49b,c), which is much larger than the previous method. TEM-EDXS analysis only shows the presence of Mn atoms, which proves that all the residues of SDS were eliminated.

Despite promising results, the solutions have shown to be unstable in time. After 2 weeks in the fridge, the colloidal solutions have precipitated, which is 4 weeks earlier than the time reported in the literature [41]. Drop casting depositions of these nanosheets

are in progress. The depositions need to be fast and it will be important to verify that the nanosheets monolayer remains stable in time.

Conclusion

$[MnO_2]^{\delta-}$ nanosheets have been synthesized by the oxidation of $MnCl_2$ by H_2O_2 and by the reduction of $KMnO_4$ by SDS. The reduction synthesis has shown to be very fast. However, a mix of nanosheets, nanowires, and nanocrystals with a lateral size of 200 nm, along with Ca and S pollutions have been obtained. Further experiments need to be done to master this synthesis. For the oxidation synthesis, large $[MnO_2]^{\delta-}$ nanosheets from 500 to 4 µm have been obtained without any secondary phase and pollutions. However, the solution is stable for only 2 weeks. The next step is to deposit the $[MnO_2]^{\delta-}$ nanosheets on various substrates, study their stability. Then, depositions of perovskites on these nanosheets are planned to obtain their (111) orientation.

Conclusions and perspectives

In this chapter were presented the different syntheses, depositions, and characterizations of nanosheets realized during this thesis.

The $[Ca_2Nb_3O_{10}]^-$ nanosheets were successfully obtained and deposited on various substrates by the Langmuir-Blodgett and the drop casting techniques. Syntheses in a platinum crucible are in progress to obtain homogenous-sized crystals to get larger nanosheets after exfoliation. It has also been shown that the $[Ca_2Nb_3O_{10}]^-$ nanosheets resist to HF treatment and that it is possible to deoxidize Si substrate even after the deposition of the nanosheets. The results concerning the deposition of various perovskites thin films on CNO nanosheets are presented in the chapter 4.

The nanosheets $[K_{4-x}Nb_6O_{17}]^{x-}$ were successfully obtained and deposited for the first time by the Langmuir-Blodgett and the drop casting techniques. However, further investigations on the exfoliation are needed to master the thickness of the nanosheets. Depositions of perovskites on these nanosheets are in progress to obtain their (110) orientation, in collaboration with the CRISMAT laboratory.

$[Ti_{0.87}O_2]^{0.52-}$ nanosheets were also successfully obtained. Large crystals were obtained by MSS and the nanosheets were densely deposited on silica substrates by the

drop casting technique. The $[Ti_{0.87}O_2]^{0.52-}$ will be used for the growth perovskite in their (110) orientation.

$[Cs_4W_{11}O_{36}]^{2-}$ were successfully obtained and deposited on various substrates by the Langmuir-Blodgett and the drop casting techniques. Depositions of perovskites on these nanosheets are in progress to obtain their (111) orientation, in collaboration with the CRISMAT laboratory.

$[MnO_2]^{\delta-}$ nanosheets were synthesized by the oxidation of $MnCl_2$ and the reduction reaction of $KMnO_4$. The results are promising but further investigations need to be performed to obtain pure and stable solution of nanosheets. Depositions on substrates are in progress and will be used for the growth of perovskites in their (111) orientation.

References

[1] T. Tokumitsu, K. Toda, T. Aoyagi, D. Sakuraba, K. Uematsu, M. Sato, Powder Neutron Diffraction Study of Layered Perovskite, $KCa_2Nb_3O_{10}$, J. Ceram. Soc. Japan. 114 (2006) 795–797. https://doi.org/10.2109/jcersj.114.795.

[2] P.T.P. Le, J.E. ten Elshof, G. Koster, Shape Control of $Ca_2Nb_3O_{10}$ Nanosheets: Paving the Way for Monolithic Integration of Functional Oxides with CMOS, ACS Appl. Nano Mater. 3 (2020) 9487–9493. https://doi.org/10.1021/acsanm.0c02137.

[3] Y. Song, N. Iyi, T. Hoshide, T.C. Ozawa, Y. Ebina, R. Ma, N. Miyamoto, T. Sasaki, Accordion-like swelling of layered perovskite crystals via massive permeation of aqueous solutions into 2D oxide galleries, Chem. Commun. 51 (2015) 17068–17071. https://doi.org/10.1039/C5CC05408G.

[4] H. Yuan, M. Nguyen, T. Hammer, G. Koster, G. Rijnders, J.E. ten Elshof, Synthesis of $KCa_2Nb_3O_{10}$ Crystals with Varying Grain Sizes and Their Nanosheet Monolayer Films As Seed Layers for PiezoMEMS Applications, ACS Appl. Mater. Interfaces. 7 (2015) 27473–27478. https://doi.org/10.1021/acsami.5b09456.

[5] P.T.P. Le, K. Hofhuis, A. Rana, M. Huijben, H. Hilgenkamp, G.A.J.H.M. Rijnders, J.E. ten Elshof, G. Koster, N. Gauquelin, G. Lumbeeck, C. Schüßler-Langeheine, H. Popescu, F. Fortuna, S. Smit, X.H. Verbeek, G. Araizi-Kanoutas, S. Mishra, I. Vaskivskyi, H.A. Dürr, M.S. Golden, Tailoring Vanadium Dioxide Film Orientation Using Nanosheets: a Combined Microscopy, Diffraction, Transport, and Soft X-Ray in Transmission Study, Adv. Funct. Mater. 30 (2020) 1900028. https://doi.org/10.1002/adfm.201900028.

[6] T. Tanaka, Y. Ebina, K. Takada, K. Kurashima, T. Sasaki, Oversized Titania Nanosheet Crystallites Derived from Flux-Grown Layered Titanate Single Crystals, Chem. Mater. 15 (2003) 3564–3568. https://doi.org/10.1021/cm034307j.

[7] L.-Q. Cheng, K. Wang, J.-F. Li, Synthesis of highly piezoelectric lead-free $(K,Na)NbO_3$ one-dimensional perovskite nanostructures, Chem. Commun. 49 (2013) 4003. https://doi.org/10.1039/c3cc41371c.

[8] L. Cheng, K. Chen, Z. Xu, Simple preparation method of functional ceramic niobium potassium oxide $K_6Nb_{10.8}O_{30}$ nanowire, CN110483043, 2019.

[9] Y. Ebina, K. Akatsuka, K. Fukuda, T. Sasaki, Synthesis and In Situ X-ray Diffraction Characterization of Two-Dimensional Perovskite-Type Oxide Colloids with a Controlled Molecular Thickness, Chem. Mater. 24 (2012) 4201–4208. https://doi.org/10.1021/cm302480h.

[10] A.J. Jacobson, J.T. Lewandowski, J.W. Johnson, Ion exchange of the layered perovskite $KCa_2Nb_3O_{10}$ by protons, Journal of the Less Common Metals. 116 (1986) 137–146. https://doi.org/10.1016/0022-5088(86)90224-9.

[11] Y. Chen, X. Zhao, H. Ma, S. Ma, G. Huang, Y. Makita, X. Bai, X. Yang, Structure and dehydration of layered perovskite niobate with bilayer hydrates prepared by exfoliation/self-assembly process, Journal of Solid State Chemistry. 181 (2008) 1684–1694. https://doi.org/10.1016/j.jssc.2008.06.014.
[12] F.F. Xu, Y. Bando, Y. Ebina, T. Sasaki, Modification of crystal structures in perovskite-type niobate nanosheets, Philosophical Magazine A. 82 (2002) 2655–2663. https://doi.org/10.1080/01418610208240058.
[13] T. Nakato, K. Ito, K. Kuroda, C. Kato, Photochemical behavior of perovskite-related layered niobates $HA_2Nb_3O_{10}$ (A = Ca, Sr) intercalated with methylviologen, Microporous Materials. 1 (1993) 283–286. https://doi.org/10.1016/0927-6513(93)80071-2.
[14] P. Xu, T.J. Milstein, T.E. Mallouk, Flat-Band Potentials of Molecularly Thin Metal Oxide Nanosheets, ACS Appl. Mater. Interfaces. 8 (2016) 11539–11547. https://doi.org/10.1021/acsami.6b02901.
[15] Y. Zhang, S. Li, Z. Li, H. Liu, X. Liu, J. Chen, X. Fang, High-Performance Two-Dimensional Perovskite $Ca_2Nb_3O_{10}$ UV Photodetectors, Nano Lett. 21 (2021) 382–388. https://doi.org/10.1021/acs.nanolett.0c03759.
[16] H. Yuan, D. Dubbink, R. Besselink, J.E. ten Elshof, The Rapid Exfoliation and Subsequent Restacking of Layered Titanates Driven by an Acid-Base Reaction, Angew. Chem. Int. Ed. 54 (2015) 9239–9243. https://doi.org/10.1002/anie.201502539.
[17] A.P. Dral, D. Dubbink, M. Nijland, J.E. ten Elshof, G. Rijnders, G. Koster, Atomically Defined Templates for Epitaxial Growth of Complex Oxide Thin Films, JoVE. (2014) 52209. https://doi.org/10.3791/52209.
[18] Y. Shi, M. Osada, Y. Ebina, T. Sasaki, Single Droplet Assembly for Two-Dimensional Nanosheet Tiling, ACS Nano. 14 (2020) 15216–15226. https://doi.org/10.1021/acsnano.0c05434.
[19] B.-W. Li, M. Osada, Y. Ebina, K. Akatsuka, K. Fukuda, T. Sasaki, High Thermal Robustness of Molecularly Thin Perovskite Nanosheets and Implications for Superior Dielectric Properties, ACS Nano. 8 (2014) 5449–5461. https://doi.org/10.1021/nn502014c.
[20] M. Osada, K. Akatsuka, Y. Ebina, H. Funakubo, K. Ono, K. Takada, T. Sasaki, Robust High-κ Response in Molecularly Thin Perovskite Nanosheets, ACS Nano. 4 (2010) 5225–5232. https://doi.org/10.1021/nn101453v.
[21] C. Wang, M. Osada, Y. Ebina, B.-W. Li, K. Akatsuka, K. Fukuda, W. Sugimoto, R. Ma, T. Sasaki, All-Nanosheet Ultrathin Capacitors Assembled Layer-by-Layer *via* Solution-Based Processes, ACS Nano. 8 (2014) 2658–2666. https://doi.org/10.1021/nn406367p.
[22] T. Matsumoto, H. Tanaka, T. Kawai, S. Kawai, STM-imaging of a $SrTiO_3$(100) surface with atomic-scale resolution, Surface Science Letters. 278 (1992) L153–L158. https://doi.org/10.1016/0167-2584(92)90249-5.
[23] M.R. Castell, Scanning tunneling microscopy of reconstructions on the $SrTiO_3$ surface, Surface Science. 505 (2002) 1–13. https://doi.org/10.1016/S0039-6028(02)01393-6.
[24] T. Kubo, H. Nozoye, Surface structure of $SrTiO_3$(100), Surface Science. 542 (2003) 177–191. https://doi.org/10.1016/S0039-6028(03)00998-1.
[25] M. Gasperin, M.T. Le Bihan, Mecanisme d'hydratation des niobates alcalins lamellaires de formule $A_4Nb_4O_{17}$ (A = K, Rb, Cs), Journal of Solid State Chemistry. 43 (1982) 346–353. https://doi.org/10.1016/0022-4596(82)90251-1.
[26] K. Teshima, Y. Niina, K. Yubuta, T. Suzuki, N. Ishizawa, T. Shishido, S. Oishi, Environmentally Friendly Growth of Layered K4Nb6O17 Crystals from a KCl Flux, Eur. J. Inorg. Chem. 2007 (2007) 4687–4692. https://doi.org/10.1002/ejic.200700493.
[27] M.A. Bizeto, V.R.L. Constantino, Layered $H_2K_2Nb_6O_{17}$ exfoliation promoted by n-butylamine, Materials Research Bulletin. 39 (2004) 1811–1820. https://doi.org/10.1016/j.materresbull.2004.07.001.
[28] G. Du, Q. Chen, Y. Yu, S. Zhang, W. Zhou, L.-M. Peng, Synthesis, modification and characterization of $K_4Nb_6O_{17}$-type nanotubes, J. Mater. Chem. 14 (2004) 1437. https://doi.org/10.1039/b317095k.
[29] G.B. Saupe, C.C. Waraksa, H.-N. Kim, Y.J. Han, D.M. Kaschak, D.M. Skinner, T.E. Mallouk, Nanoscale Tubules Formed by Exfoliation of Potassium Hexaniobate, Chem. Mater. 12 (2000) 1556–1562. https://doi.org/10.1021/cm981136n.
[30] M.C. Sarahan, E.C. Carroll, M. Allen, D.S. Larsen, N.D. Browning, F.E. Osterloh, $K_4Nb_6O_{17}$-derived photocatalysts for hydrogen evolution from water: Nanoscrolls versus nanosheets, Journal of Solid State Chemistry. 181 (2008) 1678–1683. https://doi.org/10.1016/j.jssc.2008.06.021.
[31] N. Miyamoto, T. Nakato, Liquid Crystalline Nanosheet Colloids with Controlled Particle Size Obtained by Exfoliating Single Crystal of Layered Niobate $K_4Nb_6O_{17}$, J. Phys. Chem. B. 108 (2004) 6152–6159. https://doi.org/10.1021/jp0363545.

[32] X. Liu, W. Que, P. Chen, Y. Tian, J. Liu, Z. He, H. Zhou, L. Bing Kong, Facile preparation of protonated hexaniobate nanosheets and its enhanced photocatalytic activity, Nanotechnology. 28 (2017) 235702. https://doi.org/10.1088/1361-6528/aa6b4f.
[33] K. Fukuda, Y. Ebina, T. Shibata, T. Aizawa, I. Nakai, T. Sasaki, Unusual Crystallization Behaviors of Anatase Nanocrystallites from a Molecularly Thin Titania Nanosheet and Its Stacked Forms: Increase in Nucleation Temperature and Oriented Growth, J. Am. Chem. Soc. 129 (2007) 202–209. https://doi.org/10.1021/ja0668116.
[34] M. Miyauchi, A. Kondo, D. Atarashi, E. Sakai, Tungstate nanosheet ink as a photonless and electroless chromic device, J. Mater. Chem. C. 2 (2014) 3732–3737. https://doi.org/10.1039/C3TC32513J.
[35] K. Fukuda, K. Akatsuka, Y. Ebina, R. Ma, K. Takada, I. Nakai, T. Sasaki, Exfoliated Nanosheet Crystallite of Cesium Tungstate with 2D Pyrochlore Structure: Synthesis, Characterization, and Photochromic Properties, ACS Nano. 2 (2008) 1689–1695. https://doi.org/10.1021/nn800184w.
[36] K. Nakamura, Y. Oaki, H. Imai, Monolayered Nanodots of Transition Metal Oxides, J. Am. Chem. Soc. 135 (2013) 4501–4508. https://doi.org/10.1021/ja400443a.
[37] T. Shibata, T. Ohnishi, I. Sakaguchi, M. Osada, K. Takada, T. Kogure, T. Sasaki, Well-Controlled Crystal Growth of Zinc Oxide Films on Plastics at Room Temperature Using 2D Nanosheet Seed Layer, J. Phys. Chem. C. 113 (2009) 19096–19101. https://doi.org/10.1021/jp9074288.
[38] R.E. Marsh, I. Bernal, More space-group changes, Acta Crystallogr B Struct Sci. 51 (1995) 300–307. https://doi.org/10.1107/S0108768194011857.
[39] K. Kai, Y. Yoshida, H. Kageyama, G. Saito, T. Ishigaki, Y. Furukawa, J. Kawamata, Room-Temperature Synthesis of Manganese Oxide Monosheets, J. Am. Chem. Soc. 130 (2008) 15938–15943. https://doi.org/10.1021/ja804503f.
[40] Y. Wang, Y.-Z. Zhang, D. Dubbink, J.E. ten Elshof, Inkjet printing of δ-MnO_2 nanosheets for flexible solid-state micro-supercapacitor, Nano Energy. 49 (2018) 481–488. https://doi.org/10.1016/j.nanoen.2018.05.002.
[41] Z. Liu, K. Xu, H. Sun, S. Yin, One-Step Synthesis of Single-Layer MnO_2 Nanosheets with Multi-Role Sodium Dodecyl Sulfate for High-Performance Pseudocapacitors, Small. 11 (2015) 2182–2191. https://doi.org/10.1002/smll.201402222.

Chapter 4: Orientation control of oxides and metal grown on nanosheets seed layers

Introduction

This chapter presents the characterizations and physical properties of oxides and metallic thin films deposited on $[Ca_2Nb_3O_{10}]^-$ nanosheets in the framework of the ANR PolyNash project. As previously mentioned, the aim of oxides nanosheets as seed layers is to facilitate the growth of highly crystallized and oriented oxides thin films on various substrates, such as glass or silicon, and to compare their orientation and properties to their growth on standard single crystal oxides substrates generally used for epitaxial growth. Different deposition methods have been employed in order to investigate the suitability of the nanosheets for deposition in a wide range of conditions.

The first part describes the deposition of the ferroelectric $KNbO_3$ by PLD on $[Ca_2Nb_3O_{10}]^-$ nanosheets on glass. A comparison is made between the growth of $KNbO_3$ on these NS, on (001)$SrTiO_3$, and directly on glass to show the influence of the nanosheets. These depositions have been realized at the ISCR laboratory.

The next part is about the deposition of the multiferroic oxide $BiFeO_3$ by CSD on $[Ca_2Nb_3O_{10}]^-$ nanosheets on silica and silicon. Comparisons between the growth of $BiFeO_3$ directly on silica and silicon and the growth using nanosheets will be developed in the study. These depositions have been realized in collaboration with Dr Valérie Bouquet from the ISCR laboratory.

The growth of magnetic $La_{0.67}Sr_{0.33}MnO_3$ films by PLD on these nanosheets was also investigated. The magnetic properties of the films were compared to those obtained on (001)STO and pristine glass substrate. This work was realized in collaboration with the CRISMAT of Caen.

Then, the growth of $SrVO_3$ and $CaVO_3$ as transparent conducting oxide by PLD on $[Ca_2Nb_3O_{10}]^-$ nanosheets will be detailed. Optical and transport properties were compared

to those of the epitaxial films. This work was realized in collaboration with the CRISMAT and CIMAP laboratories of Caen, the PPrime laboratory of Poitiers, and the GEMaC laboratory of Versailles.

The last part is about the orientation control of platinum electrodes grown by sputtering on silicon using $[Ca_2Nb_3O_{10}]^-$ nanosheets as a seed layer. Highly (111) and (200)Pt thin films have been obtained at very low temperature compared to the classic TiO_2/Si substrates used for the Pt growth. This work has been made in collaboration with the CRISMAT laboratory of Caen.

The figures and comments reported in this chapter have been obtained in the framework of collaborations and reproduced with the authorization of the authors.

1. Orientation control of $KNbO_3$ film grown on glass substrates by $[Ca_2Nb_3O_{10}]^-$ nanosheets seed layer

This work has been published in Thin Solid films within the framework of an oral presentation at the EMRS conference in 2019 [1].

1.1. Introduction

$KNbO_3$ (KNO) is a ferroelectric material with a high electro-optic coefficient, which could be promising for linear and non-linear optics [2,3]. This material possesses high piezoelectric and large electro-mechanic constants, which is interesting for acoustic waves applications [4]. The CSM team (ISCR) is specialized in the deposition of this material by PLD, and more generally of the $K(Ta,Nb)O_3$ system films deposition, especially for application in frequency agile microwave electronics [5,6]. It was thus natural to study the growth of this KNO perovskite phase on the $[Ca_2Nb_3O_{10}]^-$ nanosheets (NS).

The determined lattice constants of these NS by in-plane XRD are $a \simeq 3.84$ Å and $b \simeq 3.87$ Å, which are close to those of the KNO pseudo-cubic lattice $a_{pc} = 3.97$ Å, $b_{pc} = 4.03$ Å, and $c_{pc} = 4.04$ Å (at room temperature, KNO is orthorhombic, with $a = 3.971$ Å, $b = 5.692$ Å, $c = 5.719$ Å, space group $Amm2$, JCPDS card N°01-071-0946, Annexe A, p. 206

[7]). Consequently, highly textured thin films are expected thanks to the low lattice mismatch between the NS and KNO lattices which is about 4 %.

In this study, KNO thin films were deposited by pulsed laser deposition (PLD) on glass covered with NS, and on single-crystalline (001)$SrTiO_3$ (STO) substrate for comparison.

1.2. Thin films deposition conditions

For the PLD deposition, the ceramic target was prepared using KNO powder synthesized by solid-state reaction, with an excess of potassium provided by addition of potassium nitrate to the precursors, in order to counterbalance the potassium loss that occurs during the deposition due to the volatility of K_2O. The PLD deposition of KNO was realized on glass substrates (surface: 10 × 10 mm^2, 2 mm thick) uncovered and covered by NS, and on 5 × 5 mm^2, 0.5 mm thick (001)STO (*Pm*-3*m*, *a* = 3.905 Å, JCPDS card N°01–073–0661, Annexe A, p. 207, Crystal GmbH). Before KNO deposition, STO substrates were successively ultrasonically cleaned in acetone for 5 min and isopropyl alcohol for 5 min. The KNO ceramic target was ablated with the KrF excimer set at an energy of 225 mJ, a fluence of 2–3 J cm^{-2}, and a 2 Hz frequency. The KNO films were grown at a substrate-target distance of 60 mm under 30 Pa oxygen partial pressure during a deposition time of 15 min. Using a pyrometer, the temperature measured at the substrate surface was 550°C for the deposition on STO and 600°C for the film on glass.

1.3. Thin films characterizations

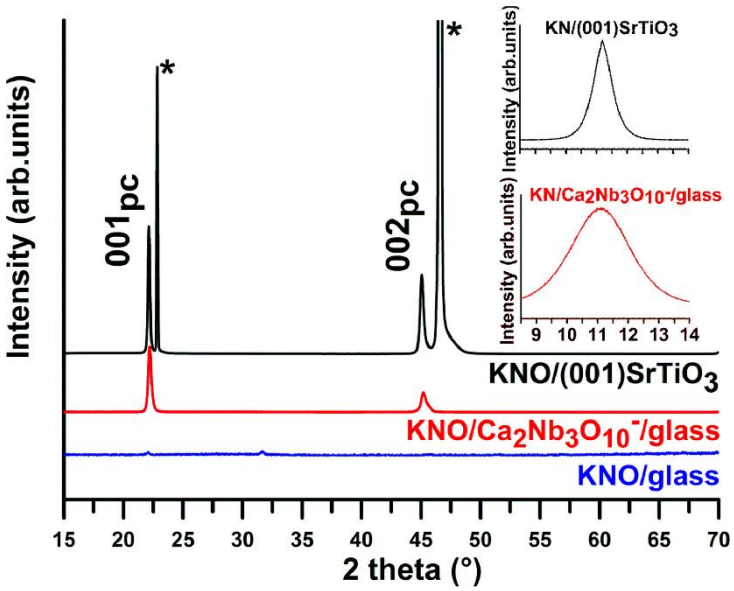

Figure 4.1. θ-2θ XRD patterns of KNO thin films deposited on (001)STO at 550°C (black), on NS/glass at 600°C (red), and on glass at 600°C (blue: the intensity was multiplied by 50 to enhance the signal display) (*: STO). Insets: corresponding (001) KNO rocking curves (ω scans).

XRD patterns of KNO thin films grown by PLD on (001)STO, on glass, and NS/glass substrates are displayed in Figure 4.1. The KNO film deposited on glass is poorly crystallized (the intensity was multiplied by 50 in order to enhance the signal on noise ratio) and the diagram presents both 001 and 110 reflections. In the two other cases, only 00*h* peaks are observed, indicating a preferential orientation growth of the niobate films, and demonstrating that the NS induced an oriented growth on the glass substrate. The film on STO is obtained at a surface substrate temperature of 550°C, while pure KNO films are obtained on NS/glass at a surface substrate temperature of 600°C. This higher temperature is probably due to the thickness of the glass substrate (2 mm) which is higher than the one of the STO substrate (0.5 mm). At higher temperatures than 650°C, the film presents a secondary phase in addition to KNO. TEM-EDXS analyses showed that the sample contains K, Nb, Na, Ba, and O elements, indicating diffusion of elements from the glass substrate (of composition approximatively $Si_{19.7}Na_{14.2}Ba_9Nb_6O_{51}$) through the film at this temperature.

The rocking curves (ω-scan) displayed in insets of the Figure 4.1 show low mosaicity for KNO on STO with the full-width-at-half-maximum (FWHM) value of $\Delta\omega = 0.7°$, and a higher mosaicity of KNO on NS/glass with $\Delta\omega = 2.1°$, indicating that the crystallites are less aligned on the latter.

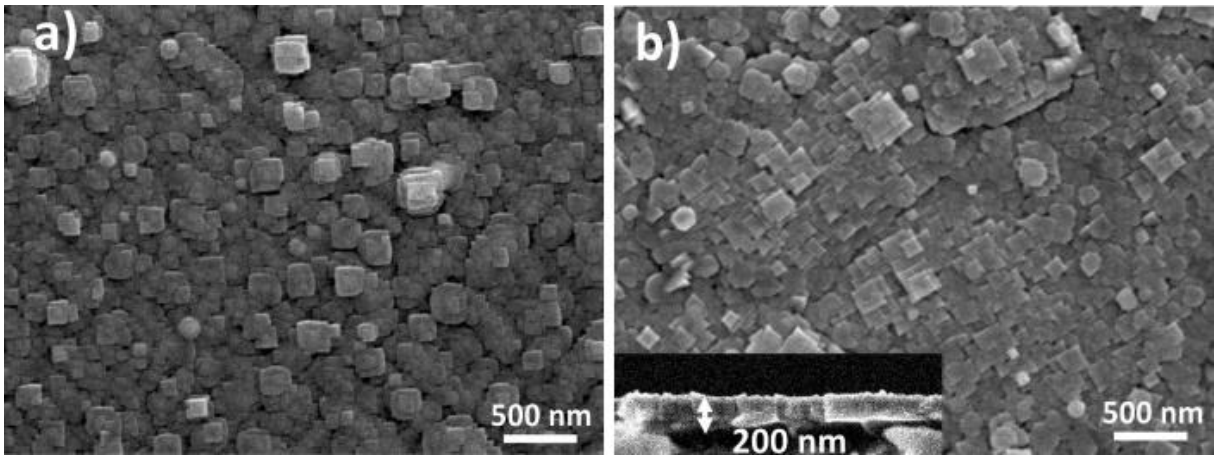

Figure 4.4.2. SEM micrographs of KNO thin films deposited on (001)STO at 550°C (a) and on NS/glass at 600°C (b). Inset: cross-sectional view of the KNO film on NS/glass, showing the 200 nm thick film.

The films morphology was also investigated by SEM in in-plane and cross-sectional views as shown in Figure 4.2. The film deposited on (001)STO shows a dense area of epitaxial square-shaped KNO crystals with lateral size lying between 50 and 230 nm, while the film deposited on NS/glass shows a textured growth. This film is also made of square-shaped crystals of the same size. This shape is characteristic of (001)-oriented KNO grains [5]. It appears that the surface morphology of the KNO film was influenced by the underlying NS and that the grains grown on the same NS present an identical in-plane orientation.

1.4. Conclusion

To conclude, highly-textured (001) $KNbO_3$ film has been grown on glass using $[Ca_2Nb_3O_{10}]^-$ nanosheets as a seed layer. The importance of the growth temperature was investigated. It has been shown that for growth temperature higher than 650°C, a diffusion of the elements of the substrate in the film was observed, showing the importance of limiting the growth temperature and knowing the composition of the substrate. For lower temperatures, around 600°C, the films were found to have a high crystalline quality similar to the films epitaxially grown on single crystalline (001)$SrTiO_3$, with only a slightly higher mosaicity. Therefore, this method allows the growth of preferentially oriented ferroelectric $KNbO_3$ films on low-cost substrates.

2. Influence of nanosheets seed layers on the growth of $BiFeO_3$ thin films synthesized by CSD

This work has been published in Thin Solid Films within the framework of an oral and poster presentation at the E-MRS conference of 2019 [8], in collaboration with Valérie Bouquet from the ISCR laboratory, in CSM group, who realized the Chemical Solution Deposition of $BiFeO_3$.

2.1 Introduction

$BiFeO_3$ (BFO) is a material with a rhombohedral distorted perovskite structure that exhibits multiferroic properties at room temperature. The bulk material displays high Curie temperature (T_C ~1103 K) and Néel temperature (T_N ~ 643 K), which makes it one of the most promising multiferroics materials for electronics, spintronics, or piezotronics applications [9]. Referring to literature, epitaxial BFO thin film on (100)STO shows a strong improvement of the magnetization and ferroelectricity compared to the bulk, with a remanent polarization above 50 μC/cm² (10 times higher than the bulk) and piezoelectric response of 70 pm/V, thanks to the lattice strains caused by the epitaxial growth [10]. However, those properties are only obtained for BFO epitaxial films, which limit the growth to single crystalline substrates. In this work, the $[Ca_2Nb_3O_{10}]^-$ NS have been used to overcome the substrate limitation. BFO has a rhombohedral lattice with a = 3.952 Å and α = 89.6° (*R*3*c*; hexagonal settings: a = 5.5976 Å, c = 13.967 Å; JCPDS card N°01-071-2494, Annexe A, p. 208) [11]. This lattice is close to the one of the NS. In this work, BFO has been deposited by CSD to allow the growth of (001)BFO thin films on low-cost substrates such as silica and silicon thanks to the nanosheets.

2.2. Thin films deposition conditions

The BFO thin films were prepared by CSD using the polymeric precursor method (Pechini process) to prepare the coating solution (cf. Chapter 2). The latter was synthesized using iron nitrate $Fe(NO_3)_3{\cdot}9H_2O$ and $Bi(NO_3)_3{\cdot}5H_2O$ precursors. The obtained coating solution was spin-coated at 1000 rpm for 3 s followed by a rotational speed at 4000 rpm for 10 s on 10×10 mm² amorphous silica and 10×10 mm² (100)Si

substrates. The wet films were then thermally treated in air at 400°C for 3 h and calcinated at 500°C for 2 h. Two layers of coating solution were deposited for each film. The pyrolysis was carried out after each deposition step, whereas the crystallization treatment was only performed once the 2 layers were deposited. The thickness of each layer is around 300 nm.

2.3. Thin films characterizations

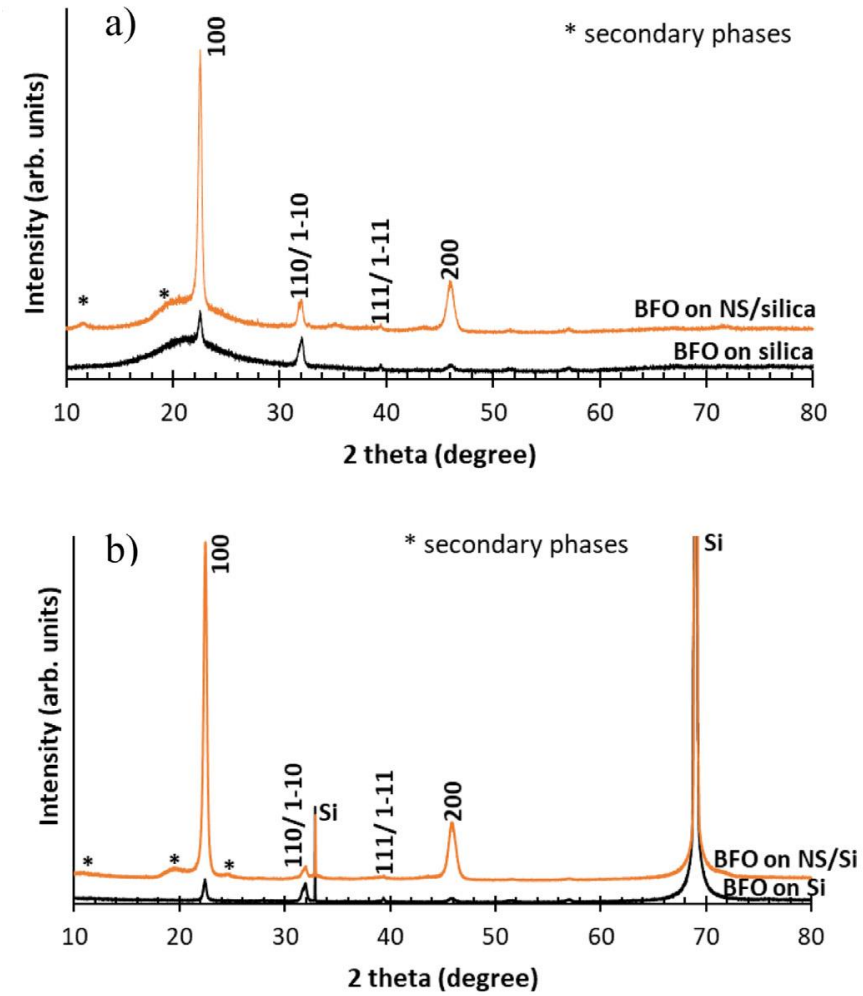

Figure 4.3. θ-2θ XRD patterns of BFO thin films (a) synthesized at 500°C on NS/silica and (b) on Si and NS/(100)Si [8].

Figure 4.3a displays the XRD patterns of BFO on silica and NS/silica. It can be observed that BFO grown directly on silica leads to a polycrystalline film with low intensity peaks, while the BFO film deposited on NS/silica presents a preferential 001 orientation. Minors 110 and 111 peaks are observed, probably caused by part on the substrate uncovered by nanosheets. These results are comparable to those of Nagasaka *et al*. who deposited Mn-doped BFO on (111)Pt/TiO_2/(100)Si and (111)Pt/stainless steel

substrates [12]. However, additional peaks of weak intensities can be observed which could be attributed to a reaction between the nanosheets with BFO and/or with the substrate leading to the formation of a secondary phase, possibly $Bi_{5.96}Ca_{1.76}Nb_{0.28}O_{11.14}$ (JCPDS card No. 00-079-9855, Annexe A, p. 209) for the peak at $2\theta = 19.8°$. However, it is difficult to confirm with certainty the presence of this phase with only one visible peak.

The other minor peaks correspond to a layered phase with a lattice constant $c \simeq 14.1–14.3$ Å. XRD of the NS on silicon was measured to compare the inter-reticular distance to the one obtained with the BFO film (Figure 4.4). An inter reticular distance of about 15.4 Å was found, which is in agreement with a previous study [13]. This shift from 15.4 to 14.1–14.3 Å might be due to the formation of a layered Bi/Si-$[Ca_2Nb_3O_{10}]^-$. The XRD patterns of BFO on silicon and NS/silicon are displayed in Figure 4.3b. The results observed are similar to those obtained on silica, with the same observed extra peaks.

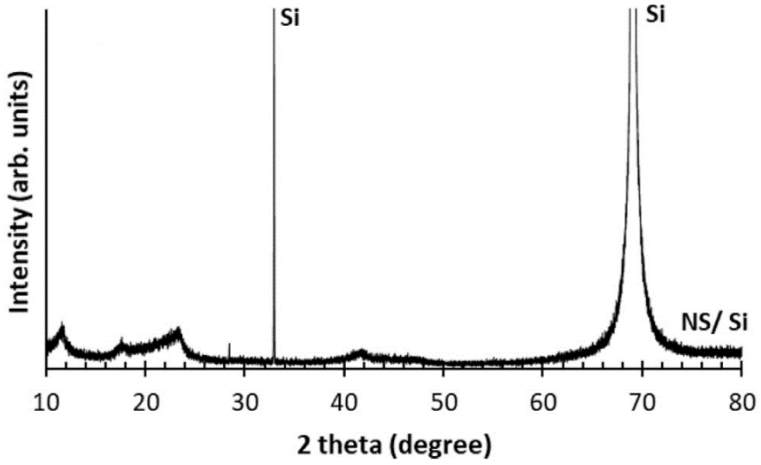

Figure 4.4.4. θ-2θ XRD pattern of the nanosheets deposited on Si substrate [8].

2.4. Conclusion

To conclude, this work shows that it is possible to obtain highly oriented (100)BFO film deposited by CSD on silica and silicon using $[Ca_2Nb_3O_{10}]^-$ nanosheets. However, secondary phases appeared which may correspond to interdiffusion between the BFO film and the nanosheets.

3. Orientation control and physical properties of $La_{0.67}Sr_{0.33}MnO_3$ films grown on glass substrates covered by $[Ca_2Nb_3O_{10}]^-$ nanosheets seed layer

The manganite thin films were deposited and characterized in the CRISMAT laboratory. The results have been published in ACS Applied Materials and Interfaces, in collaboration with colleagues of the CRISMAT laboratory of Caen: Alexis Boileau, Marie Dallocchio, Adrian David, Ulrike Lüders, Bernard Mercey, Alain Pautrat, Wilfrid Prellier, and Arnaud Fouchet [14].

3.1. Introduction

Among complex oxides, the $La_{0.67}Sr_{0.33}MnO_3$ manganite (LSMO) is a reference material thanks to its notable electronic and magnetic properties [15,16], which makes it interesting for sensor, spintronics, magneto-optical, and optoelectronic applications [17–20]. However, these properties are obtained for epitaxial LSMO films which are grown on expensive single crystal substrates. The growth of LSMO directly on silicon leads to very poorly crystallized quality films with poor electronic and magnetic properties. In order to obtain highly oriented (100)LSMO films on low cost substrates, the NS were used as a seed layer since the pseudo-cubic lattice constant of LSMO is a_{pc} = 3.86 Å (space group *R*-3*c*; hexagonal settings: *a* = 5.508 Å, *c* = 13.371 Å, JCPDS card N° 01-089-8098, Annexe A, p. 211 [21]). Therefore the orientation of the LSMO film is expected. The electronic and magnetic properties of the obtained LSMO films have been measured at CRISMAT and compared to those obtained on (100)STO substrates and glass substrates (GS).

3.2. Thin films deposition conditions

The PLD depositions of LSMO were realized in the CRISMAT laboratory. LSMO thin films have been grown on NS/GS, pristine glass, and (001)STO. A KrF excimer laser (λ = 248 nm) was used with a repetition rate of 2 Hz and the laser fluence was adjusted to obtain a deposition rate close to 0.1 Å per laser pulse. A $La_{0.67}Sr0_{.33}MnO_3$ polycrystalline target was used, which has been prepared by solid state reaction. The deposition was

carried out under oxygen–ozone mixture conditions [22] and the deposition was 5×10^{-4} mbar. The thickness of the films is around 50 nm. The depositions have been realized at 550°C and 645°C. Only the results at 645°C will be described in the following part.

3.3. Structural analyses of the films

AFM was performed on the LSMO films deposited on GS and NS/GS (Figure 4.5). For LSMO/GS, the surface is uniform with an estimated average particle size of 40 nm. On the other hand, LSMO/NS/GS, the films cover the NS and the interstices and larger particles size is observed (~50 nm) compared to those of LSMO/GS.

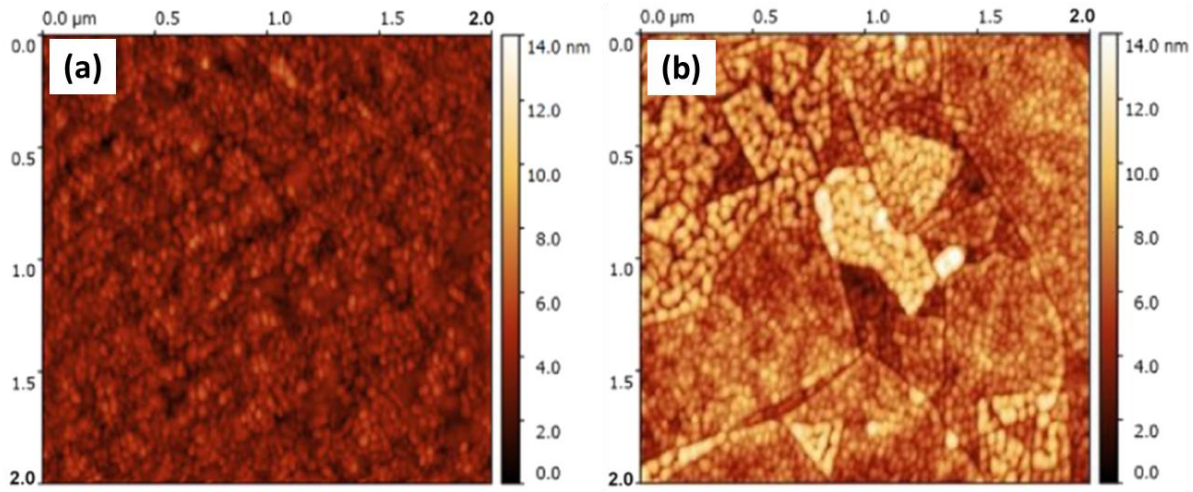

Figure 4.5. AFM images of LSMO films grown on GS (a) and on NS/GS (b) [14].

The XRD diagrams displayed in Figure 4.6 show the results obtained for LSMO grown directly on GS and GS/NS at 645°C. The LSMO thin film obtained on GS is polycrystalline while the LSMO film grown on NS/GS presents a strong (001) preferential orientation. The LSMO/GS diffractogram was indexed in hexagonal settings. The lattice constants were found to be a = 5.50(2) Å and c = 13.37(8) Å, which are close to those reported by Hibble *et al.* [21]. For LSMO/NS/GS, the peaks are labeled according to the pseudocubic lattice. The lattice constant was found to be 3.83(6) Å, which is close to the theoretical value. In the magnification of the latter diffractogram, some weak peaks of polycrystalline LSMO can be observed. These results confirm that the nanosheets allow the growth of highly (001) oriented LSMO on glass. The average size of the crystallite domains was also determined using the Scherrer's formula to compare with the values obtained by AFM. The size for LSMO/GS sample was found to be 34 nm while it is about

40 nm for LSMO/NS/GS. These results are close to those observed by AFM and confirm that the growth of LSMO/NS/GS induces larger particles size.

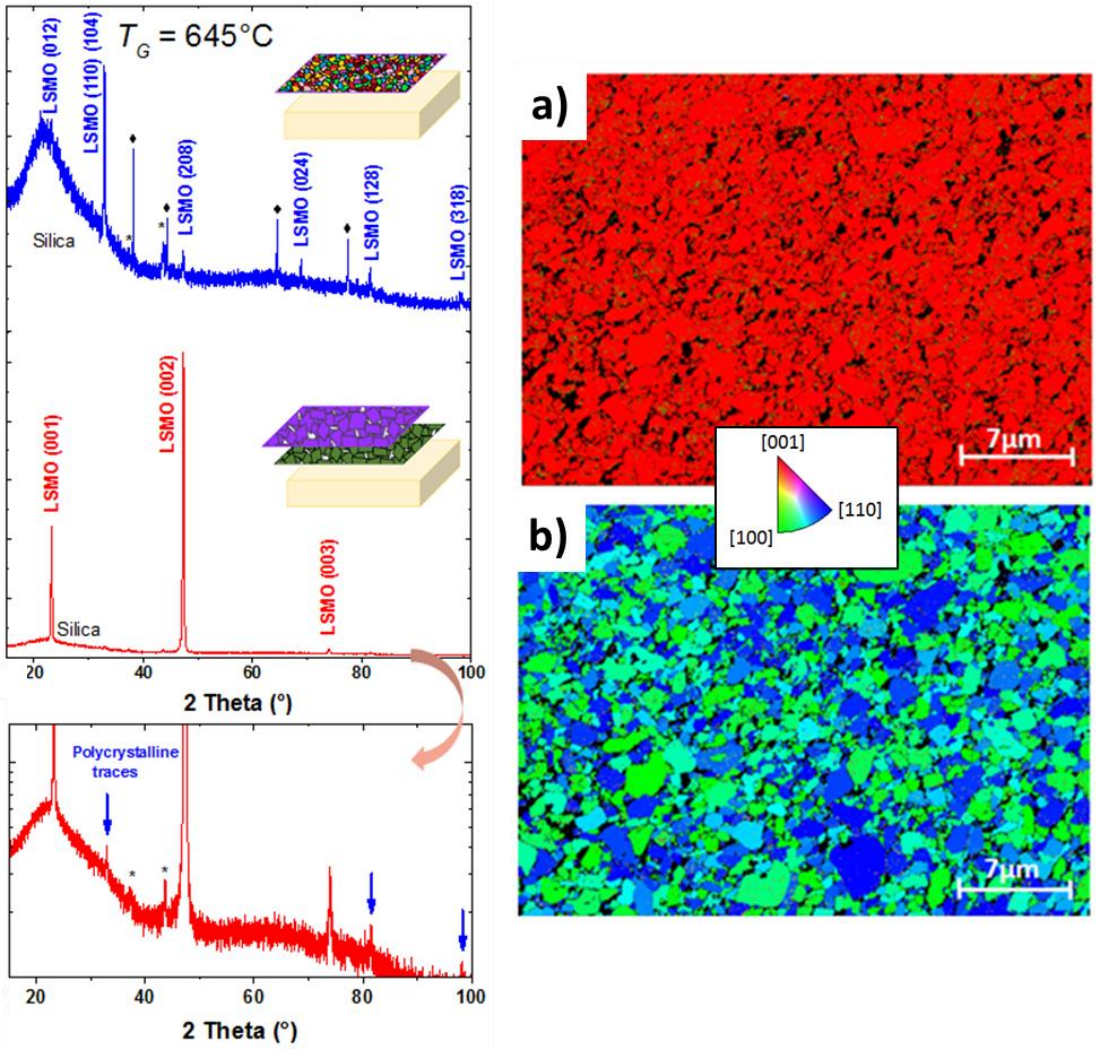

Figure 4.6. On the left, X-ray diffractograms of the LSMO thin film grown on GS (blue) and NS/GS substrates (red). Magnification of the LSMO/NS/GS films diffractogram reveals peaks attributed to the polycrystalline phase. Stars (*) and diamond (♦) symbols refer to the instrumental artifact and silver traces, respectively. On the right, the EBSD maps of LSMO thin film deposited on glass substrate coated by NS, (a) out-of-plane and (b) in-plane configuration [14].

Figure 4.6a,b shows the electron backscattered diffraction (EBSD) maps of the thin film deposited on NS/GS. In Figure 4.6a, the out-of-plane map confirms the full (001) out of the plane orientation of the film induced by the NS. The in-plane view map shows that only the [100] and [110] directions are present, showing in-plane disorientation of the crystalline domains.

3.4. Magnetism measurements

Figure 4.7a shows the magnetization of the LSMO film grown on STO, NS/GS, and on GS, as a function of the temperature under a field of 0.05 T. It can be observed that the magnetization of the LSMO thin film grown on nanosheets is much higher than the one of LSMO/GS (+172 emu.cm^{-3}). Furthermore, the magnetization of LSMO/NS/GS is close to the one of LSMO/(001)STO. In the inset is displayed the Curie temperatures (T_c) measured for each film by the derivative method under a field of 0.005 T. The measured T_c for the LSMO/GS and LSMO/STO are 348 K and 332 K respectively, which is consistent with the data reported in the literature [22,23]. The difference of T_c between the two films is due to the tensile strain induced by the lattice mismatch between the substrate and the film. For the epitaxial film, there is a mismatch of -1.15% between the substrate and the film leading to a distortion of the perovskite structure and a tilting of the O-Mn-O bonds [24,25], which leads to the diminution of T_c compared to the bulk. On the other hand, the LSMO/GS film is polycrystalline, which means that there are no strains between the film and the substrate. For LSMO/NS/GS, the T_c was measured about 337 K, which is between the T_c of LSMO/GS and LSMO/(001)STO. It can be explained by the fact that there is a local epitaxy of the film on each nanosheet, which leads to local strains of the film, and all nanosheets do not have the same orientation in the substrate plane (texturation), which leads to a slackening of the strains in the film.

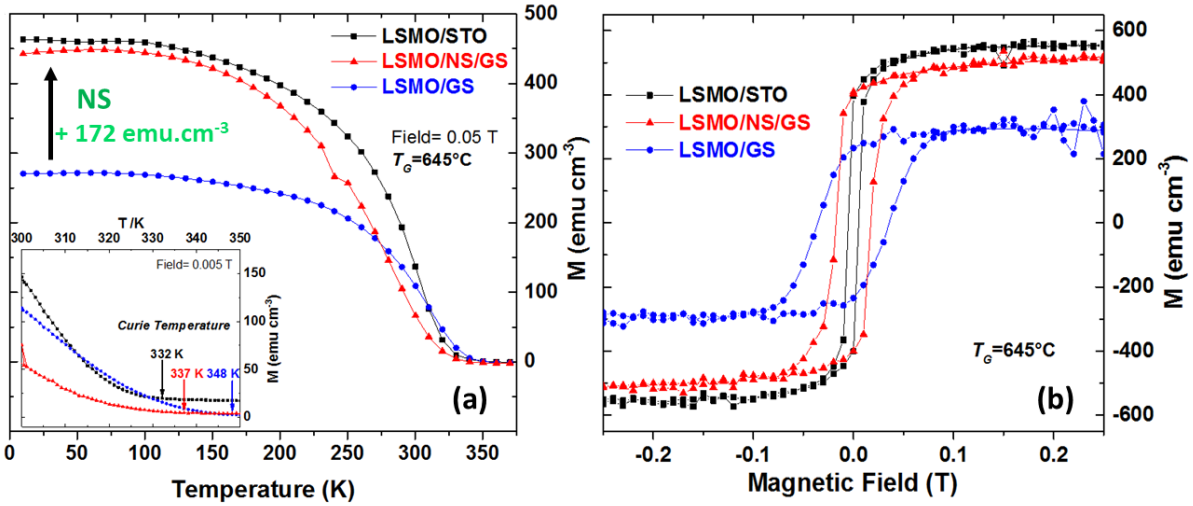

Figure 4.7. (a) Temperature-dependent magnetization curves of LSMO films on GS (blue), NS/GS (red), and (001)STO (black). A magnetic field of 0.05 T and 0.005 T (in inset) was applied parallel to the surface for all the zero field cooled. (b) Hysteresis loops acquired at 100 K of LSMO thin films for GS, NS cover GS, and (001)STO substrates [14].

In Figure 4.7b is displayed the magnetizations of the films as a function of the magnetic field. The hysteresis was acquired at 100 K to get the highest magnetization. It can be observed that the remanent magnetic field B_R and the saturation magnetic field B_{Sat} are higher for LSMO/STO and LSMO/NS/GS compared to LSMO/GS. Furthermore, the magnetization of LSMO/NS/GS is close to the one of LSMO/(001)STO which confirms the increase of the film quality engendered by the NS. Similar behavior is observed for the coercivity H_C. The latter depends on the structure of the films and the formation of magnetic domains. In the polycrystalline LSMO sample, the formation of magnetic domains is driven by the particle size. As there is a random distribution of each particle, the orientation of each magnetic domain is also random. Thus, a higher magnetic field is required to align all the magnetic domains, leading to a higher macroscopic coercity compared to those of LSMO/NS/GS and LSMO/(001)STO [26]. For LSMO/NS/GS, the value of H_C is lower compared to LSMO/GS thanks to the local epitaxy on the nanosheets, which leads to the formation of larger magnetic domains.

3.5. Transport properties

The resistivities of LSMO films as a function of the temperature are displayed Figure 4.8a. The resistivity of the polycrystalline LSMO film grown on GS is higher than the resistivity of films deposited on STO and NS/GS. The difference of resistivity can be explained by the high grain boundaries in the polycrystalline film on GS, which act as a local blockage to the delocalization of the electrons across the crystalline domains. Furthermore, as observed by AFM and XRD characterizations, the grain size is greater for LSMO/NS/GS compared to LSMO/GS thanks to the preferential (001) orientation of the film. This behavior favors the electron delocalization through the film and thus decreases the resistivity.

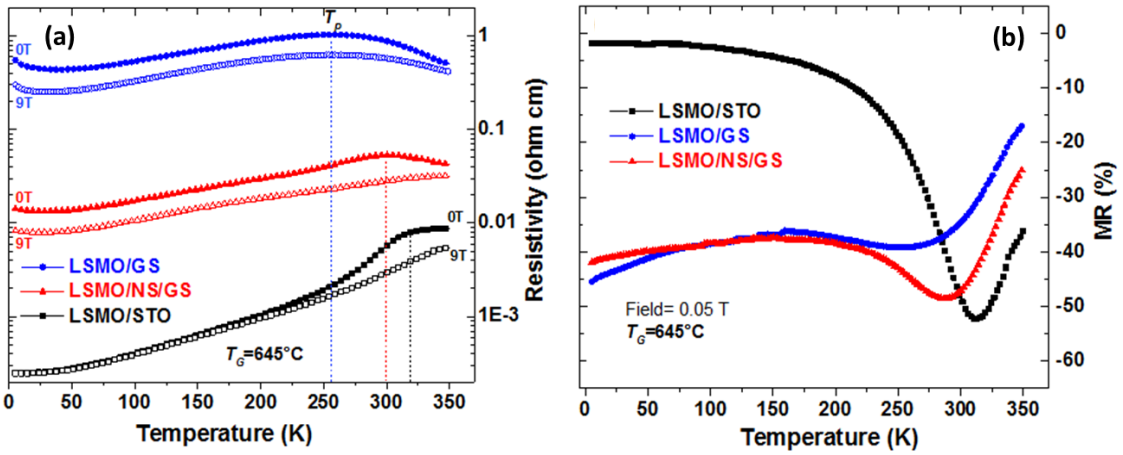

Figure 4.8. (a) Resistivities of LSMO films measured in parallel configuration at H = 0 and 9 T. (b) Dependence of the magnetoresistance of films as a function of temperature [14].

The metal–insulator transition temperature (T_p) can be measured from the resistivity curve as a function of the temperature. T_p corresponds to the maximum value of resistivity measured (Figure 4.8a). This effect can also be seen on the minimum of magnetoresistance (MR) as a function of the temperature (Figure 4.8b), which is defined as $MR = 100 \times (\rho_0 - \rho_H)/\rho_0$, where ρ_0 is the zero-field resistivity, and ρ_H is the resistivity in the applied field. The T_p has been found to be 257 K, 300 K, and 312 K for LSMO/GS, LSMO/NS/GS, and LSMO/(001) STO, respectively.

At low temperature (< 200 K), the MR is almost suppressed for LSMO on STO while it remains stable at -40-50 % for LSMO/GS and LSMO/NS/GS. Therefore, in the case of LSMO/NS/GS, LSMO presents a high magnetization close to films of high quality deposited onto STO but with the magnetoresistance close to LSMO/GS. This MR at low temperature can be explained by the grain boundaries induced by the nanosheets, which leads to the textured polycrystalline structure.

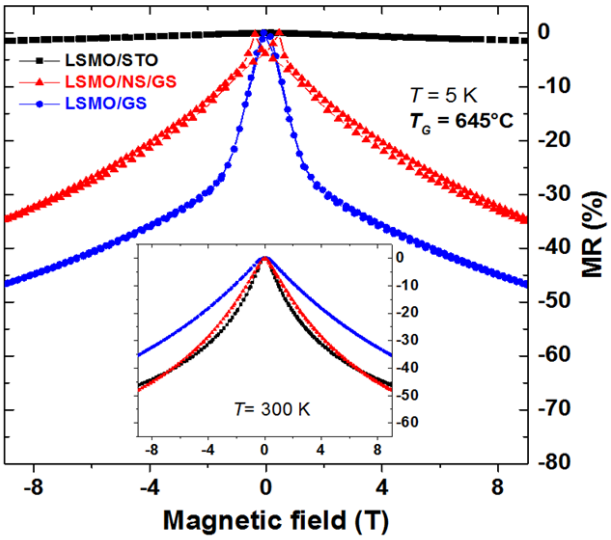

Figure 4.9. Magnetoresistance of LSMO films measured with a magnetic field applied perpendicular to the surface at 5 K and 300 K (in inset) on STO (black), NS/GS (red), and GS (blue) [14].

The MR was also measured as a function of the magnetic field at 5 K and 300K (in inset) (Figure 4.9). At 5 K, for LSMO/STO film, the MR is close to zero, while the MR is about -35% and -45% for LSMO/GS and LSMO/NS/GS. Furthermore, the MR strongly increases in the low-field region for LSMO on GS and NS/GS. This behavior, called as low-field effect, is only observed for polycrystalline and textured LSMO films and is not observed at 300 K. When the electrons travel across grains, strong spin-dependent scattering at the boundaries leads to a high zero-field resistivity. When the magnetic field increases, the domains align into a parallel configuration causing a strong decrease in resistivity. This phenomenon is very important for sensor applications [27] and the NS shows here that it is possible to adapt it to any substrate. These results show that it is possible to obtain highly oriented LSMO films on glass using NS while limiting the resistivity of the film.

3.6. Conclusion

To conclude, it has been shown that highly oriented (001)LSMO films have been obtained on glass substrate covered by $[Ca_2Nb_3O_{10}]^-$ nanosheets. These results confirm the great interest of nanosheets to obtain oriented films on random substrates. The magnetization and the coercivity of LSMO/NS/GS have shown to be close to those of LSMO/STO. On the other hand, a low-field MR is present for LSMO/NS/GS, which is close

to the property observed for a polycrystalline film. Therefore, LSMO grown on NS combines the properties of single crystalline and polycrystalline films.

The results obtained for the LSMO grown at 550°C (not shown here) also demonstrate that it is possible to obtain interesting magnetic properties at a lower temperature of growth. The decrease of the growth temperature in thin film deposition is very important as it opens new opportunities to integrate oriented LSMO film on silicon, without considering the formation of native SiO_2.

4. $SrVO_3$ and $CaVO_3$ transparent conducting oxides grown on $[Ca_2Nb_3O_{10}]^-$ nanosheets

This work has been published in Advanced Functional Materials [28], in collaboration with people from the CRISMAT and CIMAP laboratories of Caen, Pprime laboratory of Poitiers, and GEMaC laboratory of Versailles: Alexis Boileau, Simon Hurand, Ulrike Lüders, Marie Dallocchio, Bruno Bérini, Aimane Cheikh, Adrian David, Fabien Paumier, Thierry Girardeau, Philippe Marie, Christophe Labbé, Julien Cardin, Damien Aureau, Mathieu Frégnaux, Wilfrid Prellier, Yves Dumont, and Arnaud Fouchet (corresponding author). The report of these results in this manuscript aims to evaluate the impact of the use of the NS.

4.1. Introduction

Transparent conducting oxides (TCO) are an important class of materials that is widely used for flat screens, solar cells, light-emitting diodes, electrochromic cells, or transparent antennas technologies [29]. The most commonly used TCO is the indium tin oxide (ITO), which shows excellent optical transparencies and electrical resistivities [30]. However, indium is not an abundant metal, which makes ITO a quite expensive substrate. Researches have been made to find alternatives to the ITO substrates [31]. The epitaxial thin films of $CaVO_3$ (CVO) and $SrVO_3$ (SVO) vanadate perovskites have shown to present properties close to those of ITO [32]. However, the vanadates are conductors only when the films are crystallized, compared to ITO which displays those properties when amorphous [33].

As previously described for the growth of $KNbO_3$, $BiFeO_3$, or LSMO, the $[Ca_2Nb_3O_{10}]^-$ nanosheets have shown to induce highly crystallized and (001)-oriented perovskites. The other advantage of these nanosheets is they have a very low thickness (~2 nm), which makes them optically transparent. SVO has a cubic perovskite structure with a lattice constant a = 3.84 Å (space group *Pm*-3*m*, JCPDS Card N°01-089-8658, Annexe A, p. 212) [34] whereas CVO is orthorhombically (o) distorted with lattice constants a_o = 5.317 Å, b_o = 7.5418 Å, c_o = 5.339 Å (space group *Pnma*, JCPDS card N°01-089-8654, Annexe A, p. 213) and pseudo-cubic constant $a_{pc} = a_o/\sqrt{2} \simeq b_o/\sqrt{2} \simeq c_o/2 \simeq 3.77$ Å [35]. In this study, CVO et SVO were grown on nanosheets deposited on glass substrates at different temperatures. The structural analyses, transport, and optical properties of the thin films were compared to those of ITO. Spectroscopic ellipsometry measurements have also been realized but will not be described thereafter.

4.2. Thin films deposition conditions

The depositions of CVO and SVO have been realized by PLD at the GEMaC laboratory. Thin films have been grown on 5 × 5 mm^2 GS covered at 70% of NS. The laser was used with a repetition rate of 3 Hz and a laser fluence adjusted at 1.6 $J.cm^{-2}$ to get a deposition rate close to 0.1 Å per laser pulse. The laser beam is focused on a $Ca_2V_2O_7$ or a $Sr_2V_2O_7$ polycrystalline target prepared by a standard solid-state reaction. As the perovskite structure is not the most stable one in the Ca(Sr)-V-O system, the deposition was carried out under vacuum, *i.e.* in reductive conditions, to reach the perovskite phase of the vanadates films. The thicknesses of the films are around 40 nm. In order to investigate the influence of the temperature on the crystallization of the vanadate films, the substrate temperature was varied between 400 and 700°C.

4.3. Structural analyses of the $SrVO_3$ and $CaVO_3$ thin films on NS

Figure 4.10 shows the XRD diagrams of CVO and SVO grown on NS/GS, from 400 to 700°C. The crystallization of both oxides occurs between 400 and 500°C, which is similar to the growth temperature of SVO film on a single crystalline substrate [33]. Highly oriented (110) orthorhombic CVO and (001)SVO were obtained at 500°C. However, when the deposition temperature is higher than 500°C, the quality of the films decreases. This

might be explained by the partial decomposition of the NS due to the vacuum inside the chamber [13], or by the degradation of the glass substrate as its strain point is 669°C.

The XRD and EBSD were performed at CRISMAT.

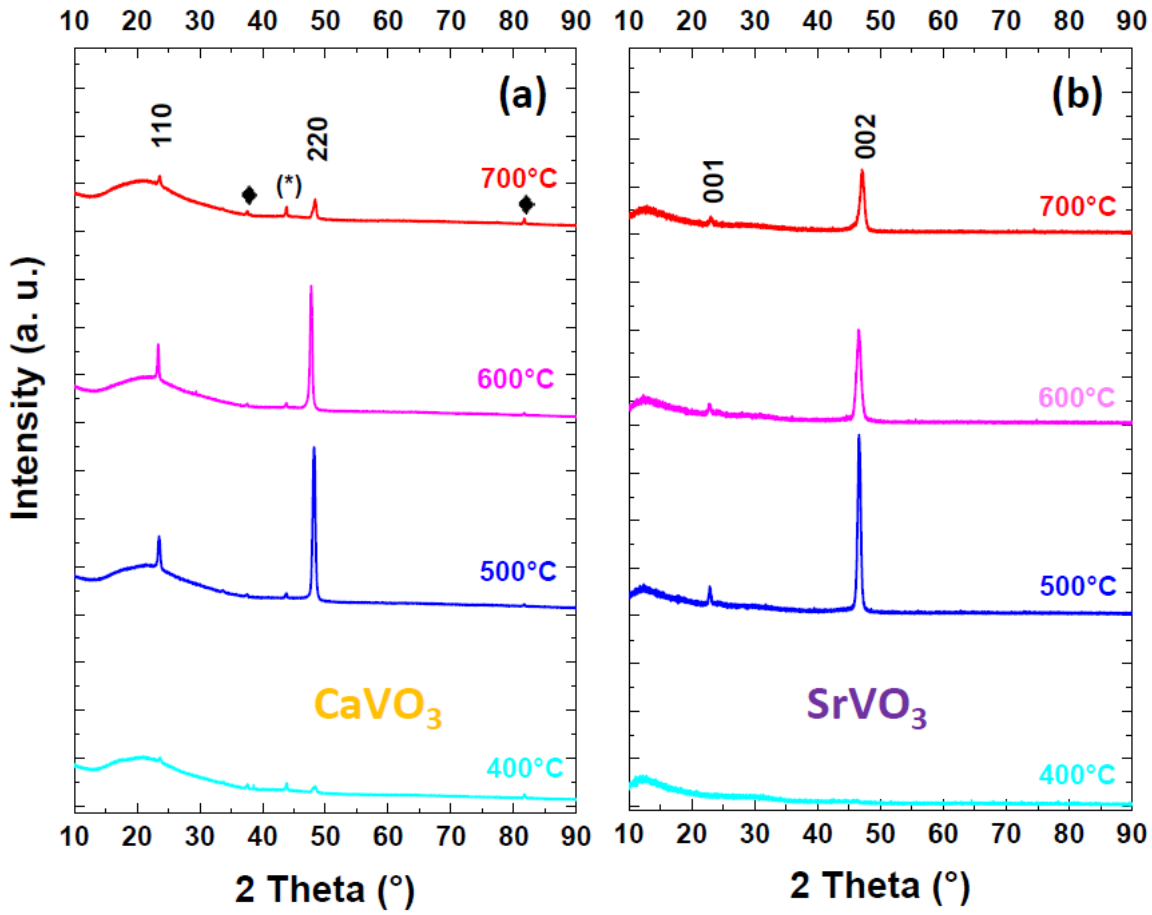

Figure 4.10. X-ray diffractograms of CVO (a) and SVO (b) thin films grown on NS/GS substrates from 400 to 700°C. The symbols (*) and (◆) refer to the peaks from the detector and the silver paste, respectively [28].

Figure 4.11 shows the EBSD maps of both films grown at 500°C. The out-of-plane configurations confirm the preferential orientation $(110)_o$ for CVO and (001)SVO induced by the NS. Furthermore, the in-plane configurations show that the other orientations are only in that plane, confirming the textured behavior of the films grown on NS. The black areas between the nanosheets covered by oxide are related to non-diffracting domains. However, the covering percentage of the crystallized phase (around 70%) is good enough for good 2D conduction.

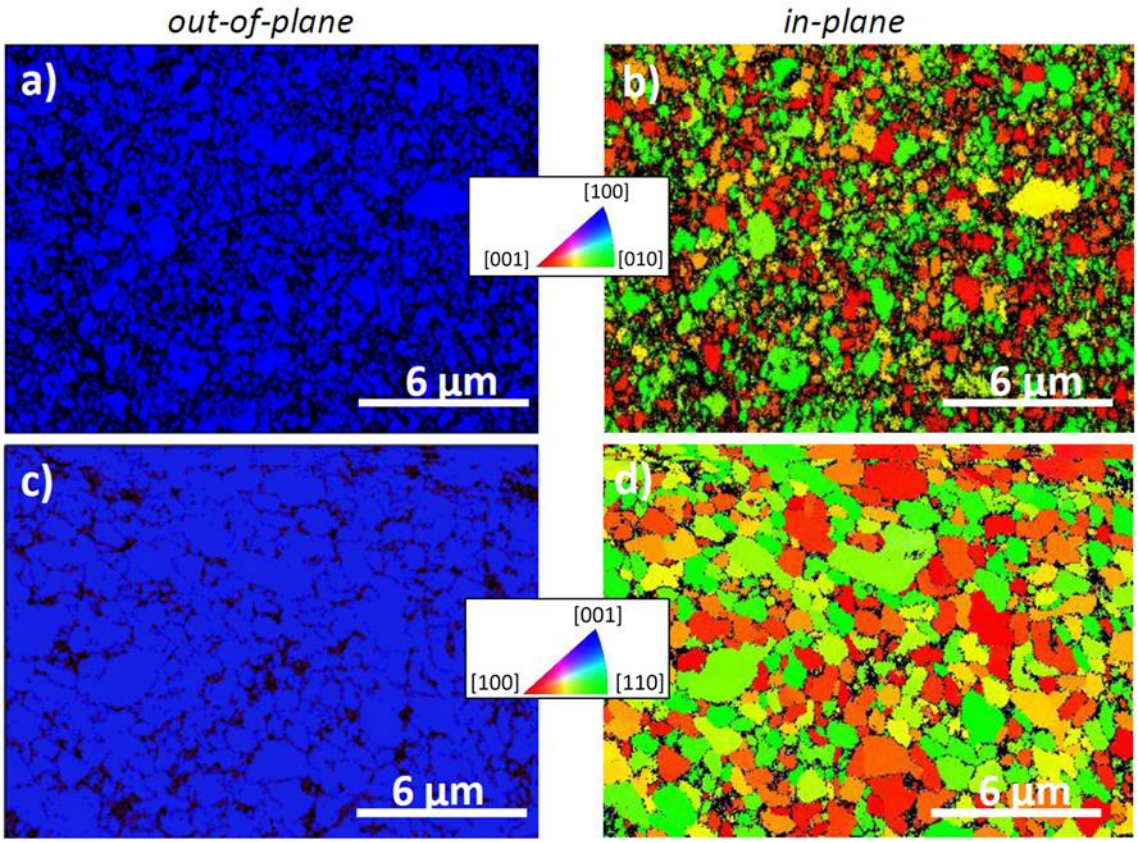

Figure 4.11. Out-of-plane and in-plane EBSD images of CVO (a-b) and SVO (c-d) thin films deposited at 500°C [28].

4.4. DC transport properties

The resistivity measurements were performed at the CRISMAT laboratory and the optical characterizations were realized at the Pprime laboratory.

The resistivities as a function of the temperature are shown in Figures 4.12a and 4.12b for oriented CVO and SVO thin films grown between 500°C and 700°C. As the vanadates films deposited at 400°C were too poorly crystallized, their resistivities were too high to be measured. The resistivities measured at 300 K have shown to be between 3.65×10^{-4} and 1.64×10^{-3} Ω.cm, which are consistent with the values of 2.84×10^{-5} Ω.cm [36] and 2.90×10^{-3} Ω.cm [37] obtained for epitaxial vanadates films. Those resistivities values are very low considering that near 30% of the obtained textured vanadate films are amorphous and the presence of grain boundaries in the structure, as observed in the EBSD maps previously presented.

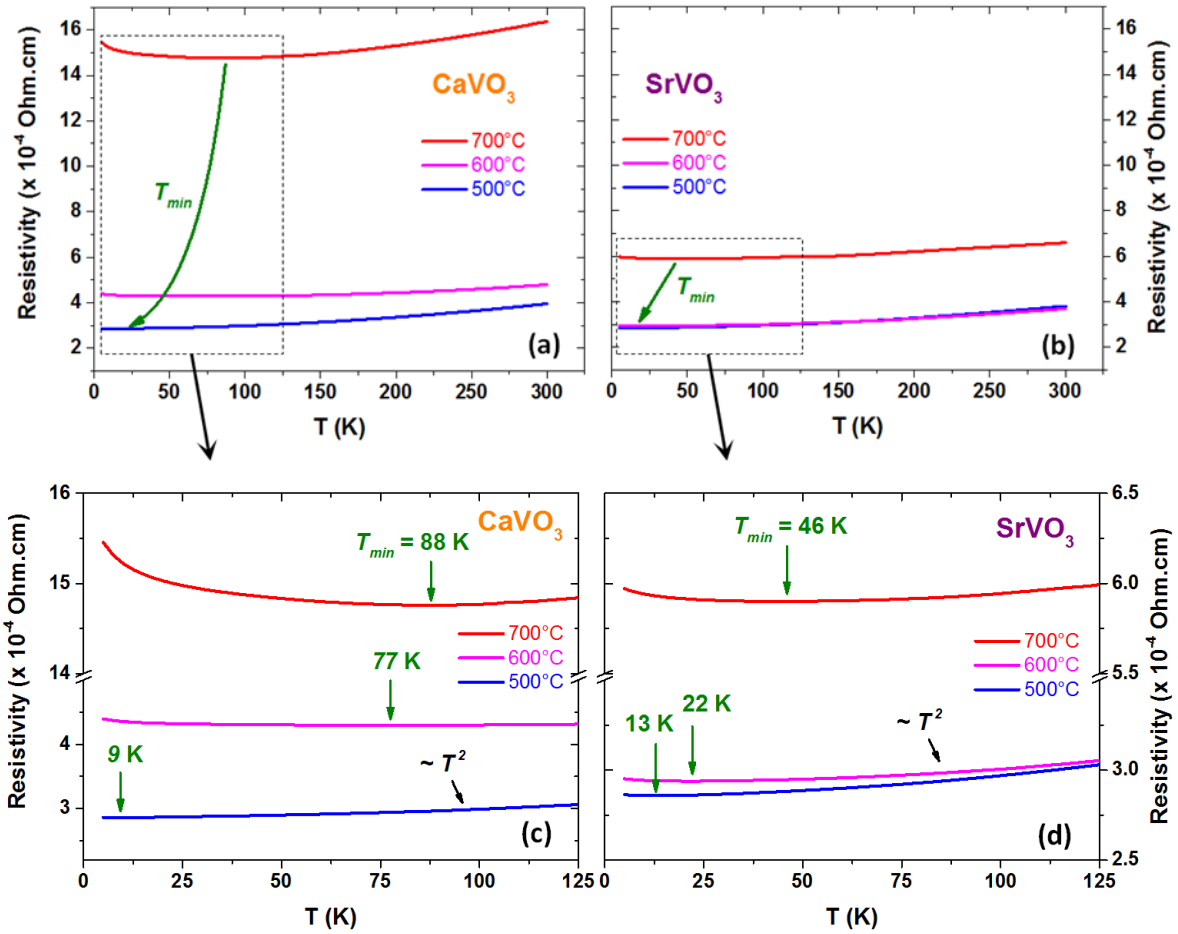

Figure 4.12.Temperature-dependent resistivity curves of CVO (a) and SVO (b) deposited on CNO NS/GS. Figures (c) and (d) focus on the resistivity upturn below T_{min} defined as the resistivity minimum occurring in the low temperature range [28].

In Figure 4.12c,d are displayed the metal-insulator transition temperatures defined as the minimum of resistivity observed at T_{min}. The measures show that T_{min} shifts with the growth temperature increasing from 9 to 88 K for CVO films and from 13 to 46 K for SVO films. Electronic localization at grain boundaries can be responsible of the upturn of the resistivity at low temperature. It shows that the metallic state can be maintained at very low temperature while the resistivities of textured vanadate films were kept closed to those of ITO [38]. These results demonstrate the excellent electrical behavior obtained using the NS.

4.5. Optical properties of the vanadate films

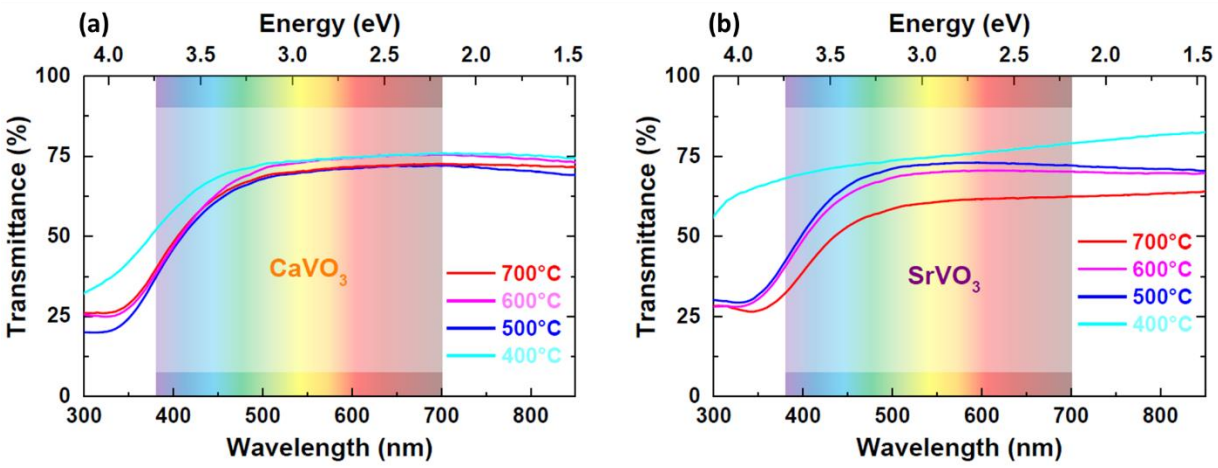

Figure 4.13. Transmission spectra of (a) CVO and (b) SVO thin films [28].

The transmission spectra of films grown at different temperatures are shown in Figure 4.13. Both vanadates films show to be transparent after 450 nm, with a transmittance from 70 to 75%, with an exception for SVO deposited at 700°C. The transmittance decreases depending on the quality and the transport properties of the film. Furthermore, the films obtained on NS display similar transmission properties to ITO films [30] and SVO and CVO single crystals [32,33]. It confirms that the NS does not degrade the transmittance of the films.

4.6. Conclusion

To conclude, the growth of CVO and SVO by PLD on glass substrates covered by NS leads to highly oriented films, and exceptional transport and optical properties, close to the performances of the standard ITO. The uncovered part of the substrate leads to amorphous regions in the vanadate films, which improve the optical transparency, while the crystallized phase allows the anisotropic electrical conduction in the film. Furthermore, the NS enable the integration of these TCOs at the relatively low temperature of 500°C.

5. Orientation control of platinum electrode grown on silicon using $[Ca_2Nb_3O_{10}]^-$ nanosheets as a seed layer

This work has been partly published in SN Applied Science [39] and the other part has been submitted to Thin Solid Films. This work has been realized in collaboration with the CRISMAT laboratory of Caen, in the framework of the PhD thesis of Jacques Manguele, under the supervision of Christophe Cibert and Gilles Poullain, and with the collaboration of Bernadette Domengès and Arnaud Fouchet.

5.1. Introduction

Platinum (Pt) is a stainless noble metal with low resistivity (10.6 μΩ.cm) which is widely used in microelectronic, especially as a bottom electrode for oxides thin films regrowth. Indeed, Pt is stable over conditions required for oxides thin films deposition and presents a cubic type structure with a lattice parameter of 3.928 Å (space group *Fm*-3*m*, JCPDS card N°00-004-0802, Annexe A, p. 215) which makes it suitable for many perovskites depositions. The Pt electrodes are conventionally deposited on $TiO_2/SiO_2/Si$ substrates. The TiO_2 layer is widely used for Pt deposition as it improves the adhesion, the crystallization, and avoids the diffusion of the Pt film in the substrate [40,41]. Pt electrodes need to be crystallized in order to allow crystal growth of ferroelectric oxides films. However, the growth temperature of Pt on this kind of substrate is about 600 to 700°C to obtain high quality electrodes [42,43], which is limiting the applications, as the temperature required for the elaboration of conventional Si-based circuits is generally lower than 500°C.

As developed in the previous parts, the $[Ca_2Nb_3O_{10}]^-$ nanosheets (NS) have shown to induce highly preferential orientation of different perovskites on widely used silicon or silica. Furthermore, it has been shown that it is possible to obtain high quality oriented film on NS at lower temperature than on single crystalline substrates. For example, it has been described previously that it was possible to obtain high quality (001) LSMO films at 550°C with interesting magnetic properties. Other examples have been described in the literature, as the achievement of highly oriented PZT films grown at 450°C [44]. In this

work, study on the growth of Pt on NS was achieved for the first time. The quality and properties of Pt films grown on the widely used $TiO_2/SiO_2/Si$ and on $NS/SiO_2/Si$ were compared at different temperatures. (111)Pt films were obtained under argon (Ar) atmospheres whereas (200)Pt films were synthesized using a mixture of Ar and oxygen (O_2) [45].

5.2. Thin films deposition conditions

Boron-doped single crystalline (100) silicon samples (NXP supplier) with a 650 nm amorphous SiO_2 obtained by thermal process were used. The radio frequency (RF) magnetron sputtering of Pt was achieved in the CRISMAT laboratory, in the framework of the PhD thesis of Jacques Manguele (in preparation). The deposition conditions of Pt are reported in Table 4.1. where standard conditions and adaptive conditions correspond to (111)Pt and (200)Pt, respectively, as optimized by J. Manguele.

Table 4.1. Experimental conditions to obtain (111) and (200) orientations of Pt. Courtesy of J. Manguele.

	Pt under standard conditions (111)Pt	Pt under adaptive conditions (200)Pt
Gas	Pure Ar	Ar 90% + O_2 10%
Total pressure	0.6 Pa	1 Pa
Sputtering power	1 W/cm^2	0.4 W/cm^2
Pt thickness	100 nm	100 nm
Deposition temperature	RT up to 625°C	RT up to 625°C

5.3. Structural analyses of the (111)Pt thin films

Figure 4.14 shows the influence of the deposition temperature on the Pt films grown on $TiO_2/SiO_2/Si$ and $NS/SiO_2/Si$ under standard conditions. For both buffer layers, the (111)Pt orientation is obtained without additional orientations. For $Pt/TiO_2/SiO_2/Si$, weak (111)Pt peaks are observed from 200°C to 475°C deposition temperature. Highly oriented (111)Pt films were obtained at temperature higher than 550°C. For $Pt/NS/SiO_2/Si$, weak (111)Pt peaks are observed at 100°C, and highly oriented (111)Pt peaks are obtained at the very low temperature of 200°C.

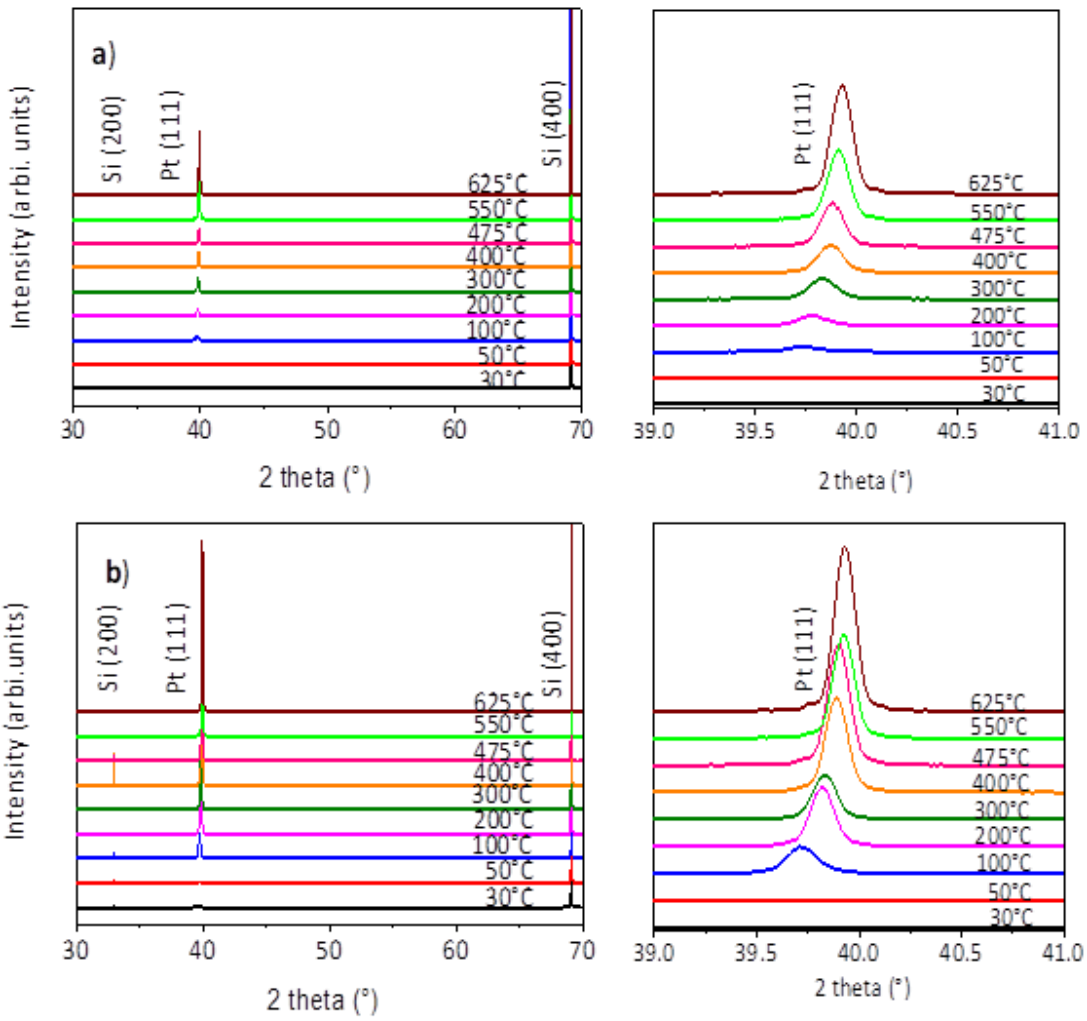

Figure 4.14. XRD diagram of Pt thin films grown at different deposition temperatures on a) $TiO_2/SiO_2/Si$ substrates and b) $NS/SiO_2/Si$ substrates. The figures on the right clearly evidence the shift of the (111)Pt line [39].

The enlargement on the (111)Pt peaks displayed in Figure 4.14 shows a regular shift of from 39.60° to 39.93° when the substrate temperature increases, for both substrates. This behavior has already been described in the literature for the deposition of Pt by sputtering on silicon substrates [46,47]. It can be explained by the difference of thermal expansion coefficients of 2.6 10^{-6} K^{-1} for silicon and 8.8 10^{-6} K^{-1} for platinum, which increases the tensile stress in the plane and decreases the Pt lattice parameter.

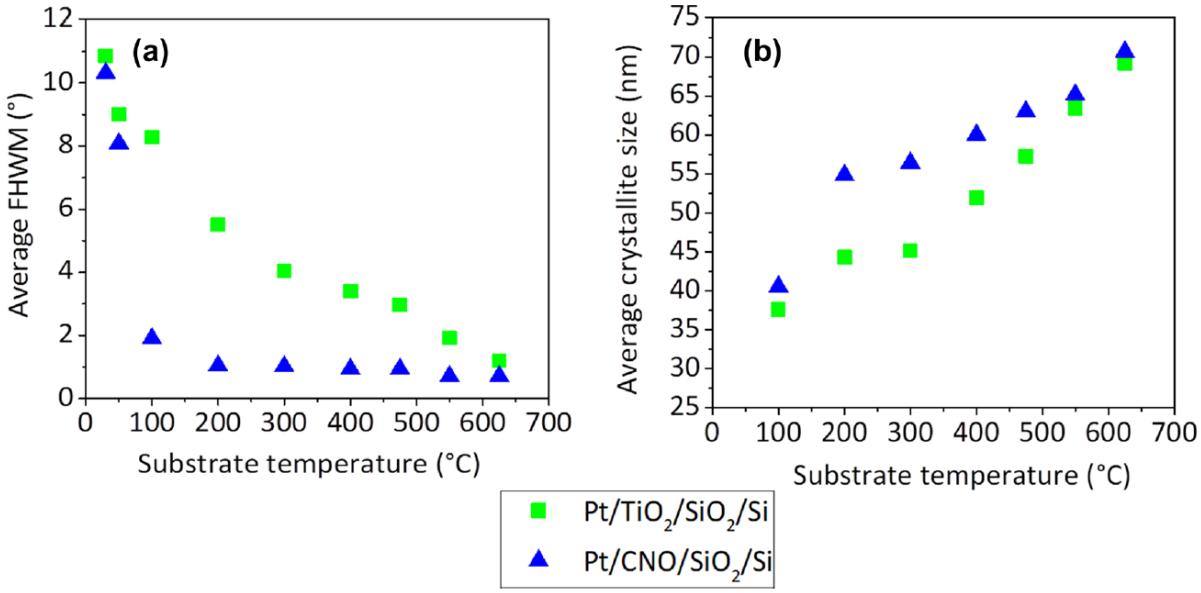

Figure 4.15. (a) Influence of the deposition temperature on the average FWHM of the rocking curve of (111) and (222) peaks. (b) Variation of the average size of the crystallites determined using the Scherrer formula (on (111) and (222) peaks) as a function of the deposition temperature [39].

In order to estimate the quality of the (111)Pt thin films, the influence of the deposition temperature on the average value of (111) and (222) FWHM of rocking curves of Pt grown on both substrates have been measured (Figure 4.15a). At temperatures higher than 600°C, the Pt thin films are highly crystallized on both substrates, with a FWHM of 1.5° on TiO_2 and 0.75° on NS at 625°C. When the temperature decreases, the FHWM of the Pt grown on $TiO_2/SiO_2/Si$ strongly increases to reach 5.5° at 200°C, while the FHWM of the Pt grown on $NS/SiO_2/Si$ remains stable around 1° until 200°C. Thus the NS allows the growth of highly crystallized and oriented (111)Pt films on silicon at 200°C.

Figure 4.15b displays the average size of the crystallites as a function of the substrate temperature. The size of the crystallites increases with the temperature for both substrates. However, at 200°C, it can be observed that the crystallite size of the (111)Pt grown on nanosheets increases (~55 nm) compared to the crystallites size of the Pt grown on $TiO_2/SiO_2/Si$ (~45 nm). Between 200°C and 500°C, the crystallites size of Pt grown on NS remains higher than the one of Pt grown on $TiO_2/SiO_2/Si$. At temperatures above 600°C, a similar average size is obtained for both substrates. This result confirms that the NS improves the quality of the Pt films.

5.4. Structural analyses of the (200)Pt thin films

The X-ray diffractograms of the Pt films grown on $TiO_2/SiO_2/Si$ and $NS/SiO_2/Si$ deposited under adaptive conditions (Table 4.1) as a function of the deposition temperature are displayed in Figure 4.16. For $Pt/TiO_2/SiO_2/Si$ (Figure 4.16a), it can be observed that whatever the temperature is, the (111)Pt orientation is obtained. These results show that the temperature is too low to obtain crystallized (200)Pt, this orientation being obtained at very high temperature (up to 750°C) according to previous studies [45,48]. Very high deposition temperatures are required on Si substrates because the (111)Pt has weaker surface energy than the (200)Pt (γ_{111} (977 $mJ.m^{-2}$) < γ_{100} (1286 $mJ.m^{-2}$) respectively).

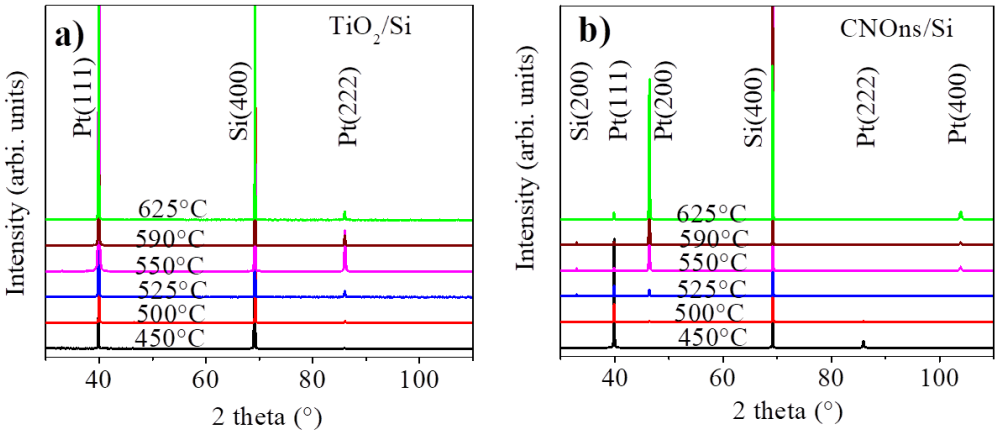

Figure 4.16. XRD of Pt thin films grown at different deposition temperatures on (a) $TiO_2/SiO_2/Si$ substrates and (b) $NS/SiO_2/Si$ substrates, using a mixture of Ar and O_2. Courtesy of J. Manguele.

For the growth of $Pt/NS/SiO_2/Si$ (Figure 4.16b), it can be observed that below 500°C, only the (111)Pt orientation is obtained. However, from the temperature of 500°C, the (200)Pt peak appears on the diffractograms. For temperatures up to 550°C, the (200)Pt peak becomes majority compared to the (111)Pt, whose the intensity decreases with the temperature. It clearly shows that the NS allows the growth of (200)Pt at moderate temperatures on SiO_2/Si substrates.

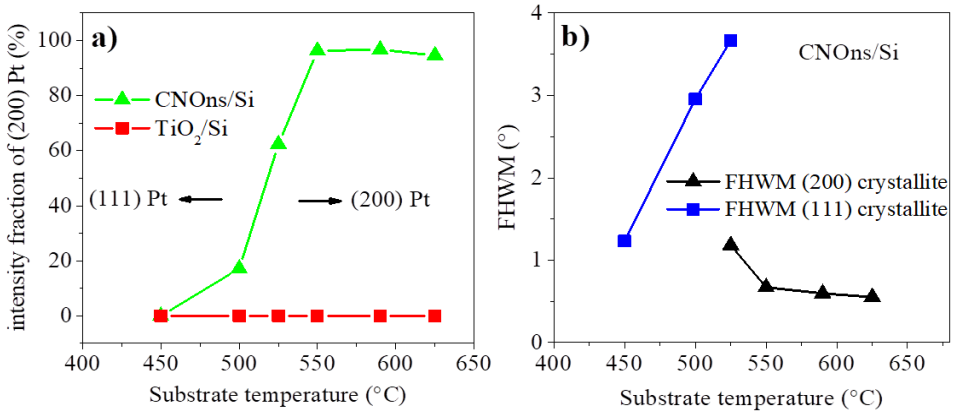

Figure 4.4.17. Influence of the deposition temperature on (a) the intensity fraction of (200)Pt and on (b) the FHWM of the rocking curve of (200) and (111) peaks. Courtesy of J. Manguele.

The intensity fractions of the (200)Pt compared to those of the (111) as a function of the temperature have been outlined Figure 4.17a to observe the switch of orientation. The transition from (200)Pt peak intensity of 20 % to the maximum of 95 % occurs between 500 and 550°C. The 5% left corresponds to the (111)Pt orientation, which can be induced by the uncovered part of the substrate by NS.

In order to check the quality of the Pt films obtained on the NS, the FHWM of the (111) and (200) peaks are displayed in Figure 4.17b. For temperatures between 200 and 400°C (not shown in the graph), highly oriented (111)Pt with FHWM <1° are obtained. Between 450 and 525°C, the quality of the (111)Pt strongly decreases with the formation of the (200)Pt. Above 550°C, highly crystallized (200)Pt is obtained (FHWM from 0.7° at 550°C to 0.5° at 625°C). Thus the NS also induces a high crystallization of the (200)Pt, even at 550°C.

5.5. Resistivity measurements of the (111) and (200)Pt thin films

In order to evaluate the possible impact of the NS on the resulting electrical properties of Pt, the resistivity of Pt films deposited in different conditions were measured. The resistivity of Pt films deposited at 30°C, 450°C, and 625°C, with comparable film thickness (in the range 90-140 nm), on $TiO_2/SiO_2/Si$ and on $NS/SiO_2/Si$ have been determined. No significant difference in resistivity is observed depending on the substrates for each deposition condition. The values of resistivity are between 18 and 24 μΩ.cm on Pt films grown under pure Ar, whereas those of films grown under Ar + O_2

display lower values (between 13 and 20 μΩ.cm), on both substrates. This small decrease might be due to the larger grain size obtained for the Ar + O_2 deposition (70-400 nm compared to 20-100 nm for pure Ar). Similar results of resistivity were observed by Lee *et al*. for (111) and (200)Pt thin films deposited on $TiO_2/SiO_2/Si$ substrates by magnetron sputtering [45].

Conclusion

In summary, the growth of (111)Pt has been achieved on $NS/SiO_2/Si$ and $TiO_2/SiO_2/Si$ for comparison. It has been shown that highly oriented and crystallized (111)Pt have been obtained on the $NS/SiO_2/Si$ at the very low temperature of 200°C. The same quality of Pt on TiO_2 is usually obtained at 625°C. Comparable values of resistivity were also obtained for each Pt film. Thus the NS opens new opportunities, especially for the elaboration of Si-based circuits.

On the other hand, highly and well-crystallized (200)Pt have been obtained under Ar + O_2 at 550°C on NS, while this orientation could not be obtained on TiO_2 even at 625°C. Higher temperatures might be requested to obtain the expected orientation on TiO_2. Thus the use of NS clearly decreased the growth temperature of (200)Pt, opening the integration of complex oxides at relatively low temperature. This is of particular interest as this orientation has shown to give better ferroelectric properties to oxide films for IR sensors, and other optoelectronic applications [49,50].

Conclusion

In this chapter was presented the growth of different oxides and metal grown on the $[Ca_2Nb_3O_{10}]^-$ nanosheets.

Highly crystallized and oriented (001)$KNbO_3$ thin films deposited by PLD have been obtained on glass substrates using the NS as a seed layer. The XRD measurements and SEM observations have confirmed the local epitaxy of the film on the NS and that the shape and average crystals size is comparable to those obtained on epitaxial films.

Highly oriented (100)BFO film deposited by CSD on silica and silicon were also obtained thanks to these NS.

Highly crystallized and oriented (001)LSMO films have been obtained. The magnetic measurements show that the magnetic properties are close to those of the epitaxial films, while low-field MR was also obtained, which is close to the property observed for a polycrystalline film.

Significant results have also been obtained for the integration of $SrVO_3$ and $CaVO_3$ as transparent conducting films on glass substrates. Thanks to the preferential orientation induced by the NS and their thin thickness, the optical and transport measurements showed that they are closed to those obtained on epitaxial thin films. These results open opportunities for the development of new low cost TCOs.

Finally, highly crystallized and oriented (111) and (200)Pt have been obtained on the NS. The required growth temperature of the (111)Pt has been decreased from 650°C to 200°C thanks to the nanosheets, and (200)Pt have also been obtained at lower temperatures than on $TiO_2/SiO_2/Si$ substrate. The Pt/NS open new opportunities for the elaboration of Si-based circuits and the integration of complex oxides at low temperature.

These results demonstrate the great interest of the NS. A wide variety of deposition techniques can be used for materials deposition. Furthermore, the growth temperature of the materials has highly decreased in most of the studies and the general properties of the obtained films are close to those of the epitaxial ones.

The perspective of this work is the growth of perovskites, such as KNO and LSMO, on the $[Ti_{0.87}O_2]^{0.52-}$, $[K_2Nb_6O_{17}]^{2-}$, and $[Cs_4W_{11}O_{36}]^{2-}$ nanosheets to obtain the (011) and (111) orientations, respectively. These depositions are in progress in collaboration with the CRISMAT laboratory.

References

[1] F. Baudouin, V. Demange, S. Ollivier, L. Rault, A.S. Brito, A.S. Maia, F. Gouttefangeas, V. Bouquet, S. Députier, B. Bérini, A. Fouchet, M. Guilloux-Viry, Orientation control of $KNbO_3$ film grown on glass substrates by $Ca_2Nb_3O_{10}^-$ nanosheets seed layer, Thin Solid Films. 693 (2020) 137682. https://doi.org/10.1016/j.tsf.2019.137682.

[2] B.T. Matthias, J.P. Remeika, Dielectric Properties of Sodium and Potassium Niobates, Phys. Rev. 82 (1951) 727–729. https://doi.org/10.1103/PhysRev.82.727.

[3] G. Shirane, H. Danner, A. Pavlovic, R. Pepinsky, Phase Transitions in Ferroelectric $KNbO_3$, Phys. Rev. 93 (1954) 672–673. https://doi.org/10.1103/PhysRev.93.672.

[4] K. Nakamura, Y. Kawamura, Orientation dependence of electromechanical coupling factors in KNbO/sub 3/, IEEE Trans. Ultrason. Ferroelectr. Freq. Control. 47 (2000) 750–755. https://doi.org/10.1109/58.842064.

[5] A. Rousseau, V. Laur, M. Guilloux-Viry, G. Tanné, F. Huret, S. Députier, A. Perrin, F. Lalu, P. Laurent, Pulsed laser deposited $KNbO_3$ thin films for applications in high frequency range, Thin Solid Films. 515 (2006) 2353–2360. https://doi.org/10.1016/j.tsf.2006.04.010.

[6] D. Fasquelle, A. Rousseau, M. Guilloux-Viry, S. Députier, A. Perrin, J.C. Carru, Dielectric and structural characterization of $KNbO_3$ ferroelectric thin films epitaxially grown by pulsed laser deposition on Nb doped $SrTiO_3$, Thin Solid Films. 518 (2010) 3432–3438. https://doi.org/10.1016/j.tsf.2010.01.005.

[7] L. Katz, H.D. Megaw, The structure of potassium niobate at room temperature: the solution of a pseudosymmetric structure by Fourier methods, Acta Crystallogr. 22 (1967) 639–648. https://doi.org/10.1107/S0365110X6700129X.

[8] V. Bouquet, F. Baudouin, V. Demange, S. Députier, S. Ollivier, L. Joanny, L. Rault, A. Fouchet, M. Guilloux-Viry, Influence of two-dimensional oxide nanosheets seed layers on the growth of (100)$BiFeO_3$ thin films synthesized by chemical solution deposition, Thin Solid Films. 693 (2020) 137687. https://doi.org/10.1016/j.tsf.2019.137687.

[9] G. Catalan, J.F. Scott, Physics and Applications of Bismuth Ferrite, Adv. Mater. 21 (2009) 2463–2485. https://doi.org/10.1002/adma.200802849.

[10] J. Wang, Epitaxial $BiFeO_3$ Multiferroic Thin Film Heterostructures, Science. 299 (2003) 1719–1722. https://doi.org/10.1126/science.1080615.

[11] J.M. Moreau, C. Michel, R. Gerson, W.J. James, Ferroelectric $BiFeO_3$ X-ray and neutron diffraction study, J. Phys. Chem. Solids. 32 (1971) 1315–1320. https://doi.org/10.1016/S0022-3697(71)80189-0.

[12] K. Nagasaka, N. Oshima, J.W. Kim, H. Shima, A. Akama, T. Kiguchi, K. Nishida, T.J. Konno, H. Funakubo, H. Uchida, Fabrication of $(100)_c$-oriented Mn-doped bismuth ferrite films on silicon and stainless steel substrates using calcium niobate nanosheets, J. Ceram. Soc. Jpn. 123 (2015) 322–328. https://doi.org/10.2109/jcersj2.123.322.

[13] B.-W. Li, M. Osada, Y. Ebina, K. Akatsuka, K. Fukuda, T. Sasaki, High Thermal Robustness of Molecularly Thin Perovskite Nanosheets and Implications for Superior Dielectric Properties, ACS Nano. 8 (2014) 5449–5461. https://doi.org/10.1021/nn502014c.

[14] A. Boileau, M. Dallocchio, F. Baudouin, A. David, U. Lüders, B. Mercey, A. Pautrat, V. Demange, M. Guilloux-Viry, W. Prellier, A. Fouchet, Textured Manganite Films Anywhere, ACS Appl. Mater. Interfaces. 11 (2019) 37302–37312. https://doi.org/10.1021/acsami.9b12209.

[15] J.M.D. Coey, M. Viret, S. von Molnár, Mixed-valence manganites, Adv. Phys. 48 (1999) 167–293. https://doi.org/10.1080/000187399243455.

[16] M.B. Salamon, M. Jaime, The physics of manganites: Structure and transport, Rev. Mod. Phys. 73 (2001) 583–628. https://doi.org/10.1103/RevModPhys.73.583.

[17] O. Rousseau, S. Flament, B. Guillet, M.L.C. Sing, L. Méchin, Magnetic Sensors Based on AMR Effect in LSMO Thin Films, Proceedings. 1 (2017) 635. https://doi.org/10.3390/proceedings1040635.

[18] S. Majumdar, S. van Dijken, Pulsed laser deposition of $La_{1-x}Sr_xMn_3$: thin-film properties and spintronic applications, J. Phys. Appl. Phys. 47 (2014) 034010. https://doi.org/10.1088/0022-3727/47/3/034010.

[19] S.M. Strutner, A. Garcia, S. Ula, C. Adamo, W.L. Richards, K. Wang, D.G. Schlom, G.P. Carman, Index of refraction changes under magnetic field observed in $La_{0.66}Sr_{0.33}MnO_3$ correlated to the magnetorefractive effect, Opt. Mater. Express. 7 (2017) 468. https://doi.org/10.1364/OME.7.000468.

[20] Yu.P. Sukhorukov, A.M. Moskvin, N.N. Loshkareva, I.B. Smolyak, V.E. Arkhipov, Ya.M. Mukovskii, A.V. Shmatok, Magnetooptical faraday effect in $La_{0.7}Sr_{0.3}MnO_{3-\delta}$ films, Tech. Phys. 46 (2001) 778–781. https://doi.org/10.1134/1.1379652.
[21] S.J. Hibble, S.P. Cooper, A.C. Hannon, I.D. Fawcett, M. Greenblatt, Local distortions in the colossal magnetoresistive manganates $La_{0.70}Ca_{0.30}MnO_3$, $La_{0.80}Ca_{0.20}MnO_3$ and $La_{0.70}Sr_{0.30}MnO_3$ revealed by total neutron diffraction, J. Phys. Condens. Matter. 11 (1999) 9221–9238. https://doi.org/10.1088/0953-8984/11/47/308.
[22] B. Mercey, A. David, O. Copie, W. Prellier, Monitoring the growth of $SrTiO_3$ and $La_{0.66}Sr_{0.33}MnO_3$ thin films using a low-pressure Reflection High Energy Electron Diffraction system, Phys. B Condens. Matter. 503 (2016) 100–105. https://doi.org/10.1016/j.physb.2016.09.023.
[23] M. Navasery, S.A. Halim, N. Soltani, G. Bahmanrokh, M. Erfani, S.K. Chen, K.P. Lim, M.M. Awang Kechik, Growth and characterization of $La_{5/8}Sr_{3/8}MnO_3$ thin films prepared by pulsed laser deposition on different substrates, J. Mater. Sci. Mater. Electron. 25 (2014) 1317–1324. https://doi.org/10.1007/s10854-014-1729-1.
[24] C. Kwon, M.C. Robson, K.-C. Kim, J.Y. Gu, S.E. Lofland, S.M. Bhagat, Z. Trajanovic, M. Rajeswari, T. Venkatesan, A.R. Kratz, R.D. Gomez, R. Ramesh, Stress-induced effects in epitaxial $(La_{0.7}Sr_{0.3})MnO_3$ films, J. Magn. Magn. Mater. 172 (1997) 229–236. https://doi.org/10.1016/S0304-8853(97)00058-9.
[25] F. Tsui, M.C. Smoak, T.K. Nath, C.B. Eom, Strain-dependent magnetic phase diagram of epitaxial $La_{0.67}Sr_{0.33}MnO_3$ thin films, Appl. Phys. Lett. 76 (2000) 2421–2423. https://doi.org/10.1063/1.126363.
[26] P. Lecoeur, P.L. Trouilloud, G. Xiao, A. Gupta, G.Q. Gong, X.W. Li, Magnetic domain structures of $La_{0.67}Sr_{0.33}MnO_3$ thin films with different morphologies, J. Appl. Phys. 82 (1997) 3934–3939. https://doi.org/10.1063/1.365700.
[27] Y. Xu, U. Memmert, U. Hartmann, Magnetic field sensors from polycrystalline manganites, Sens. Actuators Phys. 91 (2001) 26–29. https://doi.org/10.1016/S0924-4247(01)00493-9.
[28] A. Boileau, S. Hurand, F. Baudouin, U. Lüders, M. Dallocchio, B. Bérini, A. Cheikh, A. David, F. Paumier, T. Girardeau, P. Marie, C. Labbé, J. Cardin, D. Aureau, M. Frégnaux, M. Guilloux-Viry, W. Prellier, Y. Dumont, V. Demange, A. Fouchet, Highly Transparent and Conductive Indium-Free Vanadates Crystallized at Reduced Temperature on Glass Using a 2D Transparent Nanosheet Seed Layer, Adv. Funct. Mater. (2021) 2108047. https://doi.org/10.1002/adfm.202108047.
[29] R.A. Afre, N. Sharma, M. Sharon, M. Sharon, Transparent Conducting Oxide Films for Various Applications: A Review, Rev. Adv. Mater. Sci. 53 (2018) 79–89. https://doi.org/10.1515/rams-2018-0006.
[30] V. Teixeira, H.N. Cui, L.J. Meng, E. Fortunato, R. Martins, Amorphous ITO thin films prepared by DC sputtering for electrochromic applications, Thin Solid Films. 420–421 (2002) 70–75. https://doi.org/10.1016/S0040-6090(02)00656-9.
[31] C.G. Granqvist, Transparent conductors as solar energy materials: A panoramic review, Sol. Energy Mater. Sol. Cells. 91 (2007) 1529–1598. https://doi.org/10.1016/j.solmat.2007.04.031.
[32] L. Zhang, Y. Zhou, L. Guo, W. Zhao, A. Barnes, H.-T. Zhang, C. Eaton, Y. Zheng, M. Brahlek, H.F. Haneef, N.J. Podraza, M.H.W. Chan, V. Gopalan, K.M. Rabe, R. Engel-Herbert, Correlated metals as transparent conductors, Nat. Mater. 15 (2016) 204–210. https://doi.org/10.1038/nmat4493.
[33] A. Boileau, A. Cheikh, A. Fouchet, A. David, R. Escobar-Galindo, C. Labbé, P. Marie, F. Gourbilleau, U. Lüders, Optical and electrical properties of the transparent conductor $SrVO_3$ without long-range crystalline order, Appl. Phys. Lett. 112 (2018) 021905. https://doi.org/10.1063/1.5016245.
[34] M.J. Rey, Ph. Dehaudt, J.C. Joubert, B. Lambert-Andron, M. Cyrot, F. Cyrot-Lackmann, Preparation and structure of the compounds $SrVO_3$ and Sr_2VO_4, J. Solid State Chem. 86 (1990) 101–108. https://doi.org/10.1016/0022-4596(90)90119-I.
[35] H. Falcón, J.A. Alonso, M.T. Casais, M.J. Martínez-Lope, J. Sánchez-Benítez, Neutron diffraction study, magnetism and magnetotransport of stoichiometric $CaVO_3$ perovskite with positive magnetoresistance, J. Solid State Chem. 177 (2004) 3099–3104. https://doi.org/10.1016/j.jssc.2004.05.010.
[36] A. Boileau, A. Cheikh, A. Fouchet, A. David, C. Labbé, P. Marie, F. Gourbilleau, U. Lüders, Tuning of the Optical Properties of the Transparent Conducting Oxide $SrVO_3$ by Electronic Correlations, Adv. Opt. Mater. 7 (2019) 1801516. https://doi.org/10.1002/adom.201801516.
[37] A. Fouchet, M. Allain, B. Bérini, E. Popova, P.-E. Janolin, N. Guiblin, E. Chikoidze, J. Scola, D. Hrabovsky, Y. Dumont, N. Keller, Study of the electronic phase transition with low dimensionality in $SrVO_3$ thin films, Mater. Sci. Eng. B. 212 (2016) 7–13. https://doi.org/10.1016/j.mseb.2016.07.009.
[38] M. Onoda, H. Ohta, H. Nagasawa, Metallic properties of perovskite oxide $SrVO_3$, Solid State Commun. 79 (1991) 281–285. https://doi.org/10.1016/0038-1098(91)90546-8.

[39] J.J. Manguele, F. Baudouin, C. Cibert, B. Domengès, V. Demange, M. Guilloux-Viry, A. Fouchet, G. Poullain, Highly textured Pt thin film grown at very low temperature using $Ca_2Nb_3O_{10}$ nanosheets as seed layer, SN Appl. Sci. 2 (2020) 453. https://doi.org/10.1007/s42452-020-2271-9.
[40] J.O. Olowolafe, R.E. Jones, A.C. Campbell, R.I. Hegde, C.J. Mogab, R.B. Gregory, Effects of anneal ambients and Pt thickness on Pt/Ti and Pt/Ti/TiN interfacial reactions, J. Appl. Phys. 73 (1993) 1764–1772. https://doi.org/10.1063/1.353212.
[41] G.J. Willems, D.J. Wouters, H.E. Maes, Influence of the Pt electrode on the properties of sol-gel PZT-films, Microelectron. Eng. 29 (1995) 217–220. https://doi.org/10.1016/0167-9317(95)00149-2.
[42] B. Vilquin, G. Le Rhun, R. Bouregba, G. Poullain, H. Murray, Effect of in situ Pt bottom electrode deposition and of Pt top electrode preparation on PZT thin films properties, Appl. Surf. Sci. 195 (2002) 63–73. https://doi.org/10.1016/S0169-4332(02)00554-8.
[43] X. Zhu, E. Defaÿ, M. Aïd, Y. Ren, C. Zhang, J. Zhu, J. Zhu, D. Xiao, Preferential growth and enhanced dielectric properties of $Ba_{0.7}Sr_{0.3}TiO_3$ thin films with preannealed Pt bottom electrode, J. Phys. Appl. Phys. 46 (2013) 105301. https://doi.org/10.1088/0022-3727/46/10/105301.
[44] M.D. Nguyen, E.P. Houwman, H. Yuan, B.J. Wylie-van Eerd, M. Dekkers, G. Koster, J.E. ten Elshof, G. Rijnders, Controlling Piezoelectric Responses in $Pb(Zr_{0.52}Ti_{0.48})O_3$ Films through Deposition Conditions and Nanosheet Buffer Layers on Glass, ACS Appl. Mater. Interfaces. 9 (2017) 35947–35957. https://doi.org/10.1021/acsami.7b07428.
[45] D.-S. Lee, D.-Y. Park, H.-J. Woo, S.-H. Kim, J. Ha, E. Yoon, Preferred Orientation Controlled Giant Grain Growth of Platinum Thin Films on SiO_2/Si Substrates, Jpn. J. Appl. Phys. 40 (2001) L1–L3. https://doi.org/10.1143/JJAP.40.L1.
[46] M. Sreemany, S. Sen, Effect of substrate temperature and annealing temperature on the structural, electrical and microstructural properties of thin Pt films by rf magnetron sputtering, Appl. Surf. Sci. 253 (2006) 2739–2746. https://doi.org/10.1016/j.apsusc.2006.05.040.
[47] R.M. Tiggelaar, R.G.P. Sanders, A.W. Groenland, J.G.E. Gardeniers, Stability of thin platinum films implemented in high-temperature microdevices, Sens. Actuators Phys. 152 (2009) 39–47. https://doi.org/10.1016/j.sna.2009.03.017.
[48] M.H. Kim, T.-S. Park, D.-S. Lee, E. Yoon, D.-Y. Park, H.-J. Woo, D.-I. Chun, J. Ha, Highly (200)-oriented Pt films on SiO_2/Si substrates by seed selection through amorphization and controlled grain growth, J. Mater. Res. 14 (1999) 634–637. https://doi.org/10.1557/JMR.1999.0641.
[49] R. Takayama, Y. Tomita, K. Iijima, I. Ueda, Pyroelectric linear array infrared sensors made of *c* -axis-oriented La-modified $PbTiO_3$ thin films, J. Appl. Phys. 63 (1988) 5868–5872. https://doi.org/10.1063/1.340276.
[50] K. Iijima, R. Takayama, Y. Tomita, I. Ueda, Epitaxial growth and the crystallographic, dielectric, and pyroelectric properties of lanthanum-modified lead titanate thin films, J. Appl. Phys. 60 (1986) 2914–2919. https://doi.org/10.1063/1.337078.

Conclusions and perspectives

This thesis was focused on the synthesis and deposition of oxides nanosheets on various substrates for the preferentially oriented growth of complex oxides thin films. This work has been realized in the framework of the ANR PolyNASH involving the ISCR, CRISMAT, and GEMaC laboratories.

During this work, five different nanosheets were synthesized and deposited on various substrates. First, the $[Ca_2Nb_3O_{10}]^-$ nanosheets were obtained from the protonation and exfoliation of $KCa_2Nb_3O_{10}$ (KCN). KCN powders were synthesized by solid state reaction (SSR) and by K_2SO_4 and K_2MoO_4 molten salt syntheses (MSS). The latter has the great advantage to give larger crystals than by SSR. Double molten salt syntheses were developed during this thesis to increase the size homogeneity of the crystals. The KCN powder and its protonated form were studied by XRD, SEM, EDXS, and TEM. The exfoliation of the protonated phase by TBAOH leads to nanosheet with lateral dimensions from 0.1 to 1 µm from the SSR powder and up to 20 µm from the MSS powder. The nanosheets were deposited on various substrates by the Langmuir-Blodgett method and the drop casting techniques that were developed in the laboratory in the frame of this project. AFM or SEM was systematically performed to check the coverage of the nanosheets at the surface of the substrate. In-plane XRD experiments confirmed the theoretical in-plane parameters of the nanosheets. XPS experiments were realized to demonstrate that it is possible to deoxidize a Si substrate covered by nanosheets with an HF treatment, without affecting the nanosheets. Moreover, the coupled experiments of XPS and STM have demonstrated the stability of the $[Ca_2Nb_3O_{10}]^-$ nanosheets up to 160°C under UHV, and that at high temperature (360°C), oxygen vacancies were formed at the surface of the nanosheets, leading to a reduction of the niobium atoms to compensate the negative charge of the nanosheets surfaces.

$[K_{4-x}Nb_6O_{17}]^{x-}$ nanosheets have been successfully obtained from the exfoliation of $K_4Nb_6O_{17}$. The exfoliation with TBAOH of the protonated phase leads to nanoscrolls. To avoid their formation, the exfoliation was realized using *n*-propylammonium and *n*-butylammonium. These nanosheets were deposited for the first time onto glass substrates by the Langmuir-Blodgett and the drop casting techniques. However, the

depositions parameters have to be adjusted to obtain a homogenous deposition and to allow the deposition on other substrates. Further experiments have to be realized to control the nanosheets thicknesses.

The $[Ti_{0.87}O_2]^{0.52-}$ nanosheets were synthesized from the protonation and the exfoliation of the $K_{0.8}Ti_{1.73}Li_{0.27}O_4$ phase obtained by molten salt synthesis. Dense monolayers of nanosheets were obtained by the drop casting technique on various substrates.

The $[Cs_4W_{11}O_{36}]^{2-}$ nanosheets were successfully obtained by the protonation and exfoliation of the $Cs_6W_{11}O_{36}$ phase. The deposition by the Langmuir-Blodgett method and the drop casting technique show high coverage on the surface of various substrates.

$[MnO_2]^{\delta-}$ nanosheets have been synthesized by the oxidation of $MnCl_2$ by H_2O_2 and by the reduction of $KMnO_4$ by sodium lauryl sulfate. The reduction synthesis has shown to be very fast. However, a mix of nanosheets, nanowires, and nanocrystals, and elements pollution have been observed. For the oxidation synthesis, large $[MnO_2]^{\delta-}$ nanosheets have been obtained without any secondary phase and pollutions. However, the solution remains stable for only 2 weeks. The next step is to deposit the $[MnO_2]^{\delta-}$ nanosheets on various substrates and to study their stability.

The $[Ca_2Nb_3O_{10}]^-$ nanosheets were then used for the oriented growth of complex oxides and metal. At ISCR, highly crystallized and orientated (001)$KNbO_3$ and (001)$BiFeO_3$ thin films were deposited by PLD and CSD respectively on the nanosheets on silica and silicon substrates. The XRD measurements and SEM observations have confirmed the local epitaxy of the film on the nanosheets.

In collaboration with the CRISMAT laboratory, highly crystallized and oriented (001)$La_{0.67}Sr_{0.33}MnO_3$ films on glass have been obtained. The magnetic measurements show that the magnetic properties are close to those of the epitaxial films grown on single crystalline substrates, while low-field magnetoresistance was also obtained, which is close to the property observed for a polycrystalline film. Significant results have also been obtained by the integration of $SrVO_3$ and $CaVO_3$ as transparent conducting oxides (TCO) films on glass substrates. Thanks to the preferential orientation induced by the NS and their thin thickness, the optical and transport measurements showed that they are close

to those obtained on epitaxial thin films. These results open opportunities for the development of new low cost TCOs.

Finally, highly crystallized and oriented (111) and (200)Pt have been obtained on the $[Ca_2Nb_3O_{10}]^-$ nanosheets in collaboration with the CRISMAT laboratory. The growth temperature of the (111)Pt has been decreased from 650°C to 200°C thanks to the nanosheets, and (200)Pt have also been obtained at lower temperatures than on $TiO_2/SiO_2/Si$ substrate. These results open new opportunities for the elaboration of Si-based circuits and the integration of complex oxides at low temperature.

The results obtained during this thesis demonstrate the great interest of the nanosheets for the oriented growth of thin films. A wide variety of deposition techniques can be used for thin films depositions, the growth temperature of the materials has highly decreased in most of the study, and the general properties of the obtained films are close to those of the epitaxial ones. The growth of perovskites, such as $KNbO_3$ and $La_{0.67}Sr_{0.33}MnO_3$, on the $[Ti_{0.87}O_2]^{0.52-}$, $[K_2Nb_6O_{17}]^{2-}$, and $[Cs_4W_{11}O_{36}]^{2-}$ nanosheets are currently in progress to obtain the (011) and (111) orientations, respectively in collaboration with the CRISMAT laboratory.

The various interesting properties of the oxide nanosheets have also led to the synthesis of other oxide nanosheets such as $[Ti_{1.6-x/2}Fe_xCo_{0.4-x/2}O_4]^{0.8-}$ with x = 0.2–0.325, for the realization of multilayer/superlattice assemblies in the future.

Annexes

Annexe A: ICDD index cards

01-075-9853 Feb 12, 2018 11:42 AM (fbaudouin)

Status Primary **QM:** Blank **Pressure/Temperature:** Ambient **Chemical Formula:** K Ca2 (Nb3 O10)
Empirical Formula: Ca2 K Nb3 O10 **Weight %:** Ca14.37 K7.01 Nb49.95 O28.67
Atomic %: Ca12.50 K6.25 Nb18.75 O62.50 **ANX:** AB2C3X10
Compound Name: Potassium Calcium Niobium Oxide **Common Name:** Potassium dicalcium triniobate

Radiation: CuKα **λ:** 1.5406Å **d-Spacing:** Calculated **Intensity:** Calculated **I/Ic:** 3.33

SYS: Monoclinic **SPGR:** P21/m (11)
Author's Cell [AuthCell a: 7.7418(6)Å **AuthCell b:** 7.7073(6)Å **AuthCell c:** 14.859(1)Å
AuthCell β: 97.51(1)° **AuthCell Vol:** 879.01Å³ **AuthCell Z:** 4.00 **AuthCell MolVol:** 219.75]
Author's Cell Axial Ratio [c/a: 1.919 **a/b:** 1.004 **c/b:** 1.928]
Density [Dcalc: 4.216g/cm³ **Dstruc:** 4.22g/cm³] **SS/FOM:** F(30) = 166.3(0.0038, 47)
Temp: 298.000K (Ambient temperature assigned by ICDD editor) **R-factor:** 0.012

Space Group: P21/m (11) **Molecular Weight:** 557.97
Crystal Data [XtlCell a: 14.859Å **XtlCell b:** 7.707Å **XtlCell c:** 7.742Å **XtlCell α:** 90.00° **XtlCell β:** 97.51°
XtlCell γ: 90.00° **XtlCell Vol:** 879.01Å³ **XtlCell Z:** 4.00]
Crystal Data Axial Ratio [c/a: 0.521 **a/b:** 1.928 **c/b:** 1.005]
Reduced Cell [RedCell a: 7.707Å **RedCell b:** 7.742Å **RedCell c:** 14.859Å **RedCell α:** 97.51°
RedCell β: 90.00° **RedCell γ:** 90.00° **RedCell Vol:** 879.01Å³]

Crystal (Symmetry Allowed): Centrosymmetric

Pearson: mP64.00 **Subfile(s):** ICSD Pattern, Inorganic **Entry Date:** 07/27/2010
Last Modification Date: 01/17/2013

References:

Type	DOI	Reference
Primary Reference		Calculated from ICSD using POWD-12++.
Structure		"Powder neutron diffraction study of layered perovskite, K Ca2 Nb3 O10". Tokumitsu, T., Toda, K., Aoyagi, T., Sakuraba, D., Uematsu, K., Sato, M. J. Ceram. Soc. Jpn. 114, 795 (2006).

Database Comments: ANX: AB2C3X10. Analysis: Ca2 K1 Nb3 O10. Formula from original source: K Ca2 (Nb3 O10). ICSD Collection Code: 157839. Significant Warning: Reported displacement parameters on non H atoms are outside the range 0.001<U<0.1. Ueq=0.012 used in the calculation. Wyckoff Sequence: f9 e12 b a (P121/M1). Unit Cell Data Source: Powder Diffraction.

d-Spacings (198) - 01-075-9853 (Fixed Slit Intensity) - Cu Kα1 1.54056Å

2θ	d(Å)	I	h	k	l	*	2θ	d(Å)	I	h	k	l	*	2θ	d(Å)	I	h	k	l	*
5.9945	**14.731500**	999	0	0	1		31.3775	2.848550	506m	2	0	3		40.6164	2.219380	2	-1	3	3	
11.5195	7.675390	1	1	0	0		31.3775	2.848550	m	-2	0	4		40.9490	2.202120	14m	2	0	5	
12.0054	7.365770	183	0	0	2		32.5073	2.752080	18	0	1	5		40.9490	2.202120	m	-2	0	6	
12.9527	6.829130	5	0	1	1		32.9085	**2.719440**	567m	2	2	0		41.4500	2.176650	2	1	2	5	
13.6767	6.469230	1	1	0	1		32.9085	**2.719440**	m	-2	2	1		41.7058	2.163890	1	1	1	6	
15.5341	5.699640	2	-1	0	2		33.6327	2.662520	159	0	2	4		41.9124	2.153700	1m	3	0	3	
16.6343	5.325030	8	0	1	2		34.0482	2.630970	28m	2	2	1		41.9124	2.153700	m	-3	1	4	
17.7308	4.998140	5	1	0	2		34.0482	2.630970	m	-2	2	2		42.1349	2.142840	3	-3	2	1	
18.0498	4.910510	165	0	0	3		34.7674	2.578180	2	-3	0	1		42.2993	2.134890	15m	2	3	0	
19.3530	4.582680	3	-1	1	2		35.4382	2.530900	1	0	3	1		42.2993	2.134890	m	3	2	0	
20.1366	4.406090	1	-1	0	3		35.5804	2.521110	1	-3	0	2		42.6660	2.117390	18m	2	1	5	
21.1687	4.193540	1	1	1	2		35.8885	2.500170	9m	2	0	4		42.6660	2.117390	m	-2	1	6	
21.4384	4.141380	8	0	1	3		35.8885	2.500170	m	-2	0	5		42.9400	2.104510	174m	0	0	7	
23.0603	3.853650	298	0	2	0		36.2276	2.477540	14m	2	2	2		42.9400	2.104510	m	-1	0	7	
23.1574	3.837700	369m	2	0	0		36.2276	2.477540	m	-2	2	3		43.2192	2.091560	24m	2	3	1	
23.1574	3.837700	m	-1	1	3		36.5679	2.455260	14	0	0	6		43.2192	2.091560	m	-2	3	2	
23.8474	3.728200	15	0	2	1		36.7267	2.445010	3m	1	2	4		43.5221	2.077700	1m	3	1	3	
24.1452	3.682890	219	0	0	4		36.7267	2.445010	m	-3	1	1		43.5221	2.077700	m	3	2	1	
24.6971	3.601820	111m	2	0	1		36.8635	2.436250	3m	1	3	0		43.6770	2.070690	5m	0	2	6	
24.6971	3.601820	m	-2	0	2		36.8635	2.436250	m	-1	0	6		43.6770	2.070690	m	-3	0	5	
25.3991	3.503840	1	-1	0	4		37.0283	2.425780	10m	0	3	2		43.9817	2.057050	1	-1	2	6	
25.5196	3.487570	1	1	1	3		37.0283	2.425780	m	3	1	0		44.4155	2.037960	1	-3	2	3	
25.9140	3.435380	23m	2	1	0		37.1230	2.419810	4	-1	3	1		44.6714	2.026880	1m	0	1	7	
25.9140	3.435380	m	-2	1	1		37.5028	2.396170	7m	-3	0	3		44.6714	2.026880	m	-1	1	7	
26.0748	3.414560	62	0	2	2		37.5028	2.396170	m	-3	1	2		45.0179	2.012080	1m	2	3	2	
26.8064	3.323000	3	0	1	4		37.6407	2.387710	8	1	3	1		45.0179	2.012080	m	-2	3	3	
27.3151	3.262260	28m	2	1	1		37.7973	2.378180	8m	2	1	4		45.4440	1.994200	2	1	3	4	
27.3151	3.262260	m	-2	1	2		37.7973	2.378180	m	-2	1	5		45.7091	1.983250	1	3	0	4	
27.5531	3.234620	103m	2	0	2		38.4011	2.342160	6m	0	2	5		46.3777	1.956200	22m	2	0	6	
27.5531	3.234620	m	-2	0	3		38.4011	2.342160	m	-1	3	2		46.3777	1.956200	m	-2	0	7	
27.9490	3.189700	5m	-1	1	4		38.7860	2.319800	8	-1	1	6		46.9045	1.935450	202m	0	3	5	
27.9490	3.189700	m	-1	2	2		39.0164	2.306630	2	-1	2	5		46.9045	1.935450	m	-4	0	1	
28.1889	3.163090	1	1	0	4		39.2992	2.290680	27m	2	2	3		47.1270	1.926830	193	0	4	0	
29.4388	**3.031580**	606	0	2	3		39.2992	2.290680	m	-2	2	4		47.3350	1.918850	13m	4	0	0	
29.9228	2.983640	21m	2	1	2		39.5563	2.276380	6	0	3	3		47.3350	1.918850	m	-1	3	5	
29.9228	2.983640	m	-2	1	3		39.9552	2.254570	6	1	0	6		47.5532	1.910550	12m	0	4	1	
30.3109	2.946310	28	0	0	5		40.1690	2.243060	2	-3	0	4		47.5532	1.910550	m	2	2	5	
30.7991	2.900710	3	-1	2	3		40.5002	2.225480	1	3	1	2		47.8369	1.899880	2	-3	0	6	

2θ	d(Å)	I	h	k	l	*	2θ	d(Å)	I	h	k	l	*	2θ	d(Å)	I	h	k	l	*
47.9576	1.895380	1m	2	1	6		53.1444	1.721970	51m	2	4	0		57.2033	1.609050	5	-1	1	9	
47.9576	1.895380	m	-2	1	7		53.1444	1.721970	m	-2	4	1		57.7152	1.595990	195m	2	2	7	
48.3251	1.881820	1	3	2	3		53.2872	1.717690	11m	4	2	0		57.7152	1.595990	m	2	4	3	
48.5919	1.872110	11m	4	0	1		53.2872	1.717690	m	-4	2	2		58.1262	1.585680	4m	1	2	8	
48.5919	1.872110	m	-4	0	3		53.4248	1.713590	39m	4	0	3		58.1262	1.585680	m	-3	2	7	
48.8143	1.864100	10m	0	4	2		53.4248	1.713590	m	-4	0	5		58.2712	1.582080	11m	2	0	8	
48.8143	1.864100	m	4	1	0		53.6380	1.707280	41m	0	4	4		58.2712	1.582080	m	-2	0	9	
49.2953	1.847030	85m	0	2	7		53.6380	1.707280	m	2	1	7		58.9376	1.565770	55m	4	2	3	
49.2953	1.847030	m	-1	2	7		53.9209	1.698990	14m	2	4	1		58.9376	1.565770	m	-4	2	5	
49.4550	1.841440	23m	0	0	8		53.9209	1.698990	m	-2	4	2		59.6076	1.549760	1m	2	1	8	
49.4550	1.841440	m	1	3	5		54.2426	1.689670	2m	-1	4	4		59.6076	1.549760	m	-2	1	9	
50.1007	1.819210	2m	3	0	5		54.2426	1.689670	m	-3	3	4		59.8779	1.543410	1m	-3	4	1	
50.1007	1.819210	m	-4	1	3		54.4431	1.683920	10m	4	2	1		59.8779	1.543410	m	-5	0	2	
50.2884	1.812860	1	3	3	0		54.4431	1.683920	m	-4	2	3		60.1373	1.537370	1m	4	3	0	
50.6621	1.800360	19m	1	4	2		54.8652	1.671960	2m	2	3	5		60.1373	1.537370	m	-4	3	2	
50.6621	1.800360	m	4	0	2		54.8652	1.671960	m	4	1	3		60.3226	1.533090	1	0	5	1	
50.8642	1.793680	19m	0	1	8		55.2400	1.661500	1	0	2	8		60.6244	1.526180	6m	2	4	4	
50.8642	1.793680	m	0	4	3		55.4618	1.655380	22m	2	4	2		60.6244	1.526180	m	-2	4	5	
51.3013	1.779420	2	3	3	1		55.4618	1.655380	m	-2	4	3		60.9124	1.519650	4m	3	4	1	
51.4380	1.775010	1	0	3	6		55.8308	1.645310	2m	3	2	5		60.9124	1.519650	m	4	0	5	
51.7072	1.766400	10m	-1	3	6		55.8308	1.645310	m	-1	0	9		61.0841	1.515790	6m	0	4	6	
51.7072	1.766400	m	-1	4	3		56.1452	1.636840	10	0	0	9		61.0841	1.515790	m	-5	1	1	
52.1666	1.751920	49m	2	0	7		56.3592	1.631130	146m	4	2	2		61.2178	1.512800	2m	1	5	0	
52.1666	1.751920	m	-2	0	8		56.3592	1.631130	m	-4	2	4		61.2178	1.512800	m	4	3	1	
52.4283	1.743790	186m	2	2	6		56.8844	1.617310	8m	4	0	4		61.3985	1.508780	2m	0	5	2	
52.4283	1.743790	m	-2	2	7		56.8844	1.617310	m	-4	0	6		61.3985	1.508780	m	-1	4	6	
52.8927	1.729570	49m	1	4	3		57.0658	1.612600	10m	0	4	5		61.4635	1.507340	2m	0	2	9	
52.8927	1.729570	m	-4	2	1		57.0658	1.612600	m	-3	3	5		61.4635	1.507340	m	-1	5	1	

Status Primary **QM:** Star **Pressure/Temperature:** Ambient **Chemical Formula:** Ca Nb2 O6
Empirical Formula: Ca Nb2 O6 **Weight %:** Ca12.45 Nb57.73 O29.82 **Atomic %:** Ca11.11 Nb22.22 O66.67
Compound Name: Calcium Niobium Oxide **Mineral Name:** Fersmite, syn

Radiation: CuKα **λ:** 1.5406Å **Filter:** Graph Mono **d-Spacing:** Diff. **Cutoff:** 17.70
Intensity: Diffractometer

SYS: Orthorhombic **SPGR:** Pcan (60)
Author's Cell [AuthCell a: 5.7479(5)Å **AuthCell b:** 14.9866(16)Å **AuthCell c:** 5.2263(5)Å
AuthCell Vol: 450.20Å³ **AuthCell Z:** 4.00 **AuthCell MolVol:** 112.55 **]**
Author's Cell Axial Ratio [c/a: 0.909 **a/b:** 0.384 **c/b:** 0.349 **]** **Density [Dcalc:** 4.749g/cm³ **]**
SS/FOM: F(30) = 65.1(0.0105, 44) **Temp:** 298.000K (Author provided temperature)

Space Group: Pcan (60) **Molecular Weight:** 321.89
Crystal Data [XtlCell a: 5.748Å **XtlCell b:** 14.987Å **XtlCell c:** 5.226Å **XtlCell α:** 90.00° **XtlCell β:** 90.00°
XtlCell γ: 90.00° **XtlCell Vol:** 450.20Å³ **XtlCell Z:** 4.00 **]**
Crystal Data Axial Ratio [c/a: 0.909 **a/b:** 0.384 **c/b:** 0.349 **]**
Reduced Cell [RedCell a: 5.226Å **RedCell b:** 5.748Å **RedCell c:** 14.987Å **RedCell α:** 90.00°
RedCell β: 90.00° **RedCell γ:** 90.00° **RedCell Vol:** 450.20Å³ **]**

Crystal (Symmetry Allowed): Centrosymmetric

Pearson: oP36.00 **Mineral Classification:** Columbite (Supergroup), O2a6b2c (Group)
Subfile(s): Mineral Related (Mineral , Synthetic), Inorganic, NBS Pattern, Primary Pattern **Entry Date:** 11/07/1988
Last Modification Date: 01/11/2013

Cross-Ref PDF #'s: 00-009-0170 (Primary), 00-011-0619 (Deleted), 00-016-0375 (Alternate), 00-018-0302 (Alternate), 00-031-0289 (Alternate), 01-072-2118 (Primary), 04-001-7554, 04-001-7758, 04-005-5896, 04-006-0934

References:

Type	DOI	Reference
Primary Reference		Wong-Ng, W., McMurdie, H., Paretzkin, B., Hubbard, C., Dragoo, A., NBS (USA). ICDD Grant-in-Aid (1988).
Structure		1. Husson, E., Repelin, Y., Nguyen, Q., Brusset, H. Mater. Res. Bull. 12, 1199 (1977).
Structure		2. Krylov, E., Alexeev, Yu. Zh. Obshch. Khim. 25, 1052 (1955).
Unit Cell		Wong-Ng, W., McMurdie, H., Paretzkin, B., Hubbard, C., Dragoo, A. Powder Diffr. 4, 119 (1989).

Database Comments: Additional Patterns: For cubic form see 00-009-0170 (2). To replace 00-011-0619, 00-018-0302 and 00-031-0289. See PDF 01-072-2118. Color: Light yellow. Structures: Stoichiometric amounts of "Ca C O3" and "Nb2 O5" were mixed, heated to 850 C overnight, and twice overnight to 1300 C with regrinding. The unit cell and space group were determined by Husson et al. (1). A cubic form was reported by Krylov and Alexeev (2). Temperature of Data Collection: The approximate temperature of data collection was 298 K. Unit Cell Data Source: Powder Diffraction.

d-Spacings (69) - 00-039-1392 (Fixed Slit Intensity) - Cu Kα1 1.54056Å

2θ	d(Å)	I	h	k	l	*	2θ	d(Å)	I	h	k	l	*	2θ	d(Å)	I	h	k	l	*
11.7817	7.505130	8	0	2	0		47.3769	1.917250	3	2	1	2		63.1262	1.471580	6	1	8	2	
16.4986	5.368540	5	1	1	0		47.8078	1.900970	5	3	1	0		64.9351	1.434890	1	2	7	2	
23.5794	3.769970	19	1	3	0		48.2256	1.885470	14	2	6	0		65.2733	1.428270	3m	3	4	2	
23.7474	3.743680	18m	1	1	1		48.5828	1.872440	1m	2	2	2		67.3659	1.388900	1	2	9	1	
25.9164	3.435070	10	1	2	1		48.8168	1.864010	1	1	5	2		67.5540	1.385490	7	4	0	1	
29.1813	**3.057740**	100	1	3	1		50.5185	**1.805140**	29	0	6	2		67.8849	1.379540	2	4	1	1	
31.0942	2.873850	10	2	0	0		51.0016	1.789170	10	3	3	0		68.7780	1.363790	1	1	9	2	
33.2712	2.690620	15	1	4	1		51.1177	1.785380	9	3	1	1		68.8471	1.362590	1	4	2	1	
33.6702	2.659640	<1	1	5	0		51.4897	1.773350	17	2	6	1		70.5418	1.333950	1	2	5	3	
34.2781	2.613850	8	0	0	2		54.1435	1.692530	4	3	3	1		72.5786	1.301450	3	0	1	4	
34.8380	2.573110	5	0	1	2		55.4294	1.656270	3m	0	7	2		72.6907	1.299720	3m	4	4	1	
35.6161	2.518660	10	2	0	1		56.4943	1.627550	11	1	2	3		73.4737	1.287790	<1	2	10	1	
35.8901	2.500060	11	0	6	0		56.6236	1.624140	8	2	5	2		73.7057	1.284310	<1	3	1	3	
36.3980	2.466330	2	0	2	2		57.0014	1.614270	1	3	5	0		74.0086	1.279800	<1	2	6	3	
37.6610	2.386470	1	2	2	1		57.5802	1.599410	<1	1	9	0		75.6018	1.256740	4	3	9	0	
38.8600	2.315550	2	0	3	2		58.2926	1.581550	7	1	3	3		75.8595	1.253110	2	3	7	2	
40.0539	2.249240	6	2	3	1		60.1822	1.536330	2	3	1	2		76.1975	1.248390	3	3	3	3	
42.0279	2.148050	4	1	3	2		60.4973	**1.529080**	23m	2	6	2		76.4011	1.245570	5m	4	6	0	
43.2409	2.090560	4	2	4	1		61.1972	1.513260	3	3	2	2		76.6751	1.241800	2	4	2	2	
45.1018	2.008530	3	1	4	2		61.6553	1.503110	<1	2	8	1		78.1335	1.222230	2	3	9	1	
46.0549	1.969160	7	0	5	2		62.2524	1.490120	2	2	0	3		78.3778	1.219030	1	3	4	3	
46.9727	1.932800	10	2	0	2		62.6042	1.482590	7	2	1	3		78.9628	1.211460	6	4	6	1	
47.1068	1.927610	6	2	5	1		62.9151	1.476010	9	3	3	2		79.2193	1.208180	4	0	11	2	

Status Primary **QM:** Star **Pressure/Temperature:** Ambient **Chemical Formula:** K6 Nb10.8 O30
Empirical Formula: K6 Nb10.8 O30 **Weight %:** K13.66 Nb58.41 O27.94 **Atomic %:** K12.82 Nb23.08 O64.10
ANX: A6B11X30 **Compound Name:** Potassium Niobium Oxide

Radiation: CuKα **λ:** 1.5406Å **d-Spacing:** Calculated **Intensity:** Calculated **I/Ic:** 2.25

SYS: Tetragonal **SPGR:** P4/mbm (127)
Author's Cell [AuthCell a: 12.537(2)Å **AuthCell c:** 3.9730(1)Å **AuthCell Vol:** 624.46Å³ **AuthCell Z:** 1.00
AuthCell MolVol: 624.46 **] Author's Cell Axial Ratio [c/a:** 0.317 **]**
Density [Dcalc: 4.568g/cm³ **Dstruc:** 4.57g/cm³ **] SS/FOM:** F(30) = 112.8(0.0070, 38)
Temp: 298.000K (Ambient temperature assigned by ICDD editor) **R-factor:** 0.057

Space Group: P4/mbm (127) **Molecular Weight:** 1717.96
Crystal Data [XtlCell a: 12.537Å **XtlCell b:** 12.537Å **XtlCell c:** 3.973Å **XtlCell α:** 90.00°
XtlCell β: 90.00° **XtlCell γ:** 90.00° **XtlCell Vol:** 624.46Å³ **XtlCell Z:** 1.00 **]**
Crystal Data Axial Ratio [c/a: 0.317 **a/b:** 1.000 **c/b:** 0.317 **]**
Reduced Cell [RedCell a: 3.973Å **RedCell b:** 12.537Å **RedCell c:** 12.537Å **RedCell α:** 90.00°
RedCell β: 90.00° **RedCell γ:** 90.00° **RedCell Vol:** 624.46Å³ **]**

Crystal (Symmetry Allowed): Centrosymmetric

Pearson: tP46.80 **Subfile(s):** ICSD Pattern, Inorganic **Entry Date:** 07/27/2010
Last Modification Date: 01/17/2013

References:

Type	DOI	Reference
Primary Reference		Calculated from ICSD using POWD-12++.
Structure		"Crystal structure of potassium niobate, K6 Nb10.80 O30, a partially filled tetragonal tungsten bronze-type structure". Becker, P., Held, P. Z. Kristallogr.-New Cryst. Struct. 215, 319 (2000).

Database Comments: ANX: A6B11X30. Analysis: K6 Nb10.8 O30. Formula from original source: K6 Nb10.8 O30. ICSD Collection Code: 409464. Wyckoff Sequence: j3 i h g2 d c a(P4/MBM). Unit Cell Data Source: Single Crystal.

d-Spacings (183) - 01-070-5051 (Fixed Slit Intensity) - Cu Kα1 1.54056Å

2θ	d(Å)	I	h	k	l	*	2θ	d(Å)	I	h	k	l	*
9.9694	8.865000	1	1	1	0		51.4772	1.773750	m	6	2	1	
14.1168	6.268500	61	2	0	0		52.0280	1.756260	95	5	4	1	
15.7931	5.606720	348	2	1	0		52.5978	1.738570	4	6	4	0	
20.0153	4.432500	27	2	2	0		53.0483	1.724860	62	3	2	2	
22.3585	**3.973000**	676m	0	0	1		54.1916	1.691140	82	6	3	1	
22.3585	**3.973000**	m	3	1	0		54.6554	1.677880	10	4	0	2	
24.5330	3.625550	1	1	1	1		55.1841	1.663050	150	4	1	2	
25.5975	3.477140	386	3	2	0		55.7093	1.648610	33	3	3	2	
26.5400	3.355750	19	2	0	1		56.8162	1.619090	248	7	1	1	
27.4923	3.241640	283	2	1	1		57.3532	1.605200	7	6	5	0	
28.4538	3.134250	50	4	0	0		57.8437	1.592750	1	6	4	1	
29.3488	**3.040670**	667	4	1	0		58.3533	1.580050	34	7	2	1	
30.1832	2.958490	207m	2	2	1		58.8818	1.567120	8	8	0	0	
30.1832	2.958490	m	3	3	0		59.3857	1.555020	12	8	1	0	
31.8619	**2.806340**	999m	3	1	1		59.8019	1.545190	2	5	1	2	
31.8619	**2.806340**	m	4	2	0		60.8823	1.520330	43m	7	3	1	
34.2415	2.616560	343	3	2	1		60.8823	1.520330	m	8	2	0	
35.7815	2.507400	6	4	3	0		61.2923	1.511140	2	5	2	2	
36.4839	2.460720	53m	4	0	1		62.3366	1.488310	22	6	5	1	
36.4839	2.460720	m	5	1	0		62.8444	1.477500	14m	4	4	2	
37.2053	2.414650	45	4	1	1		62.8444	1.477500	m	6	6	0	
37.9149	2.371070	2	3	3	1		63.3297	1.467340	58	8	3	0	
38.6429	2.328060	9	5	2	0		63.7308	1.459070	25	5	3	2	
39.3013	2.290560	11	4	2	1		63.7919	1.457820	27m	7	5	0	
40.6763	2.216250	11	4	4	0		63.7919	1.457820	m	8	0	1	
41.9863	2.150080	67	5	3	0		64.2732	1.448060	1	8	1	1	
42.6018	2.120430	6	4	3	1		64.6916	1.439700	1	6	0	2	
43.2372	2.090730	15m	5	1	1		65.1692	1.430300	5	6	1	2	
43.2372	2.090730	m	6	0	0		65.7054	1.419920	8	8	2	1	
43.8915	2.061070	11	6	1	0		66.5910	1.403170	74m	6	2	2	
45.6301	1.986500	314	0	0	2		66.5910	1.403170	m	8	4	0	
45.7329	1.982270	218	6	2	0		67.0617	1.394460	15	5	4	2	
46.3339	1.957950	35	5	4	0		67.6099	1.384480	1m	6	6	1	
46.9038	1.935480	10m	1	1	2		67.6099	1.384480	m	9	1	0	
46.9038	1.935480	m	4	4	1		68.0570	1.376470	54	8	3	1	
48.0031	1.893690	4m	2	0	2		68.5225	1.368250	23	7	5	1	
48.0031	1.893690	m	5	3	1		68.9278	1.361190	73m	6	3	2	
48.6805	1.868910	169	6	3	0		68.9278	1.361190	m	7	6	0	
49.2299	1.849330	24	6	0	1		70.8488	1.328920	7	8	5	0	
49.7985	1.829540	1	6	1	1		71.2283	1.322770	131	7	1	2	
50.2910	1.812770	3	2	2	2		72.1981	1.307370	2m	6	4	2	
51.4772	1.773750	408m	5	5	0		72.1981	1.307370	m	9	1	1	

2θ	d(Å)	I	h	k	l	*	2θ	d(Å)	I	h	k	l	*
72.5935	1.301220	1	7	2	2		89.2057	1.096970	10	5	4	3	
72.9505	1.295730	1	2	0	3		89.7861	1.091380	5	11	1	1	
73.4021	1.288870	7	2	1	3		90.9361	1.080550	8	6	3	3	
73.5555	1.286560	8	9	2	1		91.0840	1.079180	8	11	2	1	
74.4748	1.272940	30	9	4	0		91.5346	1.075040	1	10	6	0	
74.7517	1.268910	5	2	2	3		91.8943	1.071770	25m	9	4	2	
74.8470	1.267530	7	7	3	2		91.8943	1.071770	m	11	4	0	
74.9232	1.266430	8	7	7	0		92.3266	1.067880	7m	7	7	2	
75.3516	1.260290	2	8	5	1		92.3266	1.067880	m	8	8	1	
75.6470	1.256100	35	3	1	3		93.1010	1.061020	30	7	1	3	
75.8175	1.253700	25	10	0	0		93.1934	1.060210	31m	9	7	1	
76.2631	1.247480	5m	6	5	2		93.1934	1.060210	m	10	0	2	
76.2631	1.247480	m	10	1	0		93.6267	1.056440	4	10	1	2	
76.9822	1.237610	15	3	2	3		94.4017	1.049800	5	7	2	3	
77.5958	1.229350	9m	8	0	2		94.9274	1.045370	9m	10	2	2	
77.5958	1.229350	m	10	2	0		94.9274	1.045370	m	12	0	0	
77.9626	1.224480	7	8	1	2		95.4361	1.041140	2	12	1	0	
78.3112	1.219900	4	4	0	3		95.7972	1.038170	8m	9	5	2	
78.4799	1.217700	9	9	5	0		95.7972	1.038170	m	11	5	0	
78.7523	1.214170	6	4	1	3		96.2876	1.034180	1	11	4	1	
78.9021	1.212240	27	9	4	1		96.5744	1.031870	1	7	3	3	
79.2869	1.207320	28m	7	7	1		96.7417	1.030530	3	12	2	0	
79.2869	1.207320	m	8	2	2		97.1024	1.027660	2m	10	3	2	
79.8010	1.200830	2	10	3	0		97.1024	1.027660	m	10	7	0	
80.2216	1.195590	23	8	6	1		97.8828	1.021540	3	6	5	3	
80.6603	1.190190	25	10	1	1		98.8500	1.014120	2m	8	7	2	
81.0424	1.185540	8	6	6	2		98.8500	1.014120	m	12	3	0	
81.4804	1.180270	37m	8	3	2		99.1945	1.011520	2	8	0	3	
81.4804	1.180270	m	8	7	0		99.7832	1.007130	2	12	1	1	
81.9179	1.175070	7m	7	5	2		100.2219	1.003900	1m	10	4	2	
81.9179	1.175070	m	10	2	1		100.2219	1.003900	m	11	5	1	
82.2615	1.171030	1	4	3	3		100.6806	1.000560	9m	9	6	2	
82.8465	1.164240	43m	9	5	1		100.6806	1.000560	m	11	6	0	
82.8465	1.164240	m	10	4	0		100.9523	0.998600	2	8	2	3	
83.3000	1.159050	3	9	6	0		101.1023	0.997524	4	12	2	1	
84.1523	1.149470	1	10	3	1		101.7034	0.993250	10	0	0	4	
84.5313	1.145280	2	8	4	2		102.0040	0.991137	8	12	4	0	
85.3078	1.136830	1	4	4	3		102.8900	0.985000	4m	9	9	0	
85.4735	1.135050	2m	9	1	2		102.8900	0.985000	m	11	1	2	
85.4735	1.135050	m	11	1	0		103.1642	0.983128	9	8	3	3	
85.8890	1.130620	1	8	7	1		103.6088	0.980119	5	7	5	3	
86.1750	1.127600	1	5	3	3		104.1492	0.976507	23	11	2	2	
86.7749	1.121340	23	11	2	0		105.1002	0.970266	15	11	6	1	
87.0424	1.118580	3	6	0	3		105.4916	0.967740	11	8	8	2	
87.6218	1.112670	7	9	6	1		106.1615	0.963473	3	3	1	4	
88.0741	1.108120	10	8	8	0		106.4488	0.961664	8m	11	7	0	
88.4328	1.104550	5	8	5	2		106.4488	0.961664	m	12	4	1	
88.7735	1.101190	15m	6	2	3		107.1990	0.957002	1	9	1	3	
88.7735	1.101190	m	9	3	2		107.3531	0.956055	1	9	9	1	
88.9388	1.099570	5	9	7	0								

Status Primary **QM:** Star **Pressure/Temperature:** Ambient **Chemical Formula:** H Ca2 Nb3 O10 ·1.5 H2 O
Empirical Formula: Ca2 H4 Nb3 O11.5 **Weight %:** Ca14.66 H0.74 Nb50.96 O33.64
Atomic %: Ca9.76 H19.51 Nb14.63 O56.10 **Compound Name:** Calcium Niobium Hydrogen Oxide Hydrate

Radiation: CuKα **λ:** 1.5418Å **d-Spacing:** Diff. **Intensity:** Diffractometer

SYS: Tetragonal **Author's Cell [AuthCell a:** 3.8540(4)Å **AuthCell c:** 16.225(2)Å **AuthCell Vol:** 241.00Å³ **]**
Author's Cell Axial Ratio [c/a: 4.210 **]** **SS/FOM:** F(30) = 38.0(0.0152, 52)
Temp: 298.000K (Ambient temperature assigned by ICDD editor)

Molecular Weight: 546.90
Crystal Data [XtlCell a: 3.854Å **XtlCell b:** 3.854Å **XtlCell c:** 16.225Å **XtlCell α:** 90.00° **XtlCell β:** 90.00°
XtlCell γ: 90.00° **XtlCell Vol:** 241.00Å³ **]** **Crystal Data Axial Ratio [c/a:** 4.210 **a/b:** 1.000 **c/b:** 4.210 **]**
Reduced Cell [RedCell a: 3.854Å **RedCell b:** 3.854Å **RedCell c:** 16.225Å **RedCell α:** 90.00°
RedCell β: 90.00° **RedCell γ:** 90.00° **RedCell Vol:** 241.00Å³ **]**

Crystal (Symmetry Allowed): Centrosymmetric

Pearson: t?? **Subfile(s):** Primary Pattern, Inorganic **Entry Date:** 11/25/1986
Last Modification Date: 01/11/2013

References:

Type	DOI	Reference
Primary Reference		Jacobson, A., Lewandowski, J., Johnson, J. J. Less-Common Met. 116, 137 (1986).

d-Spacings (35) - 00-039-0915 (Fixed Slit Intensity) - Cu Kα1 1.54056Å

2θ	d(Å)	I	h	k	l	*	2θ	d(Å)	I	h	k	l	*	2θ	d(Å)	I	h	k	l	*
5.4205	**16.290000**	100	0	0	1		38.8347	2.317000	9	0	0	7		56.5378	1.626400	7	1	1	8	
10.8693	**8.133000**	28	0	0	2		40.7214	2.213900	3	1	0	6		58.1334	1.585500	5	2	1	4	
16.3682	5.411000	4	0	0	3		44.6477	2.027900	22	0	0	8		62.6790	1.481000	2	2	0	7	
21.8843	**4.058000**	47	0	0	4		45.6470	1.985800	2	1	0	7		66.9345	1.396800	4	2	0	8	
23.0521	3.855000	10	1	0	0		47.1460	1.926100	5	2	0	0		67.9992	1.377500	7	1	0	11	
25.5611	3.482000	2	1	0	2		47.4807	1.913300	1	2	0	1		68.8522	1.362500	1	2	2	0	
28.4190	3.138000	13	1	0	3		48.5480	1.873700	1	2	0	2		71.8023	1.313600	2	2	1	8	
32.0028	2.794300	21	1	0	4		50.8454	1.794300	8	1	0	8		72.8415	1.297400	1	1	1	11	
32.8295	2.725800	5	1	1	0		51.7576	1.764800	7	1	1	7		74.2457	1.276300	2	1	0	12	
33.2956	2.688700	1	1	1	1		52.5577	1.739800	2	2	0	4		77.9082	1.225200	1	3	0	4	
36.1482	2.482800	1	1	0	5		53.1167	1.722800	2	2	1	0		78.3495	1.219400	1	3	1	0	
36.8941	2.434300	1	1	1	3		55.9754	1.641400	3	2	1	3								

Status Primary **QM:** Star **Pressure/Temperature:** Ambient **Chemical Formula:** H Ca2 Nb3 O10 (H2 O)0.5
Empirical Formula: Ca2 H2 Nb3 O10.5 **Weight %:** Ca15.16 H0.38 Nb52.70 O31.76
Atomic %: Ca11.43 H11.43 Nb17.14 O60.00 **ANX:** A4B6X21
Compound Name: Hydrogen Calcium Niobium Oxide Hydrate
Common Name: Hydrogen dicalcium decaoxotriniobate(V) hemihydrate

Radiation: CuKα **λ:** 1.5406Å **d-Spacing:** Calculated **Intensity:** Calculated **I/Ic:** 5.49

SYS: Tetragonal **SPGR:** P4/mbm (127)
Author's Cell [AuthCell a: 5.4521(6)Å **AuthCell c:** 14.414(2)Å **AuthCell Vol:** 428.46Å³ **AuthCell Z:** 2.00
AuthCell MolVol: 214.23] **Author's Cell Axial Ratio [c/a:** 2.644]
Density [Dcalc: 4.099g/cm³ **Dstruc:** 4.08g/cm³] **SS/FOM:** F(30) = 280.6(0.0029, 37)
Temp: 293.000K (Author provided temperature) **R-factor:** 0.058

Space Group: P4/mbm (127) **Molecular Weight:** 528.89
Crystal Data [XtlCell a: 5.452Å **XtlCell b:** 5.452Å **XtlCell c:** 14.414Å **XtlCell α:** 90.00° **XtlCell β:** 90.00°
XtlCell γ: 90.00° **XtlCell Vol:** 428.46Å³ **XtlCell Z:** 2.00]
Crystal Data Axial Ratio [c/a: 2.644 **a/b:** 1.000 **c/b:** 2.644]
Reduced Cell [RedCell a: 5.452Å **RedCell b:** 5.452Å **RedCell c:** 14.414Å **RedCell α:** 90.00°
RedCell β: 90.00° **RedCell γ:** 90.00° **RedCell Vol:** 428.46Å³]

Crystal (Symmetry Allowed): Centrosymmetric

Pearson: tP35.00 **Pearson w/o H:** tP31 **Subfile(s):** ICSD Pattern, Inorganic **Entry Date:** 07/27/2010
Last Modification Date: 01/17/2013

References:

Type	DOI	Reference
Primary Reference		Calculated from ICSD using POWD-12++.
Structure		"Structure and dehydrogenation of layered perovskite niobate with bilayer hydrates prepared by exfoliation/self-assemby process". Chen Yufeng, Zhao Xinhua, Ma Hui, Ma Shulan, Huang Gailing, Makita, Y., Bai Xuedong, Yang Xiaojing J. Solid State Chem. 181, 1684 (2008).

Database Comments: ANX: A4B6X21. Analysis: H2 Ca2 Nb3 O10.5. Formula from original source: H Ca2 Nb3 O10 (H2 O)0.5. ICSD Collection Code: 246002. Calculated Pattern Original Remarks: Given R-value is Rp. Authors give positions of O(5) and H(1) as an "virtual species" WO, whose scattering factors were set equal to the sums of one O and four H atoms. Temperature of Data Collection: 293 K. Wyckoff Sequence: k g f2 e3 a (P4/MBM). Unit Cell Data Source: Single Crystal.

d-Spacings (199) - 01-077-4249 (Fixed Slit Intensity) - Cu Kα1 1.54056Å

2θ	d(Å)	I	h	k	l	*	2θ	d(Å)	I	h	k	l	*
6.1267	**14.414000**	999	0	0	1		53.8962	1.699710	26	2	2	4	
12.2709	7.207000	189	0	0	2		54.6939	1.676790	2	3	1	2	
18.4508	4.804670	186	0	0	3		55.9132	1.643080	134	2	0	7	
23.0507	**3.855220**	498	1	1	0		56.3156	1.632290	5	1	1	8	
23.8727	3.724310	4	1	1	1		56.6750	1.622790	194	3	1	3	
24.6854	3.603500	99	0	0	4		57.4632	1.602390	12m	0	0	9	
26.1931	3.399410	16	1	1	2		57.4632	1.602390	m	2	2	5	
29.6858	**3.006910**	657	1	1	3		58.6324	1.573190	1	2	1	7	
30.9953	2.882800	13	0	0	5		59.3757	1.555260	85	3	1	4	
32.8264	2.726050	401	2	0	0		61.2474	1.512140	1	3	2	0	
33.4252	2.678570	28	2	0	1		61.6399	1.503450	11m	2	0	8	
34.0272	2.632550	198	1	1	4		61.6399	1.503450	m	2	2	6	
35.1677	2.549740	3	2	0	2		62.7417	1.479670	9m	1	1	9	
36.8321	2.438250	7	2	1	0		62.7417	1.479670	m	3	1	5	
37.4031	2.402330	20m	0	0	6		64.2240	1.449050	1	2	1	8	
37.4031	2.402330	m	2	1	1		64.6061	1.441400	6m	0	0	10	
37.9161	2.371000	33	2	0	3		64.6061	1.441400	m	3	2	3	
38.9798	2.308710	30m	1	1	5		66.3740	1.407230	100	2	2	7	
38.9798	2.308710	m	2	1	2		66.7232	1.400710	3	3	1	6	
41.4969	2.174300	4m	2	0	4		67.0677	1.394350	1	3	2	4	
41.4969	2.174300	m	2	1	3		67.8101	1.380880	1	2	0	9	
43.9347	2.059140	132	0	0	7		68.8223	1.363020	50	4	0	0	
44.8456	2.019410	6	2	1	4		69.1726	1.356970	3	4	0	1	
45.7710	1.980710	16	2	0	5		69.5740	1.350120	57	1	1	10	
47.1068	1.927610	239	2	2	0		70.2196	1.339280	8m	2	1	9	
47.5519	1.910600	14	2	2	1		70.2196	1.339280	m	4	0	2	
48.8688	1.862150	24m	2	1	5		71.2810	1.321920	63m	3	1	7	
48.8688	1.862150	m	2	2	2		71.2810	1.321920	m	4	1	0	
50.1865	1.816300	95	1	1	7		71.6335	1.316280	2m	2	2	8	
50.6022	1.802350	56m	0	0	8		71.6335	1.316280	m	4	1	1	
50.6022	1.802350	m	2	0	6		71.9491	1.311280	10m	0	0	11	
51.0068	1.789000	35	2	2	3		71.9491	1.311280	m	4	0	3	
53.0732	1.724110	96	3	1	0		72.6323	1.300620	1	4	1	2	
53.4817	1.711900	1m	2	1	6		73.6549	1.285070	11	3	3	0	
53.4817	1.711900	m	3	1	1		73.9952	1.280000	1m	3	2	6	

2θ	d(Å)	I	h	k	l	*
73.9952	1.280000	m	3	3	1	
74.3860	1.274240	23m	2	0	10	
74.3860	1.274240	m	4	0	4	
75.0141	1.265120	1	3	3	2	
76.7014	1.241440	28m	1	1	11	
76.7014	1.241440	m	3	3	3	
77.3806	1.232230	6m	2	2	9	
77.3806	1.232230	m	4	0	5	
78.3702	1.219130	46m	3	2	7	
78.3702	1.219130	m	4	2	0	
78.7043	1.214790	5	4	2	1	
79.0447	1.210410	11	3	3	4	
79.7038	1.202050	1m	0	0	12	
79.7038	1.202050	m	4	2	2	
81.0457	1.185500	4	4	0	6	
81.3627	1.181680	13m	2	0	11	
81.3627	1.181680	m	4	2	3	
82.0315	1.173730	4m	3	1	9	
82.0315	1.173730	m	3	3	5	
83.7148	1.154360	11m	2	1	11	
83.7148	1.154360	m	2	2	10	
84.3943	1.146790	4	1	1	12	
85.3311	1.136580	36	4	0	7	
86.6293	1.122850	3	4	2	5	
87.6228	1.112660	1	4	1	7	
88.0091	1.108770	3	0	0	13	
88.3017	1.105850	55	3	1	10	
88.9777	1.099190	3m	2	0	12	
88.9777	1.099190	m	3	2	9	
89.9107	1.090190	12m	3	3	7	
89.9107	1.090190	m	4	3	0	
90.2311	1.087150	14m	4	0	8	
90.2311	1.087150	m	4	2	6	
90.6001	1.083680	2	2	2	11	
91.2652	1.077510	1m	2	1	12	
91.2652	1.077510	m	4	3	2	
92.1750	1.069240	13	5	1	0	
92.5845	1.065580	2m	1	1	13	
92.5845	1.065580	m	4	1	8	
93.4848	1.057670	1	5	1	2	
94.4902	1.049050	49	4	2	7	
94.8248	1.046230	2	3	3	8	
95.1262	1.043710	34m	3	1	11	
95.1262	1.043710	m	5	1	3	
95.8180	1.038000	1	4	0	9	
96.8620	1.029570	5	0	0	14	
97.1770	1.027070	10	2	0	13	
97.4308	1.025070	15	5	1	4	
98.1541	1.019440	1m	2	2	12	
98.1541	1.019440	m	4	1	9	
99.0736	1.012430	1	5	2	0	
99.4054	1.009940	1m	2	1	13	
99.4054	1.009940	m	5	2	1	
100.4122	1.002510	3m	3	3	9	
100.4122	1.002510	m	5	1	5	
101.4969	0.994711	7	1	1	14	
102.1161	0.990353	5m	3	2	11	
102.1161	0.990353	m	4	0	10	
102.8077	0.985564	3	3	1	12	
104.0968	0.976855	1	5	1	6	
104.4236	0.974691	1m	4	1	10	
104.4236	0.974691	m	5	2	4	
105.1328	0.970055	1	4	2	9	
106.1091	0.963804	17m	4	3	7	
106.1091	0.963804	m	4	4	0	
106.2099	0.963167	18	2	0	14	
106.5366	0.961114	6m	0	0	15	
106.5366	0.961114	m	2	2	13	
106.8421	0.959209	16	3	3	10	
107.4764	0.955300	2m	4	4	2	
107.4764	0.955300	m	5	2	5	
108.5306	0.948936	17m	2	1	14	
108.5306	0.948936	m	5	1	7	
109.2003	0.944979	5m	4	0	11	
109.2003	0.944979	m	4	4	3	
109.9647	0.940541	1	3	2	12	
110.9351	0.935027	11	5	3	0	
111.3750	0.932570	4m	1	1	15	
111.3750	0.932570	m	3	1	13	
111.6895	0.930830	18m	4	1	11	
111.6895	0.930830	m	4	2	10	
112.3433	0.927256	1	5	3	2	
114.1240	0.917809	25m	3	3	11	
114.1240	0.917809	m	5	3	3	
114.8509	0.914071	2	4	4	5	
116.0300	0.908149	15m	2	2	14	
116.0300	0.908149	m	5	2	7	
116.2866	0.906883	2	6	0	1	
116.4102	0.906276	2	2	0	15	
116.6599	0.905056	14	5	3	4	
117.4648	0.901173	1m	0	0	16	
117.4648	0.901173	m	4	0	12	
118.4942	0.896320	1	6	1	0	
118.8870	0.894501	2m	2	1	15	
118.8870	0.894501	m	4	4	6	
119.2455	0.892856	5m	4	2	11	
119.2455	0.892856	m	6	0	3	
120.0066	0.889413	2m	4	1	12	
120.0066	0.889413	m	5	3	5	
121.2439	0.883955	13	3	1	14	
121.9066	0.881101	2m	6	0	4	
121.9066	0.881101	m	6	1	3	
122.7550	0.877517	3m	1	1	16	
122.7550	0.877517	m	3	3	12	
123.8718	0.872916	18	4	4	7	
124.2583	0.871354	1	5	3	6	
124.6427	0.869816	1m	4	3	10	
124.6427	0.869816	m	6	1	4	
125.4464	0.866649	1	6	0	5	
126.6434	0.862053	20	6	2	0	
127.1566	0.860126	6m	2	2	15	
127.1566	0.860126	m	4	0	13	
127.5246	0.858760	28	5	1	10	
128.2928	0.855951	4m	4	2	12	
128.2928	0.855951	m	6	2	2	
129.5816	0.851365	18m	3	2	14	
129.5816	0.851365	m	5	3	7	
129.9985	0.849915	5m	4	4	8	
129.9985	0.849915	m	6	0	6	
130.4088	0.848504	7	6	2	3	
131.2694	0.845594	1m	2	1	16	
131.2694	0.845594	m	5	4	2	
133.1443	0.839486	2m	3	1	15	
133.1443	0.839486	m	3	3	13	
133.4893	0.838396	5m	4	3	11	
133.4893	0.838396	m	6	2	4	
135.8089	0.831335	16	6	0	7	
136.9278	0.828092	17m	1	1	17	
136.9278	0.828092	m	5	1	11	

00-021-1297 Feb 27, 2015 2:49 PM (Izenkhri)

Status Primary **QM:** Blank **Pressure/Temperature:** Ambient **Chemical Formula:** K4 Nb6 O17 ·3 H2 O
Empirical Formula: H6 K4 Nb6 O20 **Weight %:** H0.58 K15.04 Nb53.61 O30.77
Atomic %: H16.67 K11.11 Nb16.67 O55.56 **Compound Name:** Potassium Niobium Oxide Hydrate

Radiation: CrKα **λ:** 2.2909Å **Filter:** V Beta **d-Spacing:** D.S. **Intensity:** Visual
Camera Diameter: 114.60

SYS: Orthorhombic **SPGR:** P2212 (17)
Author's Cell [AuthCell a: 7.85Å **AuthCell b:** 37.67Å **AuthCell c:** 6.46Å **AuthCell Vol:** 1910.28Å³
AuthCell Z: 4.00 **AuthCell MolVol:** 477.57]
Author's Cell Axial Ratio [c/a: 0.823 **a/b:** 0.208 **c/b:** 0.171]
Density [Dcalc: 3.616g/cm³ **Dmeas:** 3.37g/cm³] **SS/FOM:** F(13) = 0.6(0.069, 341)
Temp: 298.000K (Ambient temperature assigned by ICDD editor)

Space Group: P2212 (17) **Molecular Weight:** 1039.87
Crystal Data [XtlCell a: 7.850Å **XtlCell b:** 37.670Å **XtlCell c:** 6.460Å **XtlCell α:** 90.00° **XtlCell β:** 90.00°
XtlCell γ: 90.00° **XtlCell Vol:** 1910.28Å³ **XtlCell Z:** 4.00]
Crystal Data Axial Ratio [c/a: 0.823 **a/b:** 0.208 **c/b:** 0.171]
Reduced Cell [RedCell a: 6.460Å **RedCell b:** 7.850Å **RedCell c:** 37.670Å **RedCell α:** 90.00°
RedCell β: 90.00° **RedCell γ:** 90.00° **RedCell Vol:** 1910.28Å³]

εα: =2.22 **πωβ:** =2.36 **εγ:** =2.43

Crystal (Symmetry Allowed): Non-centrosymmetric, Enantiomorphic, Optical Activity, Piezo (2nd Harm.)

Pearson: oP144.00 **Pearson w/o H:** oP120 **Subfile(s):** Primary Pattern, Inorganic
Last Modification Date: 01/11/2013

References:

Type	DOI	Reference
Primary Reference		Nassau, Shiever, Bernstein. J. Electrochem. Soc. 116, 348 (1969).

Database Comments: Unit Cell Data Source: Powder Diffraction.

d-Spacings (13) - 00-021-1297 (Fixed Slit Intensity) - Cu Kα1 1.54056Å

2θ	d(Å)	I	h	k	l	*	2θ	d(Å)	I	h	k	l	*	2θ	d(Å)	I	h	k	l	*
4.6469	19.000000	60	0	2	0		31.5656	**2.832000**	80	0	12	1		47.9948	1.894000	60	0	19	1	
9.3015	**9.500000**	100	0	4	0		38.2005	2.354000	40	0	16	0		53.4110	1.714000	60	1	18	2	
14.0012	**6.320000**	80	0	6	0		40.7003	2.215000	40	0	16	1		58.3148	1.581000	60	1	1	4	
21.3413	4.160000	20	1	5	1		43.1014	2.097000	40	0	17	1								
27.5065	3.240000	40	2	3	1		45.4247	1.995000	40	0	18	1								

$K_4Nb_6O_{17}\_3H_2O$
Space Group: P222
a= 7.85000 b= 37.67000
c= 6.46000

h	k	l	dhkl	2Theta	Mult
0	1	0	37.6700	2.343	2
0	2	0	18.8350	4.688	2
0	3	0	12.5567	7.034	2
0	4	0	9.4175	9.383	2
1	0	0	7.8500	11.262	2
1	1	0	7.6849	11.505	4
0	5	0	7.5340	11.736	2
1	2	0	7.2459	12.205	4
1	3	0	6.6563	13.291	4
0	0	1	6.4600	13.696	2
0	1	1	6.3671	13.897	4
0	6	0	6.2783	14.095	2
0	2	1	6.1106	14.484	4
1	4	0	6.0299	14.678	4
0	3	1	5.7444	15.412	4
1	5	0	5.4356	16.294	4
0	7	0	5.3814	16.459	2
0	4	1	5.3271	16.628	4
1	0	1	4.9881	17.767	4
1	1	1	4.9450	17.923	8
0	5	1	4.9041	18.074	4
1	6	0	4.9031	18.077	4
1	2	1	4.8219	18.384	8
0	8	0	4.7087	18.830	2
1	3	1	4.6357	19.129	8
0	6	1	4.5023	19.702	4
1	7	0	4.4386	19.988	4
1	4	1	4.4080	20.128	8
0	9	0	4.1856	21.209	2
1	5	1	4.1591	21.346	8
0	7	1	4.1347	21.473	4
1	8	0	4.0380	21.994	4
2	0	0	3.9250	22.635	2
1	6	1	3.9055	22.750	8
2	1	0	3.9039	22.760	4
2	2	0	3.8425	23.128	4
0	8	1	3.8052	23.358	4
0	10	0	3.7670	23.598	2
2	3	0	3.7462	23.731	4
1	9	0	3.6934	24.076	4
1	7	1	3.6583	24.310	8
2	4	0	3.6229	24.551	4
0	9	1	3.5127	25.334	4
2	5	0	3.4809	25.569	4
0	11	0	3.4245	25.997	2
1	8	1	3.4241	26.001	8
1	10	0	3.3962	26.218	4
2	0	1	3.3544	26.551	4
2	1	1	3.3412	26.658	8
2	6	0	3.3281	26.764	4
2	2	1	3.3024	26.977	8
0	10	1	3.2541	27.385	4
2	3	1	3.2407	27.500	8
0	0	2	3.2300	27.593	2
0	1	2	3.2182	27.697	4
1	9	1	3.2063	27.801	8
0	2	2	3.1835	28.004	4
2	7	0	3.1711	28.116	4
2	4	1	3.1599	28.218	8
0	12	0	3.1392	28.408	2
1	11	0	3.1389	28.411	4
0	3	2	3.1282	28.510	4
2	5	1	3.0644	29.117	8
0	4	2	3.0553	29.205	4
0	11	1	3.0257	29.497	4
2	8	0	3.0149	29.605	4
1	10	1	3.0061	29.694	8
1	0	2	2.9870	29.888	4
1	1	2	2.9777	29.984	8
0	5	2	2.9687	30.077	4
2	6	1	2.9586	30.182	8
1	2	2	2.9502	30.270	8
1	12	0	2.9147	30.647	4
1	3	2	2.9059	30.742	8
0	13	0	2.8977	30.832	2
0	6	2	2.8722	31.113	4
2	9	0	2.8631	31.214	4
1	4	2	2.8472	31.392	8
2	7	1	2.8466	31.399	8
0	12	1	2.8235	31.664	4
1	11	1	2.8232	31.666	8
1	5	2	2.7767	32.211	8
0	7	2	2.7694	32.298	4
2	8	1	2.7320	32.752	8
1	13	0	2.7184	32.921	4
2	10	0	2.7178	32.929	4
1	6	2	2.6973	33.186	8
0	14	0	2.6907	33.270	2
0	8	2	2.6636	33.619	4
1	12	1	2.6568	33.707	8
0	13	1	2.6439	33.877	4
2	9	1	2.6175	34.229	8
3	0	0	2.6167	34.240	2
1	7	2	2.6117	34.308	8
3	1	0	2.6104	34.325	4
3	2	0	2.5918	34.579	4
2	11	0	2.5804	34.736	4
3	3	0	2.5616	34.999	4
0	9	2	2.5571	35.063	4
1	14	0	2.5453	35.230	4
1	8	2	2.5223	35.563	8
3	4	0	2.5212	35.580	4
0	15	0	2.5113	35.723	2
1	13	1	2.5056	35.808	8
2	10	1	2.5051	35.815	8
2	0	2	2.4941	35.979	4
2	1	2	2.4886	36.061	8
0	14	1	2.4839	36.132	4
2	2	2	2.4725	36.304	8
3	5	0	2.4718	36.314	4
0	10	2	2.4520	36.618	4
2	12	0	2.4515	36.625	4
2	3	2	2.4463	36.707	8
1	9	2	2.4314	36.940	8
3	0	1	2.4253	37.037	4
3	1	1	2.4202	37.116	8
3	6	0	2.4153	37.195	4
2	4	2	2.4109	37.264	8
3	2	1	2.4054	37.354	8
2	11	1	2.3963	37.500	8
1	15	0	2.3919	37.572	4
3	3	1	2.3812	37.747	8
1	14	1	2.3681	37.964	8
2	5	2	2.3677	37.971	8
0	16	0	2.3544	38.194	2
3	7	0	2.3532	38.213	4
0	11	2	2.3497	38.273	4
3	4	1	2.3486	38.291	8
0	15	1	2.3407	38.426	4
1	10	2	2.3405	38.429	8
2	13	0	2.3312	38.588	4
2	6	2	2.3179	38.820	8
3	5	1	2.3086	38.982	8
2	12	1	2.2920	39.275	8
3	8	0	2.2872	39.361	4
2	7	2	2.2629	39.803	8
3	6	1	2.2623	39.812	8
1	16	0	2.2551	39.945	4

0	12	2	2.2512	40.018	4	3	3	2	2.0071	45.137	8	4	3	1	1.8571	49.010	8
1	11	2	2.2510	40.021	8	1	5	3	2.0020	45.258	8	2	4	3	1.8511	49.181	8
1	15	1	2.2431	40.168	8	0	7	3	1.9992	45.323	4	1	16	2	1.8490	49.238	8
2	14	0	2.2193	40.618	4	1	14	2	1.9992	45.324	8	2	17	1	1.8489	49.242	8
3	9	0	2.2188	40.628	4	0	18	1	1.9909	45.523	4	2	18	0	1.8467	49.305	4
0	17	0	2.2159	40.683	2	3	4	2	1.9874	45.608	8	4	7	0	1.8437	49.390	4
0	16	1	2.2120	40.757	4	0	19	0	1.9826	45.724	2	1	19	1	1.8424	49.427	8
3	7	1	2.2111	40.775	8	0	15	2	1.9826	45.725	4	4	4	1	1.8415	49.453	8
2	8	2	2.2040	40.913	8	3	11	1	1.9792	45.808	8	1	20	0	1.8315	49.741	4
2	13	1	2.1928	41.131	8	1	6	3	1.9716	45.995	8	2	5	3	1.8313	49.748	8
1	12	2	2.1639	41.705	8	3	5	2	1.9630	46.208	8	2	14	2	1.8291	49.810	8
0	13	2	2.1569	41.847	4	4	0	0	1.9625	46.220	2	3	9	2	1.8288	49.819	8
3	8	1	2.1561	41.864	8	4	1	0	1.9598	46.286	4	0	17	2	1.8272	49.866	4
0	0	3	2.1533	41.920	2	0	8	3	1.9583	46.326	4	0	11	3	1.8229	49.992	4
0	1	3	2.1498	41.992	4	2	12	2	1.9528	46.464	8	4	5	1	1.8220	50.018	8
3	10	0	2.1491	42.007	4	4	2	0	1.9519	46.485	4	1	10	3	1.8186	50.119	8
2	9	2	2.1425	42.141	8	3	13	0	1.9420	46.736	4	3	15	0	1.8119	50.318	4
0	2	3	2.1394	42.206	4	4	3	0	1.9390	46.814	4	4	8	0	1.8115	50.330	4
1	17	0	2.1325	42.348	4	1	7	3	1.9374	46.855	8	0	20	1	1.8082	50.427	4
1	16	1	2.1291	42.419	8	3	6	2	1.9343	46.934	8	2	6	3	1.8079	50.435	8
0	3	3	2.1224	42.561	4	1	18	1	1.9298	47.050	8	3	14	1	1.8015	50.628	8
2	15	0	2.1154	42.708	4	2	17	0	1.9296	47.055	4	4	6	1	1.7990	50.702	8
0	4	3	2.0992	43.055	4	2	16	1	1.9271	47.121	8	0	21	0	1.7938	50.860	2
2	14	1	2.0989	43.061	8	1	19	0	1.9223	47.246	4	3	10	2	1.7892	51.000	8
3	9	1	2.0984	43.070	8	1	15	2	1.9222	47.247	8	2	7	3	1.7814	51.239	8
0	17	1	2.0960	43.123	4	4	4	0	1.9212	47.273	4	1	17	2	1.7797	51.294	8
0	18	0	2.0928	43.193	2	3	12	1	1.9192	47.326	8	4	9	0	1.7769	51.380	4
1	13	2	2.0798	43.475	8	0	9	3	1.9148	47.441	4	0	12	3	1.7757	51.416	4
2	10	2	2.0796	43.481	8	0	16	2	1.9026	47.765	4	1	11	3	1.7757	51.418	8
3	11	0	2.0792	43.489	4	3	7	2	1.9020	47.781	8	2	18	1	1.7756	51.421	8
1	0	3	2.0766	43.546	4	1	8	3	1.9000	47.832	8	4	7	1	1.7729	51.503	8
1	1	3	2.0735	43.615	8	4	5	0	1.8991	47.857	4	2	19	0	1.7697	51.604	4
0	5	3	2.0704	43.683	4	0	19	1	1.8954	47.958	4	2	15	2	1.7696	51.605	8
0	14	2	2.0674	43.751	4	2	13	2	1.8903	48.095	8	1	20	1	1.7621	51.844	8
1	2	3	2.0641	43.823	8	2	0	3	1.8879	48.160	4	0	18	2	1.7563	52.025	4
1	3	3	2.0488	44.168	8	2	1	3	1.8855	48.224	8	2	8	3	1.7523	52.155	8
3	10	1	2.0392	44.387	8	0	20	0	1.8835	48.279	2	3	16	0	1.7502	52.222	4
0	6	3	2.0369	44.441	4	2	2	3	1.8785	48.417	8	1	21	0	1.7487	52.269	4
3	0	2	2.0332	44.525	4	4	0	1	1.8778	48.436	4	3	11	2	1.7483	52.283	8
3	1	2	2.0302	44.593	8	3	14	0	1.8759	48.488	4	3	15	1	1.7446	52.404	8
1	4	3	2.0279	44.648	8	4	1	1	1.8754	48.500	8	4	8	1	1.7442	52.415	8
1	17	1	2.0251	44.714	8	4	6	0	1.8731	48.564	4	4	10	0	1.7405	52.536	4
1	18	0	2.0221	44.781	4	0	10	3	1.8695	48.665	4	1	12	3	1.7320	52.814	8
3	2	2	2.0215	44.798	8	4	2	1	1.8685	48.692	8	0	21	1	1.7284	52.931	4
2	16	0	2.0190	44.855	4	2	3	3	1.8669	48.736	8	0	13	3	1.7284	52.933	4
2	11	2	2.0161	44.924	8	3	8	2	1.8666	48.744	8	2	9	3	1.7209	53.179	8
2	15	1	2.0103	45.059	8	1	9	3	1.8602	48.922	8	1	18	2	1.7140	53.412	8
3	12	0	2.0100	45.068	4	3	13	1	1.8598	48.934	8	4	9	1	1.7132	53.436	8

Status Primary **QM:** Blank **Pressure/Temperature:** Ambient
Chemical Formula: K0.8 (Li0.133 Ti0.867)2 O4 **Empirical Formula:** K0.8 Li0.266 O4 Ti1.734
Weight %: K17.36 Li1.02 O35.52 Ti46.09 **Atomic %:** K11.76 Li3.91 O58.82 Ti25.50 **ANX:** AB2X4
Compound Name: Potassium Lithium Titanium Oxide

Radiation: CuKα **λ:** 1.5406Å **d-Spacing:** Calculated **Intensity:** Calculated **I/Ic:** 2.27

SYS: Orthorhombic **SPGR:** Cmcm (63)
Author's Cell [AuthCell a: 3.8237(2)Å **AuthCell b:** 15.532(1)Å **AuthCell c:** 2.9727(3)Å
AuthCell Vol: 176.55Å³ **AuthCell Z:** 2.00 **AuthCell MolVol:** 88.28 **]**
Author's Cell Axial Ratio [c/a: 0.777 **a/b:** 0.246 **c/b:** 0.191 **]**
Density [Dcalc: 3.389g/cm³ **Dstruc:** 3.39g/cm³ **]** **SS/FOM:** F(30) = 853.0(0.0011, 33)
Temp: 298.000K (Ambient temperature assigned by ICDD editor) **R-factor:** 0.05

Space Group: Cmcm (63) **Molecular Weight:** 180.18
Crystal Data [XtlCell a: 3.824Å **XtlCell b:** 15.532Å **XtlCell c:** 2.973Å **XtlCell α:** 90.00° **XtlCell β:** 90.00°
XtlCell γ: 90.00° **XtlCell Vol:** 176.55Å³ **XtlCell Z:** 2.00 **]**
Crystal Data Axial Ratio [c/a: 0.777 **a/b:** 0.246 **c/b:** 0.191 **]**
Reduced Cell [RedCell a: 2.973Å **RedCell b:** 3.824Å **RedCell c:** 7.998Å **RedCell α:** 103.83°
RedCell β: 90.00° **RedCell γ:** 90.00° **RedCell Vol:** 88.27Å³ **]**

Crystal (Symmetry Allowed): Centrosymmetric

Pearson: oC13.60 **Subfile(s):** ICSD Pattern, Inorganic **Entry Date:** 07/27/2010
Last Modification Date: 01/17/2013 **Cross-Ref PDF #'s:** 04-011-4447 (Related Phase)

References:

Type	DOI	Reference
Primary Reference		Calculated from ICSD using POWD-12++ (2004).
Structure		"A mixed alkali metal titanate with the lepidocrocite-like layered structure. preparation, crystal structure, protonic form, and acid-base intercalation properties". Sasaki, T., Kooli, F., Iida, M., Michiue, Y., Takenouchi, S., Yajima, Y., Izumi, F., Chakoumakos, B.C., Watanabe, M. Chem. Mater. 10, 4123 (1998).

Database Comments: ANX: AB2X4. Analysis: K0.8 Li0.266 O4 Ti1.734. Formula from original source: K0.8 (Li0.133 Ti0.867)2 O4. ICSD Collection Code: 86641. Significant Warning: Reported displacement parameters on non H atoms are outside the range 0.001<U<0.1. Ueq=0.012 used in the calculation. Wyckoff Sequence: c4(CMCM). Unit Cell Data Source: Powder Diffraction.

d-Spacings (117) - 01-089-5420 (Fixed Slit Intensity) - Cu Kα1 1.54056Å

2θ	d(Å)	I	h	k	l	*	2θ	d(Å)	I	h	k	l	*
11.3846	**7.766000**	999	0	2	0		76.9822	1.237610	m	3	3	0	
22.8836	3.883000	18	0	4	0		79.0846	1.209900	11	1	11	1	
23.9475	3.712850	50	1	1	0		79.4287	1.205520	23	2	10	0	
29.0063	**3.075790**	904	1	3	0		80.9450	1.186720	9	0	12	1	
32.2164	2.776260	125	0	2	1		81.4863	1.180200	3m	0	8	2	
34.6220	2.588670	114	0	6	0		81.4863	1.180200	m	3	5	0	
37.2632	2.411030	12	1	5	0		82.0553	1.173450	51	2	0	2	
38.0927	**2.360410**	409	0	4	1		82.5111	1.168120	5	3	1	1	
38.7730	2.320550	35	1	1	1		83.1929	1.160270	6	2	2	2	
42.2446	2.137530	61	1	3	1		84.7804	1.142550	5	3	3	1	
46.4778	1.952220	247	0	6	1		84.9787	1.140390	23	1	13	0	
46.7497	1.941500	15	0	8	0		86.5889	1.123270	1	2	4	2	
47.5189	1.911850	245	2	0	0		87.1818	1.117150	6	2	10	1	
48.5795	1.872560	83	1	5	1		87.9433	1.109430	2	0	14	0	
49.0295	1.856420	32	2	2	0		88.3672	1.105200	1	3	7	0	
53.3700	1.715220	3	2	4	0		89.2965	1.096090	7	3	5	1	
56.5712	1.625520	4	0	8	1		90.9587	1.080340	12	1	9	2	
57.0762	1.612330	144	1	7	1		91.6641	1.073860	13	0	10	2	
58.5748	1.574600	45	2	2	1		92.2273	1.068770	14	2	6	2	
58.6406	1.572990	44	1	9	0		92.6792	1.064740	4	1	13	1	
59.4623	1.553200	39	0	10	0		96.0718	1.035930	17	3	7	1	
60.1149	1.537890	34	2	6	0		97.4066	1.025260	5	3	9	0	
62.4607	1.485650	178m	0	0	2		99.6295	1.008270	10	2	12	1	
62.4607	1.485650	m	2	4	1		100.1714	1.004270	3	2	8	2	
63.6927	1.459850	10	0	2	2		100.8318	0.999468	1	1	15	0	
67.2869	1.390340	49	1	9	1		102.3272	0.988883	11	1	11	2	
67.8654	1.379890	3	1	1	2		103.1931	0.982931	2	0	2	3	
68.0486	1.376620	8	0	10	1		104.2093	0.976108	1	0	12	2	
68.6551	1.365930	93	2	6	1		105.0256	0.970750	3	0	16	0	
68.8672	1.362240	9	2	8	0		105.2593	0.969236	11	3	9	1	
70.2798	1.338280	77	1	3	2		105.8145	0.965674	1	3	1	2	
71.1168	1.324570	21	1	11	0		106.6940	0.960131	9m	0	4	3	
73.3941	1.288990	16	0	6	2		106.6940	0.960131	m	2	14	0	
74.6559	1.270300	1	3	1	0		107.1360	0.957390	3	1	1	3	
75.0058	1.265240	1	1	5	2		107.3743	0.955925	11	4	0	0	
76.9822	1.237610	28m	2	8	1		108.1724	0.951080	19	3	3	2	

2θ	d(Å)	I	h	k	l	*
108.5595	0.948764	3	4	2	0	
108.7967	0.947356	21	1	15	1	
109.0057	0.946122	6	3	11	0	
109.5112	0.943164	2	1	3	3	
110.7129	0.936278	16	2	10	2	
112.1676	0.928211	1	4	4	0	
112.6835	0.925419	8	0	6	3	
113.1746	0.922794	1	0	16	1	
114.3742	0.916515	4	1	5	3	
115.0275	0.913173	1	2	14	1	
116.7182	0.904772	20	1	13	2	
116.9088	0.903847	6	4	2	1	
117.3837	0.901561	3	3	11	1	
118.4045	0.896738	4	4	6	0	
120.1816	0.888631	4m	0	14	2	
120.1816	0.888631	m	1	17	0	
120.7705	0.886023	13	4	4	1	
121.5586	0.882594	1	0	8	3	
122.0561	0.880464	11	1	7	3	
123.5652	0.874166	4	2	2	3	
124.1785	0.871675	9	3	13	0	
124.7586	0.869355	1	2	12	2	
125.7256	0.865564	4	2	16	0	
126.4228	0.862889	1	0	18	0	
127.5880	0.858526	17	4	6	1	
127.7279	0.858011	16m	2	4	3	
127.7279	0.858011	m	4	8	0	
129.5702	0.851405	5	1	17	1	
131.7622	0.843958	6	3	9	2	
133.4842	0.838412	8	1	9	3	
134.1114	0.836457	2	3	13	1	
134.4633	0.835375	1	0	10	3	
135.2588	0.832968	13	2	6	3	
135.9051	0.831052	2	2	16	1	
136.7212	0.828683	5	0	18	1	
138.3925	0.824003	1	4	8	1	
142.2329	0.814096	6	4	10	0	
142.7867	0.812762	4	0	16	2	
145.6804	0.806166	3	2	14	2	
146.6938	0.804002	15m	3	15	0	
146.6938	0.804002	m	4	0	2	
147.9974	0.801327	1	2	8	3	
148.9706	0.799409	6m	1	19	0	
148.9706	0.799409	m	4	2	2	
149.6322	0.798143	7	3	11	2	

Status Primary **QM:** Star **Pressure/Temperature:** Ambient **Chemical Formula:** Cs4 W11 O35
Empirical Formula: Cs4 O35 W11 **Weight %:** Cs17.07 O17.98 W64.94 **Atomic %:** Cs8.00 O70.00 W22.00
Compound Name: Cesium Tungsten Oxide

Radiation: CuKá **:** 1.5406Å **Filter:** Ni Beta **d-Spacing:** Diff. **Cutoff:** 29.40 **Intensity:** Diffractometer

SYS: Orthorhombic **SPGR:** Pbc21 (29)
Author's Cell [AuthCell a: 14.6686(10)Å **AuthCell b:** 52.3971(26)Å **AuthCell c:** 7.7356(8)Å
AuthCell Vol: 5945.52Å³ **AuthCell Z:** 8.00 **AuthCell MolVol:** 743.19 **]**
Author's Cell Axial Ratio [c/a: 0.527 **a/b:** 0.280 **c/b:** 0.148 **]**
Density [Dcalc: 6.958g/cm³ **Dmeas:** 6.92g/cm³ **]** **SS/FOM:** F(30) = 24.4(0.0050, 247)
Temp: 293.000K (Author provided temperature) **Melting Point:** 1253 K

Space Group: Pbc21 (29) **Molecular Weight:** 3113.95
Crystal Data [XtlCell a: 14.669Å **XtlCell b:** 52.397Å **XtlCell c:** 7.736Å **XtlCell :** 90.00°
XtlCell : 90.00° **XtlCell :** 90.00° **XtlCell Vol:** 5945.52Å³ **XtlCell Z:** 8.00 **]**
Crystal Data Axial Ratio [c/a: 0.527 **a/b:** 0.280 **c/b:** 0.148 **]**
Reduced Cell [RedCell a: 7.736Å **RedCell b:** 14.669Å **RedCell c:** 52.397Å **RedCell :** 90.00°
RedCell : 90.00° **RedCell :** 90.00° **RedCell Vol:** 5945.52Å³ **]**

Crystal (Symmetry Allowed): Non-centrosymmetric, Optical Activity, Pyro / Piezo (p), Piezo (2nd Harm.)

Pearson: oP400.00 **Subfile(s):** Inorganic, Primary Pattern **Entry Date:** 11/16/2000
Last Modification Date: 01/12/2013

References:

Type	DOI	Reference
Primary Reference		Lisoivan, I., Inst. of Inorganic Chemistry, Novosibirsk, Russia. ICDD Grant-in-Aid (2000).
Unit Cell		Solodovnikov, S., Ivannikova, N., Solodovnikova, Z., Zolotova, E. Inorg. Mater. (Engl. Transl.) 34, 845 (1998).

Database Comments: Color: Light yellow. General Comments: Space group may also be `Pbn21`. Melting Point: 1253 K. Sample Preparation: Prepared by solid-state reaction of "Cs2 C O3" and "W O3" at 750-900 C for 100 hours. Temperature of Data Collection: Pattern taken at 293(2) K.

d-Spacings (116) - 00-051-1891 (Fixed Slit Intensity) - Cu K1 1.54056Å

2	d(Å)	I	h	k	l	*	2	d(Å)	I	h	k	l	*	2	d(Å)	I	h	k	l	*
3.3720	26.180400	10	0	2	0		43.8000	2.065160	m	4	16	2		68.9868	1.360170	m	6	29	2	
6.7320	13.119200	3	0	4	0		44.0920	2.052160	4	6	3	2		69.7709	1.346790	6m	2	27	4	
10.1130	8.739470	2	0	6	0		44.6540	2.027630	2m	0	22	2		69.7709	1.346790	m	4	24	4	
13.0820	6.761930	4	2	3	0		44.6540	2.027630	m	6	5	2		70.7411	1.330680	4	8	0	4	
13.4980	6.554460	12	0	8	0		44.9310	2.015770	3m	0	26	0		71.4199	1.319690	2m	4	15	5	
14.7220	6.012150	4	2	5	0		44.9310	2.015770	m	2	21	2		71.4199	1.319690	m	8	24	2	
20.3210	4.366510	2	0	12	0		46.9359	1.934230	12m	0	0	4		72.1202	1.308590	2m	2	37	2	
22.2370	3.994420	2	2	11	0		46.9359	1.934230	m	4	22	1		72.1202	1.308590	m	10	12	2	
22.9710	**3.868420**	31	0	0	2		47.8019	1.901190	6m	0	24	2		76.0940	1.249830	2	0	32	4	
23.2170	3.827990	2	0	2	2		47.8019	1.901190	m	5	21	0		76.7540	1.240720	1m	0	40	2	
23.9580	3.711240	1	0	4	2		47.9270	1.896520	3	1	4	4		76.7540	1.240720	m	10	18	2	
24.2520	3.666910	3	4	0	0		48.4910	1.875770	24m	2	27	0		77.2891	1.233460	7m	4	40	0	
25.1650	3.535910	3	0	6	2		48.4910	1.875770	m	4	24	0		77.2891	1.233460	m	10	23	0	
26.0710	3.415050	3	2	1	2		49.5250	1.839000	6m	1	8	4		78.2028	1.221320	3	8	32	0	
26.3240	3.382800	1	4	6	0		49.5250	1.839000	m	6	13	2		79.7277	1.201750	4	10	25	0	
26.5270	3.357370	15	2	3	2		49.6831	1.833520	12m	3	17	3		81.4169	1.181030	1	4	42	0	
26.7430	3.330740	31	0	8	2		49.6831	1.833520	m	8	0	0		81.9002	1.175280	2m	2	44	0	
27.2130	**3.274270**	63	0	16	0		50.2389	1.814530	1	7	5	2		81.9002	1.175280	m	4	40	2	
27.4030	3.252000	21	2	5	2		50.7469	1.797550	1m	2	8	4		82.8057	1.164710	2m	8	32	2	
27.8610	**3.199570**	100	4	8	0		50.7469	1.797550	m	3	1	4		82.8057	1.164710	m	9	16	4	
28.2210	3.159570	1	4	5	1		51.7151	1.766150	3	4	26	0		84.3173	1.147640	2m	8	11	5	
28.6570	3.112480	2m	0	10	2		54.3038	1.687910	9m	2	27	2		84.3173	1.147640	m	10	25	2	
28.6570	3.112480	m	2	7	2		54.3038	1.687910	m	4	24	2		88.6575	1.102330	1m	7	30	4	
29.4430	3.031160	2m	2	8	2		55.0960	1.665500	7m	5	25	1		88.6575	1.102330	m	12	3	3	
29.4430	3.031160	m	4	7	1		55.0960	1.665500	m	6	22	1		89.0998	1.098000	1m	12	16	2	
29.7100	3.004520	2	4	10	0		55.4570	1.655510	19m	1	24	3		89.0998	1.098000	m	13	11	0	
30.2840	2.948870	1	2	9	2		55.4570	1.655510	m	3	29	1		89.7515	1.091710	1	0	48	0	
30.6890	2.910870	2	0	18	0		56.1239	1.637410	8	0	32	0		92.4711	1.066590	2m	1	49	0	
32.1870	2.778730	6	2	11	2		57.0098	1.614050	1m	5	1	4		92.4711	1.066590	m	12	24	0	
33.6500	2.661190	17	4	0	2		57.0098	1.614050	m	7	4	3		95.7581	1.038490	2	0	50	1	
34.3530	2.608320	11m	2	13	2		57.3111	1.606280	7	8	8	2		96.4736	1.032680	1m	8	32	4	
34.3530	2.608320	m	4	4	2		57.5700	1.599670	14	8	16	0		96.4736	1.032680	m	12	18	3	
35.9011	2.499320	8	0	16	2		57.8851	1.591710	3m	0	30	2		97.0519	1.028060	1m	1	49	2	
36.4140	2.465280	15	4	8	2		57.8851	1.591710	m	9	2	1		97.0519	1.028060	m	13	21	0	
36.7439	2.443900	1m	2	15	2		61.4418	1.507820	3	0	32	2		97.9821	1.020770	2m	1	47	3	
36.7439	2.443900	m	6	0	0		62.8041	1.478350	5	8	16	2		97.9821	1.020770	m	10	25	4	
41.3239	2.183000	1	0	24	0		67.0601	1.394490	3m	3	36	0		99.4161	1.009860	1m	4	48	2	
42.0441	2.147260	2	2	19	2		67.0601	1.394490	m	4	32	2		99.4161	1.009860	m	11	1	5	
43.8000	2.065160	10m	3	23	0		68.9868	1.360170	3m	3	37	0								

Status Primary **QM:** Star **Pressure/Temperature:** Ambient **Chemical Formula:** Cs0.3 (W O3)
Empirical Formula: Cs0.3 O3 W **Weight %:** Cs14.67 O17.66 W67.66 **Atomic %:** Cs6.98 O69.77 W23.26
ANX: AB3X9 **Compound Name:** Cesium Tungsten Oxide **Common Name:** cesium tungstate

Radiation: CuKá **:** 1.5406Å **d-Spacing:** Calculated **Intensity:** Calculated **I/Ic:** 11.65

SYS: Hexagonal **SPGR:** P63/mcm (193)
Author's Cell [AuthCell a: 7.4049(1)Å **AuthCell c:** 7.6098(1)Å **AuthCell Vol:** 361.36Å³ **AuthCell Z:** 6.00
AuthCell MolVol: 60.23 **] Author's Cell Axial Ratio [c/a:** 1.028 **]**
Density [Dcalc: 7.492g/cm³ **Dstruc:** 7.49g/cm³ **] SS/FOM:** F(30) = 528.1(0.0018, 32)
Temp: 298.000K (Ambient temperature assigned by ICDD editor) **R-factor:** 0.024

Space Group: P63/mcm (193) **Molecular Weight:** 271.72
Crystal Data [XtlCell a: 7.405Å **XtlCell b:** 7.405Å **XtlCell c:** 7.610Å **XtlCell :** 90.00° **XtlCell :** 90.00°
XtlCell : 120.00° **XtlCell Vol:** 361.36Å³ **XtlCell Z:** 6.00 **]**
Crystal Data Axial Ratio [c/a: 1.028 **a/b:** 1.000 **c/b:** 1.028 **]**
Reduced Cell [RedCell a: 7.405Å **RedCell b:** 7.405Å **RedCell c:** 7.610Å **RedCell :** 90.00°
RedCell : 90.00° **RedCell :** 120.00° **RedCell Vol:** 361.36Å³ **]**

Crystal (Symmetry Allowed): Centrosymmetric

Pearson: hP25.80 **Subfile(s):** Inorganic, ICSD Pattern **Entry Date:** 07/27/2010
Last Modification Date: 01/17/2013

References:

Type	DOI	Reference
Primary Reference		Calculated from ICSD using POWD-12++ (1997).
Structure		"Hexagonal and pyrochlore-type cesium tungstate synthesized from cesium peroxo-polytungstate and their redox chemistry". Oi, J., Kishimoto, A., Kudo, T. J. Solid State Chem. 103, 176 (1993).

Database Comments: ANX: AB3X9. Analysis: Cs0.3 O3 W1. Formula from original source: Cs0.3 (W O3). ICSD Collection Code: 72618. Wyckoff Sequence: k j g b(P63/MCM). Unit Cell Data Source: Powder Diffraction.

d-Spacings (139) - 01-081-1244 (Fixed Slit Intensity) - Cu K1 1.54056Å

2	d(Å)	I	h	k	l	*	2	d(Å)	I	h	k	l	*	2	d(Å)	I	h	k	l	*
13.7975	6.412830	93	1	0	0		76.5004	1.244200	14	1	0	6		108.1483	0.951225	m	5	2	3	
23.3599	**3.804900**	262	0	0	2		77.8515	1.225950	72m	4	0	4		108.8293	0.947163	8	6	1	2	
24.0157	3.702450	28	1	1	0		77.8515	1.225950	m	4	1	3		110.1006	0.939761	9	4	1	6	
26.7547	3.329310	23	1	1	1		78.4392	1.218230	6	3	3	1		111.5101	0.931821	19	6	0	4	
27.2300	**3.272270**	426	1	0	2		78.6587	1.215380	6	5	0	2		112.2854	0.927570	2	3	1	7	
27.8003	**3.206420**	999	2	0	0		78.9278	1.211910	59	4	2	0		112.6474	0.925613	9	4	4	0	
33.7503	2.653510	238	1	1	2		79.8793	1.199850	13	1	1	6		113.2985	0.922137	1	4	3	4	
36.6198	2.451900	196	2	0	2		81.5541	1.179390	13	2	0	6		113.4559	0.921305	1	1	1	8	
38.9659	2.309500	14	2	1	1		82.0137	1.173940	7	3	3	2		114.0049	0.918428	3m	4	4	1	
42.2429	2.137610	8	3	0	0		82.8839	1.163810	1	3	2	4		114.0049	0.918428	m	5	1	5	
43.1968	2.092590	5	1	1	3		83.5356	1.156380	6	3	1	5		114.4510	0.916119	1	7	0	0	
44.2712	2.044270	113	2	1	2		83.6801	1.154750	22	4	2	2		115.2708	0.911942	22m	2	0	8	
47.7683	1.902450	97	0	0	4		83.9450	1.151780	2	5	1	0		115.2708	0.911942	m	6	1	3	
48.8271	1.863640	87	3	0	2		85.1244	1.138810	7	5	1	1		115.7475	0.909552	6	5	3	1	
49.1761	1.851230	209	2	2	0		86.2064	1.127270	1	4	1	4		116.9511	0.903642	1	5	2	4	
49.9636	1.823880	6	1	0	4		86.5428	1.123750	12	2	1	6		117.3285	0.901825	2	5	0	6	
50.7104	1.798760	1	2	2	1		87.9095	1.109770	3	3	3	3		117.8416	0.899382	3	4	4	2	
51.3266	1.778600	8	3	1	0		88.6524	1.102380	19	5	1	2		119.7280	0.890666	16	5	3	2	
52.1509	1.752410	5	2	1	3		89.8510	1.090760	9	3	0	6		120.0319	0.889300	22	6	2	0	
52.8153	1.731920	20	3	1	1		92.2229	1.068810	16	6	0	0		121.1179	0.884503	3	3	3	6	
54.1570	1.692140	4	1	1	4		92.8238	1.063460	1	5	0	4		123.0697	0.876207	8	4	2	6	
55.1265	1.664650	77	2	2	2		93.4710	1.057790	1	3	2	5		123.5286	0.874316	1	3	2	7	
56.1713	1.636140	217	2	0	4		93.8794	1.054260	1	4	3	0		124.6562	0.869762	1m	4	4	3	
57.1180	1.611250	98	3	1	2		94.5280	1.048730	5	5	1	3		124.6562	0.869762	m	6	1	4	
57.4310	1.603210	114	4	0	0		94.8164	1.046300	11	2	2	6		124.8322	0.869063	1	3	0	8	
61.9562	1.496530	1m	2	1	4		95.0566	1.044290	3	4	3	1		125.6229	0.865962	11	6	2	2	
61.9562	1.496530	m	2	2	3		96.4786	1.032640	15	3	1	6		126.7512	0.861646	5	5	3	3	
62.8486	1.477410	43	4	0	2		96.7917	1.030130	3	4	1	5		127.5940	0.858504	1	4	1	7	
63.1444	1.471200	3	3	2	0		96.9361	1.028980	6	6	0	2		129.2143	0.852656	9	5	1	6	
63.8673	1.456280	10	3	1	3		97.2010	1.026880	1	5	2	0		129.6174	0.851240	1	5	2	5	
64.4527	1.444460	2	3	2	1		97.8056	1.022140	58	4	2	4		130.1477	0.849400	1	7	1	0	
65.6424	1.421130	3	3	0	4		98.3869	1.017650	1	5	2	1		131.1278	0.846068	21	2	2	8	
66.3506	1.407670	1	1	1	5		98.6053	1.015980	8	4	3	2		131.7016	0.844158	5	7	1	1	
66.7944	1.399390	1	4	1	0		101.5014	0.994679	8	4	0	6		133.3614	0.838799	1m	3	1	8	
68.0655	1.376320	9	4	1	1		101.9659	0.991404	10m	2	1	7		133.3614	0.838799	m	6	2	3	
68.2980	1.372200	44	3	2	2		101.9659	0.991404	m	5	2	2		135.4737	0.832327	15	4	4	4	
70.9822	1.326750	104	2	2	4		102.8493	0.985279	1	5	1	4		136.6126	0.828995	6	7	1	2	
71.8162	1.313380	32	4	1	2		103.9327	0.977948	1	6	1	0		137.8835	0.825404	1	5	3	4	
72.7218	1.299240	4	3	1	4		104.6005	0.973527	2	4	3	3		138.2799	0.824311	1	1	1	9	
73.3981	1.288930	2	2	1	5		105.1457	0.969971	4	6	1	1		138.8580	0.822740	3	6	1	5	
73.8222	1.282570	1	5	0	0		106.6161	0.960617	11	3	2	6		139.4802	0.821079	1	5	4	0	
74.4953	1.272640	1	3	2	3		106.9413	0.958594	2	3	3	5		140.6387	0.818068	19	4	0	8	
74.7938	1.268300	6	0	0	6		108.1483	0.951225	6m	0	0	8		140.9413	0.817299	5	6	0	6	

2	d(Å)	I	h	k	l	*
141.3222	0.816341	2	5	4	1	
141.5542	0.815763	2	3	3	7	
143.6447	0.810741	5	4	3	6	
145.9296	0.805627	40m	6	2	4	
145.9296	0.805627	m	7	1	3	
146.9700	0.803425	3	6	3	1	
147.3677	0.802604	4	5	4	2	
147.8596	0.801604	7	8	0	0	
149.6629	0.798085	6m	2	1	9	
149.6629	0.798085	m	5	2	6	

Status Primary **QM:** Indexed **Pressure/Temperature:** Ambient **Chemical Formula:** Cs W1.6 O6
Empirical Formula: Cs O6 W1.6 **Weight %:** Cs25.41 O18.35 W56.24 **Atomic %:** Cs11.63 O69.77 W18.60
ANX: A8B13X48 **Compound Name:** Cesium Tungsten Oxide **Common Name:** cesium tungsten oxide - III

Radiation: CuKá : 1.5406Å **d-Spacing:** Calculated **Intensity:** Calculated **I/Ic:** 11.53

SYS: Cubic **SPGR:** Fd-3m (227)
Author's Cell [AuthCell a: 10.213Å **AuthCell Vol:** 1065.27Å³ **AuthCell Z:** 8.00 **AuthCell MolVol:** 133.16 **]** **Density [Dcalc:** 6.523g/cm³ **Dstruc:** 6.52g/cm³ **]** **SS/FOM:** F(30) = 999.9(0.0000, 32)
Temp: 298.000K (Ambient temperature assigned by ICDD editor) **R-factor:** 0.031

Space Group: Fd-3m (227) **Molecular Weight:** 523.06
Crystal Data [XtlCell a: 10.213Å **XtlCell b:** 10.213Å **XtlCell c:** 10.213Å **XtlCell :** 90.00° **XtlCell :** 90.00° **XtlCell :** 90.00° **XtlCell Vol:** 1065.27Å³ **XtlCell Z:** 8.00 **]**
Crystal Data Axial Ratio [a/b: 1.000 **c/b:** 1.000 **]**
Reduced Cell [RedCell a: 7.222Å **RedCell b:** 7.222Å **RedCell c:** 7.222Å **RedCell :** 60.00° **RedCell :** 60.00° **RedCell :** 60.00° **RedCell Vol:** 266.32Å³ **]**

Crystal (Symmetry Allowed): Centrosymmetric

Pearson: cF68.80 **Subfile(s):** ICSD Pattern, Inorganic **Entry Date:** 07/27/2010
Last Modification Date: 01/17/2013 **Cross-Ref PDF #'s:** 04-013-4680 (Related Phase)

References:

Type	DOI	Reference
Primary Reference		Calculated from ICSD using POWD-12++ (1997).
Structure		"Synthesis and characterization of cubic pyrochlore-type rubidium and cesium tungstates with a lacunar host lattice". Driouiche, A., Abraham, F., Touboul, M., Figlarz, M. Mater. Res. Bull. 26, 901 (1991).

Database Comments: ANX: A8B13X48. Analysis: Cs1 O6 W1.6. Formula from original source: Cs W1.6 O6. ICSD Collection Code: 71337. Test from external database: Deviation of the charge sum from zero tolerable. Minor Warning: Minor test comments from ICSD exist. No e.s.d reported/abstracted on the cell dimension. Wyckoff Sequence: f c b(FD3-MZ). Unit Cell Data Source: Powder Diffraction.

d-Spacings (46) - 01-081-0012 (Fixed Slit Intensity) - Cu K1 1.54056Å

2	d(Å)	I	h	k	l	*	2	d(Å)	I	h	k	l	*	2	d(Å)	I	h	k	l	*
15.0124	5.896480	169	1	1	1		70.8059	1.329620	132	7	3	1		107.9588	0.952367	1	9	5	3	
24.6345	3.610840	187	2	2	0		74.2233	1.276630	30	8	0	0		111.4210	0.932315	6	10	4	2	
28.9721	**3.079340**	999	3	1	1		76.2458	1.247720	1	7	3	3		113.5375	0.920875	13	11	1	1	
30.2906	**2.948240**	401	2	2	2		79.5799	1.203610	11	6	6	0		117.1443	0.902710	10	8	8	0	
35.1178	2.553250	12	4	0	0		81.5616	1.179300	43	7	5	1		119.3644	0.892314	2	9	5	5	
38.3865	2.343020	1	3	3	1		82.2206	1.171510	32	6	6	2		123.1782	0.875758	8	10	6	0	
43.3681	2.084720	37	4	2	2		84.8446	1.141850	7	8	4	0		125.5475	0.866255	25	9	7	3	
46.1458	1.965490	271	5	1	1		86.8058	1.121020	2	9	1	1		126.3527	0.863156	18	10	6	2	
50.5101	**1.805420**	295	4	4	0		87.4582	1.114330	1	8	4	2		129.6624	0.851083	5	12	0	0	
53.0003	1.726310	16	5	3	1		90.0664	1.088710	9	6	6	4		132.2519	0.842354	2	11	5	1	
56.9802	1.614820	48	6	2	0		92.0227	1.070610	33	9	3	1		136.8256	0.828384	8	12	2	2	
59.2830	1.557470	100	5	3	3		95.2887	1.042360	35	8	4	4		139.7653	0.820328	19	11	5	3	
60.0382	1.539670	117	6	2	2		97.2555	1.026450	2	7	7	1		145.1136	0.807409	19	12	4	0	
63.0050	1.474120	8	4	4	4		100.5551	1.001470	10	10	2	0		148.6957	0.799944	1	9	9	1	
65.1789	1.430110	13	5	5	1		102.5516	0.987328	30	9	5	1								
68.7217	1.364770	30	6	4	2		103.2203	0.982746	19	10	2	2								

Status Primary **QM:** Indexed **Pressure/Temperature:** Ambient **Chemical Formula:** Cs6 (W11 O36)
Empirical Formula: Cs6 O36 W11 **Weight %:** Cs23.48 O16.96 W59.55 **Atomic %:** Cs11.32 O67.92 W20.75
ANX: A6B11X36 **Compound Name:** Cesium Tungsten Oxide **Common Name:** hexacesium undecatungstate

Radiation: CuKá **:** 1.5406Å **d-Spacing:** Calculated **Intensity:** Calculated **I/Ic:** 5.45

SYS: Rhombohedral **SPGR:** R-3c (167)
Author's Cell [AuthCell a: 7.261Å **AuthCell c:** 110.58(4)Å **AuthCell Vol:** 5048.94Å^3 **AuthCell Z:** 6.00
AuthCell MolVol: 841.49 **]** **Author's Cell Axial Ratio [c/a:** 15.229 **]**
Density [Dcalc: 6.701g/cm^3 **Dstruc:** 6.7g/cm^3 **]** **SS/FOM:** F(30) = 200.9(0.0041, 36)
Temp: 298.000K (Ambient temperature assigned by ICDD editor) **R-factor:** 0.056

Space Group: R-3c (167) **Molecular Weight:** 3395.76
Crystal Data [XtlCell a: 7.261Å **XtlCell b:** 7.261Å **XtlCell c:** 110.580Å **XtlCell :** 90.00°
XtlCell : 90.00° **XtlCell :** 120.00° **XtlCell Vol:** 5048.94Å^3 **XtlCell Z:** 6.00 **]**
Crystal Data Axial Ratio [c/a: 15.229 **a/b:** 1.000 **c/b:** 15.229 **]**
Reduced Cell [RedCell a: 7.261Å **RedCell b:** 7.261Å **RedCell c:** 37.097Å **RedCell :** 84.38°
RedCell : 84.38° **RedCell :** 60.00° **RedCell Vol:** 1682.96Å^3 **]**

Crystal (Symmetry Allowed): Centrosymmetric

Pearson: hR106.00 **Subfile(s):** ICSD Pattern, Inorganic **Entry Date:** 07/27/2010
Last Modification Date: 01/17/2013

References:

Type	DOI	Reference
Primary Reference		Calculated from ICSD using POWD-12++ (2004).
Additional Reference		Marsh, R.E., Bernal, I. Acta Crystallogr., Sec. B: Struct. Sci. 34, 50 (1978).
Structure		"More space-group changes". Marsh, R.E., Bernal, I. Acta Crystallogr., Sec. B: Struct. Sci. 51, 300 (1995).

Database Comments: ANX: A6B11X36. Analysis: Cs6 O36 W11. Formula from original source: Cs6 (W11 O36). ICSD Collection Code: 80133. Calculated Pattern Original Remarks: This publication corrects errors in an earlier one. Revised data of 1387 in Aa, R=0.057. Test from external database: The lattice Parameters are unusual but agree with the paper. Minor Warning: Minor test comments from ICSD exist. No e.s.d reported/abstracted on the cell dimension. Wyckoff Sequence: f7 e c4(R3-CH). Unit Cell Data Source: Single Crystal.

d-Spacings (191) - 01-083-1021 (Fixed Slit Intensity) - Cu K1 1.54056Å

2	d(Å)	I	h	k	l	*	2	d(Å)	I	h	k	l	*
4.7907	18.430000	249	0	0	6		36.4983	2.459780	m	1	1	33	
9.5899	9.215000	70	0	0	12		37.8576	2.374530	5m	1	2	2	
14.1635	6.247930	64	0	1	2		37.8576	2.374530	m	2	1	1	
14.4060	6.143330	316m	0	0	18		38.0475	2.363110	14	1	2	5	
14.4060	6.143330	m	1	0	4		38.3535	2.344960	13m	1	1	36	
15.4682	5.723760	334	0	1	8		38.3535	2.344960	m	1	2	8	
16.2018	5.466210	2	1	0	10		38.6859	2.325570	7m	2	0	32	
18.0163	4.919570	11	0	1	14		38.6859	2.325570	m	2	1	10	
19.0655	4.651140	18	1	0	16		38.9053	2.312960	3	1	2	11	
19.2478	4.607500	12	0	0	24		39.0672	2.303750	14	0	0	48	
21.3818	4.152210	5	0	1	20		39.3283	2.289050	11	2	1	13	
22.6284	3.926210	39	1	0	22		39.5647	2.275920	1	1	2	14	
24.1245	3.686000	8	0	0	30		39.8456	2.260520	5	0	2	34	
24.4990	3.630500	90	1	1	0		40.0857	2.247530	9m	1	0	46	
24.6194	3.613020	33	1	1	3		40.0857	2.247530	m	2	1	16	
24.9773	3.562050	26	1	1	6		40.3271	2.234630	8m	1	1	39	
25.2591	3.522940	189	0	1	26		40.3271	2.234630	m	1	2	17	
26.3636	3.377800	27	1	1	12		40.9840	2.200320	1	2	1	19	
26.6317	3.344400	401	1	0	28		41.3135	2.183530	1	1	2	20	
27.3604	3.256970	22	1	1	15		42.0162	2.148620	11	2	1	22	
28.4095	3.139030	199	2	0	2		42.3724	2.131380	22m	1	1	42	
28.5349	**3.125520**	999m	0	2	4		42.3724	2.131380	m	1	2	23	
28.5349	**3.125520**	m	1	1	18		43.1215	2.096070	12m	2	1	25	
29.1030	**3.065790**	451m	0	0	36		43.1215	2.096070	m	3	0	0	
29.1030	**3.065790**	m	2	0	8		43.4137	2.082640	9	3	0	6	
29.5119	**3.024240**	674m	0	1	32		43.5874	2.074740	43m	0	2	40	
29.5119	**3.024240**	m	0	2	10		43.5874	2.074740	m	1	2	26	
29.8684	2.988950	23	1	1	21		44.1913	2.047780	81	0	0	54	
30.5780	2.921180	41	2	0	14		44.4516	2.036390	121m	1	1	45	
30.9289	2.888830	93	1	0	34		44.4516	2.036390	m	2	1	28	
31.2276	2.861880	96	0	2	16		44.9618	2.014460	8m	1	0	52	
31.3428	2.851620	49	1	1	24		44.9618	2.014460	m	1	2	29	
32.7394	2.733100	61	2	0	20		45.6962	1.983780	207	0	3	18	
33.5931	2.665570	8	0	2	22		46.2050	1.963110	110	2	0	44	
33.9161	2.640920	18	0	1	38		46.6560	1.945180	12	1	1	48	
34.0230	2.632860	14	0	0	42		47.3326	1.918940	32	2	1	34	
34.6513	2.586550	30	1	1	30		47.5760	1.909690	180m	0	2	46	
35.4764	2.528260	41m	1	0	40		47.5760	1.909690	m	0	3	24	
35.4764	2.528260	m	2	0	26		48.2673	1.883940	1	0	1	56	
36.4983	2.459780	17m	0	2	28		48.8864	1.861520	3m	1	1	51	

2	d(Å)	I	h	k	l	*
48.8864	1.861520	m	2	1	37	
49.4739	1.840780	18m	0	0	60	
49.4739	1.840780	m	1	2	38	
50.0167	1.822070	21	0	3	30	
50.2176	1.815250	287m	2	2	0	
50.2176	1.815250	m	2	2	3	
50.4059	1.808910	20	2	0	50	
50.6055	1.802240	5	2	1	40	
51.1720	1.783610	21m	1	1	54	
51.1720	1.783610	m	2	2	12	
51.8627	1.761470	119m	0	2	52	
51.8627	1.761470	m	2	2	15	
52.5239	1.740840	37m	2	2	18	
52.5239	1.740840	m	3	1	5	
52.8679	1.730320	23m	0	3	36	
52.8679	1.730320	m	3	1	8	
53.2645	1.718370	3	3	1	11	
53.3485	1.715860	3m	0	1	62	
53.3485	1.715860	m	2	2	21	
53.5970	1.708490	20	1	3	13	
53.7830	1.703020	2	3	1	14	
54.2266	1.690130	16m	2	1	46	
54.2266	1.690130	m	2	2	24	
54.8567	1.672200	17m	1	2	47	
54.8567	1.672200	m	2	0	56	
55.0759	1.666060	26	1	0	64	
55.7438	1.647670	5	1	3	22	
55.9025	1.643370	6	1	1	60	
56.0460	1.639500	22m	3	0	42	
56.0460	1.639500	m	3	1	23	
56.3927	1.630240	19m	0	2	58	
56.3927	1.630240	m	2	2	30	
56.6871	1.622470	2	1	3	25	
57.0257	1.613640	48	3	1	26	
57.7386	1.595400	77m	1	3	28	
57.7386	1.595400	m	2	2	33	
58.1624	1.584780	19m	2	1	52	
58.1624	1.584780	m	3	1	29	
58.7049	1.571420	15	0	4	2	
58.7830	1.569520	16	4	0	4	
58.8955	1.566790	22m	1	2	53	
58.8955	1.566790	m	1	3	31	
59.0624	1.562760	161m	0	4	8	
59.0624	1.562760	m	2	2	36	
59.3278	1.556400	69m	3	1	32	
59.3278	1.556400	m	4	0	10	
59.5412	1.551330	65m	0	3	48	
59.5412	1.551330	m	2	0	62	
59.9464	1.541810	9	0	4	14	
60.1533	1.537000	34m	0	0	72	
60.1533	1.537000	m	1	3	34	
60.3652	1.532110	41m	1	0	70	
60.3652	1.532110	m	4	0	16	
60.8407	1.521270	5	1	1	66	
61.1538	1.514230	13	0	2	64	
61.2483	1.512120	11	0	4	20	
61.5096	1.506320	1	1	3	37	
61.7798	1.500380	3	4	0	22	
61.9834	1.495940	9	3	1	38	
62.0511	1.494470	9	2	2	42	
62.3888	1.487190	1	2	1	58	
62.9845	1.474550	17m	0	4	26	
62.9845	1.474550	m	1	3	40	
63.1205	1.471700	3	1	2	59	
63.4659	1.464520	16m	0	3	54	
63.4659	1.464520	m	3	1	41	
63.6567	1.460590	4m	2	2	45	
63.6567	1.460590	m	4	0	28	
63.9872	1.453840	2	0	1	74	
64.4552	1.444410	4m	1	3	43	
64.4552	1.444410	m	2	0	68	
64.6987	1.439560	3m	2	3	5	
64.6987	1.439560	m	3	2	4	
64.9386	1.434820	13	2	3	8	
65.0399	1.432830	6	3	1	44	
65.4000	1.425810	11m	1	2	62	
65.4000	1.425810	m	2	2	48	
65.5816	1.422300	3	3	2	13	
65.8292	1.417550	4m	0	0	78	
65.8292	1.417550	m	1	0	76	
65.9908	1.414470	15m	1	1	72	
65.9908	1.414470	m	4	0	34	
66.1395	1.411650	4m	0	2	70	
66.1395	1.411650	m	1	3	46	
66.7033	1.401080	3m	3	1	47	
66.7033	1.401080	m	3	2	19	
66.8944	1.397540	19m	2	1	64	
66.8944	1.397540	m	2	3	20	
67.4910	1.386630	2	3	2	22	
67.6327	1.384070	4m	0	3	60	
67.6327	1.384070	m	0	4	38	
67.8609	1.379970	8	1	3	49	
68.2980	1.372200	11m	4	1	0	
68.2980	1.372200	m	4	1	3	
68.5134	1.368410	5	1	4	6	
68.6420	1.366160	16m	1	1	75	
68.6420	1.366160	m	2	3	26	
69.0906	1.358380	64m	1	4	12	
69.0906	1.358380	m	2	2	54	
69.2852	1.355040	34m	2	1	67	
69.2852	1.355040	m	3	2	28	
69.5799	1.350020	23m	0	1	80	
69.5799	1.350020	m	1	3	52	
70.2244	1.339200	74	4	1	18	
70.6129	1.332780	24	0	4	44	
70.9145	1.327850	7	1	4	21	
71.4812	1.318710	11m	1	0	82	
71.4812	1.318710	m	3	2	34	
71.6706	1.315690	70m	2	1	70	
71.6706	1.315690	m	4	0	46	
72.1106	1.308740	4	0	3	66	

Status Primary **QM:** Indexed **Pressure/Temperature:** Ambient **Chemical Formula:** K Nb O3
Empirical Formula: K Nb O3 **Weight %:** K21.72 Nb51.61 O26.66 **Atomic %:** K20.00 Nb20.00 O60.00
ANX: ABX3 **Compound Name:** Potassium Niobium Oxide **Common Name:** potassium niobate

Radiation: CuKá **:** 1.5406Å **d-Spacing:** Calculated **Intensity:** Calculated **I/Ic:** 5.52

SYS: Orthorhombic **SPGR:** Amm2 (38)
Author's Cell [AuthCell a: 3.971Å **AuthCell b:** 5.692Å **AuthCell c:** 5.719Å **AuthCell Vol:** 129.27Å³
AuthCell Z: 2.00 **AuthCell MolVol:** 64.64 **]**
Author's Cell Axial Ratio [c/a: 1.440 **a/b:** 0.698 **c/b:** 1.005 **]**
Density [Dcalc: 4.625g/cm³ **Dstruc:** 4.62g/cm³ **]** **SS/FOM:** F(30) = 151.7(0.0056, 35)
Temp: 295.000K (Author provided temperature) **R-factor:** 0.021

Space Group: Cm2m (38) **Molecular Weight:** 180.00
Crystal Data [XtlCell a: 5.692Å **XtlCell b:** 5.719Å **XtlCell c:** 3.971Å **XtlCell :** 90.00° **XtlCell :** 90.00°
XtlCell : 90.00° **XtlCell Vol:** 129.27Å³ **XtlCell Z:** 2.00 **]**
Crystal Data Axial Ratio [c/a: 0.698 **a/b:** 0.995 **c/b:** 0.694 **]**
Reduced Cell [RedCell a: 3.971Å **RedCell b:** 4.034Å **RedCell c:** 4.034Å **RedCell :** 90.27°
RedCell : 90.00° **RedCell :** 90.00° **RedCell Vol:** 64.63Å³ **]**

Crystal (Symmetry Allowed): Non-centrosymmetric, Optical Activity, Pyro / Piezo (p), Piezo (2nd Harm.)

Pearson: oC10.00 **Subfile(s):** Alternate Pattern, Ceramic (Ferroelectric, Perovskite), Inorganic, ICSD Pattern
Entry Date: 07/27/2010 **Last Modification Date:** 01/17/2013

References:

Type	DOI	Reference
Primary Reference		Calculated from ICSD using POWD-12++ (2004).
Additional Reference		Hewat, A.W. Phase Transitions 38, 127 (1992).
Structure		"Cubic-tetragonal-orthorhombic-rhombohedral ferroelectric transitions in perovskite potassium niobate. Neutron powder profile refinement of the structures". Hewat, A.W. J. Phys. C: Solid State Phys. 6, 2559 (1973).

Database Comments: ANX: ABX3. Analysis: K1 Nb1 O3. Formula from original source: K (Nb O3). ICSD Collection Code: 9533. Calculated Pattern Original Remarks: Stable from 263 to 498 K (2nd ref., Tomaszewski), 498-708 K: P4mm. Temperature of Data Collection: 295 K. Minor Warning: No e.s.d reported/abstracted on the cell dimension. Wyckoff Sequence: e b a2(AMM2). Unit Cell Data Source: Powder Diffraction.

d-Spacings (89) - 01-071-0946 (Fixed Slit Intensity) - Cu K1 1.54056Å

2	d(Å)	I	h	k	l	*	2	d(Å)	I	h	k	l	*	2	d(Å)	I	h	k	l	*
22.0141	**4.034360**	433	0	1	1		78.8376	1.213070	5	1	4	2		110.4375	0.937838	17m	4	0	2	
22.3699	3.971000	212	1	0	0		79.7707	1.201210	2m	3	0	2		110.4375	0.937838	m	4	2	0	
31.2542	2.859500	275	0	0	2		79.7707	1.201210	m	3	2	0		112.4201	0.926840	5	1	0	6	
31.4063	2.846000	292	0	2	0		83.1955	1.160240	37	2	0	4		113.1919	0.922702	1	1	6	0	
31.5878	**2.830060**	999	1	1	1		83.5143	1.156620	40	2	4	0		113.8471	0.919251	5	3	2	4	
38.7742	2.320480	17	1	0	2		86.7710	1.121380	7	0	1	5		114.1067	0.917899	3	3	4	2	
44.8979	**2.017180**	378	0	2	2		87.2453	1.116500	7	0	5	1		116.9135	0.903824	16	0	2	6	
45.6543	1.985500	182	2	0	0		87.5468	1.113430	13	2	3	3		117.6254	0.900408	20	0	6	2	
50.4434	1.807650	41	0	1	3		88.2183	1.106680	12	3	2	2		117.8753	0.899223	36	2	4	4	
50.7197	1.798450	89m	0	3	1		91.0840	1.079180	37	1	1	5		119.7153	0.890723	37	4	2	2	
50.7197	1.798450	m	1	2	2		91.6059	1.074390	57m	1	5	1		121.8636	0.881285	9	1	2	6	
51.2386	1.781450	76	2	1	1		91.6059	1.074390	m	2	2	4		122.6115	0.878118	12m	1	6	2	
55.8345	1.645210	175	1	1	3		91.8435	1.072230	35	2	4	2		122.6115	0.878118	m	2	3	5	
56.0256	1.640050	167	1	3	1		92.3177	1.067960	35	3	1	3		122.9029	0.876900	8	2	5	3	
56.3679	1.630900	93	2	0	2		92.4767	1.066540	34	3	3	1		124.5566	0.870159	8	4	1	3	
56.4629	1.628380	91	2	2	0		99.5864	1.008590	22	0	4	4		124.7488	0.869394	8	4	3	1	
65.1974	1.429750	44	0	0	4		101.7744	0.992750	12	4	0	0		127.3841	0.859280	12	2	0	6	
65.5453	1.423000	49	0	4	0		103.6908	0.979568	5	0	3	5		128.3855	0.855616	27m	2	6	0	
65.9613	1.415030	179	2	2	2		103.9920	0.977553	14m	0	5	3		128.3855	0.855616	m	3	1	5	
69.8648	1.345210	25m	0	3	3		103.9920	0.977553	m	1	4	4		128.9933	0.853439	21	3	5	1	
69.8648	1.345210	m	1	0	4		104.1630	0.976415	10	2	1	5		138.9085	0.822604	29	2	2	6	
70.2009	1.339590	15	1	4	0		104.6529	0.973183	9	2	5	1		139.8803	0.820027	35	2	6	2	
70.3775	1.336660	27	2	1	3		104.9389	0.971314	5	3	0	4		141.6805	0.815450	17	4	0	4	
70.5454	1.333890	26	2	3	1		105.2665	0.969190	4	3	4	0		142.1934	0.814192	18	4	4	0	
71.1725	1.323670	6	3	0	0		106.0792	0.963993	8	4	1	1		144.5307	0.808712	4	0	1	7	
74.1581	1.277590	34	0	2	4		107.8267	0.953167	7	0	0	6		145.3567	0.806873	4	0	5	5	
74.4208	1.273730	91m	0	4	2		108.1759	0.951059	26	1	3	5		146.2005	0.805046	4	0	7	1	
74.4208	1.273730	m	1	3	3		108.5092	0.949064	27m	0	6	0		147.5453	0.802241	7	3	4	4	
75.5339	1.257700	56	3	1	1		108.5092	0.949064	m	1	5	3		149.3428	0.798693	7	4	3	3	
78.5954	1.216200	12	1	2	4		109.4789	0.943352	24	3	3	3								

Status Alternate **QM:** Indexed **Pressure/Temperature:** Ambient **Chemical Formula:** Sr Ti O3
Empirical Formula: O3 Sr Ti **Weight %:** O26.16 Sr47.75 Ti26.09 **Atomic %:** O60.00 Sr20.00 Ti20.00
ANX: ABX3 **Compound Name:** Strontium Titanium Oxide **Mineral Name:** Tausonite, syn
Common Name: strontium titanate

Radiation: CuKá **:** 1.5406Å **d-Spacing:** Calculated **Intensity:** Calculated **I/Ic:** 8.02

SYS: Cubic **SPGR:** Pm-3m (221)
Author's Cell [AuthCell a: 3.905(1)Å **AuthCell Vol:** 59.55Å^3 **AuthCell Z:** 1.00 **AuthCell MolVol:** 59.55 **]**
Density [Dcalc: 5.118g/cm^3 **Dstruc:** 5.12g/cm^3 **]** **SS/FOM:** F(20) = 999.9(0.0001, 20)
Temp: 298.000K (Author provided temperature)

Space Group: Pm-3m (221) **Molecular Weight:** 183.52
Crystal Data [XtlCell a: 3.905Å **XtlCell b:** 3.905Å **XtlCell c:** 3.905Å **XtlCell :** 90.00° **XtlCell :** 90.00°
XtlCell : 90.00° **XtlCell Vol:** 59.55Å^3 **XtlCell Z:** 1.00 **]**
Crystal Data Axial Ratio [a/b: 1.000 **c/b:** 1.000 **]**
Reduced Cell [RedCell a: 3.905Å **RedCell b:** 3.905Å **RedCell c:** 3.905Å **RedCell :** 90.00°
RedCell : 90.00° **RedCell :** 90.00° **RedCell Vol:** 59.55Å^3 **]**

Crystal (Symmetry Allowed): Centrosymmetric

Pearson: cP5.00

Subfile(s): Alternate Pattern, ICSD Pattern, Inorganic, Ceramic (Perovskite), Common Phase, Mineral Related (Mineral , Synthetic)

Entry Date: 07/26/2010 **Last Modification Date:** 01/17/2013

References:

Type	DOI	Reference
Primary Reference		Calculated from ICSD using POWD-12++ (2004).
Additional Reference		Meyer, G.M., Nelmes, R.J., Hutton, J. Acta Crystallogr., Sec. A: Cryst. Phys., Diffr., Theor. Crystallogr. 37, 916 (1981).
Additional Reference		Meyer, G.M., Nelmes, R.J., Hutton, J. Golden Book of Phase Transitions, Wroclaw 1, 1 (2002).
Additional Reference		Meyer, G.M., Nelmes, R.J., Hutton, J. J. Phys. C: Solid State Phys. 14, 1713 (1981).
Structure		"High-resolution (direct space) studies of anharmonic motion associated with the structural phase transition in Sr Ti O3". Meyer, G.M., Nelmes, R.J., Hutton, J. Ferroelectrics 21, 461 (1978).

Database Comments: ANX: ABX3. Analysis: O3 Sr1 Ti1. Formula from original source: Sr (Ti O3). ICSD Collection Code: 23076. Calculated Pattern Original Remarks: Stable above 105 K (4th ref., Tomaszewski), 65-105 K: I4/mcm. Temperature of Data Collection: 298 K. Minor Warning: No R factors reported/abstracted. Wyckoff Sequence: c b a(PM3-M). Unit Cell Data Source: Single Crystal.

d-Spacings (20) - 01-073-0661 (Fixed Slit Intensity) - Cu K1 1.54056Å

2	d(Å)	I	h	k	l	*	2	d(Å)	I	h	k	l	*	2	d(Å)	I	h	k	l	*
22.7529	3.905000	33	1	0	0		72.5644	1.301670	12	2	2	1		108.8396	0.947102	8	4	1	0	
32.3964	**2.761250**	999	1	1	0		77.1845	1.234870	119	3	1	0		113.6245	0.920417	71	4	1	1	
39.9556	2.254550	194	1	1	1		81.7212	1.177400	40	3	1	1		118.5914	0.895868	17	3	3	1	
46.4708	**1.952500**	382	2	0	0		86.2054	1.127280	52	2	2	2		123.8058	0.873184	77	4	2	0	
52.3450	1.746370	22	2	1	0		90.6675	1.083050	5	3	2	0		129.3604	0.852141	8	4	2	1	
57.7857	**1.594210**	323	2	1	1		95.1322	1.043660	129	3	2	1		135.3991	0.832549	44	3	3	2	
67.8240	1.380630	183	2	2	0		104.1879	0.976250	24	4	0	0								

Status Alternate **QM:** Indexed **Pressure/Temperature:** Ambient **Chemical Formula:** Bi Fe O3
Empirical Formula: Bi Fe O3 **Weight %:** Bi66.80 Fe17.85 O15.34 **Atomic %:** Bi20.00 Fe20.00 O60.00
ANX: ABX3 **Compound Name:** Bismuth Iron Oxide **Common Name:** bismuth iron(III) oxide

Radiation: CuKá **:** 1.5406Å **d-Spacing:** Calculated **Intensity:** Calculated **I/Ic:** 8.77

SYS: Rhombohedral **SPGR:** R3c (161)
Author's Cell [AuthCell a: 5.5876(3)Å **AuthCell c:** 13.867(1)Å **AuthCell Vol:** 374.94Å^3 **AuthCell Z:** 6.00
AuthCell MolVol: 62.49 **]** **Author's Cell Axial Ratio [c/a:** 2.482 **]**
Density [Dcalc: 8.313g/cm^3 **Dstruc:** 8.31g/cm^3 **]** **SS/FOM:** F(30) = 999.9(0.0000, 32)
Temp: 298.000K (Ambient temperature assigned by ICDD editor) **R-factor:** 0.09

Space Group: R3c (161) **Molecular Weight:** 312.83
Crystal Data [XtlCell a: 5.588Å **XtlCell b:** 5.588Å **XtlCell c:** 13.867Å **XtlCell :** 90.00° **XtlCell :** 90.00°
XtlCell : 120.00° **XtlCell Vol:** 374.94Å^3 **XtlCell Z:** 6.00 **]**
Crystal Data Axial Ratio [c/a: 2.482 **a/b:** 1.000 **c/b:** 2.482 **]**
Reduced Cell [RedCell a: 5.588Å **RedCell b:** 5.588Å **RedCell c:** 5.637Å **RedCell :** 60.29°
RedCell : 60.29° **RedCell :** 60.00° **RedCell Vol:** 124.98Å^3 **]**

Crystal (Symmetry Allowed): Non-centrosymmetric, Pyro / Piezo (p), Piezo (2nd Harm.)

Pearson: hR10.00 **Subfile(s):** Ceramic (Ferroelectric), ICSD Pattern, Inorganic **Entry Date:** 07/26/2010
Last Modification Date: 01/17/2013

References:

Type	DOI	Reference
Primary Reference		Calculated from ICSD using POWD-12++ (1997).
Additional Reference		Moreau, J.M., Michel, C., Gerson, R., James, W.J. Phase Transitions 38, 127 (1992).
Additional Reference		Moreau, J.M., Michel, C., Gerson, R., James, W.J. Solid State Commun. 7, 701 (1969).
Structure		"Ferroelectric Bi Fe O3 X-Ray and neutron diffraction study". Moreau, J.M., Michel, C., Gerson, R., James, W.J. J. Phys. Chem. Solids 32, 1315 (1971).

Database Comments: ANX: ABX3. Analysis: Bi1 Fe1 O3. Formula from original source: Bi Fe O3. ICSD Collection Code: 15299. Calculated Pattern Original Remarks: Stable up to 1083 K (3rd ref., Tomaszewski), decomposes above 1123 K. Minor Warning: 7%<R factor<12% (for single crystal). Wyckoff Sequence: b a2(R3CH). Unit Cell Data Source: Single Crystal.

d-Spacings (71) - 01-071-2494 (Fixed Slit Intensity) - Cu K1 1.54056Å

2	d(Å)	I	h	k	l	*	2	d(Å)	I	h	k	l	*	2	d(Å)	I	h	k	l	*
22.3861	**3.968150**	798	0	1	2		79.6195	1.203110	35	0	2	10		113.4318	0.921432	1	2	1	13	
31.7246	**2.818170**	996	1	0	4		80.2288	1.195500	59	2	2	6		113.9231	0.918854	1	3	1	11	
32.0087	**2.793800**	999	1	1	0		80.5330	1.191750	26	0	4	2		114.3459	0.916661	21	2	0	14	
37.5870	2.391000	13	1	1	3		83.6064	1.155580	6	0	0	12		115.3375	0.911606	17	4	0	10	
38.9367	2.311170	93	0	0	6		84.8125	1.142200	44	4	0	4		116.3373	0.906634	21	4	2	2	
39.4115	2.284410	308	2	0	2		87.7763	1.111110	1	1	3	7		119.7863	0.890403	23	2	2	12	
45.6891	1.984070	431	0	2	4		88.3874	1.105000	67	2	1	10		121.1786	0.884239	43	2	4	4	
50.2762	1.813270	3	2	1	1		89.2872	1.096180	37	2	3	2		122.7196	0.877665	1	1	1	15	
51.2583	1.780810	300	1	1	6		92.3311	1.067840	44	1	1	12		124.3522	0.870977	45m	1	2	14	
51.6419	1.768480	168	1	2	2		93.0816	1.061190	58	3	1	8		124.3522	0.870977	m	1	4	9	
56.3325	1.631840	150	0	1	8		93.5320	1.057260	72	3	2	4		125.4492	0.866638	33	3	2	10	
56.8714	1.617650	352	2	1	4		93.6822	1.055960	73	4	1	0		126.1892	0.863780	28	3	3	6	
57.0504	1.613000	206	3	0	0		95.8229	1.037960	1	1	2	11		126.5617	0.862362	19	1	5	2	
60.5950	1.526850	1	1	2	5		96.1999	1.034890	1	2	2	9		129.0855	0.853112	10	1	0	16	
66.2756	1.409080	70	2	0	8		96.8783	1.029440	1	1	4	3		131.4439	0.845012	16	5	0	8	
66.9291	1.396900	120	2	2	0		101.8757	0.992037	21	0	4	8		132.0472	0.843022	40	5	1	4	
69.6283	1.349200	1	1	1	9		105.0826	0.970380	27	0	1	14		134.5654	0.835063	1	1	3	13	
69.9482	1.343810	1	2	1	7		106.0167	0.964389	47	1	3	10		135.2003	0.833143	1	2	3	11	
70.5971	1.333040	73	1	0	10		106.6417	0.960457	62	4	1	6		136.1662	0.830288	1	2	4	7	
71.2314	1.322720	90	0	3	6		106.9551	0.958508	15	5	0	2		136.4923	0.829342	1	1	5	5	
71.5482	1.317640	58	3	1	2		110.1657	0.939388	27	3	0	12		141.4910	0.815920	9	0	2	16	
75.5043	1.258120	101	1	2	8		110.9666	0.934850	38	2	3	8		144.4807	0.808825	32	4	2	8	
75.9687	1.251580	117	1	3	4		111.4491	0.932159	28	0	5	4		145.5266	0.806501	21	6	0	0	
79.2272	1.208080	2	3	1	5		111.6103	0.931267	25	3	3	0								

Status Primary **QM:** Indexed **Pressure/Temperature:** Ambient
Chemical Formula: Bi5.96 Ca1.76 Nb0.28 O11.14 **Empirical Formula:** Bi5.96 Ca1.76 Nb0.28 O11.14
Weight %: Bi81.93 Ca4.64 Nb1.71 O11.72 **Atomic %:** Bi31.14 Ca9.20 Nb1.46 O58.20 **ANX:** A2B6X11
Compound Name: Calcium Bismuth Niobium Oxide

Radiation: CuKα **λ:** 1.5406Å **d-Spacing:** Calculated **Intensity:** Calculated **I/Ic:** 8.22

SYS: Monoclinic **SPGR:** P21/m (11)
Author's Cell [AuthCell a: 9.3334(4)Å **AuthCell b:** 3.7956(1)Å **AuthCell c:** 9.6195(3)Å
AuthCell β: 110.101(2)° **AuthCell Vol:** 320.02Å³ **AuthCell Z:** 1.00 **AuthCell MolVol:** 320.02 **]**
Author's Cell Axial Ratio [c/a: 1.031 **a/b:** 2.459 **c/b:** 2.534 **]**
Density [Dcalc: 7.889g/cm³ **Dstruc:** 7.89g/cm³ **]** **SS/FOM:** F(30) = 999.9(0.0004, 41)
Temp: 293.000K (Author provided temperature)

Space Group: P21/m (11) **Molecular Weight:** 1520.31
Crystal Data [XtlCell a: 9.620Å **XtlCell b:** 3.796Å **XtlCell c:** 9.333Å **XtlCell α:** 90.00° **XtlCell β:** 110.10°
XtlCell γ: 90.00° **XtlCell Vol:** 320.02Å³ **XtlCell Z:** 1.00 **]**
Crystal Data Axial Ratio [c/a: 0.970 **a/b:** 2.534 **c/b:** 2.459 **]**
Reduced Cell [RedCell a: 3.796Å **RedCell b:** 9.333Å **RedCell c:** 9.620Å **RedCell α:** 110.10°
RedCell β: 90.00° **RedCell γ:** 90.00° **RedCell Vol:** 320.02Å³ **]**

Crystal (Symmetry Allowed): Centrosymmetric

Pearson: mP19.14 **Subfile(s):** ICSD Pattern, Inorganic, Primary Pattern **Entry Date:** 11/20/2012
Last Modification Date: 01/30/2013

References:

Type	DOI	Reference
Primary Reference		Calculated from ICSD using POWD-12++.
Structure		"The structure and ionic conductivity of the fluorite-related isostructural materials Bi20 Ca7 Nb O39.5, Bi10.75 Ca4.375 Ga O22 and quenched Bi9 Re O17". Thompson, M., Greaves, C. Solid State Ionics 181, 1674 (2010).

Database Comments: ANX: A2B6X11. Analysis: Bi5.96 Ca1.76 Nb0.28 O11.14. Formula from original source: Bi5.96 Ca1.76 Nb0.28 O11.14. ICSD Collection Code: 169439. Temperature of Data Collection: 293 K. Test from external database: Deviation of the charge sum from zero tolerable. Minor Warning: Minor test comments from ICSD exist. Wyckoff Sequence: e11 (P121/M1). Unit Cell Data Source: Powder Diffraction.

d-Spacings (198) - 01-079-9855 (Fixed Slit Intensity) - Cu Kα1 1.54056Å

2θ	d(Å)	I	h	k	l	*	2θ	d(Å)	I	h	k	l	*	2θ	d(Å)	I	h	k	l	*
9.7830	9.033560	4	0	0	1		38.8665	2.315180	8	3	1	0		52.5019	1.741520	1	2	2	0	
10.0836	8.764890	43	1	0	0		39.0043	2.307320	2	-4	0	2		52.9405	1.728120	1	-4	1	4	
11.3878	7.763860	2	-1	0	1		39.8847	2.258390	1	0	0	4		53.4646	1.712410	11m	-2	1	5	
16.3194	5.427090	1	1	0	1		41.2418	2.187160	12m	4	0	0		53.4646	1.712410	m	-4	0	5	
18.7393	4.731360	1	-1	0	2		41.2418	2.187160	m	-3	0	4		54.0416	1.695480	7	-5	0	4	
19.2177	4.614640	11	-2	0	1		41.7954	2.159460	1m	2	0	3		54.8087	1.673550	15m	1	2	2	
19.6381	4.516780	1	0	0	2		41.7954	2.159460	m	-4	0	3		54.8087	1.673550	m	-5	1	2	
20.2464	4.382440	1	2	0	0		42.2301	2.138230	5m	1	1	3		55.2779	1.660450	65m	1	0	5	
22.8900	3.881930	1	-2	0	2		42.2301	2.138230	m	-3	1	3		55.2779	1.660450	m	-3	1	5	
25.0709	3.548970	92	1	0	2		42.8477	2.108830	1	3	1	1		56.2814	1.633200	174m	3	1	3	
25.4329	3.499270	68m	0	1	1		44.7060	2.025390	42m	1	0	4		56.2814	1.633200	m	-5	1	3	
25.4329	3.499270	m	2	0	1		44.7060	2.025390	m	-1	1	4		56.7795	1.620050	101m	5	0	1	
27.7996	**3.206500**	306	-1	0	3		45.1227	2.007650	3	-2	1	4		56.7795	1.620050	m	-3	2	1	
28.6768	**3.110380**	999m	1	1	1		45.8047	1.979330	11m	4	0	1		57.3388	1.605570	14m	0	2	3	
28.6768	**3.110380**	m	-3	0	1		45.8047	1.979330	m	-4	1	1		57.3388	1.605570	m	-2	2	3	
29.6401	3.011450	50m	0	0	3		45.9944	1.971610	2	-4	1	2		57.4295	1.603250	14	-2	0	6	
29.6401	3.011450	m	-2	0	3		46.7670	1.940820	184m	0	1	4		57.8954	1.591450	1m	3	2	0	
30.1603	2.960680	1m	-1	1	2		46.7670	1.940820	m	-4	0	4		57.8954	1.591450	m	5	1	0	
30.1603	2.960680	m	-3	0	2		47.3365	1.918790	2	-2	0	5		58.4722	1.577120	16m	-1	0	6	
30.4688	2.931400	1	-2	1	1		47.8956	1.897690	225m	4	1	0		58.4722	1.577120	m	-3	0	6	
30.5732	2.921630	1	3	0	0		47.8956	1.897690	m	-3	1	4		59.1377	1.560950	18	-4	1	5	
30.7435	2.905830	2	0	1	2		48.4586	1.876950	38m	2	1	3		59.3786	1.555190	69m	2	2	2	
31.1469	2.869110	3	2	1	0		48.4586	1.876950	m	-4	1	3		59.3786	1.555190	m	-6	0	2	
32.9776	**2.713900**	484m	2	0	2		48.8006	1.864590	3m	3	1	2		59.6886	1.547850	11m	3	0	4	
32.9776	**2.713900**	m	-2	1	2		48.8006	1.864590	m	-5	0	2		59.6886	1.547850	m	-5	1	4	
34.6364	2.587630	3m	1	0	3		49.0746	1.854820	2m	0	2	1		60.1084	1.538040	1m	4	0	3	
34.6364	2.587630	m	-3	0	3		49.0746	1.854820	m	1	2	0		60.1084	1.538040	m	-6	0	3	
34.8452	2.572600	2	2	1	1		49.3101	1.846510	1	-3	0	5		60.4397	1.530400	1m	1	2	3	
35.3598	2.536330	1	3	0	1		49.3980	1.843430	1m	-1	2	1		60.4397	1.530400	m	-3	2	3	
36.6579	2.449440	1	-1	1	3		49.3980	1.843430	m	-5	0	1		60.9182	1.519520	1m	1	1	5	
37.3472	2.405800	1	-3	1	1		50.4715	1.806710	21m	0	0	5		60.9182	1.519520	m	3	2	1	
37.5243	2.394850	1	-1	0	4		50.4715	1.806710	m	3	0	3		61.5368	1.505720	2m	0	0	6	
38.0046	2.365680	2	-2	0	4		51.0741	1.786800	11	1	1	4		61.5368	1.505720	m	-4	0	6	
38.1165	2.358990	3m	0	1	3		51.4545	1.774480	1	2	0	4		61.8580	1.498670	5	2	0	5	
38.1165	2.358990	m	-2	1	3		51.8652	1.761390	1	-1	2	2		62.2631	1.489890	1	5	1	1	
38.5326	2.334470	23	-3	1	2		52.0628	1.755170	2m	5	0	0		62.3794	1.487390	1	-1	2	4	
38.7836	2.319940	8	-4	0	1		52.0628	1.755170	m	-2	2	1		62.7101	1.480340	1m	-2	2	4	

2θ	d(Å)	I	h	k	l	*
62.7101	1.480340	m	-6	0	4	
62.8728	1.476900	1	-2	1	6	
63.0861	1.472420	1	5	0	2	
63.2537	1.468920	2	-4	2	1	
63.4088	1.465700	1	-4	2	2	
63.6459	1.460810	1	6	0	0	
63.8643	1.456340	1m	-1	1	6	
63.8643	1.456340	m	-3	1	6	
64.0325	1.452920	1	0	2	4	
64.8199	1.437160	2	-5	1	5	
65.0104	1.433410	4m	3	1	4	
65.0104	1.433410	m	-3	2	4	
65.4113	1.425590	5m	4	1	3	
65.4113	1.425590	m	-6	1	3	
65.6992	1.420040	1	3	2	2	
65.8695	1.416780	2	-6	1	1	
66.4689	1.405450	1m	1	0	6	
66.4689	1.405450	m	-5	0	6	
66.7879	1.399510	2m	0	1	6	
66.7879	1.399510	m	-4	1	6	
67.0813	1.394100	2m	2	1	5	
67.0813	1.394100	m	-6	0	5	
67.5917	1.384810	1	1	2	4	
67.9062	1.379160	1	-6	1	4	
68.2668	1.372750	12m	5	1	2	
68.2668	1.372750	m	-2	0	7	
68.4308	1.369860	5m	4	2	1	
68.4308	1.369860	m	6	0	1	
69.1738	1.356950	34m	4	0	4	
69.1738	1.356950	m	-4	2	4	
69.6218	1.349310	1	-2	2	5	
69.9375	1.343990	1m	3	0	5	
69.9375	1.343990	m	-1	2	5	
70.8066	1.329610	5m	-4	0	7	
70.8066	1.329610	m	-7	0	3	
71.5256	1.318000	16m	1	1	6	
71.5256	1.318000	m	-5	1	6	
72.1221	1.308560	10m	0	2	5	
72.1221	1.308560	m	-6	1	5	
72.5011	1.302650	1	-7	0	1	
72.9231	1.296150	1	2	2	4	
73.2896	1.290570	10m	0	0	7	
73.2896	1.290570	m	-2	1	7	
73.5962	1.285950	2m	4	2	2	
73.5962	1.285950	m	-3	1	7	
74.8256	1.267840	10m	-1	1	7	
74.8256	1.267840	m	-5	0	7	
75.0649	1.264390	4	-5	2	4	
75.7471	1.254690	1m	-4	1	7	
75.7471	1.254690	m	-7	1	3	
75.8694	1.252970	3m	0	3	1	
75.8694	1.252970	m	7	0	0	
76.1120	1.249580	17m	1	2	5	
76.1120	1.249580	m	-1	3	1	
77.3858	1.232160	52m	1	3	1	
77.3858	1.232160	m	5	2	1	
77.9414	1.224760	21m	2	1	6	
77.9414	1.224760	m	-6	1	6	
78.1647	1.221820	6m	0	1	7	
78.1647	1.221820	m	-1	3	2	
78.4684	1.217850	1m	0	3	2	
78.4684	1.217850	m	1	0	7	
78.8469	1.212950	10m	-1	2	6	
78.8469	1.212950	m	-3	2	6	
79.6362	1.202900	42m	6	1	2	
79.6362	1.202900	m	-6	2	2	
79.9089	1.199480	8m	3	2	4	
79.9089	1.199480	m	5	0	4	
80.0733	1.197430	2	-2	0	8	
80.2773	1.194900	1m	4	2	3	
80.2773	1.194900	m	-6	2	3	
80.5582	1.191440	3m	1	3	2	
80.5582	1.191440	m	-6	0	7	
80.9228	1.186990	1m	7	0	1	
80.9228	1.186990	m	-7	1	5	
81.2537	1.182990	1m	3	0	6	
81.2537	1.182990	m	-4	0	8	
81.5398	1.179560	1m	0	2	6	
81.5398	1.179560	m	-4	2	6	
81.8258	1.176160	3m	2	2	5	
81.8258	1.176160	m	-1	3	3	
82.1660	1.172150	3m	-1	0	8	
82.1660	1.172150	m	-3	3	1	
82.6680	1.166300	4m	0	3	3	
82.6680	1.166300	m	6	0	3	
82.9178	1.163420	2m	5	2	2	
82.9178	1.163420	m	-3	3	2	

Status Alternate **QM:** Star **Pressure/Temperature:** Ambient **Chemical Formula:** (La0.7 Sr0.3) (Mn O3)
Empirical Formula: La0.7 Mn O3 Sr0.3 **Weight %:** La42.94 Mn24.26 O21.19 Sr11.61
Atomic %: La14.00 Mn20.00 O60.00 Sr6.00 **ANX:** ABX3
Compound Name: Strontium Lanthanum Manganese Oxide

Radiation: CuKα **λ:** 1.5406Å **d-Spacing:** Calculated **Intensity:** Calculated **I/Ic:** 5.73

SYS: Rhombohedral **SPGR:** R-3c (167)
Author's Cell [AuthCell a: 5.50850(3)Å **AuthCell c:** 13.37171(5)Å **AuthCell Vol:** 351.39Å³
AuthCell Z: 6.00 **AuthCell MolVol:** 58.56 **]** **Author's Cell Axial Ratio [c/a:** 2.427 **]**
Density [Dcalc: 6.421g/cm³ **Dstruc:** 6.42g/cm³ **]** **SS/FOM:** F(30) = 516.9(0.0019, 31)
Temp: 300.000K (Author provided temperature) **R-factor:** 0.059

Space Group: R-3c (167) **Molecular Weight:** 226.46
Crystal Data [XtlCell a: 5.509Å **XtlCell b:** 5.509Å **XtlCell c:** 13.372Å **XtlCell α:** 90.00° **XtlCell β:** 90.00°
XtlCell γ: 120.00° **XtlCell Vol:** 351.39Å³ **XtlCell Z:** 6.00 **]**
Crystal Data Axial Ratio [c/a: 2.427 **a/b:** 1.000 **c/b:** 2.427 **]**
Reduced Cell [RedCell a: 5.475Å **RedCell b:** 5.476Å **RedCell c:** 5.476Å **RedCell α:** 60.40°
RedCell β: 60.40° **RedCell γ:** 60.40° **RedCell Vol:** 117.13Å³ **]**

Crystal (Symmetry Allowed): Centrosymmetric

Pearson: hR10.00 **Subfile(s):** ICSD Pattern, Inorganic, Alternate Pattern, Ceramic (Ferroelectric)
Entry Date: 07/27/2010 **Last Modification Date:** 01/17/2013

References:

Type	DOI	Reference
Primary Reference		Calculated from ICSD using POWD-12++.
Structure		"Local distortions in the colossal magnetoresistive manganates La0.70 Ca0.30 Mn O3, La0.80 Ca0.20 Mn O3 and La0.70 Sr0.30 Mn O3 revealed by total neutron diffraction". Hibble, S.J., Cooper, S.P., Hannon, A.C., Fawcett, I.D., Greenblatt, M. J. Phys.: Condens. Matter 11, 9221 (1999).

Database Comments: ANX: ABX3. Analysis: La0.7 Mn1 O3 Sr0.3. Formula from original source: (La0.7 Sr0.3) (Mn O3). ICSD Collection Code: 88412. Temperature of Data Collection: 300 K. Wyckoff Sequence: e b a(R3-CH). Unit Cell Data Source: Powder Diffraction.

d-Spacings (74) - 01-089-8098 (Fixed Slit Intensity) - Cu Kα1 1.54056Å

2θ	d(Å)	I	h	k	l	*	2θ	d(Å)	I	h	k	l	*	2θ	d(Å)	I	h	k	l	*
22.8817	3.883320	200	0	1	2		81.0127	1.185900	2	3	1	5		114.1906	0.917464	38	0	5	4	
32.4810	**2.754250**	995	1	1	0		82.0010	1.174090	18	0	4	2		114.5493	0.915614	59	2	3	8	
32.6832	**2.737670**	999	1	0	4		82.2206	1.171510	36	2	2	6		115.1493	0.912556	56	3	0	12	
38.3865	2.343020	13	1	1	3		82.6603	1.166390	20	0	2	10		117.8787	0.899207	1m	2	4	1	
40.1038	2.246560	242	2	0	2		86.5879	1.123280	64	4	0	4		117.8787	0.899207	m	3	3	3	
40.4406	2.228620	88	0	0	6		87.4602	1.114310	23	0	0	12		118.7447	0.895158	1	3	1	11	
46.7456	**1.941660**	605	0	2	4		89.8489	1.090780	1	3	2	1		119.1148	0.893454	15m	2	1	13	
51.0707	1.786910	4	2	1	1		90.1751	1.087680	1	1	3	7		119.1148	0.893454	m	4	2	2	
52.5226	1.740880	52	1	2	2		90.9900	1.080050	14	2	3	2		119.8656	0.890046	8	4	0	10	
52.7966	1.732490	45	1	1	6		91.6432	1.074050	11	2	1	10		120.6218	0.886678	9	2	0	14	
57.9465	1.590170	207	3	0	0		95.4518	1.041010	85	4	1	0		124.4857	0.870442	64	2	4	4	
58.0749	1.586960	350	2	1	4		95.5609	1.040110	90	3	2	4		125.5496	0.866247	69	2	2	12	
58.4591	1.577440	166	0	1	8		95.8901	1.037410	70	3	1	8		128.5415	0.855054	1	5	1	1	
62.0257	1.495020	1	1	2	5		96.4376	1.032970	68	1	1	12		129.2412	0.852561	1	4	1	9	
68.0199	1.377130	148	2	2	0		98.9015	1.013730	1m	1	4	3		130.0153	0.849857	8	1	5	2	
68.4894	1.368830	153	2	0	8		98.9015	1.013730	m	2	3	5		130.3002	0.848876	8	3	3	6	
71.6090	1.316670	3m	1	3	1		99.3987	1.009990	1	2	2	9		130.8738	0.846923	10	3	2	10	
71.6090	1.316670	m	2	2	3		99.6739	1.007940	1	1	2	11		131.7437	0.844019	8	1	2	14	
71.9529	1.311220	1	2	1	7		105.0133	0.970830	40	0	4	8		136.2724	0.829979	48	5	1	4	
72.1821	1.307620	1	1	1	9		108.4165	0.949617	1	3	2	7		136.7470	0.828609	30	5	0	8	
72.8070	1.297930	18	3	1	2		109.2768	0.944531	7	5	0	2		138.6895	0.823195	25	1	0	16	
73.0350	1.294440	24	0	3	6		109.5077	0.943184	18	1	4	6		141.4773	0.815954	1	1	5	5	
73.4897	1.287550	10	1	0	10		109.9705	0.940508	8	1	3	10		142.5389	0.813356	1	2	3	11	
77.5291	1.230240	123	1	3	4		110.6672	0.936536	4	0	1	14		143.0795	0.812066	1	1	3	13	
77.8636	1.225790	126	1	2	8		114.0713	0.918083	33	3	3	0								

Status Alternate **QM:** Star **Pressure/Temperature:** Ambient **Chemical Formula:** Sr (V O3)
Empirical Formula: O3 Sr V **Weight %:** O25.73 Sr46.97 V27.31 **Atomic %:** O60.00 Sr20.00 V20.00
ANX: ABX3 **Compound Name:** Strontium Vanadium Oxide **Common Name:** strontium vanadate(IV)

Radiation: CuKá **:** 1.5406Å **d-Spacing:** Calculated **Intensity:** Calculated **I/Ic:** 8.2

SYS: Cubic **SPGR:** Pm-3m (221)
Author's Cell [AuthCell a: 3.8409(1)Å **AuthCell Vol:** 56.66Å^3 **AuthCell Z:** 1.00 **AuthCell MolVol:** 56.66 **]**
Density [Dcalc: 5.467g/cm^3 **Dstruc:** 5.47g/cm^3 **]** **SS/FOM:** F(20) = 999.9(0.0003, 20)
Temp: 298.000K (Ambient temperature assigned by ICDD editor) **R-factor:** 0.06

Space Group: Pm-3m (221) **Molecular Weight:** 186.56
Crystal Data [XtlCell a: 3.841Å **XtlCell b:** 3.841Å **XtlCell c:** 3.841Å **XtlCell :** 90.00° **XtlCell :** 90.00°
XtlCell : 90.00° **XtlCell Vol:** 56.66Å^3 **XtlCell Z:** 1.00 **]**
Crystal Data Axial Ratio [a/b: 1.000 **c/b:** 1.000 **]**
Reduced Cell [RedCell a: 3.841Å **RedCell b:** 3.841Å **RedCell c:** 3.841Å **RedCell :** 90.00°
RedCell : 90.00° **RedCell :** 90.00° **RedCell Vol:** 56.66Å^3 **]**

Crystal (Symmetry Allowed): Centrosymmetric

Pearson: cP5.00 **Subfile(s):** ICSD Pattern, Inorganic, Alternate Pattern **Entry Date:** 07/27/2010
Last Modification Date: 01/17/2013

References:

Type	DOI	Reference
Primary Reference		Calculated from ICSD using POWD-12++.
Structure		"Synthesis, crystal structure, stoichiometry and magnetic properties of (Ca1-x Srx) V O3". Garcia-Jaca, J., Mesa, J.L., Insausti, M., Larramendi, J.I.R., Arriortua, M.I., Rojo, T. Mater. Res. Bull. 34, 289 (1999).

Database Comments: ANX: ABX3. Analysis: O3 Sr1 V1. Formula from original source: Sr (V O3). ICSD Collection Code: 88982. Wyckoff Sequence: d b a(PM3-M). Unit Cell Data Source: Powder Diffraction.

d-Spacings (20) - 01-089-8658 (Fixed Slit Intensity) - Cu K1 1.54056Å

2	d(Å)	I	h	k	l	*	2	d(Å)	I	h	k	l	*	2	d(Å)	I	h	k	l	*
23.1379	3.840900	27	1	0	0		73.9749	1.280300	14	2	2	1		111.5582	0.931555	13	4	1	0	
32.9522	**2.715930**	999	1	1	0		78.7190	1.214600	116	3	1	0		116.6080	0.905309	72	4	1	1	
40.6516	2.217540	186	1	1	1		83.3863	1.158070	45	3	1	1		121.8921	0.881163	23	3	3	1	
47.2931	**1.920450**	371	2	0	0		88.0091	1.108770	51	2	2	2		127.5000	0.858851	79	4	2	0	
53.2869	1.717700	23	2	1	0		92.6194	1.065270	8	3	2	0		133.5667	0.838153	13	4	2	1	
58.8439	**1.568040**	316	2	1	1		97.2466	1.026520	128	3	2	1		140.3211	0.818883	45	3	3	2	
69.1150	1.357960	178	2	2	0		106.6789	0.960225	24	4	0	0								

Status Alternate **QM:** Star **Pressure/Temperature:** Ambient **Chemical Formula:** Ca (V O3)
Empirical Formula: Ca O3 V **Weight %:** Ca28.83 O34.53 V36.64 **Atomic %:** Ca20.00 O60.00 V20.00
ANX: ABX3 **Compound Name:** Calcium Vanadium Oxide **Common Name:** calcium vanadate(IV)

Radiation: CuKá **:** 1.5406Å **d-Spacing:** Calculated **Intensity:** Calculated **I/Ic:** 2.9

SYS: Orthorhombic **SPGR:** Pnma (62)
Author's Cell [AuthCell a: 5.3171(5)Å **AuthCell b:** 7.5418(8)Å **AuthCell c:** 5.3396(5)Å
AuthCell Vol: 214.12Å³ **AuthCell Z:** 4.00 **AuthCell MolVol:** 53.53 **]**
Author's Cell Axial Ratio [c/a: 1.004 **a/b:** 0.705 **c/b:** 0.708 **]**
Density [Dcalc: 4.312g/cm³ **Dstruc:** 4.31g/cm³ **]** **SS/FOM:** F(30) = 51.6(0.0114, 51)
Temp: 298.000K (Ambient temperature assigned by ICDD editor) **R-factor:** 0.054

Space Group: Pcmn (62) **Molecular Weight:** 139.02
Crystal Data [XtlCell a: 5.340Å **XtlCell b:** 7.542Å **XtlCell c:** 5.317Å **XtlCell :** 90.00° **XtlCell :** 90.00°
XtlCell : 90.00° **XtlCell Vol:** 214.12Å³ **XtlCell Z:** 4.00 **]**
Crystal Data Axial Ratio [c/a: 0.996 **a/b:** 0.708 **c/b:** 0.705 **]**
Reduced Cell [RedCell a: 5.317Å **RedCell b:** 5.340Å **RedCell c:** 7.542Å **RedCell :** 90.00°
RedCell : 90.00° **RedCell :** 90.00° **RedCell Vol:** 214.12Å³ **]**

Crystal (Symmetry Allowed): Centrosymmetric

Pearson: oP20.00 **Prototype Structure:** Gd Fe O3 **Prototype Structure (Alpha Order):** Fe Gd O3
LPF Prototype Structure: Gd Fe O3,oP20,62 **LPF Prototype Structure (Alpha Order):** Fe Gd O3,oP20,62
Subfile(s): Inorganic, ICSD Pattern, Alternate Pattern **Entry Date:** 07/27/2010
Last Modification Date: 01/17/2013

References:

Type	DOI	Reference
Primary Reference		Calculated from ICSD using POWD-12++.
Structure		"Synthesis, crystal structure, stoichiometry and magnetic properties of (Ca1-x Srx) V O3". Garcia-Jaca, J., Mesa, J.L., Insausti, M., Larramendi, J.I.R., Arriortua, M.I., Rojo, T. Mater. Res. Bull. 34, 289 (1999).

Database Comments: ANX: ABX3. Analysis: Ca1 O3 V1. Formula from original source: Ca (V O3). ICSD Collection Code: 88978. Wyckoff Sequence: d c2 b(PNMA). Unit Cell Data Source: Powder Diffraction.

d-Spacings (187) - 01-089-8654 (Fixed Slit Intensity) - Cu K1 1.54056Å

2	d(Å)	I	h	k	l	*	2	d(Å)	I	h	k	l	*	2	d(Å)	I	h	k	l	*
20.3615	4.357930	8	0	1	1		68.0334	1.376890	3	2	2	3		91.4799	1.075540	2	4	3	2	
23.5939	3.767690	153m	0	2	0		70.4841	1.334900	48	0	0	4		92.3904	1.067310	2	1	4	4	
23.5939	3.767690	m	1	0	1		70.6209	1.332650	167	2	4	2		92.6949	1.064600	2m	4	0	3	
26.4218	3.370500	10	1	1	1		70.8268	1.329280	40	4	0	0		92.6949	1.064600	m	4	4	1	
33.5967	**2.665290**	999m	0	0	2		72.0877	1.309100	2	4	1	0		93.7019	1.055790	4m	3	1	4	
33.5967	**2.665290**	m	1	2	1		73.0166	1.294720	3	1	0	4		93.7019	1.055790	m	3	5	2	
35.7825	2.507330	7	2	1	0		73.3332	1.289910	2	4	0	1		94.7319	1.047010	1	1	0	5	
37.6700	2.385920	12	1	0	2		74.2627	1.276050	8m	1	1	4		94.9011	1.045590	1m	2	6	2	
37.7692	2.379880	19	2	0	1		74.2627	1.276050	m	1	5	2		94.9011	1.045590	m	3	4	3	
39.5850	2.274800	29m	0	3	1		74.4556	1.273220	3	3	3	2		95.2188	1.042940	1	5	0	1	
39.5850	2.274800	m	1	1	2		75.5445	1.257550	7m	0	6	0		95.9330	1.037060	1	1	1	5	
41.4041	2.178960	50	0	2	2		75.5445	1.257550	m	1	4	3		96.4202	1.033110	1	5	1	1	
41.5261	2.172840	46	2	2	0		75.7116	1.255190	4m	3	0	3		97.3049	1.026060	2	3	2	4	
43.2276	2.091170	1	1	3	1		75.7116	1.255190	m	3	4	1		99.6497	1.008120	62m	1	6	3	
44.9202	2.016230	19	1	2	2		75.8203	1.253660	2	4	2	0		99.6497	1.008120	m	2	4	4	
45.0061	2.012580	13	2	2	1		76.8918	1.238840	1	3	1	3		99.8142	1.006900	44m	3	6	1	
48.2700	**1.883840**	502m	0	4	0		77.9573	1.224550	3	1	2	4		99.8142	1.006900	m	4	4	2	
48.2700	**1.883840**	m	2	0	2		78.2669	1.220480	5	4	2	1		100.0447	1.005200	33	5	2	1	
49.8523	1.827690	10m	2	1	2		80.4833	1.192360	70m	1	6	1		100.9635	0.998520	1	2	7	0	
49.8523	1.827690	m	2	3	0		80.4833	1.192360	m	3	2	3		101.1369	0.997276	1	4	5	0	
52.8591	1.730590	8m	1	3	2		80.6807	1.189940	30	4	0	2		102.0294	0.990959	1	2	0	5	
52.8591	1.730590	m	2	3	1		81.7179	1.177440	2m	2	1	4		102.4640	0.987934	1	5	0	2	
54.3966	1.685250	26m	1	4	1		81.7179	1.177440	m	2	5	2		103.2666	0.982432	4m	1	5	4	
54.3966	1.685250	m	2	2	2		81.8900	1.175400	2m	4	1	2		103.2666	0.982432	m	1	7	2	
54.5062	1.682120	9	3	0	1		81.8900	1.175400	m	4	3	0		103.3832	0.981642	3m	2	7	1	
55.9613	1.641780	2	3	1	1		82.9953	1.162530	1	3	4	2		103.3832	0.981642	m	3	3	4	
60.0009	**1.540540**	235m	0	4	2		84.0112	1.151040	6m	0	5	3		103.5288	0.980658	2m	4	3	3	
60.0009	**1.540540**	m	1	2	3		84.0112	1.151040	m	1	3	4		103.5288	0.980658	m	4	5	1	
60.1874	1.536210	199m	2	4	0		85.2707	1.137230	2m	0	6	2		105.6796	0.966535	1	1	3	5	
60.1874	1.536210	m	3	2	1		85.2707	1.137230	m	2	2	4		105.8980	0.965143	1	3	5	3	
61.4545	1.507540	1	2	3	2		85.3515	1.136360	2	2	6	0		106.1844	0.963328	1	5	3	1	
62.8273	1.477860	5m	2	4	1		86.4536	1.124680	1	1	5	3		107.0706	0.957794	1m	2	6	3	
62.8273	1.477860	m	3	0	2		86.6149	1.123000	1m	3	3	3		107.0706	0.957794	m	3	6	2	
64.0997	1.451560	4m	0	5	1		86.6149	1.123000	m	3	5	1		107.4143	0.955680	1	5	2	2	
64.0997	1.451560	m	2	1	3		87.6802	1.112080	1m	1	6	2		109.5867	0.942725	13	0	8	0	
64.2215	1.449100	3	3	1	2		87.6802	1.112080	m	2	6	1		109.7253	0.941922	16	4	0	4	
66.6920	1.401290	1m	1	3	3		89.9853	1.089480	29	0	4	4		111.0005	0.934660	1m	4	1	4	
66.6920	1.401290	m	1	5	1		90.3085	1.086420	28	4	4	0		111.0005	0.934660	m	4	5	2	
66.8679	1.398030	2	3	3	1		91.2369	1.077770	1	2	3	4		112.3321	0.927317	1	4	4	3	

2	d(Å)	I	h	k	l	*
113.3396	0.921919	1m	0	7	3	
113.3396	0.921919	m	2	3	5	
113.8031	0.919481	1	5	3	2	
114.7261	0.914708	3m	1	8	1	
114.7261	0.914708	m	3	0	5	
114.8955	0.913844	1	4	2	4	
115.0829	0.912892	1m	5	0	3	
115.0829	0.912892	m	5	4	1	
116.0304	0.908147	1m	1	7	3	
116.0304	0.908147	m	3	1	5	
116.2106	0.907257	1	3	7	1	
116.4100	0.906277	1	5	1	3	
117.3210	0.901861	1	1	6	4	
117.6630	0.900229	1	4	6	1	
119.8907	0.889933	9	0	0	6	
120.1148	0.888929	48m	3	2	5	
120.1148	0.888929	m	3	6	3	
120.4896	0.887262	35	5	2	3	
120.7342	0.886183	8	6	0	0	
121.6869	0.882042	1	4	3	4	
122.1351	0.880128	1	6	1	0	
122.7055	0.877724	1m	1	0	6	
122.7055	0.877724	m	2	4	5	
123.0076	0.876465	1m	1	8	2	
123.0076	0.876465	m	2	8	1	
123.5508	0.874225	1	6	0	1	
124.1376	0.871840	5m	0	5	5	
124.1376	0.871840	m	1	1	6	
124.4210	0.870701	3m	3	5	4	
124.4210	0.870701	m	3	7	2	
124.9974	0.868410	1	6	1	1	
125.5771	0.866140	1	0	2	6	
125.7957	0.865293	1	2	6	4	
126.0955	0.864139	1	4	6	2	
126.4773	0.862682	1	6	2	0	
127.1617	0.860107	1m	1	5	5	
127.1617	0.860107	m	3	3	5	
127.7734	0.857844	1m	5	3	3	
127.7734	0.857844	m	5	5	1	
128.5921	0.854872	2	1	2	6	
129.5037	0.851638	1	6	2	1	
131.7777	0.843907	13	2	0	6	
132.0371	0.843055	41m	2	8	2	
132.0371	0.843055	m	4	4	4	
132.6515	0.841061	11	6	0	2	
134.2989	0.835879	1m	6	1	2	
134.2989	0.835879	m	6	3	0	
135.6659	0.831757	1	5	0	4	
136.7264	0.828668	4	1	3	6	
136.9026	0.828164	4m	0	9	1	
136.9026	0.828164	m	1	7	4	
137.4034	0.826745	1m	5	1	4	
137.4034	0.826745	m	5	5	2	
138.7716	0.822973	4m	1	8	3	
138.7716	0.822973	m	3	4	5	
139.2653	0.821649	1	5	4	3	
139.5513	0.820891	1	6	2	2	
140.6693	0.817990	1m	1	9	1	
140.6693	0.817990	m	3	7	3	
142.6329	0.813130	1m	3	6	4	
142.6329	0.813130	m	4	6	3	
146.4664	0.804481	19m	0	4	6	
146.4664	0.804481	m	1	6	5	
147.3555	0.802629	22	5	6	1	
147.6574	0.802013	13	6	4	0	
148.8829	0.799579	1m	2	3	6	
148.8829	0.799579	m	2	7	4	
149.3559	0.798668	2m	4	5	4	
149.3559	0.798668	m	4	7	2	
149.9173	0.797607	1	6	3	2	

Status Primary **QM:** Star **Pressure/Temperature:** Ambient **Chemical Formula:** Pt **Empirical Formula:** Pt
Weight %: Pt100.00 **Atomic %:** Pt100.00 **Compound Name:** Platinum **Mineral Name:** Platinum, syn

Radiation: CuKá **:** 1.5406Å **Filter:** Ni Beta **Intensity:** Diffractometer

SYS: Cubic **SPGR:** Fm-3m (225)
Author's Cell [AuthCell a: 3.9231Å **AuthCell Vol:** 60.38Å³ **AuthCell Z:** 4.00 **AuthCell MolVol:** 15.10 **]**
Density [Dcalc: 21.461g/cm³ **Dmeas:** 21.37g/cm³ **]** **SS/FOM:** F(9) = 145.2(0.0069, 9)
Temp: 299.000K (Author provided temperature)

Space Group: Fm-3m (225) **Molecular Weight:** 195.09
Crystal Data [XtlCell a: 3.923Å **XtlCell b:** 3.923Å **XtlCell c:** 3.923Å **XtlCell :** 90.00° **XtlCell :** 90.00°
XtlCell : 90.00° **XtlCell Vol:** 60.38Å³ **XtlCell Z:** 4.00 **]**
Crystal Data Axial Ratio [a/b: 1.000 **c/b:** 1.000 **]**
Reduced Cell [RedCell a: 2.774Å **RedCell b:** 2.774Å **RedCell c:** 2.774Å **RedCell :** 60.00°
RedCell : 60.00° **RedCell :** 60.00° **RedCell Vol:** 15.09Å³ **]**

Crystal (Symmetry Allowed): Centrosymmetric

CAS: 7440-06-4 **Pearson:** cF4.00 **Prototype Structure:** Cu **Prototype Structure (Alpha Order):** Cu
LPF Prototype Structure: Cu,cF4,225 **LPF Prototype Structure (Alpha Order):** Cu,cF4,225
Mineral Classification: Gold (Supergroup), 1C-disordered (Group)

Subfile(s): Common Phase, Forensic, Educational Pattern, Metals & Alloys, Primary Pattern, Inorganic, Mineral Related (Mineral , Synthetic), NBS Pattern

Last Modification Date: 01/11/2013

Cross-Ref PDF #'s: 04-001-0112, 04-001-0489, 04-001-0537, 04-001-0839, 04-001-1793, 04-002-0887, 04-002-2613, 04-002-9729, 04-002-9895, 04-003-2557, 04-003-6500, 04-003-7036, 04-003-7149, 04-004-4405, 04-004-4514, 04-004-6287, 04-004-6358, 04-004-6364, 04-004-8457, 04-004-8733, 04-007-2989, 04-011-7822, 04-011-9016

References:

Type	DOI	Reference
Primary Reference		Swanson, Tatge. Natl. Bur. Stand. (U. S.), Circ. 539 I, 31 (1953).

Database Comments: Color: Light gray metallic. Opaque Optical Data: Opaque mineral optical data on specimen from unspecified locality: RR2Re=70.3, Disp.=16, VHN50=122-129, Color values=.318, .324, 70.7, Ref.: IMA Commission on Ore Microscopy QDF. Sample Preparation: Sample prepared at NBS, Gaithersburg, Maryland, USA, and estimated to be more than 99.99% pure. Temperature of Data Collection: Pattern taken at 299 K. Unit Cell Data Source: Powder Diffraction.

d-Spacings (9) - 00-004-0802 (Fixed Slit Intensity) - Cu K1 1.54056Å

2	d(Å)	I	h	k	l	*	2	d(Å)	I	h	k	l	*	2	d(Å)	I	h	k	l	*
39.7634	**2.265000**	100	1	1	1		81.2861	**1.182600**	33	3	1	1		117.7112	0.900000	22	3	3	1	
46.2427	**1.961600**	53	2	0	0		85.7121	1.132500	12	2	2	2		122.8070	0.877300	20	4	2	0	
67.4541	1.387300	31	2	2	0		103.5078	0.980800	6	4	0	0		148.2615	0.800800	29	4	2	2	

Annexe B: List of publications, posters, and oral presentations

Publications (6)

1) *Textured Manganite Films Anywhere*
A. Boileau , M. Dallocchio, **F. Baudouin**, A. David, U. Lüders, B. Mercey, A. Pautrat, V. Demange, M. Guilloux-Viry, W. Prellier,A. Fouchet
ACS Appl. Mater. Int., **11**, (2019) 37302−37312
https://doi.org/10.1021/acsami.9b12209

2) *Orientation control of $KNbO_3$ film grown on glass substrates by $Ca_2Nb_3O_{10}^-$ nanosheets seed layer*
F. Baudouin, V. Demange, S. Ollivier, L. Rault, A.S. Brito, A.S. Maia, F. Gouttefangeas, V. Bouquet, S. Députier, B. Bérini, A. Fouchet, M. Guilloux-Viry
Thin Solid Films **693**, (2020) 137682
https://doi.org/10.1016/j.tsf.2019.137682

3) *Influence of two-dimensional oxide nanosheets seed layers on the growth of (100)$BiFeO_3$ thin films synthesized by chemical solution deposition*
V. Bouquet, **F. Baudouin**, V. Demange, S. Députier, S. Ollivier, L. Joanny, L. Rault, A. Fouchet, M. Guilloux-Viry
Thin Solid Films, **693**, (2020) 137687
https://doi.org/10.1016/j.tsf.2019.137687

4) *Highly textured Pt thin film grown at very low temperature using $Ca_2Nb_3O_{10}$ nanosheets as seed layer*
J. J. Manguele, **F. Baudouin**, C. Cibert, B. Domengès, V. Demange, M. Guilloux-Viry, A. Fouchet, G. Poullain
SN Applied Sciences, **2**, (2020) 453
https://doi.org/10.1007/s42452-020-2271-9

5) *Highly Transparent and Conductive Indium-Free Vanadates Crystallized at Reduced Temperature on Glass Using a 2D Transparent Nanosheet Seed Layer*
A. Boileau, S. Hurand, **F. Baudouin**, U. Lüders, M. Dallocchio, B. Bérini, A. Cheikh, A. David, F. Paumier, T. Girardeau, P. Marie, C. Labbé, J. Cardin, D. Aureau, M. Frégnaux, M. Guilloux-Viry, W. Prellier, Y. Dumont, V. Demange, A. Fouchet
Adv. Funct. Mater., (2021) 2108047
https://doi.org/10.1002/adfm.202108047

6) *Orientation control of Platinum electrode grown on silicon using $[Ca_2Nb_3O_{10}]^-$ nanosheets as seed layer*
J.J. Manguele, **F. Baudouin**, C. Cibert, B. Domengès, V. Demange, M. Guilloux-Viry, A. Fouchet, G. Poullain
Submitted to Thin Solid Films

Oral presentations at conferences and workshops (16)

1) *Synthèse et transfert de nanofeuillets à deux dimensions $Ca_2Nb_3O_{10}^-$ sur substrats à bas coût pour la croissance épitaxiale de $KNbO_3$ et $BiFeO_3$*
F. Baudouin, V. Demange, A. Boileau, B. Bérini, S. Ollivier, A. Da Silva Maia, S. Députier, V. Bouquet, A. Fouchet, M. Guilloux-Viry
JNano19: Journées Nanosciences, February 13-15, 2019, Rennes, France

2) *Synthesis and transfer of $Ca_2Nb_3O_{10}^-$ seed layer on low cost substrate for $KNbO_3$ and $BiFeO_3$ growth*
F. Baudouin, V. Demange, V. Bouquet, B. Bérini, S. Ollivier, S. Députier, A. Fouchet, M. Guilloux-Viry
European Materials Research Society (E-MRS) Spring Meeting, May 27-31, 2019, Nice, France

3) *Integration of highly (001)-oriented $La_{0.67}Sr_{0.33}MnO_3$ thin films onto glass substrates using $Ca_2Nb_3O_{10}^-$ nanosheets as template layer*
A. Boileau, M. Dallocchio, **F. Baudouin**, A. David, U. Lüders, B. Mercey, V. Demange, M. Guilloux-Viry, W. Prellier, A. Fouchet
European Materials Research Society (E-MRS) Spring Meeting, May 27-31, 2019, Nice, France

4) *Synthesis and transfer of $Ca_2Nb_3O_{10}^-$ seed layer on low cost substrate for complex oxides growth*
V. Demange, **F. Baudouin**, V. Bouquet, S. Ollivier, B. Bérini, F. Gouttefangeas, S. Députier, A. Fouchet, M. Guilloux-Viry
ECSSC17, September 1-4, 2019, Lille, France

5) *Tuning the properties of the new perovskite transparent conductor $SrVO_3$ and its integration on low cost substrates*
A. Boileau, A. Cheikh, A. David, C. Labbé, J. Cardin, F. Gourbilleau, M. Dallocchio, **F. Baudouin**, V. Demange, M. Guilloux-Viry, W. Prellier, A. Fouchet and U. Lüders
European Materials Research Society (E-MRS) 2019, Fall meeting, September 27-31, 2019, Warsaw, Poland.

6) *Synthesis and transfer of $Ca_2Nb_3O_{10}$ seed layer on low cost substrate for complex oxides growth*
F. Baudouin, A. Boileau, M. Dallocchio, V. Bouquet, S. Ollivier, A. David, U. Lüders, B. Mercey, L. Rault, B. Bérini, Y. Dumont, S. Députier, W. Prellier, M. Guilloux-Viry, A. Fouchet, V. Demange
GDR Oxyfun, October 1-2, 2019, Caen, France

7) *Integration of highly (001)-textured $La_{0.67}Sr_{0.33}MnO_3$ thin films onto glass substrates using $Ca_2Nb_3O_{10}^-$ nanosheets as template layer*
A. Boileau, M. Dallocchio, **F. Baudouin**, A. David, U. Lüders, B. Mercey, A. Pautrat, V. Demange, M. Guilloux-Viry, W. Prellier, A. Fouchet
GDR Meeticc, October 3-4, 2019, Caen, France.

8) Physico-chemical and electronic properties of $Ca_2Nb_3O_{10}$ 2D-perovskite on Silicon
H. Glavina, **F. Baudouin**, A. Alix, B. Lépine, J. C. Le Breton, P. Schieffer, V. Demange, P. Turban
Journée Nanomatériaux, January 14th, 2020, Rennes, France.

9) Contrôle de texturation et d'orientation de films de Pt sur silicium à l'aide de nanofeuillets $Ca_2Nb_3O_{10}$
J. J. Manguele, **F. Baudouin**, C. Cibert, B. Domengès, V. Demange, M. Guilloux-Viry, A. Fouchet, G. Poullain
Lab Meeting CRISMAT, 2020 February 13th, 2020, Caen, France.

10) *Integration of new transparent conductors $CaVO_3$ and $SrVO_3$ thin films onto glass using calcium niobate nanosheets as template layer*
A. Boileau, **F. Baudouin**, A. Cheikh, M. Dallocchio, A. David, U. Lüders, B. Bérini, Y. Dumont, C. Labbé, J. Cardin, F. Gourbilleau, S. Hurand, V. Demange, M. Guilloux-Viry, W. Prellier, A. Fouchet
European Materials Research Society (E-MRS) 2020, May 25-29, 2020, Strasbourg, France. Accepted but cancelled due to the pandemic situation.

11) Texturation à basse température et contrôle d'orientation de films minces de Pt sur substrats Si à l'aide de nanofeuillets de $Ca_2Nb_3O_{10}$
J. J. Manguele, **F. Baudouin**, C. Cibert, B. Domengès, V. Demange, M. Guilloux-Viry, A. Fouchet, G. Poullain
CRISTECH national conference, October 14-16, 2020, Ecully, France, online presentation.

12) *Local conductivity of transparent nanostructured $SrVO_3$ perovskite film on nanosheets by SSRM*
R. Coq Germanicus, A. Boileau, M. Dallocchio, **F. Baudouin**, A. David, W. Prellier, V. Demange, U. Lüders, A. Fouchet
International Scanning Probe Microscopy (ISPM), June 28-July 2, 2021, online presentation.

13) *Synthesis and transfer of nanosheets seed layer on low-cost substrates for complex oxides growth*
F. Baudouin, A. Boileau, J. J. Manguele, M. Dallocchio, S. Ollivier, C. Cibert, S. Hurand, V. Bouquet, A. David, U. Lüders, G. Poullain, B. Bérini, Y. Dumont, S. Députier, W. Prellier, M. Guilloux-Viry, A. Fouchet, V. Demange
22nd American Conference on Crystal Growth and Epitaxy (ACCGE-22), August 2-5, 2021, online presentation

14) *Highly transparent and conductive indium-free $CaVO_3$ and $SrVO_3$ crystallized at reduced temperature on glass using a 2D transparent nanosheet seed layer*
A. Boileau, S. Hurand, **F. Baudouin**, U. Lüders, M. Dallocchio, B. Bérini, A. Cheikh, A. David, F. Paumier, T. Girardeau, P. Marie, C. Labbé, J. Cardin, M. Guilloux-Viry, W. Prellier, Y. Dumont, V. Demange, A. Fouchet
Journée de la Matière Condensée, August 24-27, 2021, Rennes, online presentation

15) *Oxide nanosheets as seed layers for epitaxial growth of complex oxides*
F. Baudouin, A. Boileau, J.J. Manguele, M. Dallocchio, S. Ollivier, P. Turban, B. Lépine, C. Cibert, S. Hurand, A. David, U. Lüders, G. Poullain, B. Bérini, Y. Dumont, V. Bouquet, S. Députier, W. Prellier, M. Guilloux-Viry, A. Fouchet, V. Demange
6th edition of the International Workshop of Materials Physics (IWMP), September 14-16, 2021, Magurele, Romania

16) *Oxide nanosheets as seed layers for epitaxial growth of complex oxides*
F. Baudouin, A. Boileau, J.J. Manguele, M. Dallocchio, S. Ollivier, P. Turban, B. Lépine, C. Cibert, S. Hurand, A. David, U. Lüders, G. Poullain, B. Bérini, Y. Dumont, V. Bouquet, S. Députier, W. Prellier, M. Guilloux-Viry, A. Fouchet, V. Demange
EPIDOX: workshop on oxides epitaxy, November 17-19, 2021, online presentation

Poster presentations at conferences and workshops (4)

1) *Influence of two-dimensional oxide nanosheet seed layers on the growth of (100)$BiFeO_3$ thin films synthesized by CSD*
V. Bouquet, **F. Baudouin**, V. Demange, S. Députier, S. Ollivier, A. Fouchet, M. Guilloux-Viry
European Materials Research Society (E-MRS) 2019, May 27-31th, 2019, Nice, France.

2) *Textured Manganite Films Anywhere*
A. Boileau, M. Dallocchio, **F. Baudouin**, A.David, U. Lüders, B. Mercey, A. Pautrat, V. Demange, M. Guilloux-Viry, W. Prellier, A. Fouchet
GDR oxyfun, October 1-2, 2019, Caen, France

3) *Synthesis and transfer of nanosheets seed layer on low cost substrates for complex oxides growth*
F. Baudouin, A. Boileau, M. Dallocchio, S. Ollivier, V. Bouquet, A. David, U. Lüders, B. Mercey, B. Bérini, Y. Dumont, S. Députier, W. Prellier, M. Guilloux-Viry, A. Fouchet, V. Demange
Journée Nanomatériaux, January 14th, 2020, Rennes, France

4) *Optimization of the new transparent conducting oxide $SrVO_3$ for applications*
U. Lüders, A. Boileau, M. Rath, M. Mezhoud, O. El Khaloufi, A. Cheikh, A. David, R. Coq Germanicus, A. Fouchet, F. Gourbilleau, C. Labbé, **F. Baudouin**, V. Demange
International Workshop on Oxide Electronics, October 13-15, 2021, Genoa, Italy

UNIVERSITÉ DE RENNES 1

Synthèse et transfert de nanofeuillets oxydes sur divers substrats pour la croissance contrôlée de couches minces d'oxydes complexes selon une orientation préférentielle.

Mots clés : Nanofeuillets, Langmuir-Blodgett, drop casting, couches minces, oxydes, croissance orientée.

Résumé : Le but de ce travail est le développement de nouveaux substrats à bas coût pour la croissance contrôlée et l'étude d'oxydes fonctionnels afin de pouvoir proposer une nouvelle solution pour l'intégration d'oxydes complexes à propriétés multifonctionnelles pour l'électronique sur grandes surfaces. Cette intégration est généralement obtenue par croissance épitaxiale sur des substrats monocristallins coûteux, offrant un choix limité de substrats et d'orientations cristallographiques possible. L'objectif de cette thèse est de remplacer ces substrats monocristallins par des substrats amorphes ou peu coûteux recouverts d'un "template" cristallisé sous forme de nanofeuillets, qui servira de couche de germination pour la croissance orientée d'oxydes fonctionnels. Ces nanofeuillets à 2 dimensions (2D) sont obtenu par la protonation et l'exfoliation de phases lamellaires oxydes. Chaque nanofeuillet possède un réseau cristallographique 2D carré, rectangulaire ou hexagonal qui permettra la croissance selon une orientation spéficique. Leurs transferts sur différents substrats ont été réalisé par la technique de Langmuir-Blogett et la méthode de drop casting. Les nanofeuillets $[Ca_2Nb_3O_{10}]^-$ ont permis la croissance d'oxydes complexes à structure perovskite tel que $KNbO_3$, $BiFeO_3$, $La_{0.67}Sr_{0.33}MnO_3$, $SrVO_3$, et $CaVO_3$ selon leurs orientation [001] sur divers substrats. Des couches minces de Pt ont étalement été déposé à basse température selon leurs orientations [111] et [200] sur ce type de nanofeuillets. Les dépôts de matériaux ont été réalisé par ablation laser pulsée, voie chimique en solution et pulvérisation cathodique.

Synthesis and transfer of nanosheets seed layers on various substrates for the preferentially oriented growth of complex oxides thin films.

Keywords: 2D-nanosheets, Langmuir-Blodgett, drop casting, thin films, oxides, oriented growth.

Abstract: This work aims to propose a new solution for the growth of functional oxides on low-cost substrates and to develop the integration of high-quality complex oxides with multifunctional properties for large surface electronics. These materials are usually obtained by epitaxial growth on relatively expensive single crystalline substrates, which offer a limited choice of materials and crystallographic orientations commercially available. This thesis focuses on the replacement of these single crystalline substrates by low-cost or amorphous substrates covered by a crystalline template of molecular thickness (oxide nanosheets), that can be used as seed layers to induce epitaxy of complex oxides thin films. 2 dimensional (2D) nanosheets were obtained by the protonation and exfoliation of layered oxides. These types of nanosheets possess 2D square lattice, rectangular lattice and hexagonal lattice respectively. Their transfer on different substrates were performed by the Langmuir-Blodgett and the drop casting techniques. $[Ca_2Nb_3O_{10}]^-$ nanosheets has enabled the growth of complex oxide perovskites thin films on various substrates, such as $KNbO_3$, $BiFeO_3$, $La_{0.67}Sr_{0.33}MnO_3$, $SrVO_3$, and $CaVO_3$ along their cubic [001] orientation. Pt thin films grown along their [111] and [200] direction, deposited at very low temperature. The oxides and metal depositions have been achieved using different techniques as pulsed laser deposition, chemical solution deposition and sputtering.